# QUASISTATIC AND ULTRAFAST MAGNETIZATION DYNAMICS IN FERROMAGNETIC NANOSTRUCTURES

Corrected Copy

Thesis submitted for the degree of

**Doctor of Philosophy (Science)**

In

**Physics (Experimental)**

By

**Arundhati Adhikari**

**Department of Physics**
**University of Calcutta**
**2024**

*To my beloved family...*

# List of Publications

## Included in the thesis

1. "Anisotropic Spin-Wave Propagation in Asymmetric Width Modulated $Ni_{80}Fe_{20}$ Nanostripes", **A. Adhikari**, C. Banerjee, A. K. Mondal, A. K. Chaurasiya, S. Choudhury, J. Sinha, S. Barman, A. Barman, *Materials Science & Engineering B* 272, 115385 (2021).

2. "Active Control of Dipole-Exchange Coupled Magnon Modes in Nanoscale Bicomponent Magnonic Crystals", **A. Adhikari**, S. Majumder, Y. Otani, A. Barman *ACS Appl. Nano Mater.* 6, 7166 (2023).

3. "Ultrafast Spin Dynamics of Electrochemically Grown Heusler Alloy Films", M. R. Karim, **A. Adhikari**, S. N. Panda, P. Sharangi, S. Kayal, G. Manna, P. S. A. Kumar, S. Bedanta, A. Barman, and I. Sarkar, *J. Phys. Chem. C* 125, 10483 (2021).

4. "Room Temperature Evolution of Laser Induced Ultrafast Spin and Phonon Dynamics in 2D van der Waals Magnets $Fe_xGeTe_2$ (x = 3,4,5)", **A. Adhikari** *et al.* (manuscript accepted for publication in Adv. Func. Mater., https://doi.org/10.1002/adfm.202418006).

5. "Tunable Short-Wavelength Spin-Wave Excitation and Localization in Nanoscale Domain Structures", **A. Adhikari** *et al.* (manuscript to be submitted).

6. "Direct Evidence of Ultrafast Laser-Induced Magnetoelastic Interaction in $Ni_{80}Fe_{20}$ Nanomagnets", **A. Adhikari** *et al.* (manuscript to be submitted).

## Not included in the thesis

1. "Spin-Texture Driven Reconfigurable Magnonics in Chains of Connected $Ni_{80}Fe_{20}$ Submicron Dots", A. K. Mondal, C. Banerjee, **A. Adhikari**, A. K. Chaurasiya, S. Choudhury, J. Sinha, S. Barman, A. Barman, *Phys. Rev. B*, 101, 224426 (2020).

2. "Extreme Subwavelength Magnetoelastic Electromagnetic Antenna Implemented with Multiferroic Nanomagnets", J. L. Drobitch, A. De, K. Dutta, P. K. Pal, **A. Adhikari**, A. Barman, S. Bandyopadhyay, *Adv. Mater. Technologies*, 5, 200316 (2020).

3. "Electrodeposited Heusler Alloy Films with Enhanced Magneto-Optical Property", M. R. Karim, D. Panda, **A. Adhikari**, P. Sharangi, P. Mandal, S. Ghosh, S. Bedanta, A. Barman, I. Sarkar, *Materials Today Commun.*, 25, 101678 (2020).

# Acknowledgement

Having spent a considerable time in this tough journey of scientific pursuit, finally I have had the opportunity to express my gratitude. Firstly, I express my gratitude to Prof. (Dr.) Anjan Barman for carefully supervising my research and patiently guiding me towards the completion of my PhD. I sincerely thank him for providing me the opportunity to work in his well-equipped laboratories and the essential resources during my PhD. I feel greatly benefited from his culminating experience and expertise, his dexterity in experiments and strategic works as well as the rigour of training and consistent suggestions for improvement to grow as a researcher. I am thankful to him for his encouragement to pursue few projects almost independently. I am also grateful to Dr. Jaivardhan Sinha (SRMIST, Chennai) who co-guided me during my initial days of PhD with fruitful discussions and invaluable suggestions to conduct research. His relentless effort, punctuality, in-depth knowledge and above all the humbleness are the takeaways, I will ever cherish. I am grateful to the collaborators, Prof. Yoshichika Otani (RIKEN, Japan), Dr. Saswati Barman (IEM, India), Dr. Indranil Sarkar (INST, India), Prof. Ollav Hellwig (HZDR, Germany), Dr. Jarosław W. Kłos (AMU, Poland), Dr. Subhadeep Dutta and Dr. Mintu Mondal (IACS, India) for their profound contribution in my thesis. I convey my thanks to Prof. Supriyo Bandyopdhyay (VCU, USA) for the lecture series on Spintronics which was very much helpful to clear few concepts when I was a novice in the field. I thank also Prof. Ranjit Biswas for teaching us Research Methodology and late Prof. Sugata Mukherjee for the classes on advanced condensed matter physics. I am thankful to my seniors who not only made me acquainted with the lab culture, research activities but also maintained a joyful and dynamic environment in lab. I specially thank Dr. Chandrima Banerjee for mentoring me in my first project through which I experienced the first essence of research. I am highly inspired by the conscientious nature of Dr. Sucheta Mondal, Dr. Samiran Chaudhury, and Dr. Avinash Kr. Chaurasiya when they were active researcher of the group perusing their PhD. I sincerely thank Ms. Sucheta for her valuable inputs in optical measurements and her affability in personal space. I extend my thanks to Mr. Samiran for introducing the clean-room process and his appreciably smart work. My special thanks goes to Mr. Avinash for the amiable company full with supportive words, precious advices and discussions. I acknowledge Dr. Sourav Sahoo and Dr. Anulekha De for their help whenever I needed. My bachmates Mr. Suryanarayan Panda, Mr. Koustuv Dutta, Mr. Sudip Majumder and Mr. Amrit Kr. Mondal deserve special thanks for not only helping me to operate the experimental setups, also for genuinely showing togetherness during all ups and downs in this journey. I appreciate the way Koustuv and Surya cooperated to learn TR-MOKE setups. I also thank Sudip and Amrit for making me recognized with FMR and BLS setups. Apart from academic discussions, I had a lot informal discussions on various topics with Koustuv and Sudip, which I will cherish. I thank also Mr. Amit Barh for his help to learn the optical lithography. My thanks also goes to my seniors Dr. Santanu Pan, Dr. Kartik Adhikari and juniors Mr. Pratap Kr. Pal, Ms. Sreya Pal, Ms. Soma Dutta, Ms. Suchetana Mukherjee,

Mr. Chandan Kumar, Mr. Bikram Baghira, Mr. Sayan Mathur, and Ms. Sayanti Mondal. I acknowledge S. N. Bose Centre for providing me the fellowship and other financial grants, accommodation and the research facilities along with the beautiful library. I am also thankful to the staff of the centre for various help and assistance. I would like to thank Anuj, Rajdwip, Harmit and Daisy for spending good times together. The sweet memory of hostel days bethinks about Nivedita and Manjari. I convey my heartfelt thanks to Madhurita for her love and affection towards me and accompanying me in the cultural evenings to get relief from dismal moments. I will cherish the quality time spent with Bijoy discussing literature. I thank also my batchmates Sayantan and Didhiti. I express my thanks for Ms. Subhamita and Ms. Swarnali to involve me in the cultural programs. I am also thankful to few nonacademic staff, especially Ms. Piyali for her caring nature during my hostel stay. I appreciate the gardeners for keeping this campus pleasant and vibrant enough to make me feel refreshed and calm. The long journey of PhD was memorable and transformative as well, being full of elation and dejection. Positive and negative things came in sequence passing through which I learnt a lot and I thank all those people who made it happen.

The persons without whose presence my scientific pursuit would not be possible are my family members. I am blissful to have them by my side always and I know that their sacrifice, love and care are inexpressive by mere words. Still I must say that, it's specially the courage and positivity of my parents that used to heal me whenever I faced predicament and felt shattered. My deepest gratitude and respect to my parents, uncles and aunts, dada and didi, grandma, grandparents (maternal) for the unwavering love, trust and support. My infinite love and affection for my younger brothers Sanat, Rishi and Ribhu for being the most adoring supporters and cheer persons at each small and big achievement of mine. Being a researcher of Physics, Sanat helped me a lot during my PhD and proofread my thesis. I express my deepest respect to my late grandfather who wanted me to be educated. I extend my heartfelt thanks to masteruncle, Kanak uncle and Amar uncle for their motivating and encouraging words. I specially thank my friends Moumita, Sanchayeeta and Nila whose time to time phone calls used to be great relief for me. I convey my thanks to my teachers Mr. Arjun Mukhopadhyay, Dr. Surojit Ghosh and Dr. Satyajit Saha for their best wishes. Finally, I convey my pranāma to our ancestral tutelary deity Kalachand (Krishna) for the patience and perseverance to pass this path. My pranāma to Sri Ramakrishna, Holy mother Sarada Devi and Swami Vivekananda for their enlightening philosophy of life without which this journey towards the doctorate of philosophy would never be accomplished.

Arundhati Adhikari
S. N. Bose National Centre for Basic Sciences
Kolkata, India

# List of Abbreviations

| | | |
|---|---|---|
| 1D | : | One dimensional |
| 2D | : | Two dimensional |
| 3D | : | Three dimensional |
| 3TM | : | Three temperature model |
| ADL | : | Antidot lattice |
| AFM | : | Atomic force microscopy |
| AOM | : | Acousto-optic modulator |
| ASMW | : | Asymmetric magnonic waveguide |
| BBO | : | Barium beta-borate |
| BLS | : | Brillouin light scattering |
| BMC | : | Bicomponent magnonic crystal |
| BS | : | Beam splitter |
| BV | : | Backward volume |
| BZ | : | Brillouin zone |
| CMOS | : | Complementary metal-oxide semiconductor |
| CPW | : | Coplaner waveguide |
| CVT | : | Chemical vapor transport |
| CW | : | Continuous wave |
| DE | : | Damon-Eschback |
| DOS | : | Density of states |
| DW | : | Domain wall |
| ECD | : | Electrochemical deposition |
| EDX | : | Energy dispersive X-ray spectroscopy |
| EY | : | Elliot-Yafet |
| FFT | : | Fast Fourier transform |
| FMR | : | Ferromagnetic resonance |
| fs | : | Femtosecond |
| FWHM | : | Full width half maxima |
| FWVMS | : | Forward volume magnetostatic wave |
| GHz | : | Giga Hertz |
| GMR | : | Giant magnetoresistance |
| G-S-G | : | Ground-signal-ground |
| GVD | : | Group velocity dispersion |
| HA | : | Heusler alloy |
| HDD | : | Hard disk drive |
| HWP | : | Half wave plate |
| LBO | : | Lithium tri-borate |

| | | |
|---|---|---|
| LLG | : | Landau-Lifsitz-Gilbert |
| M3TM | : | Microscopic three temperature model |
| MBG | : | Magnonic band gap |
| MC | : | Magnonic crystal |
| MFM | : | Magnetic force microscopy |
| MHz | : | Mega Hertz |
| MO | : | Microscope objective |
| MOKE | : | Magneto optical Kerr effect |
| MRAM | : | Magnetic random access memory |
| MSSW | : | Magnetostatic surface wave |
| MTJ | : | Magnetic tunnel junction |
| mW | : | Milli Watt |
| NA | : | Numerical aperture |
| ns | : | Nano second |
| OBD | : | Optical bridge detector |
| OOMMF | : | Object oriented micromagnetic framework |
| pA | : | Pico Ampere |
| PBS | : | Polarized beam splitter |
| PEM | : | Photo elastic modulator |
| PMA | : | Perpendicular magnetic anisotropy |
| ps | : | Picosecond |
| PSSW | : | Perpendicular standing spin-wave |
| PWM | : | Plane wave method |
| RF | : | Radio frequency |
| RT | : | Room temperature |
| SAW | : | Surface acoustic wave |
| SEM | : | Scanning electron microscopy |
| SHG | : | Second harmonic generator |
| SOI | : | Spin orbit interaction |
| STT | : | Spin transfer torque |
| SW | : | Spin-wave |
| TFPI | : | Tandem Fabry Perot interferometer |
| THz | : | Tera Hertz |
| TMR | : | Tunnel magnetoresistance |
| TR-MOKE | : | Time resolved magneto optical Kerr effect |
| VNA | : | Vector network analyzer |
| VPUF | : | Verdi pumped ultrafast laser |
| VSM | : | Vibrating sample magnetometer |
| XRD | : | X-ray diffraction |

# List of Figures

# Contents

## Abstract:

The spin-based technology relying on magnetic materials and metamaterials is highly promising for next-generation microwave device engineering with inordinate energy efficiency. To this end, the control over static magnetic properties and dynamic magnetization can play significant roles to determine the applicability of the magnetic systems. Therefore, the fundamental understanding of the static and dynamics is imperative for continuous evolution of the technology. The major focus of this thesis has been put into the efficient control on the physical phenomena emerged from magnetization dynamics in diverse ferromagnetic nanostructures with distinct physical properties. To be more specific, the reconfigurabilty of the spin-wave properties has been explored in ferromagnetic metamaterials known as magnonic crystals, and ultrafast spin dynamics has been investigated in emerging materials for spintronics: Heusler alloy and van der Waals magnets. The dynamics is probed by elegant experimental tools and analyzed with the help of various theoretical models and micromagnetic simulations.

Magnonic crystals are lithographically designed periodic arrays which support spin-wave propagation at ultralow power consumption. The spin-wave features as well as the static spin-configurations of such structures are highly sensitive to various internal and external parameters. Here, using Brillouin light scattering (BLS) experiment and plane-wave method based calculations, we demonstrate the engineering of static spin states and magnonic band gap by the external field direction as well as the anisotropic character of spin-waves in dipolar coupled width-modulated waveguide array of $Ni_{80}Fe_{20}$. Further, we explore the role of varying geometrical parameter to control the spin-wave frequency, intensity as well as the propagation velocity in a series of bicomponent ($Ni_{80}Fe_{20}/Co_{50}Fe_{50}$) magnonic crystals using vector network analyzer based broadband ferromagnetic resonance (VNA-FMR) spectroscopy. Later, from time-resolved magneto-optical Kerr effect (TR-MOKE) microscopy measurements aided with micromagnetic simulations, we show the excitation of short wavelength spin-waves and their efficient tuning in nanoscale domains within antidot lattices carved in CoPd multilayer. Further, we unambiguously reveal the interplay of surface acoustic wave (SAW) with spin-wave and the resulting magnetoelastic modes in dipolar coupled nanomagnet arrays of $Ni_{80}Fe_{20}$.

The ultrafast spin dynamics of Heusler alloy, $Co_2FeSn$ and van der Waals magnets $Fe_xGeTe_2$ (x=3,4,5), were studied using TR-MOKE techniques. A faster demagnetization and moderate value of damping were revealed in the electrochemically grown $Co_2FeSn$-film. This study unlocks the potential of a cost effective synthesis approach to get pristine ferromagnetic thin film suitable for ultrafast spintronics devices. In $Fe_xGeTe_2$ (x=3,4,5), the emergence of room temperature ferromagnetism under ultrafast laser field has been explored. Besides, excitation of THz spin wave through spin-phonon coupling, conventional ultrafast demagnetization dynamics and generation of multiple GHz spin-waves have been visualized at room temperature. This study paves the way of future 2D spintronics technology.


Arundhati Adhikari

# Introduction Chapter 1

Magnetism is a subject of immense interest in science with myriad of captivating physics and their multifarious applications. One such sophisticated application was realized in 1956 implanting ferromagnetic material in the contemporary memory device, Hard disk drive (HDD). It was the first admissible step of magnetic material in modern information technology. Later, the development of nanotechnology served as a portal of advanced technology with new paradigm of fundamental physics. Nanotechnology introduced nanoscale materials with enigmatic and astonishing physical properties of quantum realm [1,2]. Especially, the symmetry breaking at the edges of a nanoscale structure leads to many finite size effects different from its bulk counterpart. In nanoscale magnetic materials, the discovery of giant magnetoresistance (GMR) in 1988 [3,4] is coined as a breakthrough of physics bringing the 2007 Nobel prize to Albert Fert and Peter Grünberg. This discovery can be considered as the cornerstone of the field named Spintronics (Spin-transport-electronics). Spintronics brought a sublime idea of decoupling the spin degrees of freedom from the charge degrees of freedom of an electron and a controlled reconciling of the duos. Soon, it was realized that the spin-up and spin-down states of the electron can be rationally deployed to encode information as data bit '0' and '1' at a speed which can easily surpass the speed of the conventional charge-based data read-write process. Further progress of research and engineering propelled spintronics technology as a potential substitute of the semiconductor technology demarcated by Moore's law [5–7].

Consequently, enroute to past three decades' journey, the field has expanded its potential from data storage to data transfer and communication system under its various subfields. Primarily, spin-based data processing or signal transfer can be functionalized by dynamic spin. Spin-current and spin-wave are the well-understood manifestation of dynamic spins. While spin-current relies on physical transfer of spin angular momentum for data transfer, spin-wave is able to encode the information in the amplitude or phase avoiding the direct transport. Therefore, the utilization of only spin-current or spin-wave instead of charge current could drastically reduce the energy lost due to Joule effect and hence much promising for an enduring greener technology. Remarkably, spin-wave can be excited with sub nm wavelength leading towards a tremendous downscaling of the host device. In addition, the broad frequency range from MHz to THz, and the nonlinear characteristics of spin-wave are advantageous for an energy efficient faster operation in microwave applications. Undoubtedly, the wave-based mechanism of information processing is very much promising to surmount the bottlenecks of binary bit mechanism of CMOS. Thereafter, spin-based functionalization can unlock exceptional opportunities of robust device construction with ultralow power consumption, compact data storage capacity, and faster operation. As a matter of fact, spin-based memory device, STT-MRAM [8,9] is presently tested for commercial use by Intel and Samsung. Additionally, various spin-wave based prototypes of microwave components like phase shifters [10–13], multiplexers [14], transistor [15], spin-valves [16], spectrum analyzer [17], directional coupler [18,19], spin-wave bus [20], receiver [21] have been realized.

Furthermore, spin-wave phase, frequency, intensity have been found to perform logic operations like conventional AND, NAND, XNOR or XOR gates [22–26], half-adder [18] etc. The advanced and complex spin-wave-based architecture is now being applied to mimic the synaptic operation of neurons under the emerging field of neuromorphic computing [27–30]. Recently, a machine-learning scheme, called reservoir computing [31] has been proposed based on nonlinear dynamical effect of nanomagnet systems. In addition, mutually synchronized magnetic nano-oscillators based on spin transfer torque [27] and spin orbit torque [28] have demonstrated compact microwave signal generation and ultrafast neuromorphic computing.

However, the prerequisite of a feasible device application is to have a very clear and concrete understanding of the core physics of the system of interest, which is possible only through extensive and comprehensive research. Here, the basic level starts by elucidating the genesis of magnetization and its dependence on various internal and external factors. Since, magnetization is synonymous to the spin angular momentum of electrons from its quantum mechanical description, the exploration of the physics of spins is significant for advancement of the nanomagnetism research and technology. This spin-physics encompasses an array of engrossing phenomena with different level of complexity e.g., GMR [3,4,32], tunneling magnetoresistance (TMR) [33–37], spin transfer torque [38,39], spin orbit torque [40] related spin Hall effect [41] and Rashba–Edelstein effect [42], spin-caloric effect [43], spin pumping [44], spin transport [45], non-local spin injection [46], spin precession [47] and damping [48], spin-phonon coupling [49], spin filtering [50], etc. Magnetic thin films, multilayers, heterostructures, patterned structures are the ideal testbeds to examine such spin-physics for their integration in future devices. Nevertheless, most of these spin related physics are effectively visualized through the lens of spin-current generation. In this regard, the precessional motion of a bunch of dipole or exchange coupled spins can give rise to spin-wave, the quanta of which is known as magnon. Spin-wave exhibits wave-like properties e.g., reflection, refraction, diffraction, interference, transmission, tunneling, dispersion, non-reciprocity etc. [51–54]. Spin-wave dispersion that gives the group velocity is an important subject of study to determine the quality of the magnetic system as a medium of information transfer. Besides, structuring of the magnetic materials in a length scale between few nm to micrometer range gives rise to many exotic spin configurations. These are facilitated by harnessing the flexibility of dipolar and exchange interactions or the anisotropy originated from spin-orbit interaction. In this regard, magnetic vortex, magnetic bubble, spin ice, stripe domain, domain wall or chiral spin textures like, skyrmion, meron have been realized by wisely choosing the materials or the geometry of the nanostructure [55]. These spin-states hold great potential to store information bit for non-volatile logic, data storage device and advanced computing schemes. Interestingly, these static microstates can have a great control on the dynamics. In addition to the static and dynamic properties of an isolated spin ensemble, the synergy between spin and other physical excitations can uncover many quiescent but intriguing physics. Based on those physics, very recently a new field named hybrid magnonics has emerged with massive interest where static spins and magnons can easily be manipulated via its interaction with different

quasiparticles like, phonon, photon, superconducting qubits, or other magnons [56]. This emerging branch of magnonics seems to be highly appealing for quantum computing. Similarly, ultrafast demagnetization is a complex physical phenomenon of sub picosecond time scale that involves a mutual coupling of spin with lattice and charge degrees of freedom [57]. This ultrafast control on magnetization is possible by shining femtosecond light pulses aiming towards all-optical switching at sub-THz frequency.

Investigating such fundamental physics at the edge of length and time scales, the basic research tries to find the controllable key parameters which might be useful to quantify the performance level of a device. For instance, the spin-flipping frequency or speed of all-optical switching can play the most vital role to determine the speed of data read-write process in the memory device. Similarly, in spin-transport, the distance up to which the spin orientation remain intact is significant as it is equivalent to transfer of a bit. The swiftly developing synthesis and fabrication techniques alongside the measurement and detection methods are making the task easy, while the timeless theoretical effort is providing a firm base of such scientific investigations.

The present thesis elucidates some of these fundamental phenomena in order to address their future aspects. The fundamental research has been tentatively accommodated in two different frames: (i) new physics in old systems and (ii) new physics in new systems. Therefore, new phenomena have been explored in systems with well-known and well-optimized material properties. In parallel, novel multifunctional materials have been introduced which are sought for adding extraordinary features with the basic physical properties. In this thesis, different nanoscale ferromagnets has been designed with the help of high precision sample fabrication facilities and the quasistatic and ultrafast spin dynamics have been unveiled with the help of state-of-the-art experimental tools. In this context, the relevant topics of nanomagnetism, which has motivated this doctoral thesis work are orchestrated. In a final note, the chapter-specific contents are delineated briefly within the objective of this thesis.

## 1.1 Static Spin State and Spin-Wave in Magnonic Crystal

Magnonic crystals (MCs) are the artificially created media for SW propagation with a spatial or temporal periodic modulation of magnetic properties. Information can be processed, stored or transferred via SW or magnon within the MCs [58]. The concept of periodicity in magnetic material was emulated from the idea of photonic and phononic crystals more than two decades ago. Recently, quasicrystal of fractal lattice, Penrose tiles, Fibonacci-lattice are showing novel aspects for next-gen technology due to their unconventional rotational symmetry. Till date, MCs have been fabricated in different forms including stripes, dots, antidots, rings, connected dots, etc. with lattice periodicity in one, two or three dimensions [59]. Among different types of MCs, magnetic stripes, antidot lattices (ADLs) and bicomponent magnonic crystals (BMCs) show greater promises for faster SW propagation to improve the operational speed of future devices.

Such periodic formation leads to spatial inhomogeneity in the internal magnetic field. As a consequence, inhomogeneous distribution of spins appears in the ground state of the system. The edge of such structures are often retains unsaturated spins which further proceed for inter element dipolar coupling. Dispersive spin-wave can be originated in such regions. Magnonic band-structures of MCs owing to Bragg reflection of the propagating SWs by the periodic modulation is of particular interest [60]. The intrinsic forbidden band in the magnonic band structure implies formation of standing or localized SWs due to spatial confinement. The SW propagation characteristics especially the energy bands as well as the static magnetic states can be effectively adjusted by controlling various material or geometrical parameters, e.g., saturation magnetization, exchange coefficient, magnetic anisotropy, size, shape, lattice arrangements etc. [61]. Further control can be achieved by means of external parameters like magnetic field strength or orientation, voltage gating, strain, rf field, laser irradiation, electric current, spin-polarized current, electrically and optically generated acoustic waves [62]. Most of these studies have been conducted in MCs made of well-known materials like $Ni_{80}Fe_{20}$ (Py), Co, Ni, CoFeB etc. possessing small in-plane anisotropy, while systems with innate perpendicular magnetic anisotropy (PMA) can also be exploited to design magnonic circuitry [6]. High perpendicular anisotropy can be created at the interface of a ferromagnet and a metal with large spin-orbit coupling, typically Pt, Pd, Ir and Au. $[Co/Pt]_n$ or $[Co/Pd]_n$ multilayers are the epitome of such high PMA materials. PMA discloses few advantages to shape the spin-wave dynamics devoid of in-plane demagnetizing effect. Therefore, PMA materials could be promoted for high scalability, high storage density and high-speed operation with a lesser wastage of energy. MCs based on PMA can give rise to complex spin configurations under special circumstances. In the present thesis, different MCs have been rigorously studied based on the above facts.

## 1.2 Spin Dynamics in Novel Materials

Identification of appropriate materials and precise optimization of the material properties are the indispensable task of nanomagnetism research for their future device implementation. For instance, the quest for materials with low damping and robust PMA is imperative to minimize the write current in STT-MRAM. Conversely, for spintronic sensor and MRAM applications, materials with high spin-polarization and efficient spin-filtering capabilities are favorable. Moreover, materials with significant spin-orbit coupling are preferred as they facilitate spin current generation and streamline magnetization switching. Additionally, reduction in damping can greatly enhance the distance for information transfer via spin-wave propagation. Therefore, one primary focus always lies on the developing high precision as well as cost-effective growth of materials and thoroughly characterizing their static and dynamic properties. Interestingly, unconventional physical phenomena may emerge as an outcome of this exploratory process. In the following, two different advanced materials are highlighted in the perspective of spintronics research and within the context of this thesis.

### 1.2.1 Heusler Alloy

Heusler alloy (HA) was first studied by Friedrich Heusler in 1903 with a composition of $Cu_2MnAl$ and was grouped with the well-known ferromagnetic materials. In 1983, the discovery of half-metallicity by Groot et al. [63] in Heusler compound uplifted its importance to the spintronics community [64,65]. The high Curie temperature (above RT) of (HA) makes them strongly reliable for room temperature spintronics application [66,67]. Furthermore, HAs are compatible with most of the substrate materials with minimal lattice mismatch, further enhancing its appeal for device application. Heusler compounds can be divided into two classes [68]: full and half HA. In general, the chemical formulas of full and half HA are respectively $X_2YZ$ and XYZ. The three elements are: a high-valence transition or noble metal X, a low-valence transition metal Y and a sp-band element Z. Ideally, the crystal structures of highest order manifest as the $L2_1$ and $C1_b$, respectively for $X_2YZ$ and XYZ. The half metallic nature is apparent under perfect crystalline ordering, giving rise to a unique electronic band structure. The signature of half-metallicity is visible when majority of the conduction band electrons occupy only a particular spin state (↑ or ↓) [69]. This leads to a degree of spin-polarization at the Fermi level expressed as: $= \frac{N_\uparrow - N_\downarrow}{N_\uparrow + N_\downarrow}$, where N↑ and N↓ represent the number of spin-up and spin-down electrons at the Fermi level in the spin dependent energy band. Due to high spin-polarization [70–73], integration of HA as a storage layer in an MTJ device can result a large MR ratio [74,75], thus reducing the wiring current and increasing storage density. In addition, the high degree of spin-polarization has been evidenced to efficiently generate spin-current in an ferromagnet/nonmagnet heterostructure [76]. Furthermore, the typical low damping of HA [77–79] renders it highly suitable for MRAM application offering faster magnetization reversal at ultralow switching current. Hence, experimental determination of the degree of spin-polarization or damping parameter is necessary for incorporation of HA as a commercial candidate. In this essence, investigation of spin dynamics using various techniques, especially the non-invasive magneto-optical approach can indirectly probe the spin-polarization as well as the damping coefficient [80–83].

### 1.2.2 van der Waals Magnets

Atomically thin 2D van der Walls (vdW) materials are anticipated for numerous innovations in the field of science and technology [84]. In the 2D limit, being insulator, semiconductor, metal as well as superconductor, these materials are a wealth of unique physical properties [85]. In 2017, the discovery of intrinsic ferromagnetism in 2D vdW materials [86,87] globally sparked the interest on 2D spintronics [88,89]. These pioneering work ensured that magnetization can be established by strong magneto-crystalline anisotropy in contrast to the Mermin-Wagner theorem (which prohibits long-range magnetic order in 2D at finite temperature due to thermal fluctuations) [90]. Interestingly, the variation of layer number in few 2D systems can render the state of magnetization from antiferromagnetic to ferromagnetic or vice versa [86]. In the broad catalog of 2D materials, magnetism has been mostly found in chromium compounds ($CrI_3$, $CrCl_3$, $CrBr_3$, $CrTe_2$, $Cr_2Te_3$, $Cr_2Ge_2Te_6$, etc.), iron germanium telluride ($Fe_xGeTe_2$), sulfur phosphorus compound and materials like $VSe_2$, $V_5Se_8$, $MnBi_2Te_4$, $VI_3$, $MnPS_3$, $FePS_3$ and so on [91,92]. $Fe_xGeTe_2$ are strong contender in this field due to relatively higher Curie temperature [93–95]. Notably, this transition temperature as well as the magnetic states are highly

sensitive to external stimulus such as gate voltage [96], light illumination [97–99], element doping, proximity effect [100], strain [101], pattering [102] or layering with other materials like topological insulator [103] etc. The distinct layered structure facilitated by weak vdW force are pertinent for emerging magnetic heterostructures for spintronics applications devoid of interfacial roughness, lattice mismatch or unwanted chemical mixing [104]. Therefore, judicial compilation of 2D magnets with other materials is necessary. Further, the layered structure can easily promote unhindered motion of spins desirable for device operation. Also, the robust PMA present in these layered materials [105] holds potential for MRAM and MTJ applications [106]. Nonetheless, spin dynamics in such materials can uncover plenty of opportunities for developing more fascinating spin dependent device.

## 1.3 Objective

As discussed above, reliable manipulation of spin is imperative in the nanomagnetism research. Thereby, the primary objective of this doctoral research was to experimentally investigate few ferromagnetic structures (magnonic crystals: waveguide of $Ni_{80}Fe_{20}$, BMC of $Ni_{80}Fe_{20}/Co_{50}Fe_{50}$, PMA antidot of Co/Pd, nanodot of $Ni_{80}Fe_{20}$, electrochemically grown $Co_2FeSn$ films, sub-micron flakes of $Fe_xGeTe_2$) with the support of micromagnetic simulations, each shedding light to a particular spin-dependent phenomenon. Each work is precisely outlined in the following except the chapters dealt with the theoretical background (Chapter 2) and methodology (Chapter 3).

Chapter 4 aims to analysis the propagation characteristics of spin-wave in a width modulated magnonic waveguide system under the influence of a variable magnetic field. This experimental study is conducted using the Brillouin Light Scattering technique. This study reveals a significant modulation of magnonic band gap by changing the external field orientation and the pivotal role of dipolar interaction. In addition, the findings lead to the design of a spin-wave XNOR/XOR prototype. Furthermore, understanding of magnon band structure and mode profiles inside the waveguide is essential to design on-chip magnonic circuits.

Chapter 5 presents important characteristics of spin-wave in a series of bicomponent magnonic crystals. This experimental study is conducted using the broadband ferromagnetic resonance spectroscopy. This study reveals a significant modulation of spin-wave frequency, power, quantization and propagation changing the external field and the pivotal role of dipolar and interfacial exchange interaction. Additionally, significant contribution of geometrical parameter in spin-wave velocity is observed.

Chapter 6 presents the experimental study of ultrafast magnetization dynamics in HA film using TR-MOKE magnetometry. The magnetic-field and pump-fluence dependent dynamics is probed to understand various dynamic parameters, e.g., ultrafast demagnetization time, remagnetization time, precessional frequency, Gilbert damping and determine their correlation at ultrafast time scale. These findings could open up new possibilities for the construction of future spintronics devices in a cost-effective manner.

In chapter 7, the ultrafast dynamic behavior of a set of 2D van der Waals ferromagnets are comprehensively studied and explained. The static characterization helped to understand crystal

structures, magnetization states and its temperature dependence. The dynamic unfolds the phonon spectra, spin-phonon coupling, laser induced ultrafast demagnetization and spin-precession at room temperature. The results are faceted towards assimilating the physical properties of a magnetic material at the 2D limit for future 2D technology.

Chapter 8 is designed to investigate the anisotropic excitation of spin-waves in a perpendicularly magnetized magnonic antidot array. In addition to the perpendicular anisotropy, a substantial in-plane anisotropy developed at the periphery of the antidot's holes aids complex spin-texture to control the spin-wave frequency. The experimental investigation was performed using TR-MOKE and simulations were performed using Mumax3.

In Chapter 9, the generation of spin-waves and surface acoustic wave by optical pumping in a longitudinally magnetized magnonic nanodot arrays is investigated. This study uncovers significant magneto-elastic coupling in ferromagnetic nanomagnet system. The experimental investigation is performed employing the time-resolved magneto-optical Kerr effect (TR-MOKE) microscopy technique supported by micromagnetic simulations. Thus, a guideline towards the emerging field of hybrid magnonics and the design and realization of magnonic devices dedicated to energy harvesting are provided.

Chapter 10 provides the conclusive remarks and future outlook of the thesis.

This chapter provides a brief description of the fundamental theory related to magnetostatics, spin-waves and ultrafast demagnetization dynamics. This theoretical description aims to ease the understanding of the experimental results delineated in this thesis. The thesis is primarily focused on the magnetization dynamics of various nanodimensional ferromagnets probed by disparate experimental methods. Ferromagnets are the class of materials having a net spontaneous magnetization [107–109]. This nonzero magnetic moment of ferromagnets relies on the quantum mechanical exchange interaction. In microscopic scenario, the magnetic moments are also influenced by many other interactions which all together determines the strength and orientation of the net magnetization i.e., the static equilibrium. In this essence, magnetic dipole-dipole interaction is one of the most fundamental interactions to control and stabilize the net magnetization of a magnetic material. Naturally, the dynamic magnetization also undergoes through the impact of these interactions. Considering all these effects, the time-evolution of net magnetization in presence of an effective magnetic field was given by a phenomenological equation proposed by Landau, Lifshitz and Gilbert. The solution of linearized Landau-Lifshitz-Gilbert (LLG) equation provides a general idea of the fundamental characteristics of spin-wave e.g., amplitude, wave vector, phase, frequency, damping and their mutual relations. Furthermore, spins are strongly interactive to other physical entities like phonon, photon, and charge (electron) or even with magnon. Ultrafast demagnetization is a phenomenon where the spin order is temporarily lost in a magnet through such interactions under high impulse laser irradiation. Another interesting phenomenon is the interaction between spin and phonon or lattice vibration with completely different aspects. The following discussion is an overview of the aforementioned facts.

## 2.1 Magnetic Energy

The static equilibrium i.e., ground state of a magnetic system is obtained through minimization of its different energies. These energies typically range from less than 1 kJ $m^{-3}$ to more than 10 MJ $m^{-3}$ [113]. The dynamic character of magnetization is strongly connected to the initial static state of magnetization and hence to the energy sources. In the following section, the origin of most common energy contributions is described briefly for a ferromagnetic material of volume V and magnetization $\boldsymbol{M}$ under application of an external magnetic field $\boldsymbol{H_{ext}}$.

### 2.1.1 Zeeman Energy

The potential energy gained by a magnet in an external magnetic field, named after Pieter Zeeman is known as Zeeman energy [110],

$$E_z = -\int_0^V \mu_0 \boldsymbol{M} \cdot \boldsymbol{H_{ext}} dV \qquad \ldots 2.1$$

where $dV$ is the elemental volume and $\mu_0$ is the vacuum permeability. This energy is minimized when $\boldsymbol{M}$ is aligned along $\boldsymbol{H_{ext}}$.

### 2.1.2 Exchange Energy

The origin of exchange energy in a magnetic system can only be explained quantum mechanically from Heisenberg model [111]. As a direct consequence of Pauli Exclusion Principle and Coulomb interaction, short range exchange interaction arises between neighboring spins. The generalized exchange Hamiltonian is often given as the sum over the Heisenberg exchange interaction of all possible pair of neighboring spins as,

$$\mathcal{H} = -\sum_{i,j} J_{ij} \boldsymbol{S_i} \cdot \boldsymbol{S_j} \qquad \dots 2.2$$

where, $\boldsymbol{S_i}$ and $\boldsymbol{S_j}$ are the quantum mechanical spin operators associated with the *i*th and *j*th atoms, respectively and $J_{ij}$ is known as the exchange integral having dimension of energy. This interaction is at the root of magnetic ordering leading to parallel ($J_{ij} > 0$) and antiparallel alignment of spins ($J_{ij} < 0$) in ferro- and antiferromagnetic materials, respectively.

In the continuum model i.e., when $\boldsymbol{M}$ is a continuous function of space, the exchange energy can be calculated from the following formula,

$$E_{exch} = A_{ex} \int_0^V (\nabla \boldsymbol{m})^2 \, dV \qquad \dots 2.3$$

where, $\boldsymbol{m}$ is the normalized value of $\boldsymbol{M}$ and $A_{ex}$ is known as the exchange stiffness constant of a material with an expression, $A_{ex} = \frac{2JS^2}{a}$ (for *bcc* lattice). Here *a* and *J* are the isotropic lattice constant and exchange integral. This short range interaction is significant upto a length scale, $l_{ex} = \sqrt{\frac{2A_{ex}}{\mu_0 {M_S}^2}}$ known as exchange length.

### 2.1.3 Dipolar Energy

Like electric dipoles, magnetic dipoles also repulse each other forcing an antiparallel alignment. The associated energy of two such interacting dipoles of moment $\boldsymbol{\mu_1}$ and $\boldsymbol{\mu_2}$ separated by a distance $\boldsymbol{r}$ is defined as [112–114],

$$E_d = \frac{\mu_0}{4\pi r^3}\left[\boldsymbol{\mu_1} \cdot \boldsymbol{\mu_2} - \frac{3}{r^2}(\boldsymbol{\mu_1} \cdot \boldsymbol{r})(\boldsymbol{\mu_2} \cdot \boldsymbol{r})\right] \qquad \dots 2.4$$

Being much weaker than exchange energy, dipolar energy is unable to create ferromagnetic order, yet dipole-dipole interaction takes key role to decide the magnetization direction in addition to stray field generation and domain formation. Inside a magnet, the dipolar energy is often called demagnetizing energy or magnetostatic self-energy while outside of the material this dipolar energy is referred to as stray field energy. The demagnetizing energy is also referred to as shape anisotropy of a magnetic specimen. In case of nanostructured ferromagnets, demagnetizing energy or shape anisotropy [115,116] originated from the internal uncompensated magnetic dipole moments plays a pivotal role in the spin-wave dynamics.

### 2.1.4 Anisotropy Energy

Magnetic anisotropy is defined as the directional preference of the magnetic moments in order to minimize the energy of the whole magnetic material. The most important anisotropy contributing in the free energy are given below:

#### 2.1.4.1 Magnetocrystalline Anisotropy

In general, for a crystalline solid the magnetic moments prefer to align along some certain symmetry axes of the crystal. The anisotropy arises due to spin-orbit interaction or the crystal field interaction or interatomic dipole-dipole interaction [113].

The generalized magnetocrystalline anisotropy energy per unit volume is given by a phenomenological expression:

$$E_{MCA} = E_0 + \sum_i b_i \alpha_i + \sum_i b_i \alpha_i \alpha_j + \sum_{ij} b_{ijk} \alpha_i \alpha_j \alpha_k + \sum_{ijkl} b_{ijkl} \alpha_i \alpha_j \alpha_k \alpha_l + \mathcal{O}(\alpha^5) \quad \ldots 2.5$$

where $b$'s are anisotropy constants and $\alpha$'s are direction cosines of magnetization.

For simple cubic and hexagonal crystals, the above expression can be deduced to the following expressions,

$$E_{cubic} = K_1\left(m_x^2 m_y^2 + m_y^2 m_z^2 + m_x^2 m_z^2\right) + K_2\left(m_x^2 m_y^2 m_z^2\right) + \cdots \quad \ldots 2.6$$

$$E_{hexa} = K_1 sin^2\theta + K_2 sin^4\theta + K_3 sin^6\theta + K_3 sin^6\theta cos6\varphi \quad \ldots 2.7$$

#### 2.1.4.2 Shape Anisotropy

Magnetization also depends on a particular shape of material and reorients itself for energy minimization if the shape is changed. This shape dependent anisotropy is a manifestation of the internal dipole-dipole interaction i.e., demagnetizing field. So, this energy has the following form [113]:

$$E_{demag} = -\frac{1}{2}\int_0^V \mu_0 \boldsymbol{M}.\boldsymbol{H_{demag}} dV \quad \ldots 2.8$$

where demagnetizing field is given in terms of demagnetizing tensor $\mathcal{N}$ and magnetization $\boldsymbol{M}$,

$$H_{demag} = -\mathcal{N}M \quad \ldots 2.9$$

#### 2.1.4.2 Volume, Surface and Interface anisotropy

The atoms at the surface of a material or interface of two materials prefer an out-of-plane orientation of their magnetic moments affected by the broken crystal symmetry. As opposed to the surface, the volume atoms give rise to an in-plane magnetic orientation bound by the crystal symmetry. Effectively, the anisotropy is a sum of these surface, interface and volume anisotropy [117] i.e.

$$K_{\text{eff}} = K_{\text{v}} + \frac{2K_{\text{S}} + K_{int}}{t} \quad \ldots 2.10$$

Here, $K_V$ is the volume dependent magnetocrystalline anisotropy constant while $K_S$ and $K_{int}$ are the surface and interface contributions, respectively. This kind of anisotropy is thickness ($t$) dependent and usual in magnetic thin films and the multilayers.

### 2.1.4.3 Strain Anisotropy

Compression or expansion of a magnet due to strain results in a directional change of magnetization. This property of magnetic material is known as magnetostriction. The associated energy depends on the elastic properties of the material. For a material with isotropic elastic properties, the strain anisotropy is simply given by [118],

$$E_{Strain} = -K_{strain} cos^2\theta \quad \ldots 2.11$$

where,

$$K_{strain} = -\frac{3\lambda\sigma}{2} = -\frac{3\lambda E\epsilon}{2} \quad 2.12$$

Here, σ is the stress tensor related to strain tensor (ϵ) via elastic modulus (Y) and given as: $\sigma = Y\epsilon$. The magnetostriction coefficient is $\lambda$.

### 2.1.4.4 Perpendicular Magnetic Anisotropy

Perpendicular magnetic anisotropy (PMA) arises as a result of shrunk volume to surface ratio [119,120]. In case of thin films or multilayered heterostructures, PMA originates at the interface when thicknesses of the associated layers are very small i.e., interface effect is prominent. Due to the lack of orbital symmetry at interface, orbitals are deformed along the perpendicular direction which enhances the spin-orbit interaction strength ($\boldsymbol{H_{SOI}}$) along that direction compared to the in-plane direction. As a result, a substantial magnetic energy ($-\boldsymbol{M}\cdot\boldsymbol{H_{SOI}}$) is gained by the surface atoms along the out-of-plane direction creating a low energy equilibrium for magnetization. Eventually, the magnetization ends up aligning along the surface normal. The PMA is often calculated as the energy consumed by an externally applied in-plane magnetic field which can turn the magnetization from out-of-plane to in-plane direction. Similarly, bulk PMA also exists in some materials due to some asymmetry developed during the growth of the material [121].

### 2.1.4.5 Configurational Anisotropy

For an array of artificially patterned magnetic structures, the equilibrium magnetization orientation depends on the shape and the geometrical arrangement of the elements. A slight change of magnetization direction in such nanostructures can cause a huge change of energy. This happens mainly due to change in inter- and intra-element dipolar coupling. This is called configurational anisotropy [122,123].

There may be additional energy in a magnetic system contributing to achieve the ground state depending on the system under investigation. Those are considered accordingly to understand the magnetic behavior. All these energies produce individual fields which are encapsulated under an effective field ($\boldsymbol{H_{eff}}$) term derivable from the net free energy. During the dynamics, magnetization precesses around this $\boldsymbol{H_{eff}}$.

## 2.2 Magnetization Dynamics

### 2.2.1 Precessional Motion

In presence of an external magnetic field ($\boldsymbol{H_{ext}}$), a spin always experiences a torque exerted by that field and starts to precess around it. A magnetic specimen is composed of numerous spins resulting the magnetization ($\boldsymbol{M}$). Thereby, $\boldsymbol{M}$ of a magnetic specimen also undergoes a similar precessional motion when it is deliberately moved from its equilibrium by small perturbation (electric current, laser pulse, voltage, thermal energy etc.) (Figure 2.1).

The precessional motion of the magnetization is described by the torque equation proposed by Lev Landau and Evgeny Lifshitz (LL) [124],

$$\frac{\mathrm{d}\boldsymbol{M}}{\mathrm{dt}} = -\gamma\left(\boldsymbol{M} \times \boldsymbol{H_{eff}}\right) \qquad \ldots 2.13$$

where $\gamma$ is the gyromagnetic ratio, given by $\left(\gamma = {}^{g\mu_B}/_{\hbar}\right)$. Here, $g$ is the Lande'g factor, $\mu_B$ is the Bohr magneton, $\hbar$ is the Planck's constant. Later, the equation was modified by Gilbert [48] with incorporation of a phenomenological damping term. Thereby, the precessional motion is described by the LLG equation given by,

$$\frac{\mathrm{d}\boldsymbol{M}}{\mathrm{dt}} = -\gamma\left(\boldsymbol{M} \times \boldsymbol{H_{eff}}\right) + \frac{\alpha}{M_S}\left(\boldsymbol{M} \times \frac{\mathrm{d}\boldsymbol{M}}{\mathrm{dt}}\right) \qquad \ldots 2.14$$

Here, $\alpha$ is called Gilbert damping parameter of the magnetic material. $\boldsymbol{H_{eff}}$ is the sum of all possible magnetic field components present in the system,

$$\boldsymbol{H_{eff}} = \boldsymbol{H_{ext}} + \boldsymbol{H_{demag}} + \boldsymbol{H_{ex}} + \boldsymbol{H_{ani}} \qquad \ldots 2.15$$

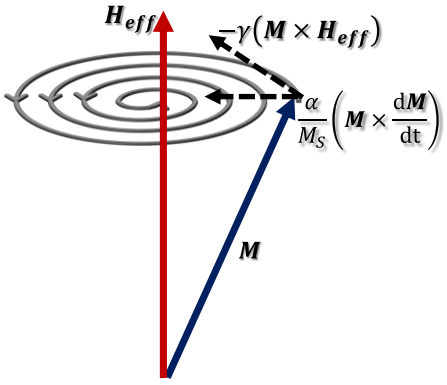


**Figure 2.1:** Schematic illustration of magnetization precession and damping.

### 2.2.2 Damping

In real system, magnetization dynamics is always associated with damping. Damping causes a gradual decrease of precessional amplitude over time and helps the magnetization vector to reach its equilibrium [125]. Thus, damping is directly correlated to energy dissipation rate of magnetization to the surroundings. Thereby, damping coefficient ($\alpha$) of a material is an important parameter to determine

and understand as it delves deeper into the underlying mechanism of magnetization dynamics [126]. There are two types of magnetic damping: direct and indirect. During direct damping, energy from the magnetic material is transferred to other adjacent materials while in indirect damping the dissipated energy is conserved within the system. Direct damping is classified into two different categories: intrinsic and extrinsic damping. Intrinsic damping is inherent and cannot be externally controlled because it arises from inevitable scattering interactions with phonons within the magnetic system. Extrinsic damping, however, emerges due to additional magnon scattering processes as well as spin pumping, spin injection etc. effects and hence, can be influenced by external factors [126].

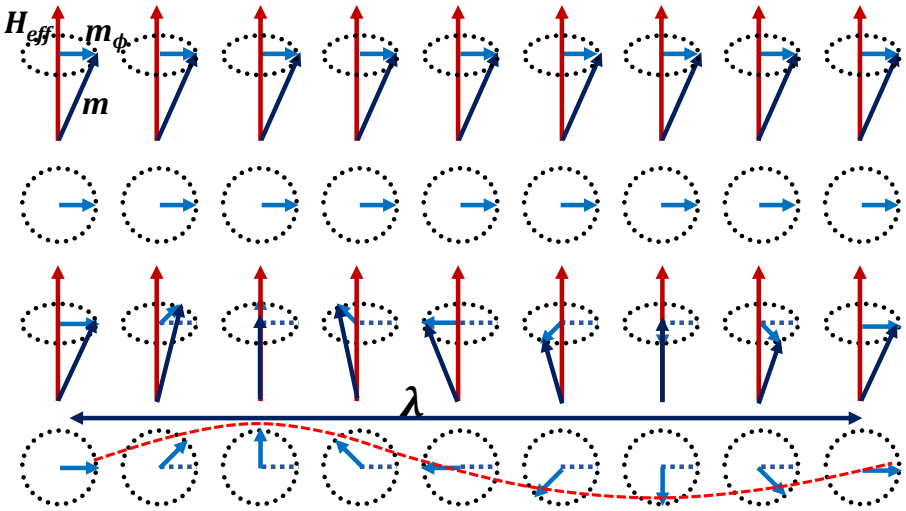


**Figure 2.2:** Magnetization precession: coherent dynamics (two up panels, top view in the lower one) and incoherent dynamics (two bottom panels, top view in the lower one).

### 2.2.3 Coherent Dynamics: Kittel Mode ($k = 0$)

The uniform precessional motion in a ferromagnetic system is a phase coherent collective motion of neighboring spins (Figure 2.2). This arises when the tips of all the participating moments point at the same direction during the time evolution. The in-phase motion is well known as ferromagnetic resonance or FMR mode in a ferromagnetic system [127]. This is also known as spin-wave with zero wave vector ($\boldsymbol{k}$). The frequency of this mode was first derived by C. Kittel considering a simplified LLG equation by omitting the damping term and hence, this FMR mode is also known as Kittel mode [128]. For a magnetic thin film (saturation magnetization $M_s$) subjected to a magnetic field of magnitude $H$, frequency of the Kittel mode is given as [129],

$$\omega_{FMR} = 2\pi f_{FMR} = \gamma\sqrt{H(H + 4\pi M_S)} \qquad \ldots 2.16$$

### 2.2.4 Incoherent Dynamics: Spin-Wave ($k \neq 0$)

The concept of spin-wave was first introduced by Bloch in 1929 as the elementary excitation of an ordered spin ensemble [130]. The quanta of spin-wave is termed as magnon. This is a result of nonuniform phase distribution over the spin ensemble. Thus, the spin-wave mainly describes the phase-

incoherent precession of spins while the phase shift between individual spins propagates in a wave manner [131]. Therefore, a spin-wave always associates a finite wave vector (***k***) and displays dispersive nature. Depending on the wavelength, spin-waves are categorized as exchange spin-wave or dipolar spin-wave [132–134]. Exchange spin-waves are short wavelength spin-waves dominated by short range exchange interaction while dipolar spin-waves have longer wavelength dominated by long range dipolar interaction. Notably, exchange spin-waves are isotropic in nature being independent of the relative orientation between ***M*** and ***k***.

In contrast, dipolar spin-waves are anisotropic and classified depending on the relative orientation between ***M*** and ***k***. When both the quantities are parallel to each other, the spin-wave is called backward volume (BV) magnetostatic *spin-wave* and it shows negative dispersion as per the following expression [135],

$$\omega_{BV} = 2\pi f_{BV} = \gamma\sqrt{\left[H\left(H + 4\pi M_S\frac{(1-e^{-2dk_{\parallel}})}{kd}\right)\right]} \quad \ldots 2.17$$

Here, the dispersion relation is given for a continuous film of thickness $d$ with saturation magnetization $\boldsymbol{M_s}$ in presence of magnetic field ***H***.

When both ***k*** and $\boldsymbol{M_s}$ are perpendicular to each other and coplanar, the spin-wave is called magnetostatic surface wave (MSSW) or Damon-Eshbach (DE) mode [136]. The dispersion relation is given by,

$$\omega_{DE} = 2\pi f_{DE} = \gamma\sqrt{[H(H + 4\pi M_S) + (2\pi M_S)^2(1-e^{-2dk_{\parallel}})]} \quad \ldots 2.18$$

Again, when ***k*** is in the plane of the sample and $\boldsymbol{M_s}$ is perpendicular to it, then the corresponding mode is called forward volume magnetostatic (FWVMS) mode [137] and the dispersion relation is given by,

$$\omega_{FV} = 2\pi f_{FV} = \gamma\sqrt{\left[(H - 4\pi M_S)\left(H - 4\pi M_S\frac{(1-e^{-2dk_{\parallel}})}{kd}\right)\right]} \quad \ldots 2.19$$

In case of a thin film, the exchange dominated mode is often a standing spin-wave along the thickness with quantization number $p$ = 1,2,3..., known as perpendicular standing spin-wave (PSSW) [138]. The dispersion relation of the PSSW mode depends on the exchange coefficient ($A_{ex}$) too and is given by the following expression,

$$\omega_{pssw} = 2\pi f_{pssw} = \sqrt{\left[\left(H + \frac{2A_{ex}}{M_S}\left(\frac{p\pi}{d}\right)^2\right)\left(H + \frac{2A_{ex}}{M_S}\left(\frac{p\pi}{d}\right)^2 + 4\pi M_S\right)\right]} \quad \ldots 2.20$$

In addition to the generation of spin-wave in a magnetic system, there are few more fundamental phenomena which occur at the ultrafast time scales. In this thesis two such phenomena, which have been studied in different magnetic systems are briefly discussed below.

### 2.2.5 Ultrafast Demagnetization

Ultrafast demagnetization is a sub picosecond phenomenon occurring at microscopic level of a magnetized system resulting temporal loss of magnetic ordering. This happens due to a direct or indirect light-matter interaction in femtosecond time scale. Ultrafast demagnetization was first observed and

explained by Beaurepaire et al. [57] in a Ni thin film directly exposed under a femtosecond pulsed laser. They observed a drastic drop of magnetization within sub-picosecond followed by a fast recovery of magnetization within few picoseconds in presence of an externally applied magnetic field. They explained these observations on basis of their proposed phenomenological three temperature model. Subsequently, these phenomena have been observed in different magnetic materials [139], multilayers [140], heterostructures etc. Based on the systems under investigation and the nature of demagnetization, different models have been proposed till date to unfold the basic mechanism of demagnetization dynamics. Among those, superdiffusive spin transport model, three temperature model, or microscopic three temperature model have been able to explain majority of the cases.

In the following sections, the last two models which have been used in this thesis are discussed.

### 2.2.5.1 Three Temperature Model

The basic model was first proposed by Beaurepaire et al. to explain the ultrafast demagnetization process and the associated time scales. It was an extended version of two temperature model [141]. In this case, the electron's spin degree of freedom is separately considered as a physical quantity and the system is considered as a resource of three temperature baths corresponding to spinless electron ($T_e$), spin ($T_s$) and lattice ($T_l$). The three subsystems are assumed to be coupled to each other for energy exchange. Due to interaction with impulsive laser pulse, the system approaches to a nonequilibrium state after absorption of laser energy by the electron subsystem. At this stage, the electrons are supposed to be in non-thermodynamic elevated temperature and hence called hot electrons. These hot electrons are distributed above Fermi level without affecting the spin angular momentum. Now, electrons of majority and minority spins start redistribution of energy by transferring the extra energy to spin subsystem. Then the spin temperature rises and spin ordering is lost resulting ultrafast demagnetization. Subsequently, the spin energy is transferred to the lattice showing a recovery of the lost magnetization. Hereafter, the hot electrons are also cooled by transferring energy to lattice and thus equilibrium is gradually re-established among the three sub systems within few picoseconds. Finally, the lattice releases the energy to the surroundings in the slow relaxation process. The temporal evolution of temperatures is given by three coupled differential equations:

$$C_e(T_e)\frac{dT_e}{dt} = -G_{el}(T_e - T_l) - G_{es}(T_e - T_s) + P(t) \quad \ldots 2.21a$$

$$C_s(T_s)\frac{dT_s}{dt} = -G_{es}(T_s - T_e) - G_{sl}(T_s - T_l) \quad 2.21b$$

$$C_l(T_l)\frac{dT_l}{dt} = -G_{el}(T_l - T_e) - G_{sl}(T_l - T_s) \quad \ldots 2.21c$$

where, $C_e$, $C_s$ and $C_l$ are the specific heat capacity of the electron, spin and lattice baths and $G_{el}$, $G_{es}$ and $G_{sl}$ are the electron-lattice, electron-spin, and spin-lattice coupling parameters, respectively. $P(t)$ is the absorbed energy from the laser pulse. $C_e$ is considered to show linear dependence on $T_e$, i.e., $C_e = \gamma T_e$, where $\gamma$ is determined by the electron density of states around the Fermi level. Solution of these

equations disentangles the temperature profiles over time delay along with the values of specific heats and coupling constants.

In 2007, Dalla Longa et al. [142] solved these equations under specific conditions and provided the time dependent magnetization according to the following equation:

$$\frac{M(t)}{M_0} = -\left[\left\{\frac{A_1}{t/t_0+1} - \frac{A_2\tau_E - A_1\tau_M}{\tau_E - \tau_M}e^{-t/\tau_M} - \frac{(A_1 - A_2)\tau_E}{\tau_E - \tau_M}e^{-t/\tau_E}\right\}H(t) + A_3\delta(t)\right] \otimes G(t) \quad \ldots 2.22$$

Here $\tau_M$ is the demagnetization time, $\tau_E$ is the fast remagnetization time, $H(t)$ is the Heaviside step function and $G(t)$ stands for the Gaussian laser-pulse. The constant $A_1$ indicates the equilibrium value of the ratio $M(t)/M_0$, while $A_2$ is proportional to the initial electronic temperature rise. The constant $A_3$ represents the magnitude of state-filling effects during pump probe temporal overlap that is described by a delta function. The magnetization here has a direct correspondence to the spin temperature. The demagnetization and remagnetization time constants of any system are obtained by fitting the ultrafast demagnetization data using the above equation.

### 2.2.5.2 Microscopic Three Temperature Model

The limitations of the three temperature model (3TM) was first addressed by Koopmans et al. [139] by the microscopic three temperature model. The 3TM was unable to properly explain the microscopic mechanism of angular momentum transfer and type-II demagnetization process of many ferromagnets. The microscopic model is more advanced to explain the process of temporal loss and recovery of spin angular momentum and also the associated time-rates by phonon mediated Elliot-Yafet [143] type spin-flip scattering mechanism. According to this model, the loss of magnetization occurs when electron's angular momentum is transferred to phonon via electron-phonon scattering. Each scattering event is assumed to have a finite probability of spin-flip costing a change of angular momentum by $\hbar$. This angular momentum is absorbed by a phonon and thus the probability of finding the electron in spin-up ($\hbar/2$) or spin-down ($-\hbar/2$) state is lost. This leads to a modification in the spin dependent energy bands near Fermi level. This model provides the rate of change of magnetization as per the following equation,

$$\frac{dm}{dt} = Rm\frac{T_p}{T_c}\left[1 - \mathrm{mcoth}\left(m\frac{T_c}{T_e}\right)\right] \quad \ldots 2.23$$

Here, $m$ (= $M/M_s$) represents the normalized magnetization and $T_p$, $T_e$ and $T_c$ denote the lattice, electron and Curie temperature, respectively. $R$ is a material specific parameter describing the type of ultrafast demagnetization. $R$ is expressed in terms of spin-flip probability ($\alpha_{sf}$), atomic volume ($V_{at}$), atomic magnetic moment ($\mu_{at}$), Debye energy ($E_D$) and electron-lattice coupling parameter ($G_{el}$) of the material:

$$R = \frac{\alpha_{sf}G_{ep}k_B T_c^2 V_{at}}{\left(\frac{\mu_{at}}{\mu_B}\right)E_D^2}$$

Here, $\mu_B$ and $k_B$ are the Bohr magneton and Boltzmann constant, respectively.

The time evolution of $T_e$ and $T_p$ are obtained by solving the following coupled differential equations:

$$C_e(T_e)\frac{dT_e}{dt} = -G_{ep}(T_e - T_p) + \nabla_z(k\nabla_z T_e) + P(t) \quad \ldots 2.24a$$

$$C_p(T_p)\frac{dT_p}{dt} = -G_{ep}(T_p - T_e) \quad \ldots 2.24b$$

### 2.2.6 Magnetoelastic Coupling

The underlying concept of magnetoelastic coupling is rooted in magnetostriction property of magnetic material. As mentioned above, magnetostriction describes the interplay between mechanical distortion and magnetization. The reverse process where a mechanical deformation leads to a change in the magnetization of a magnetized sample, is known as the inverse magnetostriction or Villari Effect. Dynamic magnetization or spin-wave can couple with the elastic wave present in magnetic specimen through this inverse process. Due to change in interatomic distance during lattice vibration or elastic wave propagation, the orbital shape changes because of orbital-lattice coupling. This results in a change of spin orientation due to strong spin-orbit interaction. Signature of magnetoelastic coupling can be understood through resonant excitation of spin-wave with enhanced amplitude and modulated damping or emergence of hybrid mode with distinct properties [144]. In general, the magnetoelastic energy of a material with cubic symmetry is expressed as [113]

$$f_{ME} = b_1\left(\epsilon_{xx}m_x^2 + \epsilon_{yy}m_y^2 + \epsilon_{zz}m_z^2\right) + 2b_2\left(\epsilon_{xy}m_x m_y + \epsilon_{yz}m_y m_z + \epsilon_{xz}m_x m_z\right) \quad \ldots 2.25$$

where $b_1$ and $b_2$ are the magnetoelastic coupling constants and $\epsilon_{ij}$ are the strain components. The magneto-elastic coupling constants can be deduced from the magnetostriction coefficients for a bulk magnetostrictive material according to the following equations:

$$b_1 = -\frac{3}{2}\lambda_{100}(c_{11} - c_{12}) \text{ and } b_2 = -3\lambda_{111}c_{44} \quad \ldots 2.26$$

$\lambda_{100}$ and $\lambda_{111}$ are the saturation magnetostriction constants measured for magnetization aligned along the (100) and (111) directions. The saturation magnetostriction coefficient for an isotropic material is defined as: $\lambda_s = \Delta l/l$ which is nothing but the strain generated by saturating magnetic field. Here, $c_{ij}$ are the elastic moduli. In the present thesis, magnetoelastic coupling between ultrafast laser generated elastic wave and spin-wave has been investigated in ferromagnetic nanostructures.

This chapter begins with a concise overview of the nanofabrication process of the ferromagnetic material and outlining few general characterization techniques. Subsequently, this chapter introduces a variety of experimental setups employed to measure the quasistatic and ultrafast magnetization dynamics in the realm of this PhD thesis. In this part, the fundamental physics theories underpinning the experimental tools have been briefly described. Next, the instrumentation is described in details with the working procedures elucidating the detection scheme which is the most crucial part of any experimental tool. The chapter ends by thoroughly describing various commercially available simulation packages and the home-built simulation tools offering a profound understanding of the subjects under investigation.

## 3.1 Fabrication and General Characterization Techniques

Fabrication of samples at nanoscale plays a significant role in the development of nanoscience and nanotechnology [145]. Thereby, the tremendous surge of interest in nanoscience has given birth to various state-of-the-art fabrication methods in the last few decades. The nanofabrication methods can be divided into two categories: top-down and bottom up. The top-down approach is extensively used to fabricate nanostructures or thin films by removing specific regions of a bulk material. The bottom-up approach is a chemical method which relies upon the self-accumulation of atoms from molecules or clusters to form nanoscale structures. However, both the methods have been widely accepted to grow pristine material at the nanoscale. In the present thesis, commercial substrates have been used in fabrication of artificially patterned nanostructures (magnonic crystals) by lithography technique while Heusler alloy and 2D van der Waals crystals have been synthesized in the laboratory by electro chemical deposition (ECD) and chemical vapor transport (CVT) methods.

The patterned nanostructures are fabricated using electron-beam lithography (EBL) in conjunction with electron-beam evaporation (EBE) and lift-off. In some cases, an additional process named ion-beam milling can be involved to fabricate specific structures. EBL is a well-established tool to transfer or 'write' a computer generated 2D layout on top of a 2D surface by highly energetic focused electron beam. Prior to the lithography, the surface is coated with an e-beam sensitive organic chemical called resist. 'Writing' is subsequently followed by development in which only the e-beam exposed (unexposed) area of the positive (negative) resist dissolves into some resist-specific solvent. At the next stage, the target material is deposited on the substrate in a vacuum environment using EBE. For the deposition, the material is placed in a crucible at the bottom of the vacuum chamber whereas the substrate is placed lining the ceiling of the chamber. The material evaporates at high temperature created by continuous electron bombardment and stick to the substrate. In the following step, lift-off is done to remove the remaining resist from the substrate along with the material on top of it. A patterned structure appears as the final product which is further cleaned by chemical wash followed by plasma etching. Thermal evaporation

and electron beam evaporation can be used to coat the surface of the magnetic structures with a thin insulating layer to avoid oxidation. Limited by electron scattering, this method provides a resolution of >10 nm.

ECD is a cost-effective, fast and simple way offering precise control over synthesis of micrometer thick alloy or metallic crystals [145]. This method is based on electrolysis process where a conducting substrate functions as cathode on which metal ions adhere to form a solid layer. The metal ions are reduced from the electrolyte, prepared by dissolving the metallic salt in an appropriate solvent. The morphology of the deposited product can be directly influenced by the voltage applied to the electrodes. In this thesis work, Heusler alloy layer grown on Pt/Ta/Si substrate by the electrochemical approach has been studied.

CVT is another widely used method to synthesis defect-free crystalline solids [145]. This method is all about chemical reactions and thermodynamic laws. In this approach, the reactants of condensed phase are transferred to gas phase in presence of a transport agent within a sealed transport ampoule. The ampoule is kept in a furnace of two temperature zones (T1 and T2) during the reaction, so that the chemical vapor (gas) can be transported from one temperature zone (T1) to another (T2). Generally, T1 zone is called the source and T2 zone is called the sink where the gaseous state condensates in crystal form.

The crystal structure can be examined through X-ray diffraction (XRD). The surface quality and the magnetic topography are inspected using the atomic force microscopy (AFM) and magnetic force microscopy (MFM) while scanning electron microscopy (SEM) can produce good quality surface image. For two-dimensional nanostructure array, these surface images are crucial to accurately determine the shape, size and symmetry of the nanomagnets.

## 3.2 Quasistatic and Dynamics Characterization Techniques

The quasistatic magnetization dynamics implies here the magnetic hysteresis when the domains of a magnetic material, subjected to an external magnetic field, rotate altering the net magnetization. Measurement of this magnetic hysteresis is therefore very crucial to clearly understand the static magnetic character (the relation between static magnetization and external magnetic field) of a material. This characterization is primarily done using a vibrating sample magnetometer (VSM) or static magneto -optical Kerr effect magnetometer (static MOKE). On the other hand, the dynamic characterization involves the measurement of various entities related to the magnetization dynamics of ultrafast timescale. In dynamic scenario, magnetization is first disrupted from equilibrium mostly by means of external perturbation, and the ensuing relaxation is captured to extract information. This dynamic encompasses a number of engrossing phenomena, e.g. ultrafast demagnetization, spin-wave generation, uniform precessional motion, spin-phonon coupled motion, domain wall motion, magnetization switching, spin pumping, spin transport etc. State-of-the-art techniques are employed to investigate these phenomena and extract the key parameters to quantify those. In the framework of the present

thesis, techniques based on time-resolved magneto optic Kerr effect (TR-MOKE), Brillouin light scattering (BLS) and ferromagnetic resonance (FMR) have been used as the relevant dynamic characterization tools while static MOKE magnetometer has been employed for the quasistatic characterization. The following sections delve into the details of these experimental methods briefly describing the basic physics lying at the heart of those methods.

### 3.2.1 Static Magneto-Optical Kerr Effect Magnetometer

#### A. Underlying Principle

The static MOKE setup works based on magneto-optical Kerr effect (MOKE) which was first observed by scientist John Kerr in 1877, as a transformative change of electromagnetic wave upon reflection from a magnetized surface [146]. Kerr revealed that the polarization axis of a linearly polarized light undergoes a distinctive rotation (Kerr rotation) adding an adequate amount of ellipticity (Kerr ellipticity) in the electric field vector. A linearly polarized light can be envisioned as a blend of left and right circularly polarized lights of equal amplitude at 90° phase difference. The absorption coefficient and refractive index for the right and left circularly polarized lights are different within a magnetized material, known as the circular dichroism and birefringes. Consequently, the incident light decomposes into two orthogonal components of different amplitude, velocity and hence phase relation, which form an elliptically polarized light on emergence from the material [147]. Mathematically, the Kerr rotation ($\theta_k$) and Kerr ellipticity ($\varepsilon_k$) can be given by a single expression,

$$\theta_k + \varepsilon_k = \frac{k}{r} \tag{3.1}$$

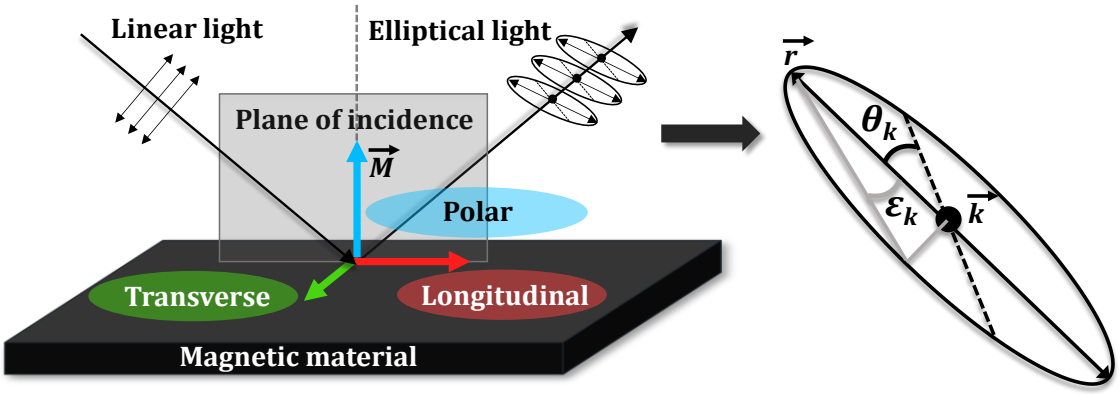


**Figure 3.1:** Schematics of polar, longitudinal and transverse MOKE geometries with the geometry of the Kerr rotation ($\theta_k$) and Kerr ellipticity ($\varepsilon_k$).

where $k$ and $r$ ($k<<r$) are the Fresnel coefficients associated with the two orthogonal components of the electric field vector of the elliptically polarized light. Both $\theta_k$ and $\varepsilon_k$ are proportional to the value of magnetization vector of the material and change sign if the magnetization flips its direction. This relation between magnetization and Kerr parameters can be described classically or quantum mechanically [148]. However, due to this magneto-optic relation, MOKE has supreme potential to unlock

the intricate world of static as well as dynamic magnetization of a material [149]. The magnetization can be investigated under three distinctive MOKE geometries defined by the relative orientation between the magnetization vector and the plane of incident light: longitudinal, transverse and polar (Figure 3.1). Notably, $\theta_k$ and $\varepsilon_k$ again depend on the angle of incidence of the light for all three geometries. In longitudinal and transverse geometries, the Kerr quantities are minimum for normal incidence of light, while for polar geometry those are always maximum.

The quasistatic characterization of magnetization e.g. magnetic hysteresis measurement can be performed in optical method exploiting static MOKE technique. This setup is configured in longitudinal geometry and hence suitable for ferromagnetic samples with in-plane magnetization. Since the MOKE signal is sensitive to the surface magnetization, this technique offers better efficacy to unpin the local magnetization in thin films and nanostructures.

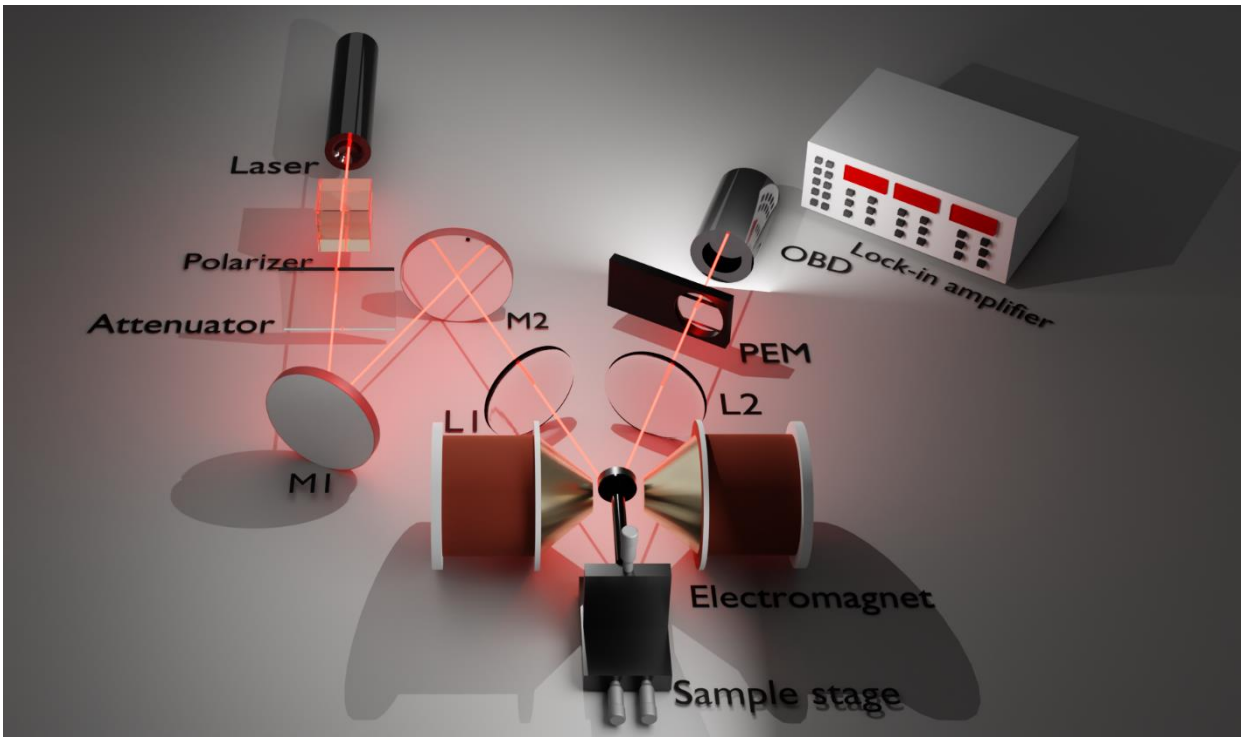


**Figure 3.2:** Schematic of static magneto-optical Kerr effect (Static-MOKE) setup.

## B. Experimental Setup

The schematic diagram of the static MOKE setup is displayed in Figure 3.2. A continuous wave laser beam of wavelength 632.8 nm sourced from a He-Ne laser first passes through a Glan-Thomson polarizer to be an s-polarized light. The polarized beam is guided by two mirrors (M1 and M2) and focused by a lens (L1) on the sample surface with a spot size of ~ 100μm. The sample is mounted exactly at the centre of two pole pieces of an electromagnet on a high precession rotating mount. The reflected beam is collimated by a single lens (L2) / lens assembly (not shown here) and then directed to an optical bridge

detector (OBD) for optical detection. An attenuator is placed in the beam path to vary the incident laser power.

### C. Data Acquisition and Detection

To measure magnetic hysteresis loop, the Kerr rotation is recorded as a function of magnetic field supplied by the electromagnet. For each value of magnetic field, Kerr rotation is analyzed by the OBD. The OBD's working principle is simple. A polarized beam splitter (PBS) basically a Wollaston prism inside the OBD splits the collected beam into two mutually orthogonal (linearly) polarized components (Figure 3.3). A couple of Si photodiodes convert these two optical signals into electrical signals (say A & B). The change in Kerr rotation stamps into the differential signal (A-B) while the sum signal presents the reflectivity (A+B). Before applying any external magnetic field, the axis of PBS is rotated to make A = B. This is called the balanced condition of OBD. As we externally apply a magnetic field, the magnetization of the sample changes. This induces a change in the plane of polarization leading to nonzero value of A-B. The output signal from OBD is measured by a lock-in amplifier which works in a phase-sensitive manner. To minimize the signal to noise ratio (SNR), the amplifier is fed with a reference signal of 50 kHz generated by a photo-elastic modulator (PEM), kept in the path of the reflected beam. The PEM introduces a periodic phase shift at 50 kHz between the two optical components. The lock-in can only detect the harmonics of this modulating frequency eliminating any other components i.e., reduces noise. The Kerr rotation which is in the unit of Volts can be converted to units of angle by multiplying a calibration factor. The calibration factor is determined by recording rotation (in degree) of the axis of PBS on both sides from its balanced condition and then noting the corresponding voltages.

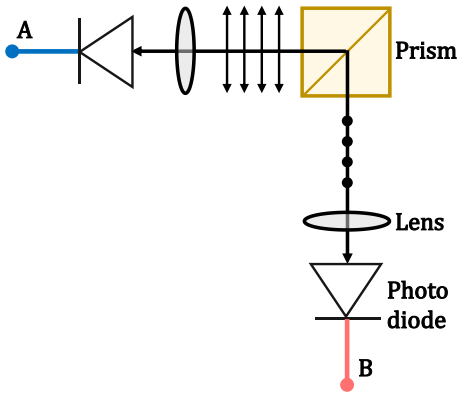


**Figure 3.3:** Schematic of the working principle of the optical bridge detector.

## 3.2.2 Time Resolved Magneto-Optical Kerr Effect Technique

TR-MOKE is an elegant all-optical non-invasive technique to investigate ultrafast kinetics of a magnetic system with high temporal resolution. Like static MOKE magnetometer, this technique also relies on the MOKE principle but designed for time-domain measurement of magnetization based on two colour pump-probe spectroscopy. Here, pump is an ultrafast pulsed laser beam ($\lambda_{pump}$ = 400 nm) that is used to

excite the dynamics and probe is another ultrafast laser beam ($\lambda_{probe}$ = 800 nm) to trace the magnetic state before or after excitation with a time resolution of femtoseconds (determined from the convolution of pump and probe pulse duration). The probing time can be expanded from few femtoseconds to few nanoseconds by controlling the arrival time of the probe at the sample. Therefore, calculation of the optical path traversed by the pump and probe beams to reach the sample surface is a very crucial part of this experimental method. In our experiment, the probe is set to go through a tunable path length to avail a time span of few femtoseconds to a maximum of few (3.2 and 4 ns here) nanoseconds. The TR-MOKE setup works in polar MOKE geometry and measures the change in the out-of-plane magnetization component as a function of relative time delay between pump and probe beams. Moreover, apart from magnetization dynamics, the dynamic change in total reflectivity which is basically a coupled imprint of electron and lattice dynamics of the sample can be measured by this technique. In this pump-probe measurement, the pump beam can be aligned for either parallel incidence or acute incidence with respect to the probe direction referred as collinear or non-collinear geometry, respectively. It is noteworthy that the excitation scheme and data analysis process remain consistent for both geometries. In this thesis, we have utilized TR-MOKE setups of both collinear and noncollinear geometries to explore a wide range of microscopic phenomena including ultrafast demagnetization dynamics, spin-waves, lattice dynamics, magnetoelastic dynamics of ferromagnetic nanostructures.

#### 3.2.2.1 Time Resolved Magneto-Optical Kerr Effect Microscope

This setup, used in collinear geometry, is capable of collecting signal from a submicrometer to sub nanometer feature size. A brief overview of the experimental setup, data collection and detection procedure is given here.

### A. Ultrafast Laser System

This setup consists of two different laser systems, one second harmonic generator, and various optical and electrical components. The first laser is a diode-pumped solid state (DPSS) laser named Millennia eV [150]. Millennia eV emits an s-polarized ($TEM_{00}$) continuous-wave (CW) green laser of wavelength 532 nm at a highly stable output power of 8 W. This 532 nm laser beam is sent to the cavity of the second laser, named Tsunami [151] for generation of mode-locked femtosecond laser pulses. Tsunami is basically an oscillator cavity system where a rod made of titanium (Ti) doped sapphire ($Al_2O_3$) crystal (Ti:sapphire) functions as the active medium and an acousto-optic modulator (AOM) is used for active mode locking. Here, lasing is achieved from the $Ti^{3+}$ ions of the Ti:sapphire crystal as a result of fluorescent transitions in the infrared regime (690-1080 nm) from its vibrational energy band $^2E_g$ to $^2T_{2g}$. This laser is then allowed to travel back and forth within the cavity reflected by a series of mirrors. The AOM is kept in this travel path to convert the CW laser to a mode-locked laser. The AOM is made of a quartz crystal and a piezoelectric transducer attached to one side of the crystal. The AOM is switched on by providing RF signal in regenerative manner to the piezoelectric transducer. At 'on' state, sound wave is generated in the quartz. Due to propagation of sound wave, a periodic pressure gradient is established

inside the crystal which acts as a transient diffraction grating for the laser light. Therefore, the laser light gets diffracted out of the cavity during each passage through the AOM enhancing the cavity loss. This cavity loss is periodic at twice the frequency of the RF signal. At this stage, the AOM is turned off leading a sudden increase of the cavity gain (low Q to high Q: Q is the ratio of gain to loss), called Q-switching [152]. This Q-switching results in a stable mode-locked condition through which a high intense laser pulses (intensity, $I_{pulse} = NI_{cw}$, N is the number of phase-locked modes) are obtained at repetition rate of 80 MHz.

Since, the refractive index of an optical medium depends on the frequency of light, each frequency within the laser pulse possess different group velocity in that medium, known as group velocity dispersion (GVD). This introduces a difference in the transit time through a medium among the pulse components. A positive GVD results in temporal broadening of the pulse. Further pulse broadening occurs due to the Ti:sapphire's self-phase modulation. When a pulsed laser is incident on Ti:sapphire crystal its refractive index (*r.i.*) changes nonlinearly with time following the intensity profile of the pulse. Due to this reason, the *r.i.* increases (velocity decreases) with time during the rising half of the Gaussian pulse and it decreases (velocity increases) for the trailing part of the pulse. Therefore, a time lag is observed between different parts of a single pulse when the pulse propagates through the crystal resulting in a temporal phase modulation. In other words, additional frequencies (blue- and red-shifted in the first and second half of the pulse respectively) of different velocity are transiently added in the frequency spectra of the pulse. This phenomenon leads to a transient increase of the pulse duration and thereby called pulse chirping or frequency chirping.

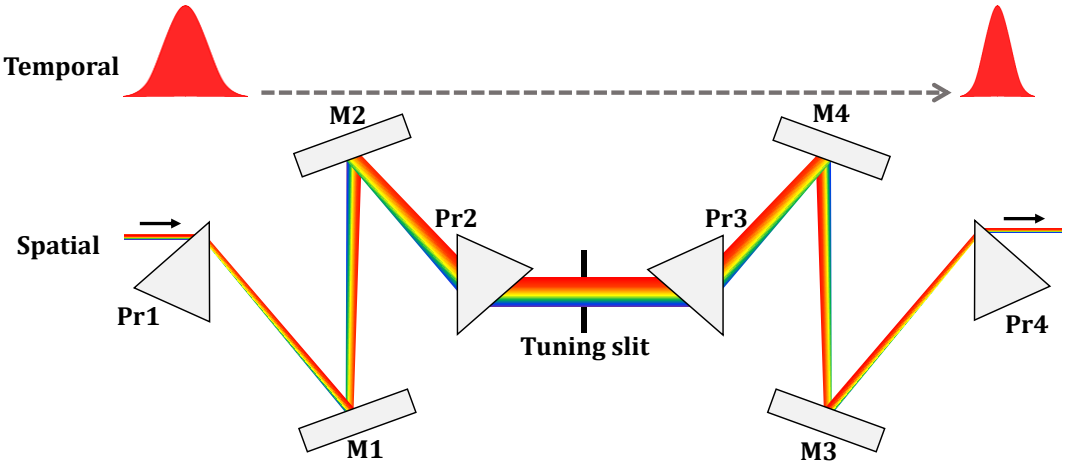


**Figure 3.4:** Pulse-duration compression of a chirped pulse by negative dispersion method using two dispersive prism (Pr)- and mirror pairs (M).

To achieve a shorter pulse, the laser is passed through two pairs of prisms. The prisms create spatial dispersion of different frequency components of the pulse. Now, optical path difference is introduced in those spatially dispersed components by properly tuning the positions of the prisms in the beam path. Then minimizing the travel-time gap between the leading and trailing frequency components of the

pulse, the total duration of the pulse is reduced as shown in Figure 3.4. The central wavelength of the output pulse can be tuned by placing a movable slit in the path of the dispersed beam. By moving the slit, the beam can be partially blocked except the required output wavelength component (λ = 800 nm here). The bandwidth is adjusted accordingly by varying the slit-width. This frequency selective method further eliminates the effect of GVD and shortens the pulsewidth. Two adjustable screws are attached outside the Tsunami to tune the slit-position and slit-width for selection of the laser output wavelength with optimized full width half maxima (FWHM) [151]. Thus, a mode-locked laser of wavelength 800 nm and pulse width 80 fs is finally obtained by the cavity at repetition rate of 80 MHz.

## B. Second Harmonic Generation

The second harmonic of the 800 nm beam is used as the pump in the TR-MOKE measurement which is generated by a second harmonic generator (SHG) [153]. This SHG functions based on the nonlinear optical effect of material and hence a nonlinear crystal is the key element of an SHG. Nonlinear effect occurs when the polarization of a dielectric material shows a nonlinear relation with the electric field i.e., the dielectric constant contains higher order term apart from the linear one. Therefore, the refractive index also becomes a superposition of different higher order terms. The second harmonic generation is possible in a noncentrosymmetric crystal under a dominating second order term of electric field in the polarization. This results the oscillating dipoles of the material to radiate electromagnetic field at frequency 2ω apart from the fundamental frequency ω in presence of an oscillating electric field at frequency ω. Here, the 800 nm beam is sent to the SHG where the nonlinear material is a thin Barium Betaborate (BBO) crystal. This crystal emits a p-polarized 400 nm light as the second harmonic along with the original 800 nm light with s-polarization. The power of the second harmonic beam is expressed as,

$$P_{SHG} \propto \frac{d_{eff}^2 P_\omega^2 l[\phi]}{A}$$

where $d_{eff}$, $P_\omega$, $l$ and $\phi$ are the effective non-linear coefficient, output power of the fundamental frequency, crystal length and phase-matching factor respectively. A is the incident area of the fundamental beam on the crystal surface, tunable by proper mirror-alignment inside the SHG cavity which is doable using the attached screws of SHG. The second harmonic is separated out from the fundamental beam using prism pairs inside the SHG. Finally, both the beams are steered to two different exit paths of the SHG with the help of multiple optics.

## C. Experimental Setup

The schematic of the experimental setup is shown in Figure 3.5. The output of Tsunami is first divided into 70:30 ratio by a beam splitter (BS1). The major part is fed to the SHG to generate 400 nm beam i.e., pump beam of the experiment. The residual part of the 800 nm beam travels in a fixed optical path guided by four mirrors (M1, M2, M3 and M4) towards a retroreflector kept on a variable motorized delay stage. During this journey, power of this beam is further attenuated using a variable attenuator A1. The

retroreflector can be moved on the delay line to introduce a variable optical path length for 800 nm henceforward. The reflected 800 nm beam is then guided by two mirrors (M5 and M6) in a straight path which then passes through a collimating lens assembly (L1 and L2). The collimated beam again passes through a Glan-Thompson polarizer to be a pure linearly polarized light. In the next step, this beam path is rotated by a mirror (M7) to make it collinear with the pump beam. The pump beam is guided to the microscope objective (MO: M-40X, N.A. = 0.65) using three mirrors (M8, M9 and M10) with reduced power (attenuated by A2). Both the beams meet on a 50:50 beam splitter (called beam combiner at this point) and enter the MO. The MO normally focuses the probe beam on the sample surface with a spot diameter of ~ 800 nm while the pump beam becomes slightly defocused with a spot diameter of ~ 1000 nm due to chromatic aberration. The beams reflect back through the same MO and follow the incident path. Here, using another beam splitter (BS2) the reflected beams are separated out from the incident beams and guided in a different path. The probe beam is filtered out using an infrared bandpass filter (red filter here) and sent to the OBD for detection of the reflectivity and Kerr rotation. Also, a viewing arrangement is done by inserting two glass slides (G1 and G2) and a CCD camera. A white light source is used to illuminate the sample surface for taking images.

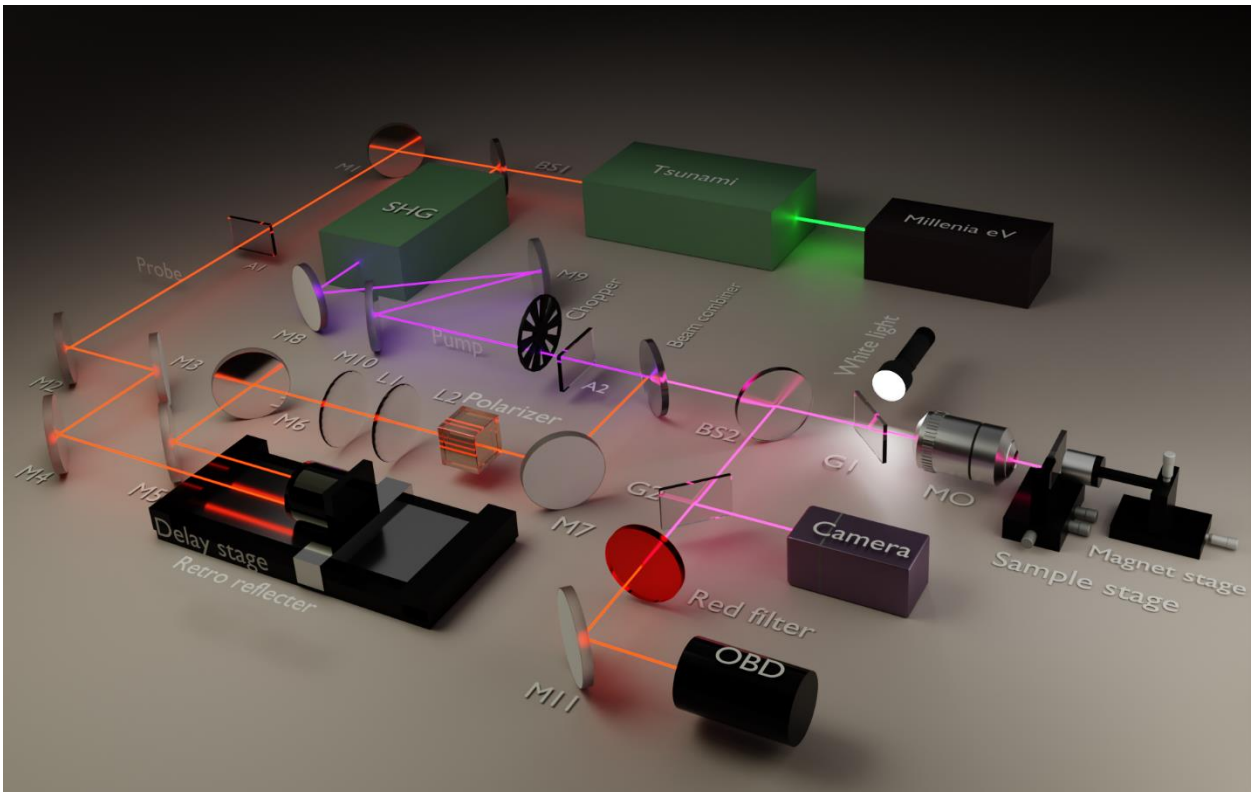


**Figure 3.5:** Schematic diagram of the time resolved magneto-optical Kerr effect (TR-MOKE) microscope.

## D. Data Acquisition and Detection

A magnetic field is applied from the backside to the sample using a permanent magnet attached to a translational x-y-z stage and the sample is kept in a sample holder attached to a motorized piezoelectric

stage facilitating very precise scanning of sample at micrometer scale in horizontal and vertical directions. For measurement of the precessional dynamics, the magnetic field is always applied with a small tilt angle with respect to the anisotropy direction in order to create a finite demagnetizing field along the pump direction. Then, high intense pump beam can unpin the magnetization from its equilibrium direction leading to precessional motion of magnetization around an effective field direction. At each time step of the measurement, the Kerr rotation associated with the z-component of magnetization is analyzed by the OBD in a similar fashion as discussed in static-MOKE setup. However, here, two separate lock-in-amplifiers are utilized for simultaneous measurement of Kerr rotation (A-B) and reflectivity (A+B) data from the OBD generated electric signals. The reference signal for both the lock-in-amplifiers is produced by a mechanical chopper by modulating the pump beam at 2 kHz frequency. As in static-MOKE, to obtain the Kerr rotation in terms of angle, the OBD is calibrated and to maximize the Kerr rotation, A-B is set to zero before the pump hits the sample.

#### 3.2.2.2 Time Resolved Magneto-Optical Kerr Effect Magnetometer

TR-MOKE magnetometer is another MOKE based dual pump-probe setup designed in non-collinear geometry. The setup is based on the amplified femtosecond laser system unlike the oscillator laser of microscopy setup. Therefore, it can generate very high energy laser pulses (~ 4 mJ/pulse) with a shorter temporal width ~ 40 fs. With the above mentioned features, this experimental setup is highly sensitive to sub femtosecond phenomena and hence more suitable for the investigation of ultrafast demagnetization dynamics apart from the precessional oscillations. The instrumentation part is described below.

##### A. Ultrafast Laser System (Libra)

Libra is the single black box comprising of assembly of electronic and optical elements [154]. It encapsulates multiple laser cavities including seed laser and pump laser and a complete regenerative amplification system to produce high intense laser pulses of very short duration ~ 40 fs. The main parts of the Libra and their working principles are briefly described here.

Vitesse is one core laser assembly of Libra which delivers laser pulses of pulse width 100 fs of wavelength 800 nm at a repetition rate of 80 MHz and average output power > 200 mW [155]. The output of Vitesse is used as the seed laser for the amplifier system. Vitesse consists of a diode pumped solid state (DPSS) continuous-wave (output wavelength, $\lambda_{verdi}$ = 532 nm) laser named Verdi and an ultrafast Ti:sapphire laser head, optically pumped by the Verdi's output. The ultrafast laser is commonly known as Verdi-pumped ultrafast laser or VPUF. The high intense pulsed output from Vitesse is obtained from VPUF through Kerr lens mode locking method which relies on the Ti:sapphire crystal's self-focusing property. More precisely, the *r.i.* of Ti:sapphire is a function of intensity of incident light. As a result, for an intense Gaussian shaped incident beam the *r.i.* varies nonlinearly following the Gaussian intensity profile. This symmetric gradient of *r.i.* of a medium helps it to act like a lens and focuses the beam within the medium as the beam propagates through the medium. This phenomenon is known as Kerr lensing and results

in a reduced diameter of the emerged beam. Incidentally, the low intense CW beams are unable in self-focusing like a pulsed light. Taking advantage of this property of Ti:sapphire crystal, the cavity arrangement is done to create a favorable condition for mode-locking. However, during Kerr-lensing the different frequency component of the beam suffers phase difference, called self-phase modulation. This leads to temporal chirping of frequency i.e., a transient add-on of new frequency components within the laser pulse which, in turn, results temporal broadening of the laser pulse. Apart from self-phase modulation, different parts of the beam experience different group velocity during the Kerr-lensing causing GVD. A positive GVD leads to further pulse broadening in time domain. These effects are minimized passing the beam through Fabry-Perot etalons made of negative dispersive mirrors kept inside the cavity. Finally, a sub-100 fs pulsed output of central wavelength 800 nm is obtained from the Vitesse.

Evolution-30 is another laser unit inside the Libra whose major component is a Q-switched pulsed laser of output wavelength 527 nm [156]. Here, an Nd:YLF is used as the gain medium and pumped by diode laser under an optimal temperature. The emission spectra of Nd:YLF contains 1047 nm and 1053 nm lines while 1053 nm is chosen for further operation due to high thermal stability. Mode-locked condition is achieved in this cavity by AOM-based Q-switching method like the Tsunami laser. This is followed by an intra-cavity frequency doubling mechanism using LBO crystal. To obtain maximum conversion (1053 nm to 527 nm) efficiency of the LBO crystal, its temperature is constantly maintained at 164.1°C using a heater. Thus, a 527 nm pulsed laser emerges out from Evolution-30 with a repetition rate of 1 KHz and average pulse energy > 20 mJ which is used as the optical pump in the amplifier cavity.

## B. Amplification and Ultrashort Pulse Generation

The final and most essential task of generating a high intense laser pulse of ultrashort duration is done by a combined contributions of a regenerative amplifier cavity and a pulse stretcher & compressor system. In the first step, the ultrashort seed pulse (800 nm) undergoes a temporal stretching technique via pulse chirping method using diffractions gratings. It results in a reduction in the peak power. Then this chirped pulse is fed to the amplifier cavity to pass through a Ti:sapphire crystal. Meanwhile, the output of Evolution-30 enters into the resonator cavity and pumps the Ti:sapphire crystal. As soon as lasing starts from Ti:sapphire crystal, the 800 nm seed laser starts to amplify within the gain medium. The regenerative amplifier can actually amplify a nano-Joule order laser pulse to a milli-Joule order pulse i.e. by a factor of $10^6$. Once the amplified pulse transits the gain medium, it is guided into the pulse compressor system. The compressor is basically another diffraction grating which introduces negative GVD to restore the initial pulsewidth holding higher energy. Finally, a stable mode-locked laser of wavelength 800 nm and pulsewidth ~40fs is achieved from Libra at a repetition rate of 1 kHz and peak energy of few mJ order.

## C. Second Harmonic Generation

The pump beam used in this experimental set-up is the second harmonic of the 800 nm beam i.e. laser of wavelength 400 nm. To generate this 400 nm laser a SHG is used with working mechanism similar to the SHG of the TR-MOKE microscope setup.

## D. Experimental Setup

This optical setup is designed like the collinear set-up except few technical changes as can be visualized from the schematic diagram in Figure 3.6. The major difference is the oblique incidence (~50°) with the probe direction) of pump beam for noncollinear geometry. Instead of MO, two confocal lenses are used in this setup to focus the pump and probe beams on the sample surface. Hence, the diameters of the pump and probe beams are larger (200 and 100 µm, respectively) offering a large areal averaging over the sample. The back reflected probe beam passes through a beam splitter. One part transited from the beam splitter is used for detection. The obliquely reflected pump beam is blocked by a light blocker. Like TMOKE microscopy, the magnetic field is applied from the backside to the sample using a permanent magnet attached to a translational x-y-z stage.

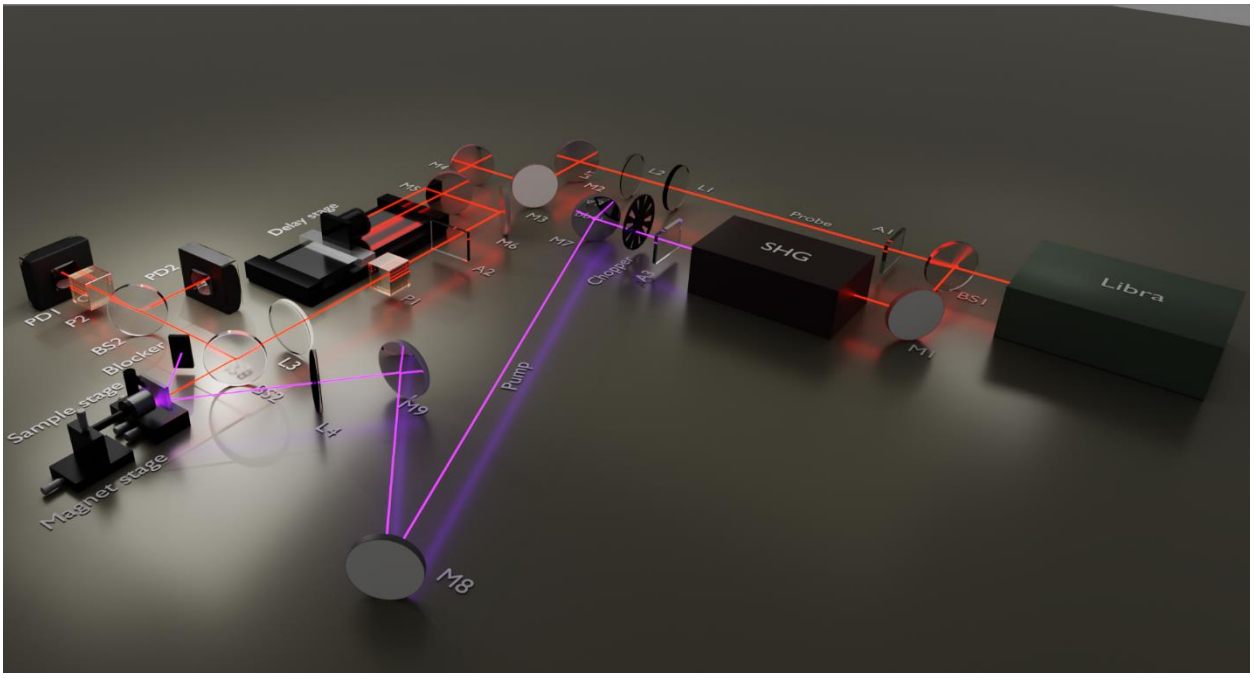


**Figure 3.6:** Schematic diagram of the time resolved magneto-optical Kerr effect (TR-MOKE) magnetometer.

## E. Data Acquisition and Detection

To detect and analyze the optical signal associated with magnetization dynamics, almost similar procedure is followed as in the microscopy set-up. In this setup, a dual photodiode-based detector assembly is used for the optical signal detection instead of OBD. Basically, the divided part of the reflected probe is again divided into two parts using another beam splitter. One part is directly sent to a Si-

photodiode to capture the optical reflectivity change while the other part is first passed through a cross polarizer (analyzer) before entering into another photodiode. The polarization axis of the analyzer is rotated by ~90° (avoiding the extinction condition) with respect to the polarization axis of the incident probe beam (in negative delay). Thus the initial optical signal to the photodiode is set to nearly zero. As soon as the polarization of the reflected light starts to vary due to MOKE, the angle between the analyzer's axis and the polarization axis of probe no longer remains at 90°. At this condition, light is allowed to pass through the analyzer and focused on the junction of Si-photodiode to produce detectable amount of signal. Both the photodiodes convert the optical signals (reflectivity and Kerr rotation) to electric signals which are analyzed and recorded simultaneously by two LabVIEW operated lock-in amplifiers (SR830, Stanford Research System). The provision of the bias field application and corresponding data record for the magnetization dynamics measurement is same as the microscopy technique which has been described in details in the previous section.

### 3.2.3 Brillouin Light Scattering Spectroscopy

In addition to TR-MOKE, another significant optical method for detecting spin-waves is Brillouin Light Scattering (BLS). Moreover, BLS exhibits versatility in its capability to detect both thermal magnons and externally pumped magnons. BLS is capable to directly map the frequency as a function of wave vector of spin-waves i.e., dispersion of spin-wave. Recently, numerous adaptations and enhancements have been introduced to expand its functionality. For instance, in the case of micro-focused BLS, laser light is concentrated to a spot size of a few hundred nanometers, allowing for the imaging of spin-waves at a very fine scale. Additionally, the phase-sensitive micro-focused BLS technique has been developed, enabling the simultaneous imaging of both the power and phase distribution of spin-waves. In the following section, the fundamentals of BLS and the function of the experimental setup have been discussed. In this setup, a specially optimized multipass Tandem Fabry-Pérot interferometer (TFPI) developed by J. R. Sandercock is used for BLS spectra analysis [157,158].

#### A. Underlying Principle

In condensed matter physics, BLS has been extensively used to optically determine the band structure of acoustic phonon or magnon modes of a material. In a semiclassical picture BLS is analogous to a Bragg reflection, where an incident light wave experiences a diffraction grating created by spin-wave. The spin-wave propagation is manifested in the periodic modulation of dielectric tensor representing a time dependent phase grating. Quantum mechanically, this is an inelastic light scattering between a photon and thermally excited phonon or magnon. This process has a finite probability of creation as well as annihilation of a magnon describing the Stokes and anti-Stokes processes. Similar to any scattering mechanism, the law of angular momentum conservation and energy conservation is obeyed here under translational invariance.

$$h\omega_s = h\omega_i \pm h\omega_m \quad \ldots 3.2a$$

$$h\boldsymbol{k}_s = h\boldsymbol{k}_i \pm h\boldsymbol{k}_m \quad \ldots 3.2b$$

Here, $\omega_i$ ($\omega_s$), $k_i$ ($k_s$) are the incident (scattered) light's frequency and wave vector while $\omega_m$ and $k_m$ are the frequency and wave vector transferred to or by a magnon. In the course of this thesis, confined thin films have been studied. Therefore, conservation laws hold only for the magnons propagating parallel to the surface of the structure as shown in the schematic of Figure 3.7. If light is incident on the sample surface at an angle $\theta$ with the surface normal, the in-plane transferred wave vector which remains conserved is $k_i sin\theta$. Further, a thermal magnon (GHz) has much smaller energy than a visible photon (THz), the energy transferred or gained by the photon is negligible during a scattering. Typically, for the spin-wave measurement a backscattered geometry is used. In this configuration, the scattered light is collected within a solid angle formed by $\boldsymbol{k_s}$ while ki and ks are collinear. As a matter of facts, $k_s \approx k_i$, and hence $k_{sw} = |(k_i - k_s)|sin\theta = 2k_i sin\theta$ where $k_i = 2\pi/\lambda_i$, $\lambda_i$ is the wavelength of the incident light. The $\theta$-dependence allows a wave vector selection between $\pm 2k_i$ in the conventional BLS measurement.

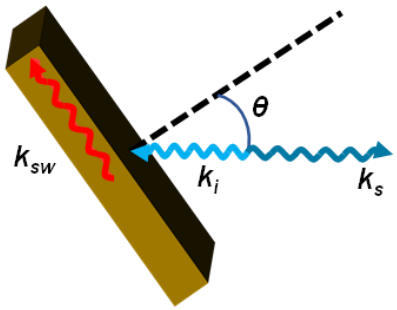


**Figure 3.7:** Schematic of wave vector exchange between photon and surface magnon upon scattering of light from a magnetized film.

The polarization of the incident light changes to the perpendicular direction upon scattering with magnon due to non-zero off-diagonal elements of the dielectric tensor.

## B. Laser

In this experimental setup, a single-mode CW diode-pumped solid state laser (Excelsior) is used. The active medium of this laser is a $Nd^{3+}$ ion doped yttrium vanadate ($Nd:YVO_4$) crystal, which emits 1064 nm due to diode-pumping. This infrared output is frequency doubled within the laser cavity by a LBO crystal to produce a visible green laser of wavelength 532 nm. This 532 nm beam exits the cavity at a steady peak power of ~ 230 mW with beam diameter of ~670 μm and beam divergence of ~ 1.03 mrad, suitable for BLS measurement.

## C. Experimental Setup

The 532 nm laser is first divided into two parts (1:9) by a beam splitter (BS1) kept at 45° (Figure 3.8). The maximum part of the beam goes straight through BS1 and passes a half-wave plate (HWP). The HWP rotates the polarization of the beam at 90° to its original polarization. A polarized beam splitter (PBS) is kept next to the HWP to break the polarization into s- and p- polarized light. The s-polarized light is steered by a series of plane dielectric mirrors (M1, M2, M3, M4) and a tiny prism mirror (Pr1)

towards the sample mounted in between the pole pieces of an electromagnet. An achromatic doublet lens (L1) focuses the incident beam on sample surface and also collects the back-scattered beam. Since, the sample is kept at the focus of L1, the back-scattered beam becomes collimated after passing L1. This collimated beam, guided by a mirror-pair (M5 and M6) is focused on another mirror (M7) by a second lens (L2). A polarizer (P1) is kept in the beam path in between M5 and M6 to allow only 90° rotated polarization caused by spin-wave (here, p-polarized) eliminating the s-polarization (elastically scattered and phonon-scattered light). A mirror M8 again reflects the beam inside the interferometer through a small pinhole.

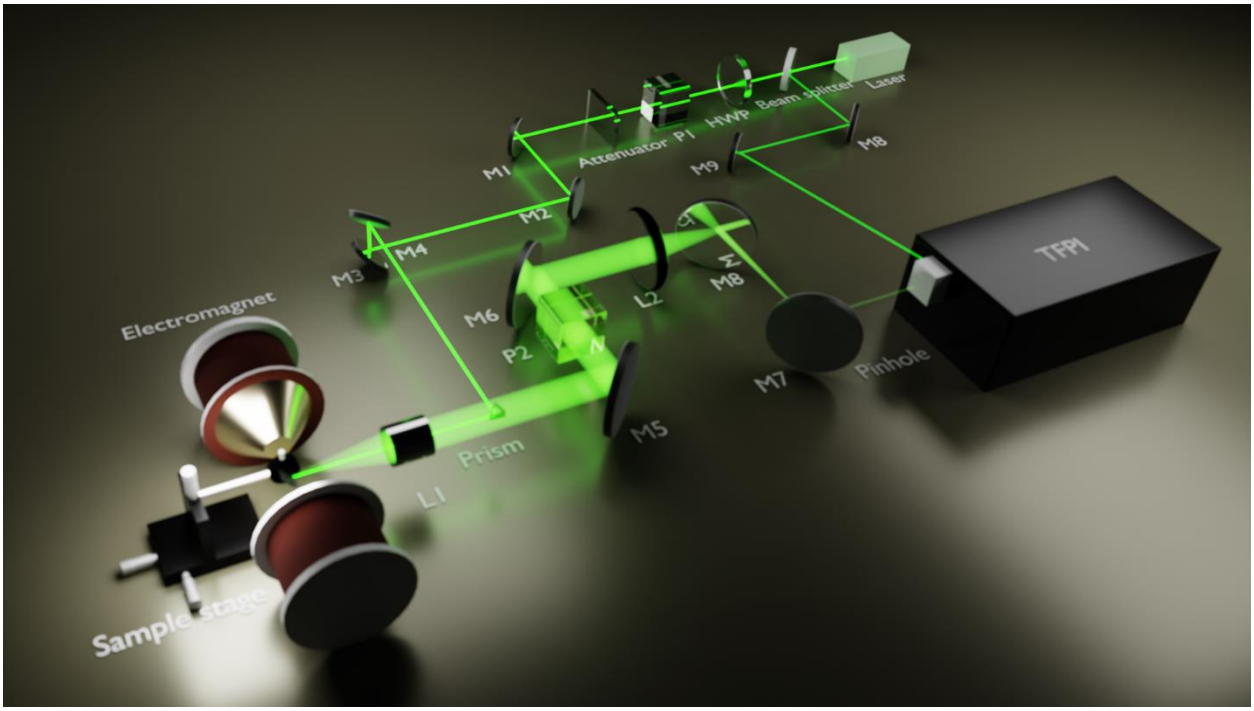


**Figure 3.8:** Schematic of conventional Brillouin light scattering (BLS) spectrometer.

Inside the TFPI as presented in Figure 3.9, the beam first approaches mirror M1′ and then passes FP1 via lens L1′ and mirror M2′. Then it goes through FP2 steered by mirror M3′. The beam is reflected back in the same path by the prism Pr1′ and again passes through FP2 and FP1 with the help of M2′ and M3′. This beam is then focused into another mirror M4′ by the same lens L1′ and follows a parallel path through the lens after being reflected from M4′. Then the beam undergoes a final pass through FP1 and FP2 completing a total of six passes and hits a single photon detector via M5′, Pr2′, M6′ and L2′ to produce a detectable signal. Here, the smaller (10%) part of the direct beam (532 nm) is used in the TFPI cavity as a reference frequency, to calculate the frequency shift in the inelastically scattered light caused by magnon. The reference beam also helps in stabilization of the mirrors to obtain a robust operation of the TFPI.

## D. Data Acquisition and Detection

The key part of the setup is TFPI used for frequency analysis. The back-scattered ray contains multiple frequencies including contributions from both the elastic and inelastic frequencies. The amplitude of elastically scattered light is almost $10^{14}$ times higher than the inelastically scattered light which makes the extraction of spin-wave frequency quite difficult. Using two FPIs of same specifications but different width (mirror separation) and operating them in tandem mode make the task convenient. In the following, the principal role and requirement of the tandem operation on the FPI pairs are discussed.

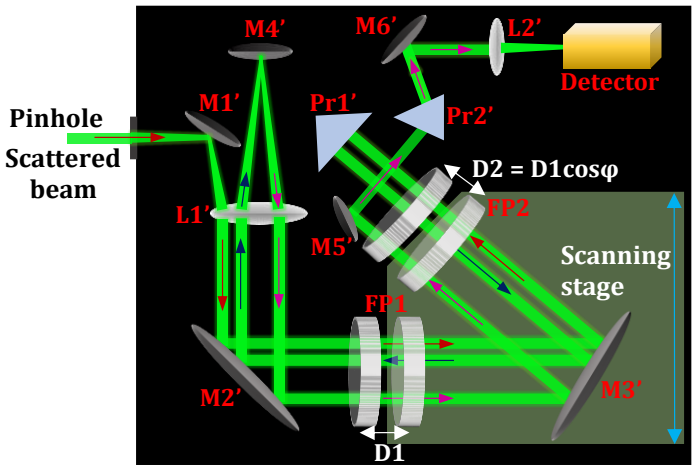


**Figure 3.9:** Top-view of the cavity of tandem Fabry-Pérot interferometer (TFPI) with the beam path.

Any conventional FPI of width $L$ can produce constructive interference fringes on transmission from an incident light of wavelength $\lambda$, if $L = m\lambda/2$ where, m is any positive integer. So, the frequency separation or the free spectral resolution (FSR) will be $\Delta f = c/2L$, where $c$ is the velocity of light in air. Now, for the first and second FPI of width L1 and L2, the FSR will be $\Delta f1 = c/2L1$ and $\Delta f2 = c/2L2$ respectively. Thus, there will be an intermixing of two sets of interference fringes created by two FPIs in the effective transmission spectra in addition to the reference beam's pattern. Naturally, the order of the fringes and hence their source wavelength cannot be recognized from the effective interferograms except the high intense reference frequency. This problem can be resolved by operating the two FPIs in synchronization i.e., in tandem mode. They are arranged in such a way so that only one order of transmission spectra of FPI1 is allowed through FPI2 while the other orders can not satisfy the $L_2=m_2\lambda/2$ relation in the FPI2. To serve the purpose, one mirror of both the FPIs are placed on a common piezoelectric stage and the mirror spacing of both the FPIs are tuned satisfying the following condition,

$$\frac{\Delta L_2}{\Delta L_1} = \frac{L_2}{L_1} = \cos\varphi \qquad \ldots 3.3$$

Further, the multiple passing (3+3) of the beam through the FPI pairs improves the contrast of the interference fringes making those sharper and narrower. The intensity of the transmission pattern of an FPI at perpendicular incidence is given by the Airy function,

$$I_t = \frac{I_0}{1 + \frac{4R}{(1-R)^2} sin^2\left(\frac{\Delta\alpha}{2}\right)} \quad \ldots 3.4$$

where $R$ is the reflectivity of the inner surface of the interferometer, $I_0$ is the intensity of the incident beam and $\alpha$ is the phase-shift after transmission. The contrast of the output of FPI for single pass is defined as,

$$c = 1 + \frac{4R}{(1-R)^2} \quad \ldots 3.5$$

This contrast enhances to nth power of a single pass for n number of passes.

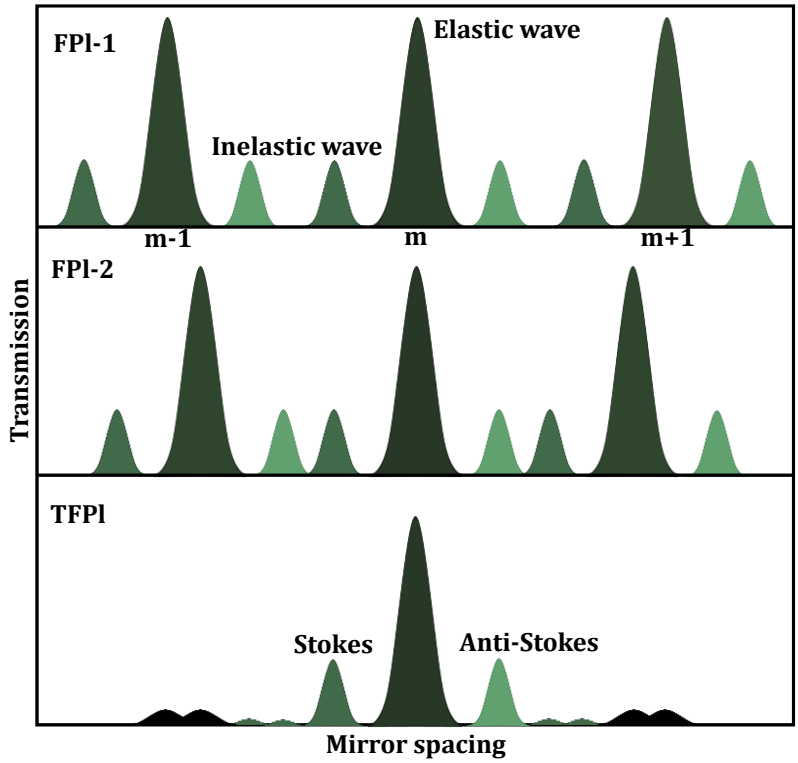


**Figure 3.10:** Interferograms of FP1 and FP2 and in TFPI.

### 3.2.4 Broadband Ferromagnetic Resonance Spectrometer

The frequency domain measurement of spin-wave dynamics is performed by employing a broadband vector network analyzer based ferromagnetic resonance (VNA-FMR) spectrometer [159]. This measurement technique is based on the fact of power absorption from a microwave signal by a magnetized specimen. This is a convenient but powerful to measure magnetic properties [160].

#### A. Underlying Principle

The magnetization vector of a ferromagnetic material starts to precess around an effective magnetic field, on application of an external magnetic field. If an alternating magnetic field ($H_{RF}$) of frequency (ω) is applied in the perpendicular direction to the external field, FMR condition [127] is achieved if

$$\omega = \gamma \sqrt{B H_{eff}} \quad \ldots 3.6$$

where $B$ is the magnetic induction resulted from effective field, $H_{eff}$. Consequently, power is absorbed by the magnetization from the alternating magnetic field. This phenomenon is called FMR.

The microwave absorption spectra can be measured as a function of frequency (10 MHz-50 GHz) or the applied dc magnetic field. These are generally called: frequency sweep and field sweep method. In the frequency sweep method, the field of the electromagnet is kept fixed, and the scattering parameters are measured as a function of frequency. This method is quick, but less sensitive compared to the field sweeping. In addition, frequency sweeps may yield signals which are non–magnetic in origin. Therefore, the raw experimental data require post–processing to eliminate the parasitic resonances from the traces. Here, it is noteworthy that the field sweep method is not suitable for magnetically unsaturated samples, because varying the applied magnetic field will gradually change the ground state of magnetization. Therefore, for taking measurements inside hysteresis loops for a material the frequency swept FMR is more appropriate which has been adopted for the present thesis. Signature of resonance is visible in the absorption spectra as a peak or dip.

## B. Experimental Setup

The key parts of the setup are a vector network analyzer (VNA, Keysight Technologies, PNA-L with model N5230C) and a customized probe station. In the following section, the details of the VNA-FMR technique are elaborated along with a brief overview of the VNA's function.

### B.1 Vector Network Analyzer (VNA)

A VNA is a high resolution stimulus-response test system, having both inbuilt microwave source and microwave signal receivers. The microwave source sends the radiofrequency (RF) current to the sample to excite the magnetization dynamics under the influence of RF magnetic field generated by the RF current. The returned signal, routed from the device under test (DUT) is acquired by the receivers. The receiver's function is to measure the magnitude as well as the phase shift of the electric signal. Therefore, a reference channel is also required, and hence a VNA comes with at least two receivers. The VNA used for this thesis work, has two ports to collect the forward and reverse reflected signals and the transmission response of the DUT in terms of well-defined scattering or S-parameters. The values of the scattering parameters are directly correlated to the strength of the microwave absorption in the DUT. To be more specific, the S–parameters represent ratios of the complex pre-and post-reflection (and transmission) standing power waves as discussed in the next paragraph. S-parameters contain both magnitude and phase information characterizing the linear performance of the device under test (DUT). In VNA, measurements with both magnitude and phase are required for the best measurement accuracy and calibration. With amplitude and phase information, one can quantify the reflection and transmission characteristics of the DUT.

### Scattering (S-) Parameters

For an electrical circuit functioning at RF frequency, generally a scattering matrix (S) is assigned. The S-matrix of an N-port network is an N-dimensional matrix of (N × N) elements where each element is a complex number. The elements get modified with the variation of the RF frequency and system impedance and easier to calculate in such a high frequency measurement system. Further, these elements which are familiar as S-parameters, can be related to the other parameters, e.g. gain, loss, reflection or transmission coefficients. Also, the impedance, admittance and h-parameters can be extracted from S-parameters. If the output and input signals at the first and second ports of a two-port networks are represented by $a_1$, $b_1$; and $a_2$,$b_2$; respectively, then the S matrix can be defined from the following equation,

$$\begin{bmatrix} b_1 \\ b_2 \end{bmatrix} = \begin{bmatrix} S_{11} & S_{12} \\ S_{21} & S_{22} \end{bmatrix} \begin{bmatrix} a_1 \\ a_2 \end{bmatrix} \quad \ldots 3.7$$

where $\begin{bmatrix} S_{11} & S_{12} \\ S_{21} & S_{22} \end{bmatrix}$ is the S-matrix and the diagonal (off-diagonal) elements are associated with reflection (transmission). Generally, S-parameters are expressed in terms of dB as $20\log_{10}|S_{ij}|$ where, i, j = 1, 2 respectively.

## B.2 Coplanar Waveguide (CPW)

The CPW is a key component of the VNA-FMR technique (Figure 3.11). Generally, the CPW is comprised of two or three conducting lines having different designs for transmission and reflection geometry. The term coplanar means all the conducting lines are in the same plane. In case of measurement in reflection geometry with a 3-line CPW the central conductor works as the signal line while the two side lines return the signal. These two conductors are also called the ground line and shorted with the signal line at one end. At the other end, both the ground lines are equally separated from the signal line by a uniform gap.

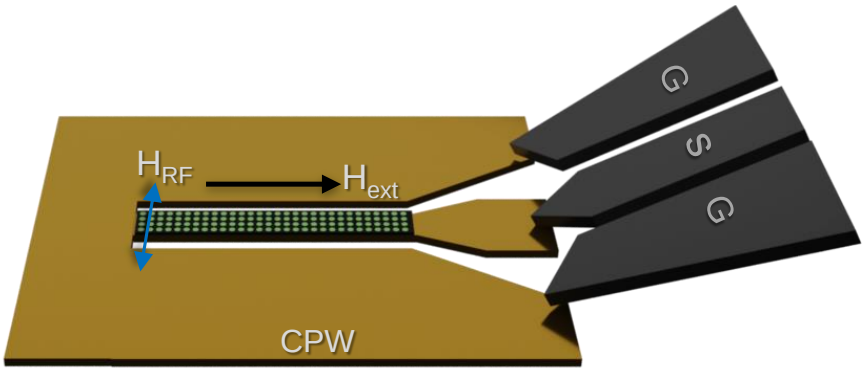


**Figure 3.11:** Schematic illustration of the RF excitation through ground-signal-ground (GSG) type antenna in the coplanar waveguide (CPW).

The characteristic impedance of the CPW is determined by this gap and the width of the signal line, which essentially matches with the impedance of the RF circuit. Here, in this thesis work, the CPW is fabricated from Au using e-beam lithography on the same substrate where the samples are fabricated.

To be more precise, the samples are fabricated either above or below the central (signal) line and a moderately thick insulating layer is placed in-between to avoid any kind of damage of the sample caused by the RF current. The oscillating magnetic field lines generated by the RF current ($I_{RF}$) become flattened near the surface of the signal line because of its rectangular shape. Hence, it produces an in-plane RF magnetic field ($\boldsymbol{H_{RF}}$) to perturb the ferromagnetic specimen from its equilibrium state leading to FMR condition in presence of an external bias magnetic field ($\boldsymbol{H_{ext}}$).

## B.3 Probe Station

This probe station is basically rest of the setup including electromagnet, microscope, camera, illuminator pairs, a high precession translation-rotation stage and non-magnetic high-frequency ground-signal-ground (G-S-G) picoprobe mounted on another high precession translational and tilt stage (micro-positioner) (Figure 3.12). The electromagnet is enabled using a bipolar power supply (KEPCO, INC. model BOP 36-6D, ± 36V & ± 6A) to produce the bias magnetic field parallel to the sample plane. The pole pieces of the electromagnet are mounted on the translation-rotational stage so that the in plane direction of the magnetic field can be varied over 360° with an angular resolution of 1°. The micro-positioner (NPS, model 800MRF-L) can precisely move the position of the picoprobe to build a proper connection with the CPW. The microscope and the camera are used for viewing purpose with the aid of the illuminator pairs (Shodensha Inc.). The viewing system is essential to properly launch the picoprobe head to the CPW. The VNA is connected to the probe station via a single high-frequency and low-noise coaxial cable (model N1501A-203). The one end of the cable is connected to one port of the VNA while the other end is attached to the picoprobe.

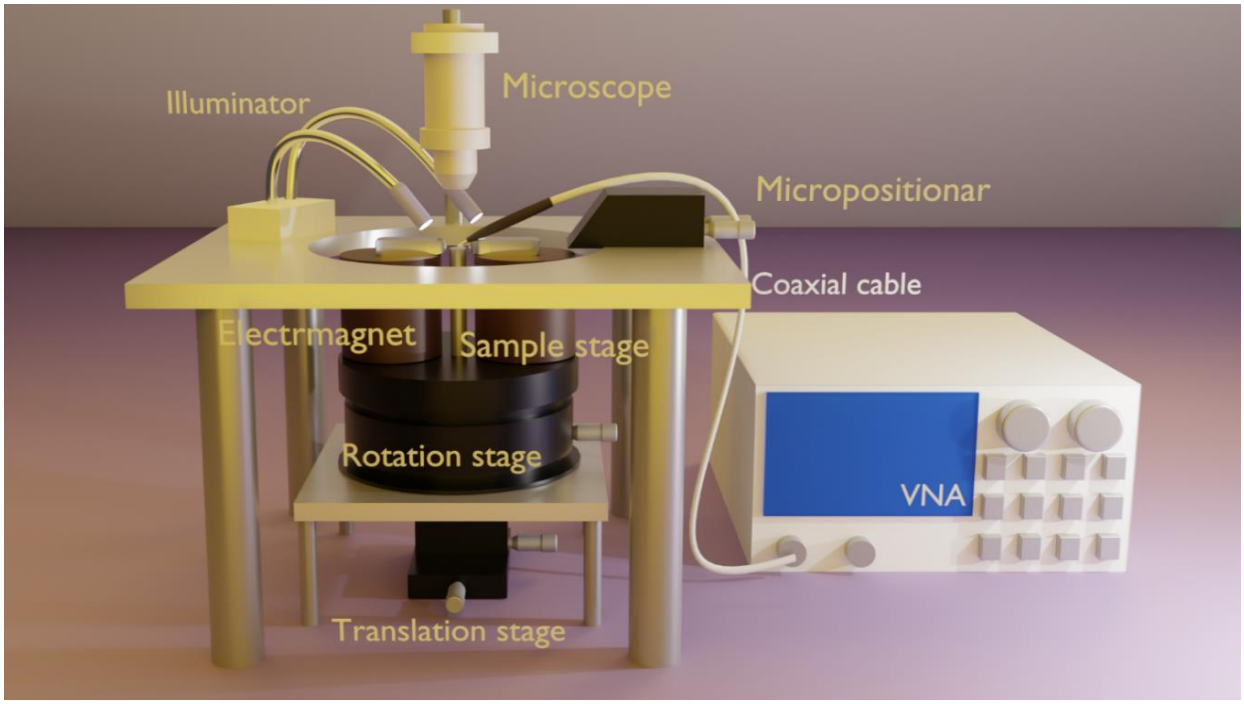


**Figure 3.12:** Schematic of the broadband VNA-FMR setup.

### C. Data Acquisition and Detection

Microwave signals with varying frequencies are launched into the CPW structure shorted at one end, using the G-S-G probe through the coaxial cable, and the back-reflected signal is collected and sent to the analyzer via the same path. Absorption of microwave energy at different frequencies by the sample produces the FMR spectra at those frequencies. The spectral intensity is recorded as the real and imaginary parts of the S-parameter in reflection geometry ($S_{11}$) at various magnetic fields. Then, the values are subtracted from the reference value taken at the maximum of bias magnetic field (±1.8 kOe). One major disadvantage of VNA-FMR technique is that it measures the scattering parameters of the whole DUT i.e., both the CPW and the sample. Due to a significant difference between the sample volume and the CPW, the absorption signal by the magnetic sample is much smaller than the total signal from the output of the CPW. Therefore, in the FMR spectra, the magnetic absorption peak appears as a blip on top of the background CPW signal. Typically, background subtraction needs to be done to isolate the sample signal from the total DUT signal. Thus, the final spin-wave spectra are obtained by eliminating such background.

## 3.3 Numerical Methods

### 3.3.1 Plane Wave Method

Plane wave method (PWM) is widely used to analytically calculate the band structure of periodically patterned structures e.g. electronic, photonic, phononic crystals etc. This method is also feasible to calculate spin-wave dispersion in periodic magnetic structures, primarily in magnonic crystals [161,162]. In this approach, the magnonic crystal is considered to be composed of ferromagnetic material *A* (scattering centres) and a nonmagnetic matrix *B*.

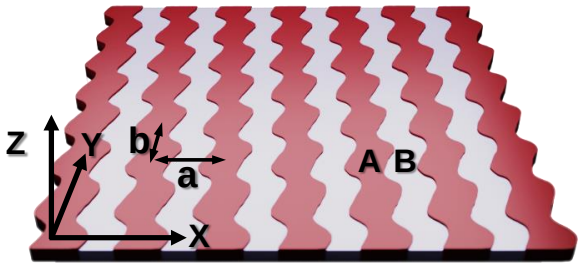


**Figure 3.13:** Schematic of the geometry of magnonic crystal in PWM calculation.

In this method, the LLG equation is solved numerically ignoring the damping term given as,

$$\frac{\partial \boldsymbol{M}(\boldsymbol{r},t)}{\partial t} = -\gamma\mu_0 \boldsymbol{M}(\boldsymbol{r},t) \times \boldsymbol{H}_{\boldsymbol{eff}}(\boldsymbol{r},t) \quad \ldots 3.8$$

Here, $\boldsymbol{M}$ and $\boldsymbol{H_{eff}}$ are respectively the dynamic magnetization and the effective magnetic field which are functions of both space and time. If the bias magnetic field i.e. Zeeman field ($\boldsymbol{H_0}$) is applied along the x-direction, then the x-component of magnetization $|m_x|$ remains undisturbed during the dynamics and

its value is much greater than the y and z components under the linear approximation. Thereby, the dynamic magnetization is simply written as,

$$\boldsymbol{M}(\boldsymbol{r},t) \cong \boldsymbol{m}(\boldsymbol{r},t) = m_y(\boldsymbol{r},t)\hat{\boldsymbol{y}} + m_z(\boldsymbol{r},t)\hat{\boldsymbol{z}} \quad \ldots 3.9a$$

and

$$|m_x| \gg |m(r,t)| \quad \ldots 3.9b$$

The dynamic magnetization is considered as a superposition of plane waves of frequency $\omega$ ($\boldsymbol{m}(\boldsymbol{r},t) \sim e^{i\omega t}$) which follows the periodicity of the patterned structure. Now, $\boldsymbol{H_{eff}}$ is the sum of magnetostatic filed (including both static and dynamic components, $\boldsymbol{H_{ms}}$), exchange field ($\boldsymbol{H_{exch}}$) and the uniform Zeeman field. The anisotropy field is not incorporated due to simplicity.

$$\boldsymbol{H_{eff}}(\boldsymbol{r},t) = H_{ms,x}\hat{\boldsymbol{x}} + \boldsymbol{h_{ms}}(\boldsymbol{r})e^{i\omega t} + \boldsymbol{H_{exch}}(\boldsymbol{r},t) + H_0\hat{\boldsymbol{x}} \quad \ldots 3.10$$

where,

$$\boldsymbol{H_{exch}}(\boldsymbol{r},t) = (\boldsymbol{\nabla} \cdot l_{ex}^2(\boldsymbol{r})\boldsymbol{\nabla})\boldsymbol{m}(\boldsymbol{r},t) \quad \ldots 3.11$$

and

$$l_{ex}(r) = \sqrt{\frac{2A_{ex}(r)}{\mu_0 M_S^2(r)}} \quad \ldots 3.12$$

In the above expressions, $l_{ex}$ is the exchange length, $A_{ex}$ is the exchange stiffness constant and $M_s$ is saturation magnetization. Incorporating the above expressions in eqn. (3.7), following eqns. are derived presenting the two components of dynamic magnetization,

$$m_y(\boldsymbol{r}) = \frac{\mu_0\gamma}{i\omega}\Big(-m_z(\boldsymbol{r})(H_0 + H_{ms}) + M_S h_{ms,z} + M_S(\boldsymbol{\nabla} \cdot l_{ex}^2(\boldsymbol{r})\boldsymbol{\nabla})m_z(\boldsymbol{r})\Big) \quad \ldots 3.13a$$

$$m_z(\boldsymbol{r}) = \frac{\mu_0\gamma}{i\omega}\Big(m_y(\boldsymbol{r})(H_0 + H_{ms}) - M_S h_{ms,y} - M_S(\boldsymbol{\nabla} \cdot l_{ex}^2(\boldsymbol{r})\boldsymbol{\nabla})m_y(\boldsymbol{r})\Big) \quad \ldots 3.13b$$

In this method, all the material parameters are supposed to follow the periodicity of the lattice, i.e.

$$M_S(\boldsymbol{r} + \boldsymbol{a}) = M_S(\boldsymbol{r}) \quad \ldots 3.14a$$

$$A_{ex}(\boldsymbol{r} + \boldsymbol{a}) = A_{ex}(\boldsymbol{r}) \quad \ldots 3.14b$$

$$l_{ex}^2(\boldsymbol{r} + \boldsymbol{a}) = l_{ex}^2(\boldsymbol{r}) \quad \ldots 3.14c$$

To solve eqns. (3.13), Bloch theorem is applied which states that the solution of a differential equation with periodic coefficients can be given as a product of plane waves and a periodic Bloch function, i.e.

$$\boldsymbol{m}(\boldsymbol{r}_\parallel) = e^{i\boldsymbol{q}\cdot\boldsymbol{r}_\parallel}\sum_G \boldsymbol{m_q}(\boldsymbol{G})e^{i\boldsymbol{G}\cdot\boldsymbol{r}_\parallel} \quad \ldots 3.17$$

where $\boldsymbol{G}$ implies the reciprocal lattice vector and $\boldsymbol{q}$ is the wave vector in the first Brillouin zone. In the reciprocal space, the other parameters can also be written by their Fourier transforms as follows,

$$M_S(\boldsymbol{r}_\parallel) = \sum_G M_S(\boldsymbol{G})e^{i\boldsymbol{G}\cdot\boldsymbol{r}_\parallel} \quad \ldots 3.15a$$

$$l_{ex}^2(\boldsymbol{r}_\parallel) = \sum_G l_{ex}^2(\boldsymbol{G})e^{i\boldsymbol{G}\cdot\boldsymbol{r}_\parallel} \quad \ldots 3.15b$$

$\boldsymbol{G} = (m\boldsymbol{a}^* + n\boldsymbol{b}^*)$ is calculated from the lattice constants ($a\hat{x}, b\hat{y}$) of the direct lattice where, $\boldsymbol{a}^* = 2\pi\frac{\boldsymbol{b}\times\hat{n}}{|\boldsymbol{a}\times\boldsymbol{b}|}$ and $\boldsymbol{b}^* = 2\pi\frac{\hat{n}\times\boldsymbol{a}}{|\boldsymbol{a}\times\boldsymbol{b}|}$. The Fourier coefficients $M_s(\boldsymbol{G})$ and $l_{ex}^2(\boldsymbol{G})$ are calculated as,

$$M_S(\boldsymbol{G}) = \frac{M_{S,A} - M_{S,B}}{|\boldsymbol{a} \times \boldsymbol{b}|} \int_s e^{-i\boldsymbol{G}\cdot\boldsymbol{r}}\, d^2r \qquad \ldots 3.16a$$

$$l_{ex}^2(\boldsymbol{G}) = \frac{l_{ex,A}^2 - l_{ex,B}^2}{|\boldsymbol{a} \times \boldsymbol{b}|} \int_s e^{-i\boldsymbol{G}\cdot\boldsymbol{r}}\, d^2r \qquad \ldots 3.16b$$

Here, $M_{S,A}$ and $M_{S,B}$ are the saturation magnetization of region A and B, respectively. Similarly, the spatial part of the dynamic magnetostatic field is also converted in the reciprocal space as follows,

$$\boldsymbol{h_{ms}}(\boldsymbol{r}_\parallel) = e^{i\boldsymbol{q}\cdot\boldsymbol{r}_\parallel} \sum_G \boldsymbol{h_{ms,q}}(\boldsymbol{G}) e^{i\boldsymbol{G}\cdot\boldsymbol{r}_\parallel} \qquad \ldots 3.18$$

The Fourier coefficients of the magnetostatic field components are deduced (at z = d/2) as,

$$h_{ms,y}(\boldsymbol{r}) = -\sum_G \frac{m_y(\boldsymbol{G})}{|\boldsymbol{q}+\boldsymbol{G}|^2} \left(q_y + G_y\right)^2 \left(1 - \cosh(|\boldsymbol{q}+\boldsymbol{G}|z)\, e^{-\frac{|\boldsymbol{q}+\boldsymbol{G}|d}{2}}\right) e^{i(\boldsymbol{q}+\boldsymbol{G})\cdot\boldsymbol{r}_\parallel} \qquad \ldots 3.19a$$

$$h_{ms,z}(\boldsymbol{r}) = -\sum_G m_z(\boldsymbol{G}) \left(\cosh(|\boldsymbol{q}+\boldsymbol{G}|z)\, e^{-\frac{|\boldsymbol{q}+\boldsymbol{G}|d}{2}}\right) e^{i(\boldsymbol{q}+\boldsymbol{G})\cdot\boldsymbol{r}_\parallel} \qquad \ldots 3.19b$$

and

$$H_{ms,x}(\boldsymbol{r}) = -\sum_G \frac{M_S(\boldsymbol{G})}{G^2} G_x^2 \left(1 - \cosh(|\boldsymbol{G}|z)\, e^{-\frac{|\boldsymbol{G}|d}{2}}\right) e^{i\boldsymbol{G}\cdot\boldsymbol{r}_\parallel} \qquad \ldots 3.19c$$

For details of the derivation it is referred to [162]. Incorporating all the Fourier transformed expressions in the dynamic magnetization of eqns. (3.13), following equations are obtained,

$$\frac{i\omega}{\gamma\mu_0} m_{z,q}(\boldsymbol{G}) = H_0 m_{y,q}(\boldsymbol{G}) + \sum_{G'} \frac{m_{y,q}(\boldsymbol{G})}{|\boldsymbol{q}+\boldsymbol{G}'|^2} \left(q_y + G_y'\right)^2 \left(1 - \cosh(|\boldsymbol{q}+\boldsymbol{G}'|z)\, e^{-\frac{|\boldsymbol{q}+\boldsymbol{G}'|d}{2}}\right) M_S(\boldsymbol{G}-\boldsymbol{G}') -$$

$$\sum_{G'} \frac{m_{y,q}(\boldsymbol{G})}{|\boldsymbol{G}-\boldsymbol{G}'|^2} (G_z - G_z')^2 \left(1 - \cosh(|\boldsymbol{G}-\boldsymbol{G}'|z)\, e^{-\frac{|\boldsymbol{G}-\boldsymbol{G}'|d}{2}}\right) M_S(\boldsymbol{G}-\boldsymbol{G}') + \sum_{G'} \sum_{G''} (\boldsymbol{q}+\boldsymbol{G}') \cdot (\boldsymbol{q} +$$

$$\boldsymbol{G}'') l_{ex}^2 (\boldsymbol{G}''-\boldsymbol{G}') M_S(\boldsymbol{G}-\boldsymbol{G}'') m_{y,q}(\boldsymbol{G}) \qquad \ldots 3.20a$$

$$\frac{i\omega}{\gamma\mu_0} m_{y,q}(\boldsymbol{G}) = -H_0 m_{z,q}(\boldsymbol{G}) + \sum_{G'} m_{z,q}(\boldsymbol{G}) \left(\cosh(|\boldsymbol{q}+\boldsymbol{G}'|z)\, e^{-\frac{|\boldsymbol{q}+\boldsymbol{G}'|d}{2}}\right) M_S(\boldsymbol{G}-\boldsymbol{G}') + \sum_{G'} \frac{m_{z,q}(\boldsymbol{G})}{|\boldsymbol{G}-\boldsymbol{G}'|^2} (G_z -$$

$$G_z')^2 \times \left(1 - \cosh(|\boldsymbol{G}-\boldsymbol{G}'|z)\, e^{-\frac{|\boldsymbol{G}-\boldsymbol{G}'|d}{2}}\right) M_S(\boldsymbol{G}-\boldsymbol{G}') - \sum_{G'} \sum_{G''} (\boldsymbol{q}+\boldsymbol{G}') \cdot (\boldsymbol{q}+\boldsymbol{G}'') l_{ex}^2 (\boldsymbol{G}'' -$$

$$\boldsymbol{G}') M_S(\boldsymbol{G}-\boldsymbol{G}'') m_{z,q}(\boldsymbol{G}) \qquad \ldots 3.20b$$

Considering finite number (N) of reciprocal lattice vectors, the above equations are deduced in a form of eigen value equations to be solved by matrix method. The matrix is constructed as,

$$\widehat{M} = \begin{bmatrix} \widehat{M}^{yy} & \widehat{M}^{yz} \\ \widehat{M}^{zy} & \widehat{M}^{zz} \end{bmatrix} \qquad \ldots 3.21$$

where, diagonal terms are considered as zero and the off-diagonal sub matrices are given by,

$$\widehat{M}_{ij}^{yz} = \delta_{ij} + \sum_l \frac{(\boldsymbol{q}+\boldsymbol{G_j})\cdot(\boldsymbol{q}+\boldsymbol{G_l})}{H_0} l_{ex}^2(\boldsymbol{G_l}-\boldsymbol{G_j}) M_S(\boldsymbol{G_i}-\boldsymbol{G_l}) + \frac{(q_y+G_{y,j})^2}{H_0|\boldsymbol{q}+\boldsymbol{G_j}|^2}\Big(1 - C(\boldsymbol{q}+\boldsymbol{G_j},z)\Big) M_S(\boldsymbol{G_i}-\boldsymbol{G_j}) - \frac{(G_{x,i}-G_{x,j})^2}{H_0|\boldsymbol{G_i}-\boldsymbol{G_j}|^2}\Big(1 - C(\boldsymbol{G_i}-\boldsymbol{G_j},z)\Big) M_S(\boldsymbol{G_i}-\boldsymbol{G_j}) \quad \dots 3.22a$$

$$\widehat{M}_{ij}^{yz} = -\delta_{ij} - \sum_l \frac{(\boldsymbol{q}+\boldsymbol{G_j})\cdot(\boldsymbol{q}+\boldsymbol{G_j})}{H_0} l_{ex}^2(\boldsymbol{G_l}-\boldsymbol{G_j}) M_S(\boldsymbol{G_i}-\boldsymbol{G_l}) - \frac{1}{H_0} C(\boldsymbol{q}+\boldsymbol{G_j},z) M_S(\boldsymbol{G_i}-\boldsymbol{G_j}) + \frac{(G_{x,i}-G_{x,j})^2}{H_0|\boldsymbol{G_i}-\boldsymbol{G_j}|^2}\Big(1 - C(\boldsymbol{G_i}-\boldsymbol{G_j},z)\Big) M_S(\boldsymbol{G_i}-\boldsymbol{G_j}) \quad \dots 3.22b$$

So, the eigen equations are can be written as,

$$\widehat{M}\boldsymbol{m_q} = i\frac{2\pi f}{\gamma\mu_0 H_0}\boldsymbol{m_q} \quad \dots 3.23$$

where, $\frac{i2\pi f}{\gamma\mu_0 H_0}$ is the eigenvalue providing the spin-wave frequency and $m_q$ is the eigenvector representing the amplitude of the dynamic magnetization as follows,

$$\boldsymbol{m_q^T} = \left[m_{y,q}(\boldsymbol{G^1}) \dots\dots\dots m_{y,q}(\boldsymbol{G^N}), m_{z,q}(\boldsymbol{G^1}) \dots\dots\dots m_{z,q}(\boldsymbol{G^N})\right] \quad \dots 3.24$$

The experimentally measured spin-wave dispersion using BLS (for this thesis) generally remains in a good agreement with the results of PWM. However, the experimental BLS intensity is compared with the square of the modulus of the dynamic magnetization as given below,

$$I_{BLS} \propto \left|\boldsymbol{m_q}(G=0)\right|^2 \quad \dots 3.25$$

The spatial profile of spin-wave can be calculated as the modulus of dynamic magnetization at each spatial point.

### 3.3.2 OOMMF

In the present thesis, the widely used object oriented micromagnetic framework (OOMMF) simulation [163] has been employed to visualize few static and dynamic magnetic properties of the samples. In particular, the ground state magnetic configuration, demagnetizing filed, exchange field, spin-wave frequency, amplitude, phase are derived from the micromagnetic simulations. At first, one bmp picture is created mimicking the sample. The 3D sample is then divided into large number of parallelepiped cells who's in-plane dimensions are taken less than the exchange length of the material. In each cell, the LLG equation is solved in iteration method for a long time to get the relaxed state of magnetization. To observe the ground state, a very high magnetic field is first applied to saturate the magnetization in the field direction and followed by application of the bias field value. The static properties are obtained at this stage. After obtaining the ground state, a small perturbation is applied to induce the precessional motion in magnetization and the system is allowed to relax for a few nanoseconds with small steps. The simulation converges when the maximum torque, $\mathbf{m} \times \mathbf{H}$ ($m = M/M_S$) is less than $10^{-6}$ A/m. Eventually, the dynamic simulation results a time dependent magnetization trace.

Performing Fast Fourier transform on that magnetization, spin-wave frequency and amplitude are obtained.

### 3.3.3 MuMax3

MuMax3 [164] is another micromagnetic simulation platform developed by DyNaMat group of Prof. Van Waeyenberge at Ghent University similar to OOMMF. This is a GPU based package. Here also, the LLG equation is solved by Runge-Kutta methods (RK45, RK23, RK12 etc.) with different convergence criteria. The process is similar to OOMMF except that MuMax3 provides an inbuilt function to relax the system towards equilibrium i.e. energy minimum.

### 3.3.4 Dotmag

To calculate the spatial power and phase distribution associated to a particular spin-wave mode, a home-built code named Dotmag [165,166] written in MATLAB, is used. While power map gives information of the spatial position of the detected mode, phase can help to recognize the dispersive nature of the same. Dotmag analyze or do post-processing of the output files obtained from the micromagnetic simulators (OOMMF, MuMax3). The three components of dynamic magnetization obtained from micromagnetic simulations can be expressed as $m_i = m(x, y, z, t)$ where i = x, y, z. This $m_i$ is a resultant oscillatory signal averaged out over the whole simulated volume. Generally, we choose $m_z$ to extract the power and phase information of various resonant modes distributed on the xy-plane at a fixed z value ($z = z_0$). To do so, a discrete Fourier transform with respect to time is performed using the Dotmag. It gives the space dependent $m_z$ at different frequencies ($f$), where frequency resolution depends upon the total simulation time and the spatial resolution depends upon the discretization of sample during micromagnetic simulation.

$$\tilde{m}_{z_0}(x, y, f) = \mathrm{FFT}\left(m_z\left(x, y, z_0, t\right)\right) \quad \ldots 3.26$$

The power (in dB) and phase (in radian) associated with a particular frequency $f = f_n$ is then calculated from the complex function $m_z$ as,

$$P_{z_0}(x, y) = 20 \log_{10}\left|\tilde{m}_{z_0}(x, y, f_n)\right| \quad \ldots 3.27a$$

$$\varphi_{z_0}(x, y) = \tan^{-1}\left(\frac{Im\left(\tilde{m}_{z_0}(x, y, f_n)\right)}{Re\left(\tilde{m}_{z_0}(x, y, f_n)\right)}\right) \quad \ldots 3.27b$$

Dotmag can also be employed to calculate the phase or group velocity of a particular spin-wave. In that case, further simulation is run in the micromagnetic simulation. The dynamic magnetization is again generated by applying a local excitation within a tiny volume element of the specimen. It is noteworthy that the excitation is applied on the ground state obtained by minimizing the energy. However, the local field is applied as a sinc pulse perpendicular to the sample plane having frequency belonging to the spin-wave frequency. During the entire process, the bias field is applied globally on the sample. The simulated magnetization data is then processed in Dotmag to separate out the time evolution of each component of magnetization in space. At a fixed spatial coordinate, the extracted magnetization is plotted as function

of time. The spin-wave phase velocity is then calculated from the slope of the $x$ (or $y$) vs $t$ plot of magnetization amplitude.

### 3.3.5 LLG Simulator

LLG simulator is another commercially available package [167], introduced and licensed by M. R. Scheinfein. At first, parameters are input to design customized simulations. Then, the simulator solves the LLG equation using finite differences for exchange energies and fields, as well as boundary elements for magnetostatic self-energies and fields. Here, the object is defined as a grid. This simulator uses rectangular pixels on a Cartesian grid. After setting up the environment, LLG initializes all of the arrays to start computing the demagnetization field coupling tensors. It calculates the field for any boundary conditions. In the present thesis, magnetostatic field distribution of nanomagnet array has been computed using the 2.50 version of the LLG simulator.

# Anisotropic Spin-Wave Propagation in Asymmetric Width-Modulated $Ni_{80}Fe_{20}$ Nanostripes Chapter 4

## 4.1 Introduction

The fundamental limitation faced by semiconductor technology while continuous downscaling of the electronic systems has led to the development of various alternative research fields over the past few decades. Magnonics is coined as one of those potential research areas to overcome the shortcomings due to its inherent short wavelength at GHz frequency, large tunability by electric and magnetic fields as well as its low losses as opposed to Joule heating in charge based devices [168–171]. Magnons are the quanta of spin-waves (SWs) which act as the carrier of energy while periodically modulated magnetic media, known as magnonic crystals (MCs) [172] act as the medium of propagation. A lot of efforts have been made to achieve reconfigurable magnonic band structure in one-dimensional (1D) and two-dimensional (2D) MCs [173,174]. This band structure can be manipulated by various active parameters, namely, the magnetic-field strength [175], application of periodic magnetic field [176], electric field [177], etc. On the other hand, passive parameters such as shape [178], size [179], aspect ratio [174], element type [180], material properties [181] have shown to tune the magnonic properties of the MCs significantly. The tunable property of MCs is imperative for their reliable and sustainable applications in SW filters [182,183], phase shifters [184], multiplexers [185], transistors [186], magnetic field sensors [187], etc. Magnonic waveguides (MWs) are key components for on-chip propagation and manipulation of signals in magnonic or spintronic circuits and significant efforts have been made to study SW waveguiding in MWs [188–190]. Introduction of nanoscale antidots in MW leads to the opening of tunable magnonic bandgap (MBG) [165,191,192]. The concept of width modulated magnonic waveguide (WMMW) in this perspective has also shown significant promises [193]. To this end, numerical study of periodic modulation of width of WMMW showed the appearance and engineering of the width and position of MBG [194], followed by proposal of a magnonic logic [195]. Further simulations on an asymmetric sawtooth shaped nanowire showed selective SW propagation controlled by domain walls [196]. Experimental study of SW propagation in WMMW of micrometer scale was reported in 2009 [197]. Furthermore, effect of the shape of the width modulation on the SW propagation has been investigated [198] and a logic gate based on periodic sinusoidal width modulation [23] has been proposed. Later, a pseudo-one-dimensional MC based on an array of asymmetric sawtooth shaped magnonic waveguide (ASMW) has been introduced and reconfigurable MBG has been demonstrated by varying the bias magnetic field orientation at two different angles [199]. However, continuous reconfigurability of MBG by systematic variation of bias-field orientation has rarely been studied, while no such report in WMMW has been found in the literature. This would be even more intriguing in ASMW due to the inherent asymmetry of the physical structure, which can easily engraft a continuously variable complex spin configuration upon rotation of bias-field direction. Being motivated from the aforementioned facts, we have experimentally investigated SW dynamics of an ASMW by continuous rotation of an in-plane bias magnetic field. We observe a large tunability of MBG and a remarkable

anisotropic behaviour of SW frequency with bias-field orientation ($\phi$) between $0° \leq \phi \leq 180°$. Furthermore, we show that the selectivity of SW frequency by selection of bias field angle can be used to encode logic bit ('1' or '0') and the system can operate as XNOR or XOR logic gate. To gain further insight from the experimental results, we have carried out micromagnetic simulation and plane-wave method (PWM)-based numerical calculations. Herein, our investigation proposes the multi-functionality of the asymmetric structure as logic gate, frequency selective SW filter as well as the frequency modulated signal (frequency shift keying) processing in digital communication system.

## 4.2 Methods

**Sample Fabrication and Characterizations:** The ASMW arrays made of $Ni_{80}Fe_{20}$ (Py) were fabricated using a combined process of electron-beam evaporation and electron-beam lithography, followed by a lift off process. The details regarding the sample fabrication can be found elsewhere [199]. The lateral dimensions of the array are: $72 \times 72$ μm$^2$ and average thickness of Py is ~30 nm. Figure 4.1(a) shows the SEM image of the ASMW array, which reveals that each ASMW is made of a large number of overlapped rectangular elements of length ~800 nm and width ~460 nm. Each rectangular element is tilted at an angle of 25° with respect to the y axis and consecutive rectangular elements are slightly overlapped with each other, forming a continuous channel of SW propagation in the ASMW. The width of each ASMW is periodically modulated giving rise to an additional periodicity along the ASMW axes. The nominal separation between two consecutive ASMW axes is 790 nm, which is considered as the lattice constant of the MC along x-direction ($a_1$). The lattice constant along y-axis ($a_2$) is calculated from the center to center distance of two rectangles which is ~800 nm. The width modulation of the nanostripes gives an asymmetric saw-tooth shape along the edges of the stripe while the separation between the edges of two nearest stripes is kept constant at ~250 nm throughout the whole length. As discussed in [199], such ASMW array shows a pseudo-one-dimensional structure, leading towards the possibility of reconfiguring its magnonic band structure by rotating a bias magnetic field w.r.t. the ASMW axis. The surface topography is scanned and the thickness is determined using atomic force microscopy (AFM). The surface image is displayed in Figure 4.1(b). The static magnetic configuration of the ASMW sample at the remanent state is measured by magnetic force microscope (MFM). The change in colour contrast in the MFM image in Figure 4.1(c) clearly reveals the presence of demagnetization regions near the short edges of the rectangular elements. The sample also possesses significantly large shape anisotropy due to its unique asymmetric structural configuration which has been evidenced from experimentally measured magnetic hysteresis loops by static magneto-optical Kerr effect (MOKE), presented in Figure 4.1(d). In the SW dynamics measurements, we have applied a bias magnetic field of magnitude $H = 850$ Oe for all $\phi$ values during angular variation.

**BLS Measurement:** We have used conventional back-scattered Brillouin light scattering (BLS) technique to experimentally measure the SW frequency spectra at specific bias-field strength, orientation and wave vector (Figure 4.2(a)). The sample and the magnet were placed in such a way to help free rotation of the magnetic field in the sample plane through $0° \leq \phi \leq 180°$ w.r.t. the axes of the

ASMWs. In our experiment, BLS spectra from thermal magnons were recorded by changing $\phi$ at an interval of 10°. The in-plane wave vector transferred to the magnetic system is defined as: $k = (4\pi/\lambda)sin\theta$, where, $\lambda$ is the wavelength of the incident light, $\theta$ is the angle of incidence which is varied for careful selection of the wave vector of SW. We have used a nearly monochromatic green solid state laser ($\lambda$ = 532 nm) with output power of 230 mW (~65 mW on the sample surface with spot area ~1.25 × $10^3$ μm$^2$). Thus, the laser power density (52 μW/μm$^2$) used in the experiment was small enough to cause any significant change in the magnetic properties of the sample or its surface degradation. For all the measurements, we have fixed $\theta$ = 10° so that the corresponding in-plane wave vector on the sample surface is $k$ = 4.1 × $10^6$ rad/m (parallel to the stripe axes) which refers to the first Brillouin zone (BZ) boundary of this MC. Since the MBG of this system occurs directly at the BZ boundary [199], measurement at this particular wave vector gives us a picture about the variation of MBG with the angle $\phi$ without the need of measuring the full magnon dispersion at each angle, which would consume a very long time.

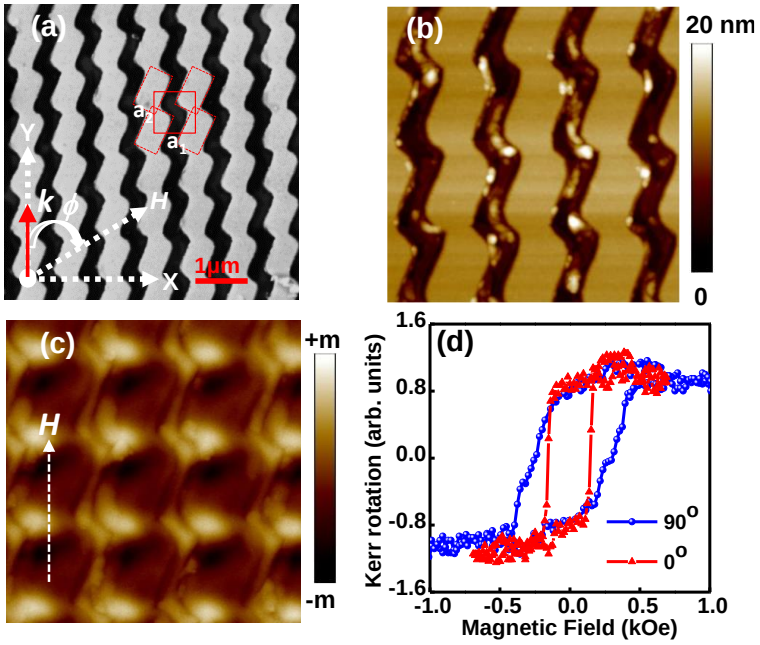


**Figure 4.1:** (a) SEM image of the ASMW. The white dashed arrows represent the coordinate axes and the in-plane applied magnetic field. The arrow of the circular arc shows that field has been rotated in clock-wise direction. The red arrow shows the direction of spin-wave wave vector. The unit cell considered for PWM calculation is shown by the 2D square outline with $a_1$ and $a_2$ as lattice constants ($a_1 = a_2 = a \approx 800$ nm). (b) AFM image of the ASMW. (c) MFM image of the ASMW at the remanent state. The direction of applied magnetic field ($H$ = 850 Oe) before bringing the field down to $H$ = 0, i.e. the remanent state is shown by the dashed arrow in the MFM image. (d) Magnetic hysteresis loops measured by static MOKE at $\phi$ = 0° and $\phi$ = 90°.

## 4.3 Results and Discussions

Figure 4.2(b) shows a representative BLS spectrum for $\phi$ = 180°, which reveals three clear and well-resolved peaks and a low intensity peak. The solid lines represent the fits with Lorentzian function to

extract the peak frequencies. The peak frequencies as a function of $\phi$ are plotted as symbols in Figure 4.2(c). The experimental frequencies clearly show a strong but asymmetric variation presumably due to the structural asymmetry and the ensuing asymmetry in the internal field profile. We have calculated the SW spectra corresponding to the specific $k$, $H$ and $\phi$ values by PWM [200] based numerical calculation. In the present calculation, we have assumed saturation magnetization, $M_S$ = 860 × $10^3$ A/m, exchange constant, $A_{ex}$ = 1.3 × $10^{-11}$ J/m and Landé g-factor, $g$ = 2 for Py. Small but finite values of $M_S$ and $A_{ex}$ (10% of the Py) are assumed for the air gap to avoid any unphysical value of the SW frequency.

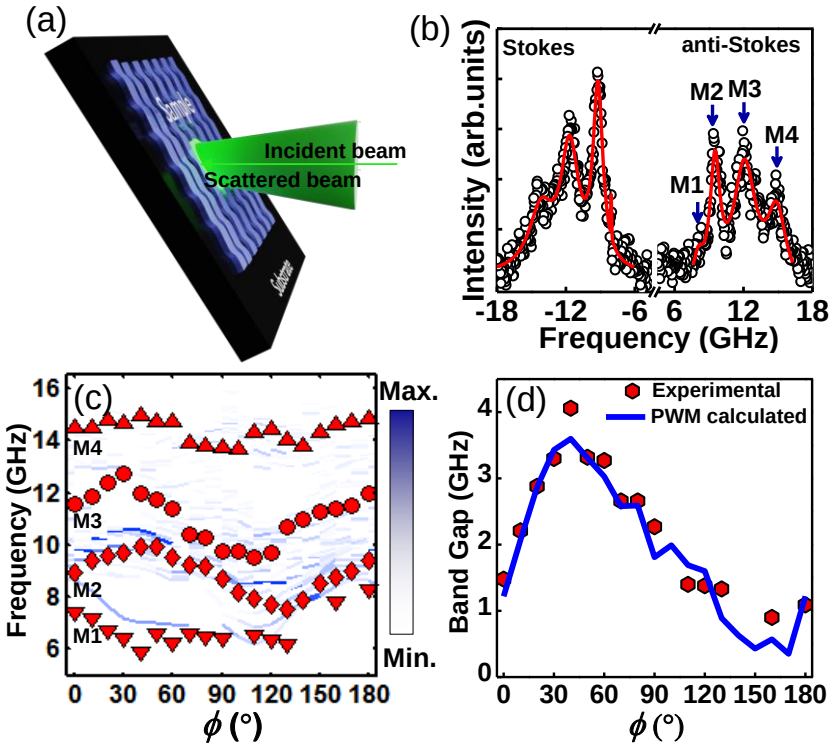


**Figure 4.2:** (a) Schematic of BLS measurement geometry. (b) The Stokes and anti-Stokes sides of representative BLS spectrum taken at the 1st BZ boundary ($k$ = 4.1 × $10^6$ rad/m) at $\phi$ = 180°. The symbols and the solid line represent the experimental data points and the fitted curve, respectively. The extracted SW modes, defined as M1, M2, M3 and M4 are shown by down arrows. (c) The experimental and PWM calculated variation of M1, M2, M3 and M4 w.r.t. $\phi$ are plotted as symbols and solid lines respectively. The variation in colour contrast of the solid lines implies the intensity variation of the excited SW as predicted by PWM. (d) The first MBG of the studied system calculated as the frequency difference between M1 and M2 is plotted as a function of $\phi$. The symbol and the solid blue line represent the experimental and PWM calculated MBG, respectively.

An additional periodic magnetic field of very high-magnitude is applied to lift the frequency contribution from the air gap far above the SW frequency regime of Py. The usage of very small values of the magnetic parameters assigned to the air gap allowed us to neglect the pinning of magnetization in the PWM calculation. The calculated SW intensity as a function of frequency for $k$ = 4.1 × $10^6$ rad/m from PWM is shown as surface plot in Figure 4.2(c). The corresponding color map, shown next to the graph, indicates

large SW intensity for the thick solid lines, which correspond to the square of the modulus of the fundamental harmonics of the x-component of magnetization in PWM. The calculated SW frequencies and intensities are generally in good agreement with the experimental data. The four modes appearing in the BLS spectra at all values of $\phi$ vary within a frequency range from 6 GHz to 15 GHz and are named as M1, M2, M3 and M4 in order of ascending frequency. Here, the linewidth of the BLS peaks is proportional to SW damping. The non-uniform magnetic structure may enhance the damping due to dephasing or interaction of the SWs with the nonuniform spin textures. However, the observed frequency splitting between the modes, anisotropy in frequency and MBG are well above the linewidth of the BLS spectra. Hence, the dephasing effects due to nonuniform magnetic structure is not significant here. The absence of some experimental data points in Figure 4.2(c) is due to the noisy spectra making it difficult to extract the SW mode frequencies accurately. M2 and M3 possess high intensity for the whole angular range, making them easily identifiable. Since the measurements have been done for a *k*-vector corresponding to the first BZ boundary, where the first MBG occurs between M1 and M2 for this system [199], we calculate the first MBG as the difference between the frequencies of M1 and M2. The anisotropic variation of frequencies of M1 and M2 are in antiphase, leading towards widening of MBG as $\phi$ increases from 0° attaining a maximum of about 4 GHz at around 40° followed by a steep decrease and a minimum of about 0.5 GHz at around 150° as shown in Figure 4.2(d). The calculated MBG vs. $\phi$, shown by the dotted line agrees well with the experimental data. This fascinating modulation of MBG with $\phi$ validates the anticipated reconfigurability of the MBG in an asymmetric width-modulated system. The two higher frequency modes (M3 and M4) also exhibit anisotropic dynamic behavior with bias field angle (see Figure A.1 of Appendix I for variation of frequency gaps associated with M2, M3 and M4). Presumably, these modes originate from hybridization of different higher harmonics.

To understand the propagating and quantized nature of the modes more clearly, we have analyzed the spatial profile (Figure 4.3(a)) of the modes, i.e. the modulus of the amplitude of the x-component of the dynamic magnetization ($|m_x|$), of the relevant modes using PWM calculation [199]. Furthermore, the propagation and quantization features are confirmed through the calculated phase distribution at small *k*-value, which are shown Figure A.2 of Appendix I. Here, the quantization and propagation characteristics of each mode at $\phi$ = 40° and 130° have been illustrated through the mode profiles since the SW frequencies show two extrema at these two angles (Figure A.3 of Appendix I). At $\phi$ = 40°, M1 is confined near the edges of the rectangular elements, while being extended through the connector channel. M2, on the other hand, resides primarily inside the rectangular element as quantized mode with nodal planes perpendicular to the bias-field axis and quantization number (n) of 6. However, it still shows significant intensity at the connector channels. The stark difference between the nature of the two modes probably leads to a large difference in their frequencies at the 1st BZ and hence a large MBG. For $\phi$ = 130°, both the modes have become quantized and the axis of modes rotate towards the bias-field axis. The mode quantization numbers are n = 2 (M1) and 4 (M2) with no significant extension of any of the two modes through the connector channel. The similarity between the two modes probably leads to smaller difference between their frequencies at the 1st BZ and hence a reduced MBG.

To explore the reason behind the anisotropy in SW frequency and MBG with the bias-field orientation, we have performed micromagnetic simulations using OOMMF and LLG simulator with same parametric values as used in the PWM calculations. Figure 4.3(b) shows the simulated ground state spin textures of the system, at $\phi$ = 40° and 130°. Despite the fact that the PWM calculations do not include the precise magnetization nonuniformity inside the magnetic structures, the overall spin directions w.r.t. the shape of the structure particularly the SW propagation channel and boundaries of the structure will give important guideline about the SW dispersion and quantization character. Here, the angular variation of in-plane applied magnetic field significantly modifies the spin direction (Figure 4.3(b)) and hence the dipolar or magnetostatic field (Figure 4.3(c)) and internal field (Figure 4.3(d)) but in different way. We observe that the spins near the connector channel (overlapped area) and the interior of the rectangular elements evolve differently with $\phi$ due to asymmetry in the structure. Also, it appears that though the anisotropy in shape preserves the propagation direction, the axes of SW modes rotate with the net magnetization.

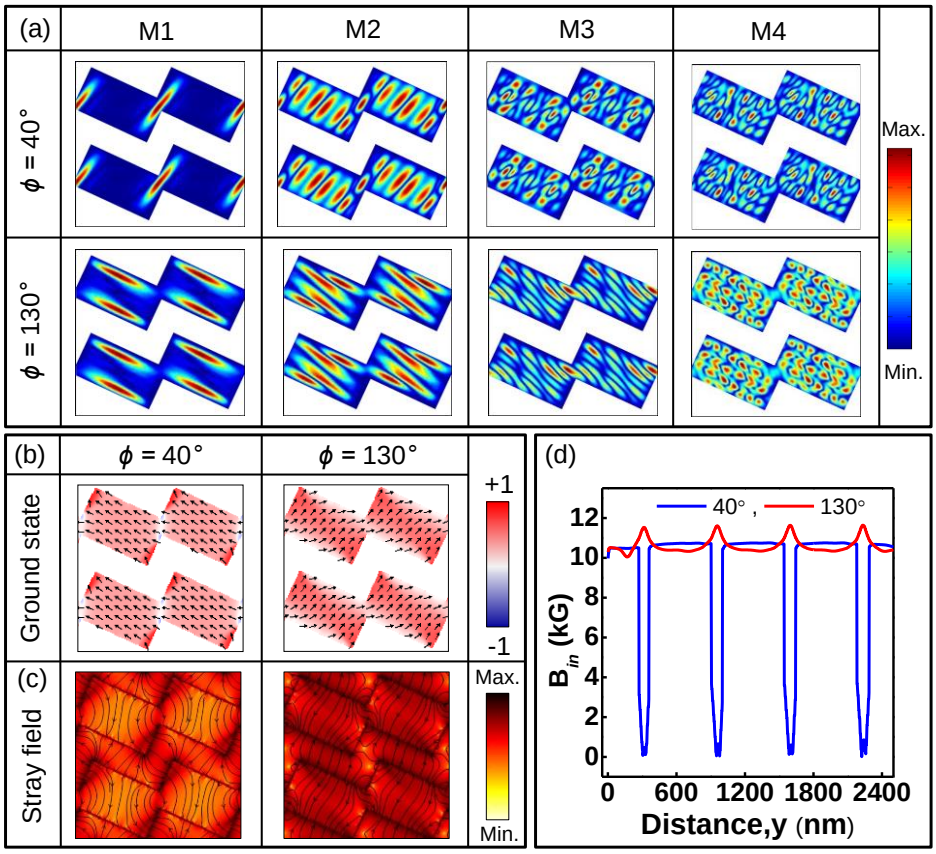


**Figure 4.3:** (a) PWM calculated spin-wave (SW) mode profiles. Simulated (b) static spin configurations and (c) magnetostatic field profiles at $\phi$ = 40° and 130° at $H$ = 850 Oe with the associated color maps. (d) Line scan of internal field ($B_{in}$) along ASMW channel for $\phi$ = 40° and 130°.

When the field is applied along the long edges of the rectangular elements, i.e. at $\phi$ = 40°, demagnetizing regions originate along the short edges of the elements. Since, the strength of demagnetizing field is

concentrated in a smaller area closer to the short edges, the effective field still remains along the long edges and the magnetization inside the elements remain high enough. The bias field lifts the magnetization direction gradually away from the stripe axes and the associated frequency of the mode M1 becomes lower due to loss of energy at the corrugations near the narrow connector channels. The bulk mode M2 becomes discretized having a higher frequency due to confinement within the finite width. At $\phi$ = 130°, the scenario is quite different, because the bias field is applied along the short edges of the rectangles while the demagnetizing regions appear along the long edges. Since, in this case the demagnetization regions are much more extended, the effective field decreases enhancing the unsaturated spins at the edges and hence larger reduction in magnetization inside the elements. At this angle, the net magnetization again points away from the propagation channel but in 90° rotated direction of $\phi$ = 40° while the SWs interacts at the opposite edges. The mode M1 shows spatial relocations at the opposite boundaries of the rectangular elements and reorientations w.r.t the propagation direction. The quantization axis of M2 also rotates following the net magnetization direction inside the rectangular shape and its amplitude get centralized along the length of the rectangle. Here the discretization occurs in the transverse direction within a relatively narrow width which reduces the quantization number as well as the frequency of M2 leading to a smaller band gap. Thus, the variation in the magnetization direction inside the waveguide and the interactions of the edge and bulk SW modes with this asymmetric corrugation result in the varying frequency difference, i.e. the MBG between M1 and M2 to be larger at $\phi$ = 40° and smaller at $\phi$= 130°. Also, the interaction between the unsaturated spins at the edges of the neighboring stripes (Figure 4.3(c)) modifies the SW dynamics significantly. The inhomogeneity of internal magnetic field has a major role for this unusual behavior of SW propagation characteristics in this periodic asymmetric structure where the saw tooth shape is responsible for breaking the mirror symmetry of the system. However, it may be worth to consider the probability of reflection and interference phenomena of SW at the periodic boundary of the ASMW for a more complete description of band engineering by tuning the in-plane bias field orientation.

Nevertheless, this ASMW is a promising candidate for carrying information through modulation of frequency. The anisotropic nature of the mode M2 may enable the system for implementation in logic operation as well as to encode bit for data transfer. If we focus carefully on the calculated frequency response of this mode for -90° ≤ $\phi$ ≤ 270° (Figure A.4 of Appendix I), the frequency of this mode is found to be periodic over the full angular scale. This behavior simply implies that frequency can be divided into two different regimes, a high frequency regime (HFR) and a low frequency regime (LFR) *w.r.t.* a reference frequency value. Considering the HFR as logic input '1'('0') and LFR as logic input '0'('1'), two different frequency regimes can be assigned with two logic bits. According to the predefined logic states, the system can operate as two-input-XNOR as well as XOR gate. Practically, instead of using an external magnet two current lines implemented underneath the substrate in crosswire like alignment will be more feasible and convenient to create the required magnetic field (Figure 4.4(a)). By reversing the current direction, the logic circuit can be switched from HFR to LFR level as shown in Figure 4.4(b).

Consequently, a change of logic state from '1'('0') to '0'('1') occurs as presented in the truth tables of Figures 4.4(c) and (d). Following the truth tables, the ASMW is expected to perform the XNOR or XOR operation. Also, the periodic appearance of high and low frequency of SW in this ASMW structure promotes its use as a key component for frequency shift keying (FSK) in digital communication technology. Here, the high and low frequency can present the logic '1' and '0' respectively in FSK modulated signals.

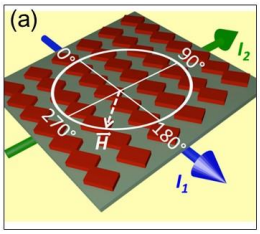


(b)

| $I_1$ | $I_2$ | O/P |
|---|---|---|
| -ve | -ve | HFR |
| -ve | +ve | LFR |
| +ve | -ve | LFR |
| +ve | +ve | HFR |

(c)

| A | B | O/P |
|---|---|---|
| 0 | 0 | 1 |
| 0 | 1 | 0 |
| 1 | 0 | 0 |
| 1 | 1 | 1 |

(d)

| A | B | O/P |
|---|---|---|
| 0 | 0 | 0 |
| 0 | 1 | 1 |
| 1 | 0 | 1 |
| 1 | 1 | 0 |

**Figure 4.4:** (a) Schematic of the proposed logic gate showing two crossed current lines $I_1$ and $I_2$ by solid arrows. (b) Truth table illustrating the performance of the proposed device. (c) Truth table of an XNOR logic gate. (d) Truth table of an XOR logic gate.

## 4.4 Conclusions

We have studied the spin-wave (SW) anisotropy of a well-defined asymmetric saw tooth shaped nanostripe array by using Brillouin light scattering (BLS) experiment and plane wave method (PWM) based numerical calculations. The shape and the static spin configuration of these asymmetric width modulated nanostripes result in an asymmetric anisotropy in SW frequency with variation of the in-plane bias field direction ($\phi$). This specific asymmetric anisotropy of different modes enables the system to show tunable magnonic band gap by varying $\phi$. Thus, reprogrammable characteristics of magnonic band gap with the in-plane bias field direction is established. Furthermore, we find that the anisotropic feature in SW frequency as well as magnonic bandgap mainly originates from the continuous variation of magnetization direction *w.r.t.* the ASMW shape with the bias field orientation in each stripe. This is further aided by the pseudo periodicity along the waveguide channel and their strong inter-stripe coupling through uncompensated spins at the corrugated edges. Moreover, the anisotropic feature of magnonic bandgap and SW frequency in such a complex system is captivating from application perspective. Broadband SW filter, rectifier and multiplexer can be designed in GHz frequency region owing to periodic variation of band gap. The guiding nature of SW through the channel of the axes may be useful for miniaturized on-chip microwave communication devices. Finally, this study reveals some key aspects of a SW propagation through width modulated nanostripe array.

# Active Control of Dipole-Exchange Coupled Magnon Modes in Nanoscale Bicomponent Magnonic Crystals Chapter5

## 5.1 Introduction

During last two decades, fundamental research on nanoscale magnonics has demonstrated great promises in developing next-generation high-speed and energy efficient technology. Novel nanopatterned magnetic structures have emerged as the elevators for upsurging this exciting research field [59,201,202]. Magnonics render several prime advantages e.g., shorter wavelength of spin-wave (SW) or magnon, large scalability, non-reciprocity, waveguiding property, non-linearity, anisotropic dispersion, reconfigurable band structure and hybridization with other quasi particles leading the possibility of its myriad applications [62,203,204]. These potential applications of magnonics are envisaged with low-loss sustainability, such as: SW filter [205–207], transistor [186,208], phase shifter [209], multiplexer [185], logic gates [210–212], directional couplers [213], memory [214], SW diodes [215–217], non-reciprocal devices [218] besides wave-based computing [219,220], signal processing [221] and more recently in neuromorphic computing [222–224]. Such rapid progress towards future technology demands the exploration of fundamental physics in a variety of systems including bi- and multi-component magnonic crystals which may provide perfect testbeds for tuning the dipole-exchange coupling of the nanomagnets.

Bicomponent magnonic crystals (BMC) can be formed as periodic array of nanomagnets embedded in a matrix of another magnetic material [225–229]. The magnetization and the internal demagnetization field of such BMCs are differently architected due to the presence of two different magnetic materials of high-contrast magnetic properties in the close vicinity of each other. Again, the presence of interface may lead to scattering, reflection and transmission of magnons at the boundary leading to reconfigurable magnonic band structure [230–234]. Other distinct phenomena like SW mode softening [235,236], chiral edge mode [237], vortex spin texture [238], magnon-magnon interaction [239], chiral SW pumping [240], may also appear due to the modified field landscapes in bicomponent nanostructures. Choudhury et al. claimed that the presence of interface exchange interaction causes the SWs to propagate faster in such BMCs [241,242]. For applications in integrated circuit or nano-devices, the main strategy will be to use the magnons with minimal power consumption which depends on the device operation time. In this essence, synergy between generation and active manipulation of magnon current are investigated on a variety of nanostructures [243]. Magnons with high group velocity at the nanoscale can efficiently serve this purpose besides the ever-increasing demand of faster device operation. BMCs with interface exchange may form a conducive platform for improving the operation speed. Interestingly, due to different characteristic properties of the constituent magnetic elements of a BMC, a large number of passive and active parameters are accessible as knobs for better control of magnon propagation than antidots, stripes or other single component waveguides.

Herein, we have investigated series of BMCs where circular shaped holes in a $Co_{50}Fe_{50}$ (CoFe) matrix are filled with $Ni_{80}Fe_{20}$ (NiFe). We have probed their SW dynamics excited by microwave current, by systematically altering the interface exchange energy by increasing the dot diameter, i.e., the overall interface area. This interface exchange plays a pivotal role to conjoin the SW dynamics of the two dissimilar materials of a BMC, which is a prerequisite for long-range magnon based coherent information processing. Magnon-magnon mode crossing have been observed in the bias field dependent SW frequencies. In addition, the transfer of SW power between two highly intense modes is observed which again varies systematically with the dot diameter. Time domain micromagnetic simulations using OOMMF [244] elucidates the relevancy of dipolar field and interfacial exchange field in the magnon spectra. Further simulations show that magnon propagation can be tractable by facile control of the filling fraction of the constituent materials.

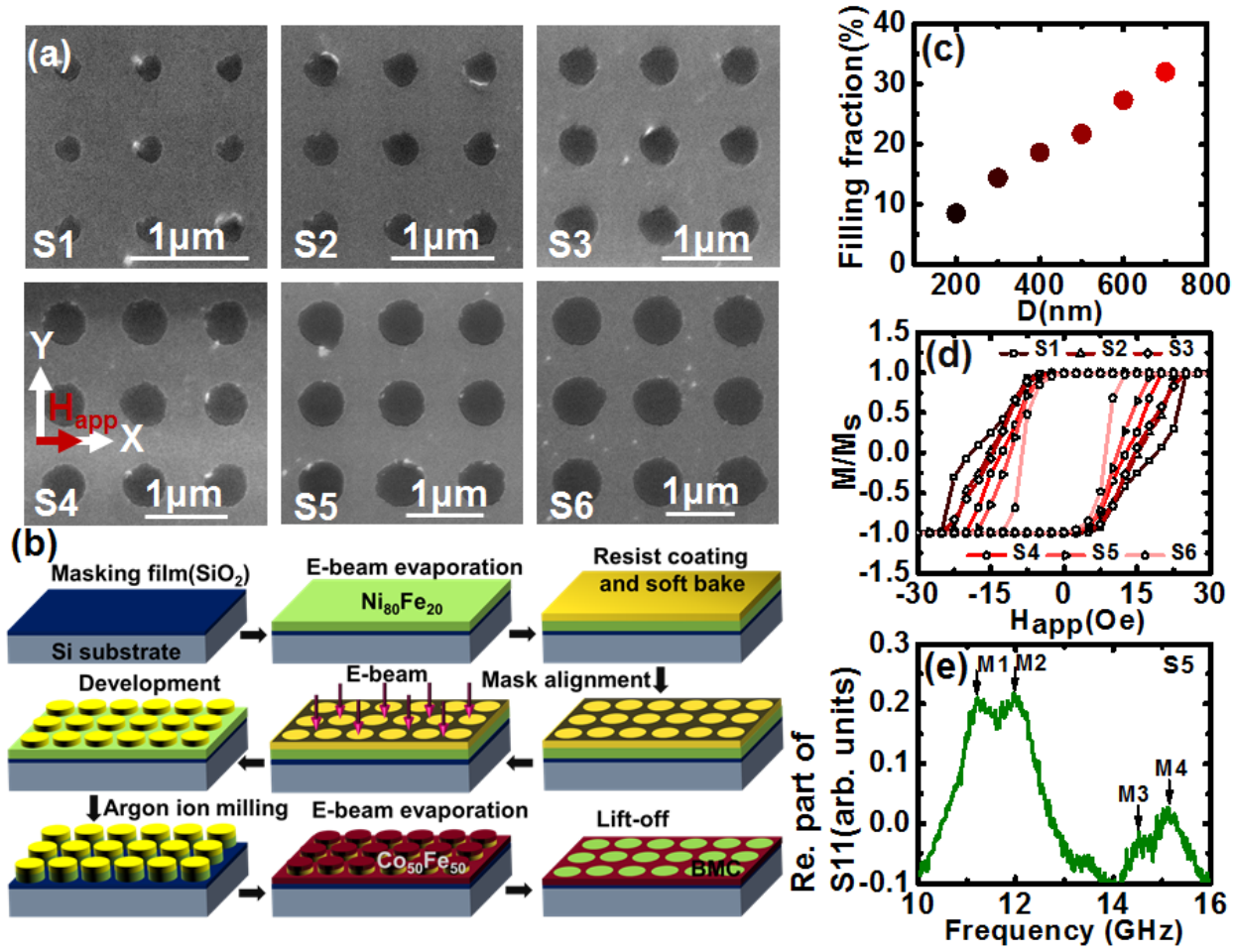


**Figure 5.1:** (a) SEM images of the bicomponent magnonic crystals (BMCs) named as S1 ($D$ = 200 nm), S2 ($D$ = 300 nm), S3 (D = 400 nm), S4 ($D$ = 500 nm), S5 ($D$ = 600 nm) and S6 ($D$ = 700 nm). (b) Schematic of the fabrication process of the BMCs. (c) Variation of filling fraction of NiFe in CoFe matrix as a function of $D$ of NiFe filled holes. (d) Simulated magnetic hysteresis loops of the samples. (e) Representative SW absorption spectra of S5 at applied bias magnetic field, $H_{app}$ = 1.2 kOe.

## 5.2 Methods

**Sample Fabrication and Characterizations:** The choice of appropriate materials with high-contrast magnetic properties forming the periodic magnetic potential and to implode the magnons in this potential is key to the development of BMCs. Besides, it is crucial to engineer the interface to enable the interelement exchange energy which remains quiescent in most cases. Fabrication of such nanoscale BMCs has been accomplished due to the efficacy of advanced multistep lithography technique. Here, the BMCs have been fabricated in the form of NiFe-filled CoFe antidot lattices arranged in square lattice symmetry. The nominal diameter ($D$) of NiFe-filled regions (dot) is 200 (S1), 300 (S2), 400 (S3), 500 (S4), 600 (S5) and 700 nm (S6) and the edge-to-edge separation between them is 450 nm (Figure 5.1(a)). The BMCs have been fabricated by a combined action of electron-beam lithography (EBL), electron-beam evaporation (EBE) and ion milling. The schematic illustration of the lithographic fabrication process of the BMCs is depicted in Figure 5.1(b). Using EBE, 20-nm-thick NiFe layer is deposited on top of self-oxidized silicon (Si)(100) substrate in an ultrahigh vacuum chamber at a base pressure of $2 \times 10^{-8}$ torr followed by a single-layer negative resist (ma-N 2405) patterning on top of it using EBL with a beam current of 100 pA. In the next step, NiFe is etched out from the base of the unexposed part of the resist pattern by argon ion milling at a base pressure of $1.8 \times 10^{-4}$ torr. Subsequently, 20-nm-thick CoFe is deposited using EBE at the same base pressure of $2 \times 10^{-8}$ torr followed by a lift off process. The filling fractions, calculated as the ratio of the area of NiFe-filled dots to that of the area of a unit cell (2 x 2 matrix), are shown in Figure 5.1(c) for all samples. Further, using maskless photolithography, a coplanar waveguide (CPW) of 150-nm-thick Au is fabricated on top of the BMCs at a base pressure of $6 \times 10^{-7}$ torr for the broadband ferromagnetic resonance (FMR) measurement. The central conducting line of this CPW having width of 30 μm and length of 300 μm and a nominal characteristic impedance of 50 Ω can cover the whole area of the sample under investigation. The spin-wave dynamics is measured in frequency sweep method employing VNA-FMR spectrometer.

**Micromagnetic Simulation:** The micromagnetic simulations are performed using the OOMMF software to reproduce the experimental findings. In OOMMF, the samples are discretized into rectangular cuboids with dimensions of $4 \times 4 \times 20$ nm$^3$. The magnetic parameters used in the simulation are exchange stiffness constants: $A_{NiFe} = 1.3 \times 10^{-11}$ Jm$^{-1}$ and $A_{CoFe} = 3 \times 10^{-11}$ Jm$^{-1}$, saturation magnetization: $M_{NiFe} = 800 \times 10^3$ Am$^{-1}$, and $M_{CoFe} = 1800 \times 10^3$ Am$^{-1}$, damping coefficients: $\alpha_{NiFe} = 0.008$ and $\alpha_{CoFe} = 0.01$, magneto-crystalline anisotropy: $K_{NiFe} = 0$ and $K_{CoFe} = 0$. The value of gyromagnetic ratio $\gamma = 18.5$ Mrads$^{-1}$Oe$^{-1}$ is considered same for both the materials and the exchange stiffness constant at the interface between NiFe and CoFe is taken to be $A_{int} = 2.1 \times 10^{-11}$ Jm$^{-1}$. In the simulations, a high magnetic field is first applied to saturate the magnetization along the bias field direction followed by reduction of the field to bias field value and appropriate relaxation to reach the equilibrium state. The equilibrium magnetic states obtained under the bias field are then subjected to a pulsed magnetic field in the transverse direction which produces a torque on the magnetization to trigger the precessional dynamics. In the following section, precise agreement between simulated dynamics and experimental dynamics

has been discussed. Additionally, using the same parameters magnetic hysteresis loops are simulated since the 150 nm thick Au layer on the top of sample surface does not allow to perform experimental hysteresis loops. However, since the dynamic behavior is well reproduced in simulation as discussed later, the simulated hysteresis loops can mimic the experimental behavior as well. A notable reduction in the coercivity is observed with increasing $D$ in the simulated magnetic hysteresis loops shown in Figure 5.1(d) along with a variation of the shape of the loops. These results unfold the reconfigurability of the magnetic behavior of the BMCs.

## 5.3 Results and Discussions

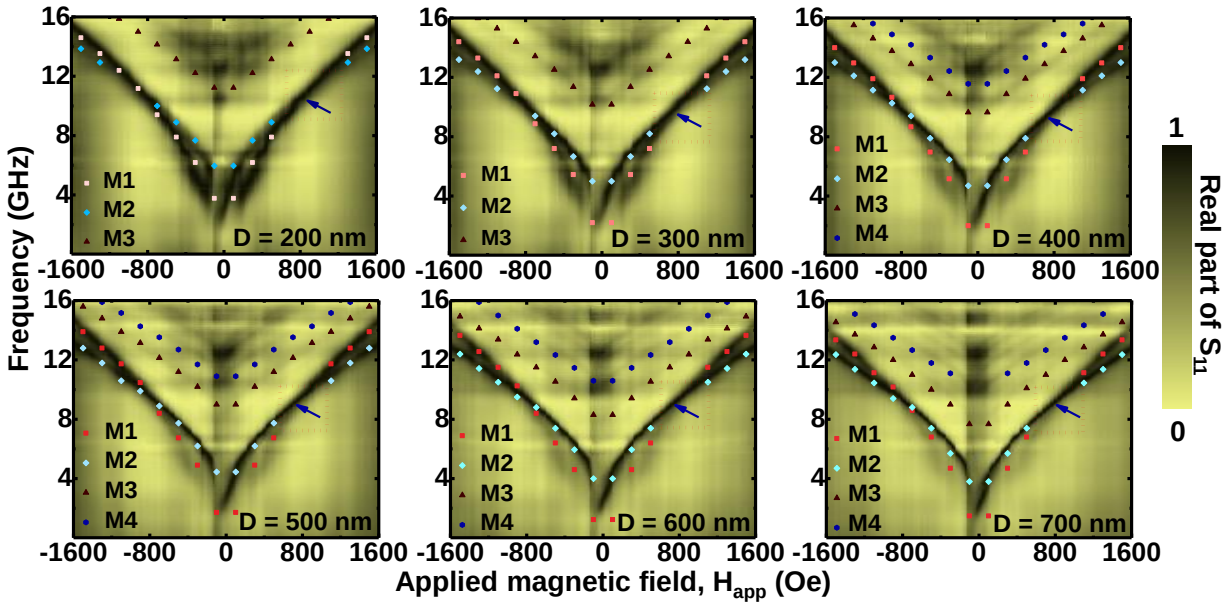


**Figure 5.2:** Experimental magnetic field dispersions of SW frequencies (surface plots) for different samples with the numerically simulated results (symbols). The color map of the surface plot is shown in the right. The blue arrows inside the red dotted box highlight the crossing of the two SW modes.

In the following, the results obtained from FMR spectroscopy and OOMMF simulations are discussed.

**FMR Spectra:** The SW absorption spectra (the real part of $S_{11}$ parameters) are obtained from broadband FMR for a wide range of externally applied bias magnetic field ($H_{app}$) for all BMCs, and Figure 5.1(e) shows one representative spectrum for S5 at $H_{app}$ = 1.2 kOe. At first, the magnetizations of the samples were saturated along the +x direction, followed by gradual reduction of the field in steps of 20 Oe from +1.6 kOe to -1.6 kOe in a single trace. The surface plots in Figure 5.2 display the bias-field-dependent SW absorption spectra of all six samples with their maximum amplitude normalized to 1. The normalized surface plots help to identify two high intensity and low frequency branches of SW, M1 and M2 prominent in all samples. In the experimental spectra, the slopes of M1 and M2 are slightly asymmetric with respect to $H_{app}$ = 0 Oe. This asymmetry indicates the presence of finite exchange interaction at the interface of NiFe and CoFe. The minimum of $df/dH$ of M2 occurs at $H_{app}$ ~ −110 Oe, which remains nearly invariant for all samples, indicating similar exchange coefficient at the interface.

It is also clear that there is a relative variation in the intensity of M1 and M2 with the variation of $H_{app}$ after they cross each other at a field $H_{cr}$ (bias field corresponding to the blue arrow in Figure 5.2). When $H_{app}$ is decreased M1 loses its intensity and M2 gains intensity after crossing in each sample. This intensity exchange between M1 and M2 occurs at different values of $H_{app}$ for different samples. It is also noteworthy that the ratio of intensity transfer is a function of $D$. To be more specific, with increasing $D$, the intensity transfer from M1 to M2 increases and M1 almost vanishes at the largest $D$ indicating the maximum transfer. It should also be noted that the number of high frequency SW modes increases and becomes prominent with increasing $D$. At lower $D$, the higher frequency modes become indistinct in the experimental spectra due to noisy background. Additionally, we observe that the frequency of the whole SW branches shifts downwards when $D$ is increased. First of all, the relative variation of intensity between M1 and M2 in the field dispersion of each sample can be attributed to the coupling between the adjacent materials. When resonance SW modes of any two-sublattice systems are excited simultaneously, the modes can be coupled due to strong dipolar interaction or exchange interaction. Such coupling is absent in the constituent dot, matrix and BMC without exchange interaction (see the simulated SW spectra in Figure A.6 of Appendix II). Here, the increase in $D$ means the increase in the interface area, which enhances the overall inter-material coupling due to an overall increment of exchange energy, because of which M1 transfers maximum energy to M2 at $D$ = 700 nm. Before the crossing of M1 and M2, at a fixed value of $H_{app}$, the intensity of M1 gets efficiently suppressed with increasing $D$ and M2 becomes more prominent. This fact can be attributed to the increase in filling fraction of NiFe. The major contribution of M1 at this field range comes from CoFe which reduces due to reduced volume of CoFe. On the other hand, M2 might have been located in the NiFe dots occupying an enlarged volume in $D$ = 700 nm and hence have higher intensity than M1. Since the saturation magnetization of CoFe is higher than that of NiFe, at saturated state the frequency of CoFe centre mode exhibits higher value. In that case, M1 belongs to the CoFe matrix and shows higher frequency at high external field, $H_{app} > H_{cr}$. At lower fields, $H_{app} < H_{cr}$, the extended demagnetization regime in CoFe as compared to NiFe reduces the frequency of M1 for all samples.

**Simulated Magnetostatics:** The OOMMF simulations reproduce important features of the experimental SW spectra with nearly same frequency and number of modes along with their relative intensity variations. Besides, the spatial profile of static demagnetizing field ($H_{de}$) and exchange field ($H_{ex}$) have been calculated using OOMMF to support the experimental observations. Figure 5.3(a) depicts a representative spatial map of $H_{de}$ calculated for $D$ = 600 nm at $H_{app}$ = 200 Oe. The average value of $H_{de}$ is calculated separately from the NiFe dots and CoFe matrix except at the interface for $H_{app}$ = 200 Oe ($H_{app} << H_{cr}$), $H_{app}$ = 1600 Oe ($H_{app} >> H_{cr}$), and an intermediate field $H_{app}$ = 800 Oe. The corresponding static magnetization profiles are shown in Figure A.5 of Appendix II. From Figure 5.3(b) and (c), we observe that with increasing $D$, $H_{de}$ reduces in the NiFe filled circular regime while in the CoFe matrix it increases, but in opposite direction of the bias field. Hence, the interlattice dipolar interaction is modified accordingly affecting the intricate SW dynamics of the BMCs. Moreover, the magnitude of $H_{de}$ is always

higher in NiFe than CoFe, i.e., when $H_{de}$ adds up with the bias field, it gives rise to a higher effective magnetic field value in the NiFe. Although $H_{de}$ lies along opposite direction to bias field in CoFe, due to its low magnitude it cannot reduce the effective magnetic field significantly due to its low magnitude. Therefore, overall the effective magnetic field is higher in samples with smaller $D$ values, causing higher frequencies of SWs, while it reduces with increasing $D$ causing a red shift in the SW frequency. Furthermore, with $H_{app}$, $H_{de}$ increases faster in samples with smaller $D$ as opposed to those with larger $D$. This is clearly manifested in their frequency spectra, where the SW frequencies reduce faster from high to low value with field in smaller $D$.

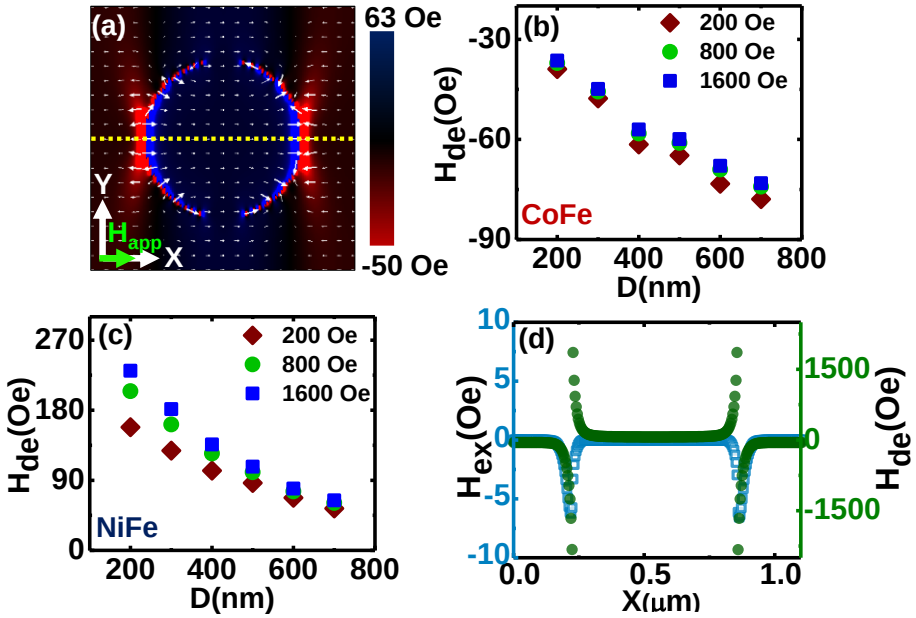


**Figure 5.3:** (a) Simulated spatial map of demagnetizing field for S5 ($D$ = 600 nm). The dashed line represents the axis of periodicity of the BMC. The red-black -blue color bar at the right side indicates the magnitude of the demagnetizing field (b) Simulated demagnetizing field values as a function of $D$ averaged from the CoFe matrix. (c) Simulated demagnetizing field values as a function of $D$ averaged from the NiFe filled holes. (d) Representative line scan of the demagnetizing field and the exchange field for S5 at $H_{app}$ = 200 Oe along the dashed line.

It is further noticeable that the collective precessional dynamics is coupled via the exchange field rather than the dynamic dipolar coupling at the NiFe/CoFe interface. At the interface, the $H_{de}$ yields opposite orientation of spins creating almost 180° dipolar configuration. This head-to-head dipolar orientation causes enormous enhancement of $H_{de}$ at the interface with quantities of opposite sign (Figure 5.3(d)). Hence, a large discontinuity is encountered by the SWs at the boundary of the two materials which could cause decoupled dynamics as well as confinement of SW within the materials. However, here the continuity in the interface exchange interaction plays a crucial role in allowing the SWs to spread through the CoFe matrix from the NiFe regions. Due to finite exchange interaction the coherence of SWs at the interface is not lost, rather it helps the system to exhibit collective SW dynamics.

**Spin-Wave Mode Characterization:** To interpret the features of the SW modes as observed in experiment and simulation, we have further simulated the spatial profiles of power and phase of each SW mode by using a home-built MATLAB based code named Dotmag [245]. The power profile gives a clear picture of the spatial map of a particular SW mode. From the phase distribution, the modes are identified as Damon Eshbach (DE)-like or backward volume (BV)-like magnetostatic modes with extended and/or standing wave (quantized) nature. We assign quantization numbers n and n´ (m and m´) for standing SWs in NiFe and CoFe regions for BV(DE)-like geometry. In Figure 5.4, we have shown the power and phase profiles of SW modes for two different samples ($D$ = 200 nm (S1) and 700 nm (S6)) at two different fields, $H_{app}$ = 200 Oe ($H_{app}$ << $H_{cr}$) and H = 1500 Oe ($H_{app}$ >> $H_{cr}$). The power and phase profiles of the other modes of these samples are shown in Figure A.6 of Appendix II.

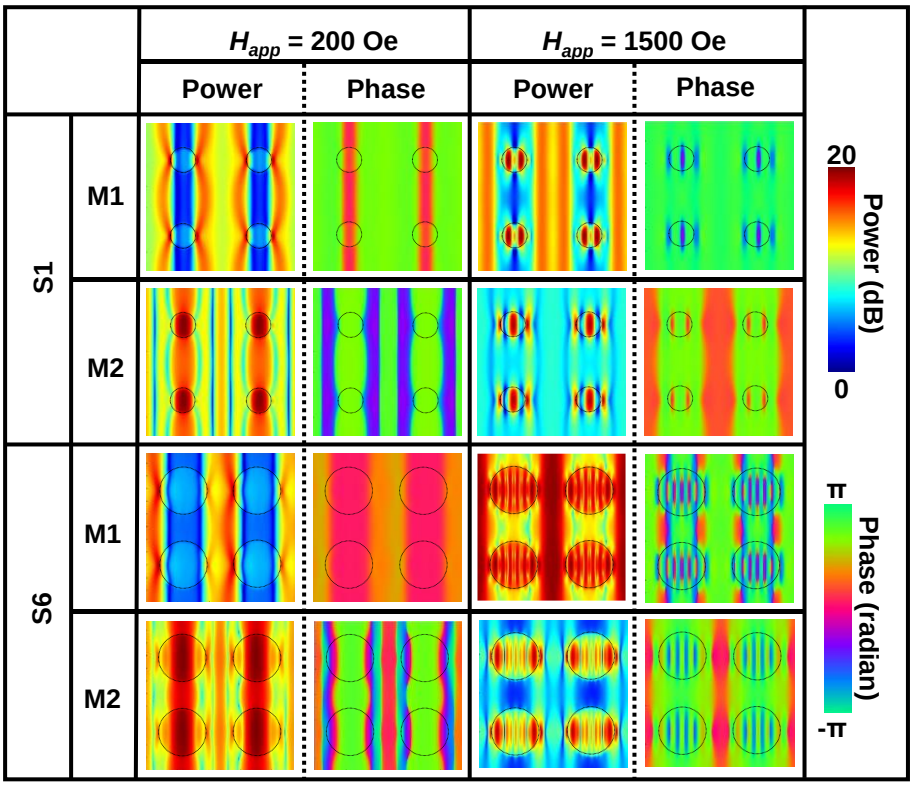


**Figure 5.4:** Simulated power and phase profiles of different SW modes for two different samples (S1 and S6) at two different values of bias magnetic field. The colour bars associated with power and phase are shown at the right.

The power profile of mode M1 at $H_{app}$ = 200 Oe shows that the maximum power is distributed vertically in the CoFe channel outside the NiFe and a minimum power at the edges of the dots for both S1 and S6. The corresponding phase distributions show M1 is extended perpendicular to the bias field direction showing its DE-like behavior in the CoFe channels. At higher field, $H_{app}$ = 1500 Oe, this channel mode now acquires finite power inside the NiFe dots in addition to spreading through the vertical channel inside the CoFe matrix in both S1 and S6. Phase profiles of S1 and S6 show that M1 is a BV-like (nodal planes perpendicular to the field direction) standing SW inside NiFe. Notably, the quantization is

different for different samples, i.e., n = 3(11) for S1(S6). Outside NiFe, M1 is still extended in the CoFe channel in the DE-like geometry without prominent quantization effect. On the other hand, in S1, M2 shows its power both in the dots and the matrix, but inside the dots its power is higher. Here, we observe center mode (CM) inside the dots and BV-like quantized mode with n´ = 3 in the matrix. At higher fields, its power shifts gradually from the CoFe channel and becomes localized inside the NiFe dots. At $H_{app}$ = 1500 Oe, we observe n = 5, a mode extended through the dot/matrix interface and n´ = 1. For S6, at $H_{app}$ = 200 Oe, the power extends through both the CoFe channels and NiFe dots with n = CM and n´ = 5. At higher field, at $H_{app}$ = 1500 Oe, the power is primarily localized inside the dots but extends through the dot/matrix interface with n = 9 and n´ = 1.

**Simulated Spin-Wave Propagation:** Measurement of the propagation properties of SWs is elusive in our experimental technique, and therefore, we have attempted to draw some insights about this aspect through micromagnetic simulations. It is envisaged that by taking advantages of the inter-material (CoFe-NiFe) exchange coupling the SWs will be able to propagate faster and longer through the BMC as opposed to its constituent dots and the antidot matrix [241].

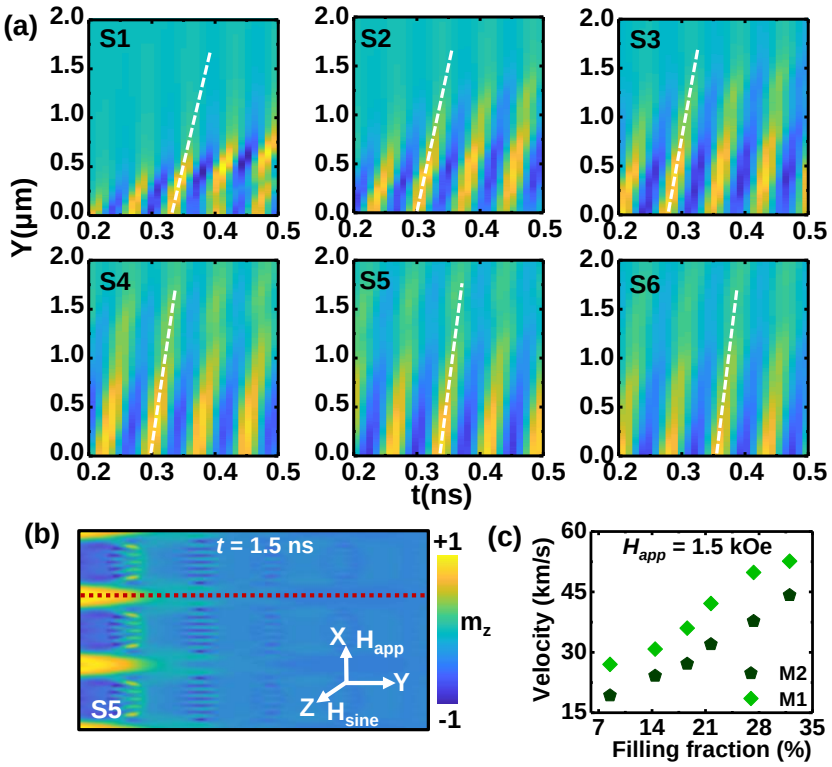


**Figure 5.5:** (a) Simulated time- and position-dependent spin deflection associated with $m_z$ component of mode M1 after local excitation at a bias field, $H_{app}$= 1.5 kOe for all six samples, S1-S6. The dashed lines represent the trace of $m_z$. (b) Representative spatial profile of $m_z$ component of SW mode M1 at $H_{app}$= 1.5 kOe for S5. The dashed line corresponds to the axis of nanochannel along which the SW propagation has been analyzed. The color map associated with $m_z$, the orientation of $H_{app}$ and the excitation field $H_{sine}$, are also shown. (c) The calculated SW velocity for M1 and M2 as a function of the filling fraction.

To verify this in the present samples, we have performed simulation by locally exciting SWs at the left end of the BMC structures. A time-varying sinusoidal excitation field with peak amplitude of 20 Oe is applied along the out-of-plane direction of the sample. The bias magnetic field is applied along the x-axis, i.e., along the width of the sample, while the SW propagates along the y-axis, i.e., in the DE geometry. We have calculated the spatial deflection of the SW peak associated with the dynamic $m_z$ component of the SW mode M1 (shown in Figure 5.5(a)) and M2 (not shown) for all samples as a function of time. SW velocity of M1 is determined from the slope of the white dashed line which represents the trace of a fixed phase of $m_z$. A similar analysis is performed for M2 too. In Figure 5.5(b), the spatial distribution of $m_z$ at $t$ =1.5 ns corresponding to excitation of mode M1 at $H_{app}$ = 1500 Oe for S5, is shown. From these analyses, we observe that the mode M1 having higher frequency can propagate faster in the CoFe channel, while mode M2 propagates with slower velocity through the same channel. Interestingly, under the same condition of excitation the SW velocity increases continuously with the filling fraction (Figure 5.5(c)) of BMC and a very high phase velocity up to 52 $kms^{-1}$ has been attained, promising the attainment of inordinate SW velocity with further optimization of magnetic and geometric parameters of the BMC. Furthermore, it is observed that the alternating magnetic field can excite SWs which are favorable by the channel through the CoFe matrix. Again, as noted in the magnetic field dispersion, for $H_{app}$ = 200 Oe, M1 almost vanishes with a minimum power while M2 receives all the power and propagates through a channel covering the NiFe dots. Therefore, we can visualize that the mode M1 can be turned on and the propagation channel through CoFe matrix can be opened only by increasing the magnetic field above the crossing field, i.e., the BMC may operate like a SW diode. On the contrary, such possibilities of switching on and off of selective SWs are nontrivial in an antidot lattice.

## 5.4 Conclusions

In summary, we have demonstrated fine tuning of the dynamic magnetic response of bicomponent magnonic crystals simply by varying the filling fraction and thereby the overall interface exchange energy between the two constituent materials CoFe and NiFe. The frequency values, number of modes and their spectral powers have been efficiently tuned with filling fraction. Further adjustment has also been achieved by varying the bias magnetic field strength. We show that broadband ferromagnetic resonance can effectively probe the dynamic response. The appropriate choice of the materials and favorable interface engineering of the bicomponent magnonic crystals have enabled significant exchange interaction at the interface which is further found to couple the collective SW dynamics of the BMC with the aid of micromagnetic simulations. Besides, the dipolar field is also found to play an important role in effectively modifying the SW spectra. Subsequently, by exploiting micromagnetic simulations we show that SW through the CoFe channel can propagate faster and this propagation velocity can be widely tuned by varying the filling fraction. Our findings demonstrate that the modified inter-material exchange interaction coupled with dipolar interaction can be leveraged for richer manipulation of SWs in bicomponent magnonic crystals, offering new possibilities in the applications of high-speed reconfigurable magnonics.

# Chapter 6 Ultrafast Spin Dynamics of Electrochemically Grown Heusler Alloy Film

## 6.1 Introduction

Heusler alloys (HAs) are highly promising material for spintronics applications due to its high spin polarization, strong magnetocrystalline anisotropy and ultralow damping [65–67,77–79,246,247]. The high spin polarization can lead to high magnetoresistance if HA is integrated in magnetic tunnel junction [74,248,249]. Moreover, playing with the stoichiometry of the constituent elements of the alloy, the spin dependent band structure as well as the resulting magnetic properties can be tuned [250,251] significantly. As a matter of fact, the Curie temperature can reach to a higher value, far above the room temperature. Especially, Co-based alloys possess high Curie temperature and ferromagnetic nature at room temperature [252]. Primarily, for spintronics research, thin films of such HAs are grown using the typical high-vacuum evaporation methods. In this essence, sputtered deposited HAs have shown reasonably low magnetic damping while few MBE grown systems are promising for high magnetoresistance. Recently, the electrochemical method has opened up an opportunity to achieve both a convenient and cost-effective growth process for large scale production [253–255]. The disadvantage of this method is the lack of long range crystallinity and the poor surface quality limiting those from heterostructures integration. To this regard, use of single-crystalline metallic surface as the substrate material has proven to improve the crystalline order of HAs. Depending on the growth process, the structural as well as the magnetic properties can vary significantly. Therefore, to harness the potential of HA for spintronics applications, a comprehensive exploration of their structural and magnetostatic properties in addition to the magnetization dynamics is imperative. This entails examining ultrafast demagnetization as well as the damping coefficient which plays pivotal role to describe the dynamics. In this regard, time-resolved magneto optical Kerr effect (TR-MOKE) technique has been proven to directly provide key insights of the magnetization dynamics occurring at femtosecond to nanosecond time scales in HA thin films [251,256–262]. Till date, this approach has been applied on sputtered deposited ultrathin films of HA to visualize their demagnetization dynamics and to extract damping coefficient, magnetic anisotropy, spin-polarization etc., while investigation on electrochemical grown film is elusive. Since, the thickness of electrodeposited film can reach to sub-micron value, the dynamics related to spin is expected to be highly modulated as compared to sputtered film. Here, we take a chance to unveil that.

We report investigation of ultrafast spin dynamics in electrochemically grown $Co_2FeSn$ film on a Pt(2 nm)/Ta(2 nm)/Si(111) substrate using TR-MOKE. The metallic top layer confirms a good surface topography of the deposited film. Using TR-MOKE, the spin dynamics is optically excited and optically probed from a local magnetization. This technique gives a direct estimation of the characteristic time scales of temporal demagnetization and subsequent relaxation through which the underlying role of many physical quantity is understood. Parallely, the analysis of precessional dynamics measured at nanosecond time scale provides information about the magnetic anisotropy as well as the damping

parameter. Further, based on the underlying physics a correlation between the demagnetization dynamics and the damping is established which says that the spin-flip scattering between the interband energy states control both the dynamics of pico- and nano- second time scales. The results shows a good agreement with the previously reported values on Co based HA. Nevertheless, these observations ensure that the cheaper method is also compatible for spintronics technology alongside the well-established growth technology.

## 6.2 Methods

**Sample Preparation and Basic Characterizations:** The HA film was grown using electrochemical deposition. Here, platinum deposited on a Ta(2 nm) coated Si(111) substrate was used as the metallic electrode. The Ta underlayer facilitates Pt adhesion on the substrate with good crystalline order. Ta and Pt were deposited using DC magnetron sputtering at a base pressure prior of ~ $1 \times 10^{-8}$ mbar. $Co_2FeSn$ (CFSn) film was then electrodeposited onto electropolished Pt(2 nm)/Ta(2 nm)/Si(111) substrate. Electrolyte solution was prepared by mixing sodium gluconate, boric acid, peptone and dissolving $CoSO_4 \cdot 7H_2O$, $FeSO_4 \cdot 7H_2O$, and $SnSO_4$ salts in it. Thin film growth subsequently followed annealing at 200°C in argon atmosphere. Finally, the substrate with CFSn was rinsed in distilled water to remove excess metal ions from its surface. Throughout the electrodeposition process, the Pt electrode on Si was accompanied by another Pt plate operating as the counter electrode while Ag/AgCl was utilized as the reference electrode. The structural and magnetic properties of the film were studied using EDAX, XRD, VSM and static-MOKE as reported in reference [263].

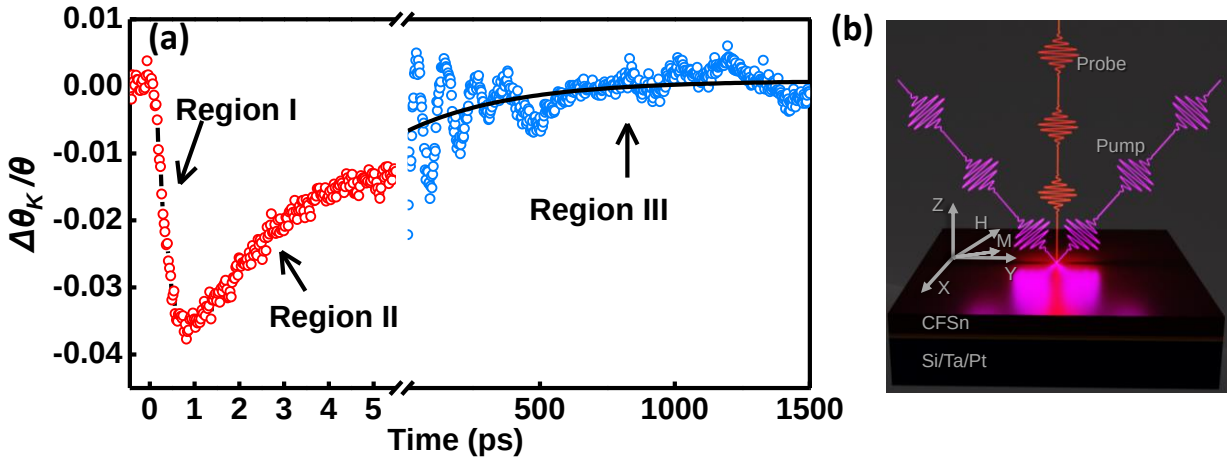


**Figure 6.1:** (a) Representative time-resolved Kerr signal as a function of pump-probe delay time. Three different temporal regimes indicate the ultrafast demagnetization (region-I), fast relaxation (region-II) and the slow relaxation with associated precessional magnetization dynamics (region-III). (b) A schematic diagram of measurement geometry.

**TR-MOKE Measurement:** The ultrafast magnetization dynamics of the CFSn thin film was studied using the custom-built TR-MOKE magnetometer based on the two-colour non-collinear pump-probe technique [264]. A bias magnetic field of about 1.5 kOe, well above the in-plane saturation magnetic field of the sample was first applied at an angle of about 45° to the sample plane to ensure a sufficient out-of-

plane demagnetizing field along the pump pulse to induce precession of magnetization of the sample. A small enough probe fluence of 2 mJ/cm$^2$ was used during the measurement to avoid laser heating while pump fluence was varied from 6.2 to 50 mJ/cm$^2$ to study the fluence-dependent dynamics. The magnetization dynamics measurements were done under ambient conditions over a broad timescale from femtosecond to nanosecond tracing the ultrafast demagnetization, relaxation and magnetization precession using appropriate time window and temporal resolution.

## 6.3 Results and Discussions

The observed peaks in the X-ray diffraction pattern are related to reflection from (111), (220) and (400) planes of CFSn. The presence of weak (111) peak confirms weak $L2_1$ phase of HA. The VSM measurement revealed the Curie temperature greater than 350 K. The two-fold symmetry in the coercivity measured from angular dependence of hysteresis loop ensures the presence of uniaxial anisotropy in the sample which is again consistent with the $L2_1$ ordering of HA. Related figures and descriptions are shown in the reference [263]. In Figure 6.1(a), a representative TR-MOKE data displays the typical three-region temporal response of the CFSn film starting with the femtosecond demagnetization (Region-I) followed by fast remagnetization (Region-II), and slow remagnetization superposed with damped precessional dynamics (Region-III). The pure precessional data is obtained by subtracting the bi-exponential background. Figure 6.1(b) shows the ultrafast demagnetization and fast remagnetization results for CFSn thin film at different pump fluences. We examined if the Kerr rotation corresponding to the demagnetization curves originates primarily from magnetic effects or any optical effects caused by the femtosecond laser irradiation [265]. To this end, we present the temporal variation of normalized reflectivity and Kerr rotation in Figure 6.2(b) and 6.2(c), respectively, at varying pump fluences and compare the relative variation of their amplitudes in Figure 6.2(d). Figure 6.2(d) clearly shows that the relative variation of reflectivity is negligibly small compared to that of the Kerr rotation, implying negligible non-magnetic contributions in the Kerr rotation data in general [80,266]. A small rise in the Kerr rotation near zero delay before the onset of the demagnetization is observed which increases with the increasing fluence. Such rise has been interpreted by optically induced spin transfer (OISTR) effect [267] in multicomponent alloys, including HAs [268,269]. However, in our system, this is contributed primarily by the reflectivity variation with time. The ultrafast de- and remagnetization can be modelled employing the widely used phenomenological thermodynamic model called three-temperature model (3TM) [57]. In 3TM this spin dynamics is understood as an equilibrium process by energy transfer between three subsystems of electron, lattice and spin. 3TM assumes presence of thermalized reservoirs of the three subsystems, whose temporal evolution is given by a set of coupled differential equations. The experimental data in Figure 6.2(a) are fitted with a phenomenological expression derived from the 3TM-based coupled rate equations given by [270,271]:

$$\frac{M(t)}{M_0} = -\left[\left\{\frac{A_1}{t/t_0+1} - \frac{A_2\tau_E - A_1\tau_M}{\tau_E - \tau_M}e^{-t/\tau_M} - \frac{(A_1 - A_2)\tau_E}{\tau_E - \tau_M}e^{-t/\tau_E}\right\}H(t) + A_3\delta(t)\right] \otimes G(t) \quad \ldots 6.1$$

Here $\tau_M$ is the demagnetization time, $\tau_E$ is the fast remagnetization time, $H(t)$ is the Heaviside step function and $G(t)$ stands for the Gaussian laser-pulse. The constant A1 indicates the equilibrium value of the ratio $\Delta\theta_k$, while $A_2$ is proportional to the initial electronic temperature rise. The constant $A_3$ represents the magnitude of state-filling effects during pump probe temporal overlap that is described by a delta function.

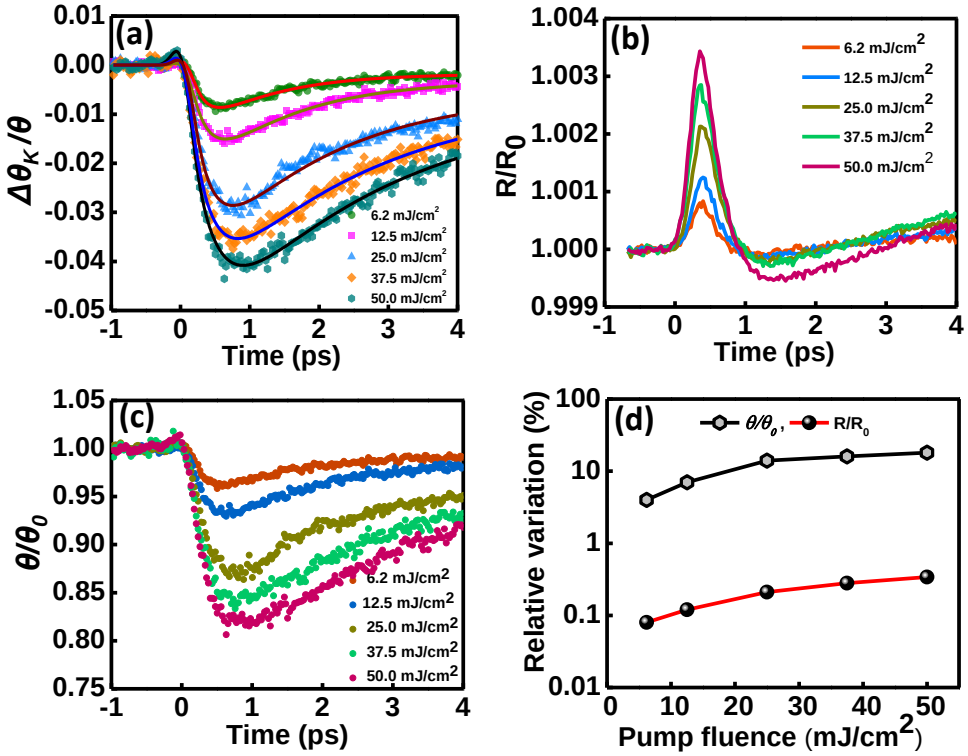


**Figure 6.2:** (a) Time-resolved Kerr rotation data representing quenching of magnetization with increasing excitation fluence. The symbols denote experimental data points and the solid lines represent the fitted curves. (b) Transient reflectivity at different pump fluences normalized w.r.t the corresponding negative delay value. (c) Kerr rotation at different pump fluences normalized w.r.t the corresponding negative delay value. (d) Relative variation of the peak values of transient Kerr rotation and reflectivity.

The values of ultrafast demagnetization time ($\tau_M$) and fast relaxation time ($\tau_E$) are found to vary monotonically from 207 fs to 349 fs and 1 ps to 2.5 ps, respectively, as pump fluence is varied from 6.2 to 50 mJ/cm$^2$ (Figure 6.3(a)). The amount of quenching of magnetization also increases by around 20% with this increase in fluence. The monotonic increase in $\tau_M$ and $\tau_E$ with pump fluence can be interpreted by considering Elliot-Yafet (EY)-like spin-flip scattering as the leading mechanism of laser induced ultrafast demagnetization process [80,81]. Previous TR-MOKE studies on ultrafast demagnetization reported faster demagnetization within few hundreds of fs in HA thin film [83,260,272] compared to slower demagnetization in epitaxially grown half-metallic systems. This is primarily related to a reduced degree of half metallicity caused by the chemical ordering of the constituent sublattices in a HA thin film. The XRD data shows that the degree of $L2_1$ ordering is weak here indicating a moderate half-metallic nature of CFSn. This moderate half-metallicity of the electrochemically grown CFSn thin film indicates

a moderate suppression of the d-band below the 4s-band, and the spin-flip scattering mechanism is still active to control the demagnetization process.

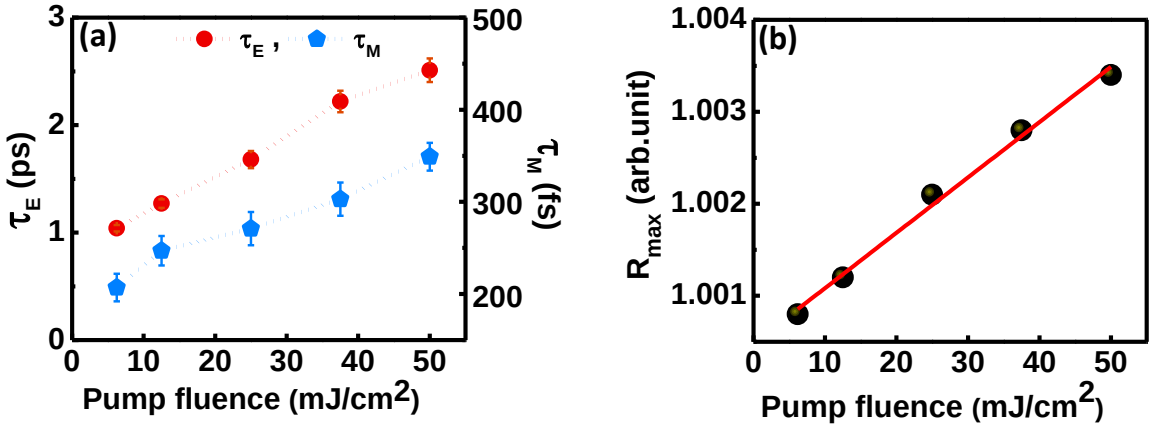


**Figure 6.3:** (a) Fluence-dependent variation of ultrafast demagnetization time ($\tau_M$) and fast relaxation time ($\tau_E$). The dotted lines are a guide to the eye. The arrows indicate the y-axis values corresponding to ($\tau_M$) and ($\tau_E$). (b) Maximum value of normalized reflectivity $((R/R_0)_{max})$ as a function of pump fluence. The solid line is a linear fit to the experimental data point.

Thus, demagnetization occurs faster through spin-flip scattering channel within hundreds of fs. Further, the presence of weak $L2_1$ ordering in the CFSn thin film indicates a lower value of spin polarization, which further implies that the minority energy gap at the Fermi level is small enough, enhancing the spin-flip scattering probability. Nevertheless, this is still similar to or somewhat better than highly controlled sputter-deposited, hence implying the high growth quality of the CFSn films by the electrochemical process. The monotonic behavior of $\tau_M$ and $\tau_e$ can be understood by the fact that on the absorption of energy from intense pump laser, hot electrons are produced above the Fermi level. As the pump fluence is increased the electron temperature increases approaching Curie temperature. Since the electron-spin interaction channel is open here, within few femtoseconds the temperature of the spin system increases to a higher value following the sharp rise of electron temperature. Figure 6.3(b) shows that the reflectivity peak increases linearly with the increase in pump fluence, which is directly related to the electron temperature [273]. The pump laser-excited hot electrons interact with the spin system via transfer of energy. Subsequently, the equilibrium of the spin system above the Fermi level is destroyed, which, in turn, increases the spin-flip scattering rate and as a result demagnetization amplitude increases while the demagnetization becomes slower. The fast remagnetization occurs within few picoseconds through the electron-lattice interaction. To extract the anisotropy parameters $K_2$ and $K_4$ experimentally we measured the time-resolved Kerr rotation at different bias magnetic field values Figure 6.4(a). The precessional frequency at different fluences is extracted by taking a fast Fourier transform (FFT) of each background subtracted Kerr signal recorded for longer delay time 6.4(b).
The bias field dependent precession frequency is fitted with Kittel formula of uniform precession as given below [128]:

$$f = \frac{\gamma}{2\pi}\sqrt{H_1 \times H_2} \quad \ldots 6.2$$

where $H_1$ and $H_2$ are respectively given by,

$$H_1 = H\cos(\theta_H - \theta_M) + H_a$$
$$H_2 = H\cos(\theta_H - \theta_M) + H_b$$

Here, $H$ is the applied magnetic field and $H_a$, $H_b$ are given by,

$$H_a = \frac{2K_2}{M_S}cos\,2\theta_M + \frac{2K_4}{M_S}cos\,4\theta_M$$
$$H_b = 4\pi M_S - \frac{K_2}{M_S}(1 - \cos 2\theta_M)$$

where, $M_S$ is the saturation magnetization, $\gamma$ is the gyromagnetic ratio of the electron, the uniaxial and biaxial magnetic anisotropies are denoted as $K_2$ and $K_4$, $\theta_M$ ($\theta_H$) is the angle between in-plane easy axis and equilibrium magnetization (applied magnetic field). The fit with eqn. (6.2) gives the value of $K_2$ = $1.5\times10^6$ erg/cm$^3$ and $K_4$ = 0.

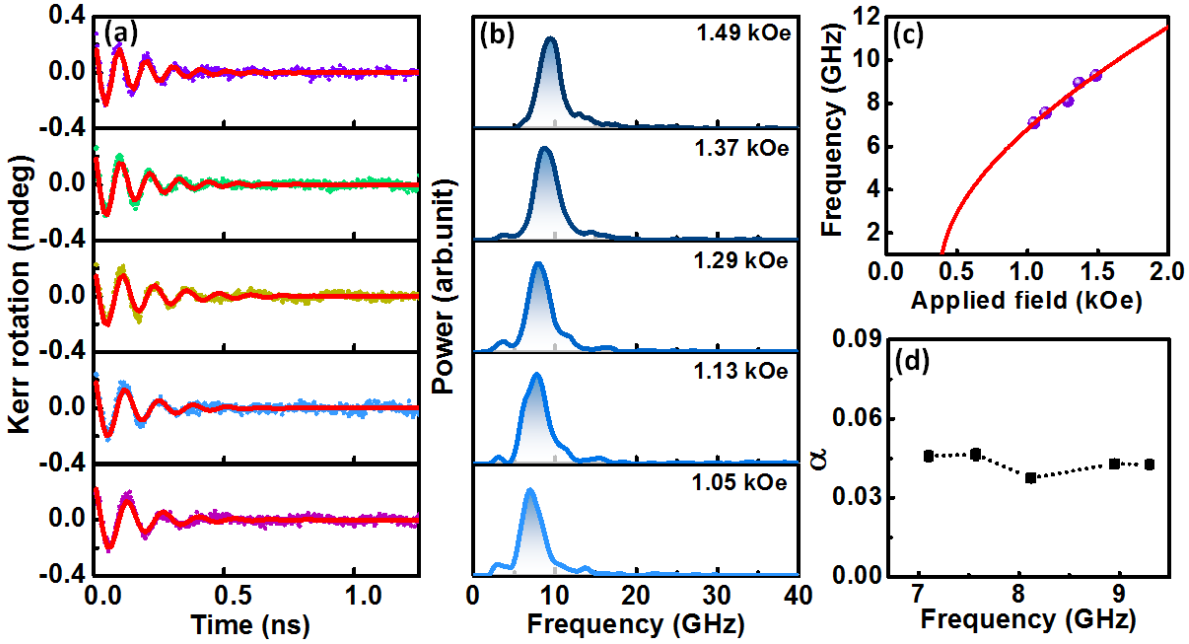


**Figure 6.4:** (a) Background subtracted time-resolved Kerr rotation data showing precessional oscillations at different bias magnetic field values. The symbols represent experimental data points and the the solid lines represent the fit using eqn. (6.3). (b) The FFT power spectra of time-resolved Kerr rotation in (a), showing the precession frequency. (c) Experimental precessional frequency as a function of bias magnetic field (symbols) and the corresponding Kittel fit (solid line). (d) Variation of damping constant (α) with frequency at fluence 37.5 mJ/cm$^2$ are shown by symbols. Dotted lines are guide to eye.

Also, the relaxation time of precessional magnetization is calculated by fitting the background subtracted Kerr rotation data with a damped sinusoidal function of the form:

$$M(t) = M(0)e^{-\frac{t}{\tau}}sin(2\pi ft + \varphi) \quad \ldots 6.3$$

where $M(0)$, $f$ and $\phi$ denote the amplitude, frequency and initial phase of the oscillation.

Subsequently, the Gilbert damping constant ($\alpha$) is determined from the precessional relaxation time ($\tau$) following equation [274,275]:

$$\alpha = \frac{2}{\gamma\tau[2H\,cos(\theta_H - \theta_M) + H_a + H_b]} \quad \ldots 6.4$$

From Figure 6.4(d) we observe that $\alpha$ remains nearly invariant with frequency, indicating intrinsic origin of damping in this system. However, the value of $\alpha$ is comparable to the order of magnitude $\approx 0.01$ for Co-based full HA [276] but larger than some recently reported UHV sputtered deposited HA thin films [261,275].

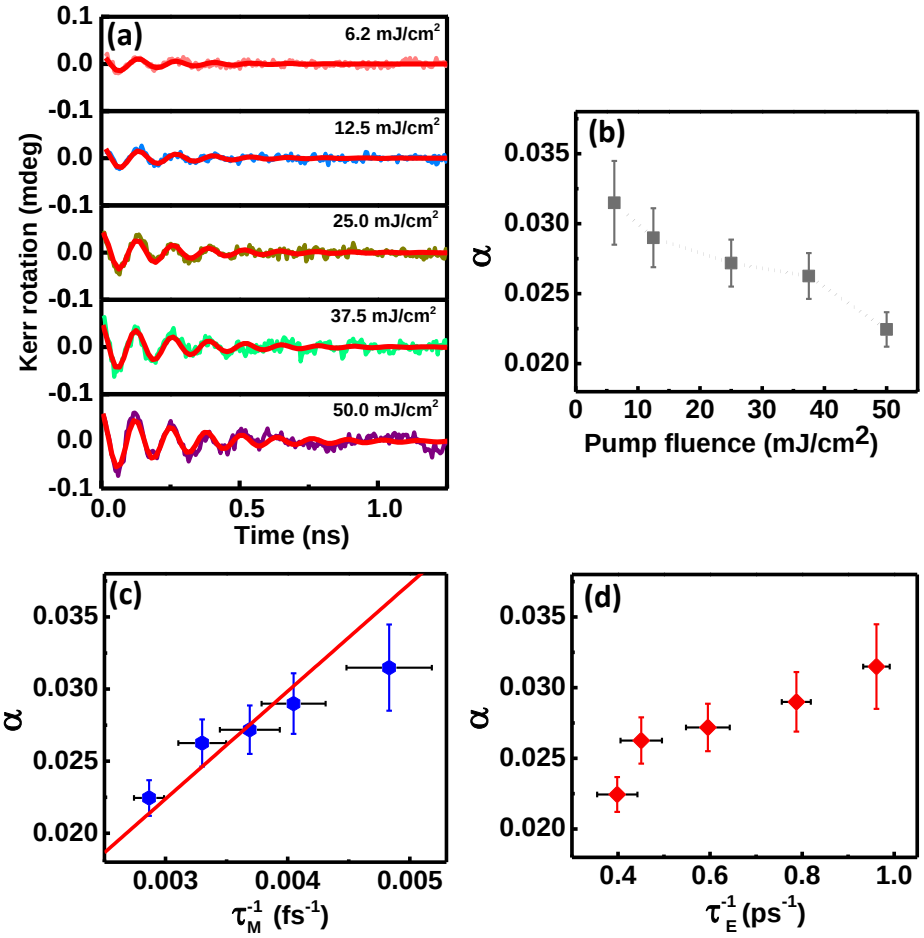


**Figure 6.5:** (a) Background subtracted Kerr rotation data with fits representing precessional magnetization dynamics at different excitation fluences. (b) Variation of damping parameter ($\alpha$) with fluence shown by symbols. Dotted line refers to guide to eye here. (c) Damping parameter ($\alpha$) as a function of inverse of ultrafast demagnetization time ($\tau_M$) shown by symbols. Solid line is the linear fit to the data. (d) Damping parameter ($\alpha$) as a function of inverse of fast relaxation time ($\tau_E$) shown by symbols.

This possible reason for larger value of $\alpha$ in the electrochemically grown film may be related to the weaker crystalline order [19]. The precessional frequency remains almost invariant with fluence but the amplitude of precessional motion shows a large dependence on excitation energy. Figure 6.5(a) shows the pump fluence dependent precessional dynamics of the CFSn film at $H$ = 1.49 kOe. The extracted

values of $\alpha$ using eqn. (6.4) are plotted in Figure 6.5(b) where we observe that $\alpha$ decreases monotonically with fluence. Figure 6.5(c) shows that $\alpha$ is inversely proportional to $\tau_M$. Although ultrafast demagnetization and precessional dynamics are apparently two different phenomena occurring at timescales differing by orders of magnitude, several studies have shown that the governing fundamental physical mechanism are related in these two phenomena. Hence, correlating these two important characteristic parameters is an important task of ultrafast magnetization dynamics. Till date the physical origin of Gilbert damping has been explained for various systems with different theoretical models. The most common and widely accepted model describes that the damping originates due to transfer of spin angular momentum in lattice through spin-flip scattering events mediated by spin-orbit coupling [81,277]. The ultrafast demagnetization is also dominated by such spin-flip scattering processes of electrons excited above Fermi level by a high energy laser-pulse. When all the channels of energy dissipation through this scattering process are available in a material the demagnetization time comprises of all possible relaxation times and defined as [81]:

$$\tau_M = \frac{\tau_{e-s}\tau_{s-l}}{\tau_{e-s} + \tau_{s-l}}$$

where $\tau_{e\text{-}s}$ is the electron-spin relaxation time and given as:

$$\tau_{e-s} = \frac{\tau_{e,0}}{c^2}(1-P)^{-1}$$

$$c \approx \frac{\xi_{SO}}{\Delta E_{ex}}$$

Here $\tau_{e,0}$ is called the electron momentum scattering rate, $c$ is the band mixing parameter which is described by spin-orbit coupling and exchange splitting energy as, $P$ indicates the spin polarization of the material. The spin-lattice relaxation time $\tau_{s\text{-}l}$ is expressed in terms of anisotropy energy $E_{ani}$ and its temperature dependency is represented by the parameter $A(T)$.

$$\tau_{s-l} = \frac{1}{A(T)|E_{ani}|^2}$$

On the other hand, the damping coefficient characterizing the precessional dynamics is defined as [277],

$$\alpha \approx \frac{\mu_B^2 D(E_F)}{\Gamma_e[\gamma M_S]}\left(\frac{\xi_{SO}}{W}\right)^2$$

where $D(E_F)$ is the density of states in Fermi level, $1/\Gamma_e$ is the electron-scattering frequency, $\xi_{SO}$ is the spin orbit interaction energy and $W$ is the d-band width. In the present scenario, the increase in laser fluence weakens the spin-orbit interaction resulting changes in $\tau_{e\text{-}s}$ and $\tau_{s\text{-}l}$. which presumably influences the demagnetization as well as damping of precessional motion in an opposite manner.

Furthermore, a similar correlation between fast relaxation time $\tau_E^{-1}$ and damping α is observed from Figure 6.5(d). It seems reasonable to predict that the same physical mechanisms are also responsible for the observed correlation between $\alpha$ and $\tau_E$. The detailed quantitative calculation correlating the distinct time scales of ultrafast magnetization dynamics has been carried out by inclusion of various models in some prior works. Koopmans et al. based on quantum mechanical treatment proposed that damping coefficient scales inversely to the demagnetization time assuming two different magnetic fields, i.e.

exchange field and total homogeneous effective field (consisting of external field, anisotropy field and demagnetization field) dominate the effective magnetic field in femtosecond and nanosecond regime [278]. Later, by using ab-initio calculation Fahnle et al. have shown that α can be either directly or inversely proportional to $\tau_M$ depending upon the dominating microscopic contribution to the magnetic damping [279]. The linear relation sustains when the damping is dominated by intraband mechanism driven conductivity-like contribution, whereas the interband mechanism driven resistivity-like contribution leads to an inverse relation between them. Zhang et al. reported that α is directly proportional to $\tau_M$ in Co/Ni multilayer due to conductivity-like contribution in damping originated from breathing Fermi surface model [280]. They also suggest that an inverse relationship between $\alpha$ and $\tau_M$ can be attributed to the nonlocal spin current in metallic heterostructure system. It should be highlighted that recently, Malik et al. has established the correlation between $\alpha$ and $\tau_E$ considering magnon dominated remagnetization in HA [281]. The ultrafast incoherent magnon generation due to interband transition of highly excited electrons and the electron-magnon interaction play crucial role in the ultrafast demagnetization and dominates over EY spin flip scattering during the remagnetization. They proposed that the decay of magnon is effectively determined by the Gilbert damping and leads to the remagnetization. Based on the above discussions, we believe that the three stages of ultrafast magnetization dynamics are connected through different quasiparticles-scattering mechanism.

To interpret our findings we again look into the phonon mediated EY type spin-flip scattering mechanism [282] among several proposed models. As described in 3TM, the remagnetization involves the cooling of the hot-electrons through energy transfer to the lattice approaching towards equilibration of both electron and lattice sub systems. This process is dominated by the EY spin-flip scattering that persists during the damping of precessional dynamics and connect both these phenomena. Recently, an inverse relationship between $\alpha$ and $\tau_M$ in half-metallic $Co_2Fe_xMn_{1-x}Si$ thin films has been explained as a consequence of resistivity-like interband scattering [251]. Hence, it is conceivable that in the electrodeposited CFSn film, resistivity-like scattering is the leading mechanism in damping, i.e. excitation of interband electron and hole (e-h) pair near band gap regime of HA and their interactions with phonon via spin dependent scattering speed up the damping during the picosecond dynamics. This e-h pair production can be enhanced by increasing fluence causing delayed relaxation as the excited e-h pair suffer more spin-dependent scattering with increasing fluence. Hence, the relation between $\tau_M$ and $\alpha$ suit well to the existing model regarding electronic contribution in laser-induced magnetization dynamics.

## 6.4 Conclusions

In conclusion, we have demonstrated that the electrochemical growth of Co-based Heusler alloy film supported on a single crystalline substrate shows improved film quality. The film shows good crystalline property with a finite $L2_1$ ordering. The static MOKE measurements reveal the presence of strong uniaxial anisotropy. By employing TR-MOKE measurements, we present magnetization dynamics study on the electrochemically grown Heusler film. From the dynamics studies, we extract ultrafast

demagnetization and relaxation times, as well as precession frequency and damping. The behavior of ultrafast magnetization dynamics can be understood using a three temperature model. The ultrafast demagnetization and relaxation times are found to increase with fluence, while the damping decreases with fluence. The damping is found to be intrinsic in nature, while it varies inversely with the ultrafast demagnetization time, most likely due to its origin in the resistivity-like interband scattering mechanism. The results presented here open up an opportunity to further explore electrochemically grown intermetallic alloy films on crystalline substrates, for realizing possible magneto optical and spintronics applications.

# Room Temperature Evolution of Laser Induced Ultrafast Spin and Phonon Dynamics in 2D Van der Waals Magnets $Fe_xGeTe_2$(x=3,4,5) Chapter 7

## 7.1 Introduction

The discovery of intrinsic ferromagnetism in two-dimensional (2D) van der Walls (vdW) crystals in 2017 [283,284], has turned to a major breakthrough for the incipient emergence of 2D-spintronics research. Hosting long range magnetic order even in the monolayer limit, such 2D-materials hold immense potential for future spintronics applications [104,285] with novel magnetic heterostructures. These heterostructures, facilitated by weak interlayer vdW force can be achieved devoid of interfacial roughness, dangling bonds, lattice mismatch or unwanted chemical mixing. However, in order to realize spintronics applications, materials with high Curie temperature ($T_C$) are essential to render robust magnetic ordering at room temperature. In this essence, $Fe_xGeTe_2$ (FxGT) [93,105] family has emerged as a promising class of vdW crystals due to relatively higher $T_C$ (220-330K) [286–288] from bulk to layer limit. Especially, F5GT exhibits $T_C$ above room temperature assisted by more Fe concentration. In this context, gate tuning [289], proximity effect [290], patterning [102], stress [101] and stacking with topological insulator [103] as well as ultrafast laser pulse mediated optical doping effect [97] have been able to elevate the $T_C$ near room temperature. Parallelly, displaying strong magnetocrystalline anisotropy endowed with other exotic physical properties [291–294], these metallic FxGT compounds are highly favorable candidates for spin valve [295], magnetic tunnel junction [296], spin tunnel field-effect transistor [297] like advanced spintronic device engineering. The unique layered structure can easily promote unhindered motion of spins desirable for device operation. Furthermore, topological skyrmion state [298,299] at room temperature has been observed in FxGT owing to novel quantum phenomena.

Optical manipulation of spin in 2D vdW magnets is of fundamental interest because it can drive engrossing phenomena like ultrafast demagnetization [300], all optical switching [98], spin-phonon coupling [301–303], topological spin-texture [304] and generation of spin-wave (SW) [96,305,306]. Besides, femtosecond laser pulse can induce and enhance transient magnetization by inverse Faraday effect [307], spin-lattice coupling [308,309] or modulation of exchange energy [97,310]. Even development of ferromagnetic state is predicted in non-magnetic material exposed under ultrafast laser through interlayer spin-dependent charge transfer [311] or non-linear spin-flip process [312]. Interestingly, the optically stabilized magnetic order is viable to much longer time window than the laser pulse duration [97,308]. The strong laser field is able to directly modify the charge carrier density, lattice symmetry or spin-orbit coupling in terms of light-matter interaction. The magnetic ordering and its interaction with other degrees of freedom is highly sensitive to these parameters. Thus, ultrafast laser can provide an efficient pathway to transiently harness the magnetic properties of vdW crystals. In this regard, time-resolved magneto-optical Kerr effect (TR-MOKE) microscopy is esteemed as one of the

most reliable optical techniques due to exquisite spatial and temporal resolution and efficacy of scanning at submicron scale. Therefore, it can yield deeper insight of the core physics occurring at microscopic level with ultrafast speed.

However, very few investigations are reported till date unraveling spin dynamics in 2D vdW magnets [96,98,300,303,313,314] using this all-optical method, while most are circumscribed by cryogenic temperature. Optical control of spin dynamics in vdW materials at room temperature is indeed a challenging task constrained by thermal spin fluctuations. Despite the difficulty, we explore the ultrafast excitation of magnetization dynamics at room temperature in chemically grown and mechanically exfoliated FxGT (x=3,4,5) crystals employing TR-MOKE microscope. In fact, FxGT compounds are sought for large magneto-optical Kerr rotation [315] facilitating optical detection. Here, we observe ferromagnetic type-I ultrafast demagnetization dynamics in all three samples in sub-picosecond time scale. The ultrafast demagnetization is a manifestation of phonon mediated spin-flip scattering as supported by the microscopic three temperature model (M3TM). Intriguingly, magnon modes with THz frequency is detected during the remagnetization of the material with a simultaneous detection of optically pumped coherent phonon modes. Moreover, for the first time we unveil coherent spin-phonon coupling in FxGT compounds by an all-optical approach. In addition, multiple SWs excitation and their magnetic field dependence nature are unfolded in the FxGT samples investigating precessional dynamics at the nanosecond time scale. The strong uniaxial anisotropy rooted at the heart of 2D magnetism is supposed to generate SWs of GHz frequency. This precise experimental demonstration of the fundamental physical phenomena at room temperature enlightens the opportunities for next generation multifunctional spintronics applications using 2D vdW ferromagnetic crystals.

## 7.2 Methods

**Sample Fabrication and Characterizations:** Single crystalline FxGT are synthesized using chemical vapor transport method using iodine as transport agent. 99.999% pure powder of Fe, Ge and Te are added together in a nominal stoichiometric proportion x:1:2 and sealed in an evacuated quartz tube. However, to avoid presence of any unoccupied Fe sites in FxGT compounds, Fe precursor is added more than the nominal value. Subsequently, the crystal is grown by placing the quartz tube in a tubular furnace for seven days with source and growth temperature of 750°C and 700°C, respectively. Once temperature of the furnace reduces to room temperature the quartz tube is taken out and broken to collect the grown crystal. This crystal was washed in ethanol to remove the excess iodine. Further, the nanometer thick flakes are created on a 100-nm-thick $Si/SiO_2$ substrate by mechanical exfoliation. In order to prepare the samples for the time-resolved measurements, the substrates with exfoliated flakes are quickly transferred to a thermal evaporation chamber where a thin layer (7 nm) of Aluminum (Al) is deposited under a base pressure of $5 \times 10^{-6}$ mbar. Naturally oxidized Al works as a capping layer to avoid possible degradation of FxGT flakes due to laser exposure during all optical pump-probe experiment. The thickness of the flakes is measured using atomic force microscopy (AFM). The room

temperature characterization of the FxGT single-crystals was performed using XRD. Magnetization measurements were carried out on those single crystals to estimate the ferromagnetic transition temperature ($T_C$). FxGT flakes were also studied using Raman spectrometer for a temperature range, 100 K- 300 K. In this experiment, 532 nm and 633 nm laser with spot diameter of 1 μm were used at room- and low temperarure respectively with power restricted below 150 μW on the sample surface.

**TR-MOKE Measurement in Nanoflakes:** We have used a Ti:Sapphire laser based ultrafast pump-probe technique (TR-MOKE microscopy) to investigate the time-resolved spin dynamics as well as the coherent phonon dynamics. Time resolved measurement was performed on micrometer sized flakes of FxGT of thickness ~260-400 nm (Figure 7.1(a)). A high intense 400 nm (3.1 eV) pump laser pulse induces the dynamics in the sample which is detected by a time delayed laser pulse of wavelength 800 nm (1.55 eV). The measurement is done in polar MOKE geometry (Figure 7.1(b)), and we can simultaneously probe the change in reflectivity (ΔR) and polarization angle of probe beam, i.e., Kerr rotation (Δθ) (originated from the magneto-optical Kerr effect) as a function of pump-probe delay time. In this pump-probe experiment, time domain data is recorded for reflectivity and Kerr rotation in the picosecond and nanosecond time window, separately.

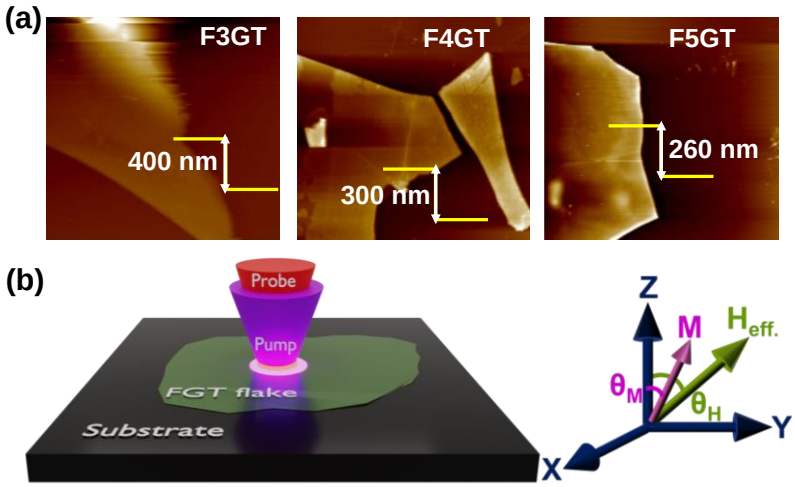


**Figure 7.1:** (a) AFM images of exfoliated $Fe_xGeTe_2$ flakes. (b) An illustrated scheme of experimental geometry used in time-resolved magneto-optical Kerr effect (TR-MOKE) microscopy.

## 7.3 Results and Discussions

**Crystal Structures and Magnetic Properties:** In the single-crystal XRD pattern, all peaks are originated from (*00l*), implying that the crystal surface is normal to the *c* axis and the plate-shaped surface is parallel to the *ab* plane. Bulk F3GT crystal, which contains $Fe_3Ge$ slabs isolated by van der Waals bonded Te double layers, possess hexagonal structure with space group P63/mmc($a = b = 3.96$ Å, and $c = 16.36$ Å) [316–318]. In F4GT, an additional Fe layer sandwiched between the two Te layers appears having weak vdW bond with the neighboring Te atoms. It has a rhombohedral structure (space group $R\bar{3}m$ ) [287,319,320] with $a = b = 4.02$ Å, and $c = 29.14$ Å. F5GT assumes a trigonal crystal structure of space group $P3m1_8$ with extra Fe atoms arranged in honeycomb geometry in between the Te

monolayers. The difference between the structural and magnetic properties of F5GT and F3GT lies in the additional Fe1 and Fe3 layers in the former [286,321]. $T_C$ for FxGT are determined to be 200 K, 265 K and 305 K respectively for x = 3, 4 and 5 as reported elsewhere [212,318,320]. The results are consistent with previously reported $T_c$ values in literature [105,287,322].

**Raman Spectra:** In the multimodal Raman spectra (Figure 7.2 (a)-(c)), mode $P_1$ at 106 $cm^{-1}$ (3.18 THz) is the substrate mode while rest are identified to originate from FxGT [320,323,324]. The origin of mode can be calculated from the lattice dynamics. $P_2$ at 115 $cm^{-1}$ (3.44 THz) is $A_{1g}(\Gamma)$ phonon mode while $P_5$ at 155 $cm^{-1}$ (4.463 THz) is mixture of $A_{1g}(\Gamma)$ and $E_{2g}(\Gamma)$ phonon modes as proposed theoretically by Luojun Du et al. [325]. The Raman shift of these two modes remain intact in the studied temperature range for each compound. Mode $P_3$ at 128 $cm^{-1}$ (3.84 THz) and $P_4$ at 143 $cm^{-1}$ (4.288 THz) are new peaks, plausibly originated due to oxidation. Mode $P_6$, observed around 282 $cm^{-1}$ (8.45 THz) with the lowest intensity vary with temperature. So, to extract the peak positions, the Raman signals were plotted seperately in the range 225 to 425 $cm^{-1}$ and fitted with Gaussian function to extract their peak frequencies with a reasonable accuracy.

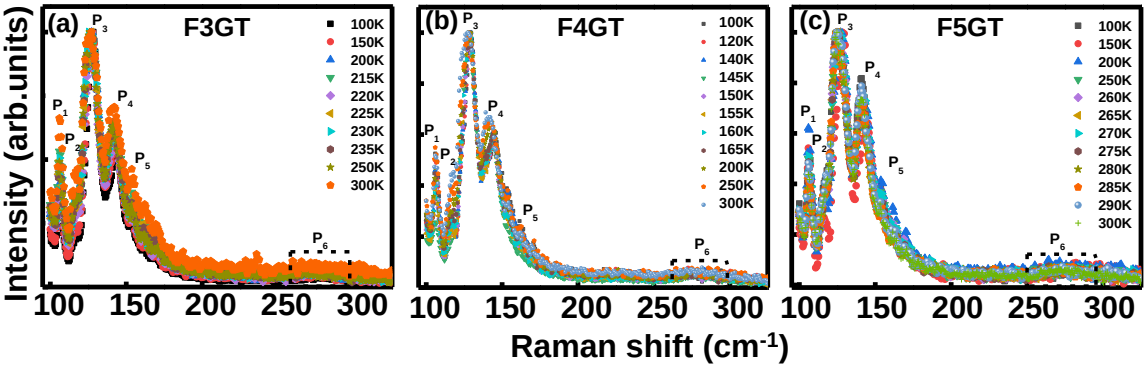


**Figure 7.2:** Temperature dependent Raman spectra for $Fe_xGeTe_2$ flakes.

**Ultrafast Dynamics at Picosecond Time Scale:** Figure 7.3(a) and (b) represent the time trace of ΔR and Δθ, respectively, at different values of external magnetic field ($H_{ext}$) for an excitation fluence 12.7 $mJ/cm^2$. The net magnetization of each sample drastically drops within few femtoseconds after the laser pulse hits the sample. The subsequent recovery of magnetization i.e. remagnetization occurs in the next picoseconds with an oscillating nature superimposed on an exponential background similar to the reflectivity signal. However, if we ignore the oscillatory signal, the remagnetization possess a *type-I* single step fast relaxation as found in many 3d ferromagnets [326]. This observation is in contrary to the recently reported *type-II* demagnetization process in 2D vdW crystals $Cr_2Ge_2Te_6$ and $Fe_3GeTe_2$ [300,314]. The plausible mechanism of demagnetization has been discussed later in the article. Meanwhile, we focus on the residual oscillations of the Kerr rotation and reflectivity subtracting the exponential background at $H_{ext}$ = 1.38 kOe as depicted in Figure 7.4(a). The corresponding Fast Fourier transforms (FFTs) are presented in Figure 7.4(b). The Kerr rotation signal unveils the photoexcited magnon modes at sub-picosecond time scale. In the FFT spectra of Kerr signal, high amplitude peaks

are observed at ~3.7 THz, 3.3 THz with a small intense peak at around 4.2 THz for each sample. Few additional small peaks appear at slightly different frequency values for different x. The very similar coherent oscillations in the transient reflectivity represent the imprinted phonon dynamics. The phonon modes are prominent at almost equal frequencies of the magnon modes implying a direct spin-phonon coupling influenced by the femtosecond laser pulse.

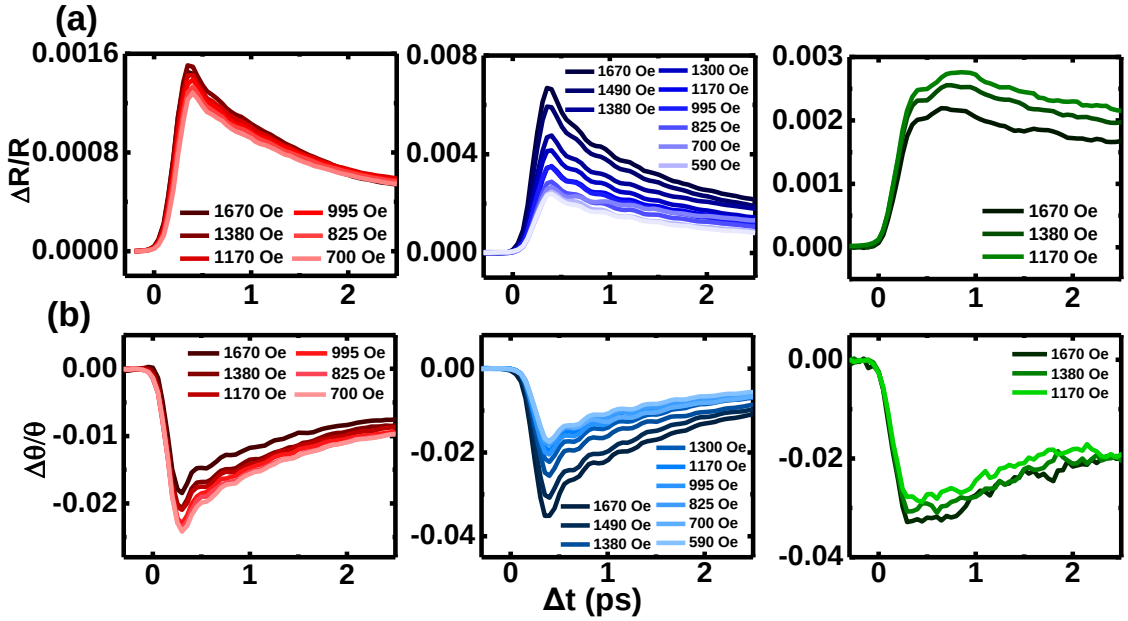


**Figure 7.3:** (a) Time-resolved reflectivity and (b) time-resolved Kerr rotation at different values of externally applied magnetic field for $Fe_3GeTe_2$ (left panels), $Fe_4GeTe_2$ (middle panels) and $Fe_5GeTe_2$ (right panels).

These phonon modes are again confirmed from the result obtained from Raman measurement. However, the high frequency phonon mode observed at 282 $cm^{-1}$ (frequency: 8.45 THz) is not visible in the TR-MOKE data. Notably, the phonon mode at ~3.7 THz belongs to the optical phonon branch at the gamma point, originated from time evolution of the diagonal elements of Raman tensor $A^1_{1g}$ [327] (evidenced from Raman spectroscopy of F3GT compound [325]). However, no such report is available for F4GT and F5GT on the phonon dynamics. Thereby, we predict that the nearly identical frequency of phonon in F4GT and F5GT might have the same origin. For the present scenario, Displacive Excitation of Coherent Phonons (DECP) [328,329] is the plausible mechanism of the THz optical phonon generation. In this method, the transient change of carrier (electron) density by the laser field leads to an alteration of the inter-ionic potential which results a displacive force to the ions. The ions shift from their equilibrium positions and oscillate around the new minima generating coherent lattice vibrations. Here, this optical phonon branch is associated with the out of plane vibration of heavy Te atoms [327]. Moreover, in FxGT, the Fe spins are coupled by Te atoms via super-exchange interaction which is a function of the distance between two nearest neighbor sites. Consequently, the vibration of Te atoms leads to the change in Fe-Te bond length. Hence, the lattice displacement of Te atoms, i.e., phonon acts as a perturbation on the ferromagnetic exchange coupling strength via spin-phonon coupling according

to the simplified formula, $J'_{ij}(u_\alpha) = J_{ij} + \frac{\partial J_{ij}}{\partial u_\alpha} u_\alpha + \frac{1}{2}\frac{\partial^2 J_{ij}}{\partial u_\alpha^2} u_\alpha^2 + \cdots$, where $i$ and $j$ are spin site indices, and $J_{ij}$ is the isotropic exchange interaction between spins at $i$ and $j$, and $u_\alpha$ represents the amplitude of phonon. The spin-phonon coupling parameter is defined as $\Gamma_{ij} = \frac{\partial J_{ij}}{\partial u_\alpha}$. The modulating exchange coupling leads to the observation of magnon modes upto few picoseconds because the lattice vibrations occur in a time scale longer than the ultrafast demagnetization.

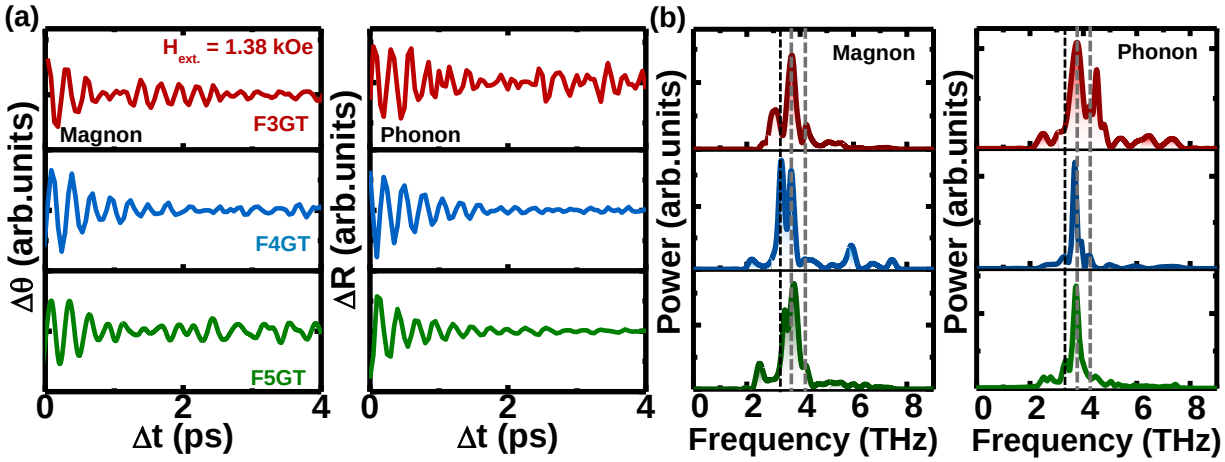


**Figure 7.4:** (a) Background subtracted Kerr rotation and reflectivity change indicating the coherent magnon and phonon dynamics respectively detected for three different samples at a magnetic field of $H_{ext}$ = 1.38 kOe. (b) Fast Fourier transform (FFT) power spectra corresponding to the time-resolved Kerr rotation and reflectivity, respectively. The peaks indicate the frequency of the excited magnon and phonon modes. The dashed lines correspond the phonon peaks detected in Raman measurement.

**Microscopic Three Temperature Model (M3TM):** The ultrafast demagnetization is well described by the extension of two temperature model in microscopic level, the M3TM proposed by Koopman et al. [326] for magnetically ordered systems. We use this model as it has been rigorously used since last two decades to quantitatively reproduce the ultrafast demagnetization process in a large number of ferromagnetic materials. This model describes the loss of magnetic order of a system upon ultrashort laser excitation based on Elliot-Yafet type spin-flip scattering events. During this scattering event, one spin flips and the associated angular momentum is transferred to the lattice. In particular, this model allows transfer of energy and angular momentum under thermal equilibrium between electron and lattice. The electrons are first excited by the impulsive laser beam above Fermi level creating non-equilibrium in the system. The electron sub-system transiently acquires an elevated temperature via electron-electron interaction. Again, an electronic state near the Fermi level is a mixture of spin-up and spin-down states caused by spin-orbit coupling. Therefore, at this stage the electron's spin flips leading to the reduction of spin ordering within few femtoseconds resulting demagnetization of the material. After attaining internal equilibrium, the electron sub-system quickly cools down to establish equilibrium with the lattice. This initiates remagnetization of the system through electron-lattice

relaxation. This proposed model involves the following equations describing the temperature evolution of the electron and lattice subsystems at thermal equilibrium.

$$C_e(T_e)\frac{dT_e}{dt} = -G_{el}(T_e - T_l) + P(t) \quad \ldots 7.1$$

$$C_l(T_l)\frac{dT_l}{dt} = -G_{el}(T_l - T_e) \quad \ldots 7.2$$

The rate of change of spin angular momentum is expressed in terms of the normalized magnetization as follows,

$$\frac{dm}{dt} = Rm\frac{T_l}{T_c}\left[1 - mcoth\left(m\frac{T_c}{T_e}\right)\right] \quad \ldots 7.3$$

$$R = \frac{\alpha_{sf} G_{el} k_B T_c^2 V_{at}}{\left(\frac{\mu_{at}}{\mu_B}\right) E_D^2}$$

Here, $T_e$ and $T_l$ are electron and lattice(phonon) temperature, $C_e$ and $C_l$ are specific heat of electron and lattice, $G_{el}$ is the macroscopic coupling constant between electron and lattice subsystems, $P(t)$ represents the Gaussian laser pulse and $m$ is the normalized magnetization. The demagnetization rate is understood from the material dependent parameter $R$. In the expression of $R$, $V_{at}$ is the atomic volume and $k_B$ is the Boltzmann constant, $\mu_{at}$ is the atomic magnetic moment, $\mu_B$ is Bohr magneton, $E_d$ is the Debye energy, and $\alpha_{sf}$ is the probability of spin-flip.

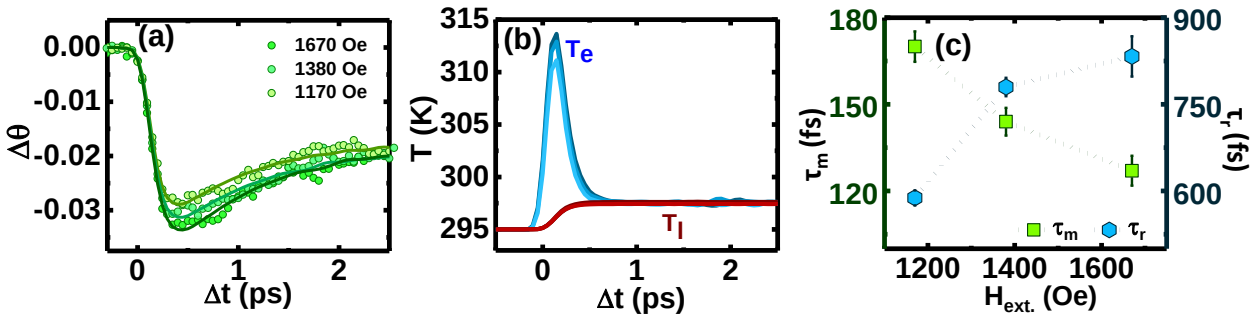


**Figure 7.5:** (a) The ultrafast demagnetization traces for $Fe_5GeTe_2$. The symbols represent the experimental data points and the solid lines are the corresponding fit to phenomenological three temperature model (3TM). (b) Temporal evolution of electron and lattice temperature calculated from M3TM at three different values of $H_{ext}$. (c) The characteristic times of demagnetization dynamics extracted from fitting with 3TM as a function of $H_{ext}$.

Figure 7.5(a) displays the normalized Kerr rotation data for F5GT considered for temporal magnetization simulations to extract $\alpha_{sf}$ and $G_{el}$ as the output parameters. The extracted spin-flip probability possesses a remarkably high value of 0.323±0.04 which increases to 0.36 at a field strength $H_{ext}$ = 1.67 kOe. This large spin-flip probability is discernible in the faster demagnetization process. This value is the maximum value reported so far for any 2D vdW magnet. The electron-lattice coupling parameter $G_{el}$ also shows relatively high value of 4.59 x $10^{18}$ $Js^{-1}m^{-3}K^{-1}$ ensuring the *type-I* fast relaxation of the dynamic magnetization. Furthermore, the electron and lattice temperatures are calculated solving the coupled eqns. (7.1) and (7.2) as shown in Figure 7.5(b). We observe a sharp rise in the electron temperature, $T_e$

which varies slightly with the application of an external magnetic field. The lattice temperature, $T_l$ starts to follow the profile of $T_e$ in a delayed time and attains the maximum value when $T_e$ drops down to almost 300 K. $T_l$ retains almost invariant nature with variation of $H_{ext}$. Further, the characteristic time constants of the demagnetization and remagnetization dynamics are determined by fitting the Kerr signal with a phenomenological expression derived from the three temperature model (3TM) [270] (Figure 7.5(c)). The extracted $\tau_m$ ranges in between 127-170 fs which is considered as the characteristics of very fast demagnetization process. We notice that demagnetization is faster at the maximum field which is consistent with the highest $\alpha_{sf}$ value at that field. A gradual increment in $\tau_r$ is noticed with increasing $H_{ext}$ which indicates the electron-phonon relaxation becomes slower. The obtained value of $\tau_r$ is similar to what generally found in typical transition metal ferromagnets. To analyze the demagnetization data we choose only F5GT which exhibits spontaneous magnetization near room temperature.

**Precessional Dynamics at Nanosecond Time Scale:** Precessional dynamics is detected in nanosecond time scale before complete equilibrium is restored in the system. During the whole experiment, the probe fluence is kept fixed at 2 mJ/cm$^2$, well below the spin-wave excitation fluence. Time resolved data is recorded with 10 ps temporal resolution for different values of $H_{ext}$. This field is applied at a tilt, $\theta_H \sim 75°$ with the sample normal to provide the necessary demagnetizing field. The high intense laser pulse triggers a rapid change in the demagnetizing field and hence in the effective field around which the magnetization precesses. Figure 7.6(a) shows the time resolved magnetization precession for three different samples after eliminating the exponential background. The residual part is then Fourier transformed to extract the SW frequencies (Figure 7.6(b)). Each sample shows three major field-dependent SW modes ($\alpha_x$, $\beta_x$, $\gamma_x$) with GHz frequency as plotted in Figure 7.6(c). The field dependence trend is quite similar to other ferromagnetic systems. Further, observation of high frequency SW modes in such a field regime is quite unusual compared to other ferromagnetic systems. We attribute this feature to the presence of significant anisotropy, which most probably has a magnetocrystalline origin in these vdW crystals. Again from the FFT spectra, we see that the lower frequency mode is present with relatively higher intensity than other two high frequency modes. This low frequency mode is presumably the excited uniform mode of the system associated with coherent precession of adjacent spins. The high frequency modes are most likely the incoherent modes with non-zero wave-vector. These modes are mainly restricted within the volume of the sample forming standing wave along the thickness. In a submicron thick layered crystal, the pump laser field transfers energy inhomogeneously along the thickness. This inhomogeneous energy distribution eventually causes incoherent phase distribution among the spins resulting standing spin-wave. These spin-waves are controlled by the strong interlayer exchange coupling beyond weak vdW forces in such layered ferromagnetic systems. Due to a limited penetration depth only a small fraction of this bulk mode is probed giving a small peak in the FFT spectra. For a more clear understanding of the nature of the SWs,

we fit the field-dependent frequency using the following equation derived from minimization of the free energy [330,331].

$$f = \frac{\gamma}{2\pi}\sqrt{\left(H_{ext}\cos(\theta_H - \theta_M) - \left(4\pi M_{eff} - \frac{2A_{ex}}{M_s}q_\perp^2\right)\cos^2\theta_M\right)\left(H_{ext}\frac{\sin\theta_H}{\sin\theta_M} - \frac{2A_{ex}}{M_s}q_\perp^2\right)} \quad \ldots 7.4$$

where, $\gamma$ is the gyromagnetic ratio given in terms of Lande $g$ factor, Bohr magnetron $\mu_B$ and Plank's constant as $\gamma = g\frac{\mu_B}{\hbar}$, $4\pi M_{\text{eff}} = 4\pi M_s - 2K/M_s$ is the effective magnetization, $K$ is out-of-plane anisotropy coefficient, $M_s$ is the saturation magnetization, $A_{ex}$ is the exchange coefficient and $q_\perp = \frac{n\pi}{d}$ represents the wave-vector associated with the standing SWs. The in-plane anisotropy is neglected here. The uniform Kittel mode is characterized by $n = 0$. The field dependent data is fitted with this eqn. (7.4) and spectroscopic $g$ factor and $K$ are estimated as fitting parameters. The extracted parameters from the $n = 0$, i.e., Kittel mode, is subsequently used to fit the field dependence of higher order modes ($n = 1, 2$).

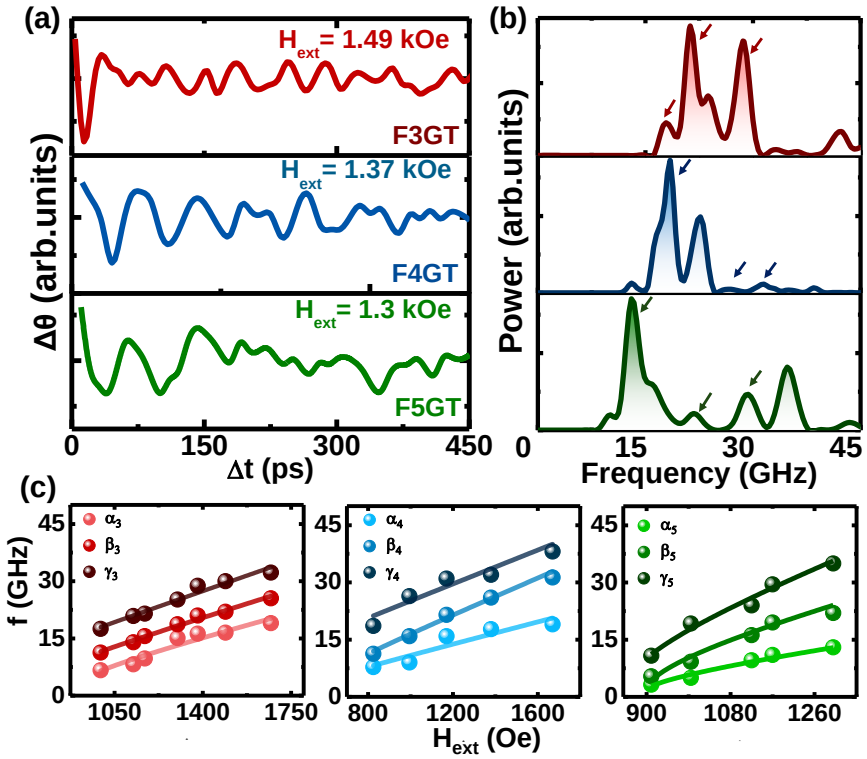


**Figure 7.6:** (a) Time-resolved Kerr rotation data at nanosecond time scale representing the laser induced precessional magnetization dynamics. (b) FFT power spectra corresponding to the time-resolved Kerr rotation. The arrows indicate detected magnon modes. (c) The magnetic field dependence of magnon frequency. The solid line represents associated theoretical fits.

The extracted parameters are displayed in the following table:

| Sample | g | K (Merg/cc) | Ms (emu/cc) |
|---|---|---|---|
| F3GT | 2.34 | 2.004 | 577 |
| F4GT | 2.38 | 2.009 | 570 |
| F5GT | 2.27 | 2.000 | 597 |

Here, the $M_s$ values are considered in a reasonable range giving the best fit to the data. The deviation from 2 in the $g$ factor clearly indicates the contribution of orbital moment in total magnetic moment of the system in these set of 2D vdW crystals. This orbital moment arises from the unquenched orbital angular momentum which also causes significant spin-orbit coupling and hence strong anisotropy in the system. The origin of spin-orbit coupling is attributed to the profound overlap of Fe-d orbitals with the neighbouring Te-p orbitals. However, a quantitative detailed analysis of the orbital contribution can be obtained from direct experiment, particularly from x-ray magnetic circular dichroism (XMCD) measurement.

In the present study, we infer that the appearance of magnetization dynamics in samples having $T_C$ below room temperature is a direct manifestation of laser induced ferromagnetic state at room temperature. Ultrafast laser induced magnetization was first understood in inverse Faraday effect [307], where the polarized electric field changes the dielectric tensor of the material in presence of a dc magnetic field and induces magnetization. In 2020, Liu et al. [97] demonstrated experimental evidence of layer dependent long range ferromagnetic order achieved by ultrafast laser in F3GT compound. They demonstrated that a large number of electrons can be injected above Fermi level by a pulse of 3.1 eV photons leading to a down shift of the Fermi level. This shift for spin-up electrons is towards higher density of states while for spin-down electrons the density of states reduces at the shifted Fermi level. This difference in density of states satisfies the Stoner criteria to sustain ferromagnetism which persist over picosecond to nanosecond range as observed in their experimental results. They predicted that the exchange interaction as well as $T_C$ is enhanced under the experimental conditions. In our pump-probe experiment, the observation of sub nanosecond precessional trace in the FxGT samples is an indication of such optically regulated ferromagnetic state for a prolonged time. The basic Heisenberg Hamiltonian in mean field approximation is written as $H = \sum_{i,j} J_{ij} S_i \cdot S_j + \sum_i A\,(S_i)^2$, where $S_{i/j}$ is the spin operator at site $i/j$, $A$ is the magnetocrystalline anisotropy. The Curie temperature is directly proportional to the exchange interaction according to the relation, $T_C = \frac{2S(S+1)}{3K_B}\left(\frac{1}{n}\sum_{i\neq j} J_{ij} + A\right)$. So, an increment in the exchange interaction can rise $T_C$ above the room temperature and initiate precessional dynamics under bias field application. Although, we lack theoretical evidence, we still argue that the electric field of the ultrafast pump laser of photon energy 3.1 eV can modify the electronic states of the material by excited carrier injection above Fermi level. The spin-dependent energy band near the Fermi level in FxGT are dominated by Fe 3d orbitals with hybridization with Ge p and Te p orbitals. Due to impulsive change in carrier density, electron redistribution occurs leading an enhancement of the spin-dependent density of states at Fermi level and increase in the spin-spin correlation strength, i.e., exchange interaction ($J_{ij}$). Eventually, magnetization emerges which again increases on application of the external magnetic field. Also, the observation of coherent magnon modes implies that long range magnetic ordering is established in FxGT at room temperature. However, quantification and determination of the enhanced $J_{ij}$ or $T_C$ by laser pulse was not possible from the experimental data. Nevertheless, we try to give a clear idea of dynamic behavior of the important quasiparticles spin and phonon, though the analysis of some

requisite spintronic parameters like magnetic damping remained elusive in our study. The noisy signal restricts us to evaluate the parameters, however our findings may show future prospects of both theoretical and experimental study of spin dynamics including all important parameters. Therefore, in order to explore the technological aspects of spin dynamics in FxGT system, further theoretical and experimental research is needed.

## 7.4 Conclusions

In conclusion, we have investigated the ultrafast demagnetization and precessional magnetization of $Fe_xGeTe_2$ at room temperature. We have employed TR-MOKE to excite and detect the dynamic response. A *type-I* single step demagnetization is noticed accompanied by THz magnon generation during the relaxation process. We are also able to excite optical phonon modes and evidenced direct spin-phonon coupling. Ferromagnetic resonance mode along with exchange controlled perpendicular standing spin-wave are also probed during the nanosecond dynamics. Based on this emergence of spin dynamics similar to well-studied ferromagnetic system, we conclude that the samples hold ferromagnetic state at room temperature which is possibly a consequence of ultrafast laser tuned exchange interaction. Nevertheless, this study invokes further investigation of the fundamental physical phenomena in 2D materials and reveals their promising aspects to incorporate in spintronic devices.

# Tunable Short-Wavelength Spin-Wave Excitation and Localization in Nanoscale Domain Structures Chapter 8

## 8.1 Introduction

Spin-wave (SW) or magnon has shown great potential of encoding and transferring information at ultrahigh processing speed with ultralow power consumption. SWs can attain ultrashort wavelength of few nm having sub GHz-THz frequency, conducive for nanoscale circuit design in microwave applications. Therefore, various approaches have been applied to efficiently excite SWs and actively manipulate its properties at nanoscale, based on which various multifunctional device prototypes have been proposed [62,219,332]. In this context, chiral spin textures like vortex, skyrmion or the non-uniform domain walls (DWs) are promising to generate such short-wavelength SWs [333–338]. Apart from SW emission, the anisotropic spin texture within a DW is capable to interact with propagating SW via its inhomogeneous internal magnetic field. SW can fully or partially transmit through DW or restrict itself within the domain reflected [339,340] by the DWs depending on DW width and wavelength. Transmission [341,342] through a DW can lead to phase modulation or route change of SW. Besides, the potential well bound by DWs due to local decrement of energy can trap SW of specific frequency within the domain leading to wave quantization [343]. Thereby, DWs has shown great prospects as reprogrammable waveguide for SW propagation [344,345] with high amplitude and reservoir of SWs dominated by dipole-exchange interaction [346]. In a reverse scenario, DW character can be modulated by SWs driving the DWs into motion [347,348] or resulting resonant excitation [349]. Several external parameters like Oersted field [350], voltage [351], charge current [352], spin-current [353,354], laser pulse [355,356], magnetic field [357,358] can efficiently tune the domain configurations including DW width, speed, chirality [359,360] and hence the interplay with SW dynamics. Such reprogrammable domain excitation followed by controllable SW emission in nanowire [354,361] with straight or curved geometry has shown profound potential of logic operation and SW computation. Therefore, guiding SWs in assistance with reconfigurable domain geometry is desirable for miniaturized device applications. However, the creation and detection of such complex spin-textures and control over those at nanoscale is a difficult task. In this regard, magnetic systems possessing high perpendicular magnetic anisotropy (PMA), dynamic dipolar coupling, antiferromagnetic coupling, interfacial Dzyalosinski-Moria interaction (iDMI) [347,359,362–364] have served as favorable platforms to exquisitely engineer complex spin-textures and adding engrossing feature like nonreciprocity [362] in SW propagation.

In the present study, confined domains and tunable DWs have been created in a CoPd multilayer having PMA by locally manipulating the magnetic anisotropy and creating closure domains of nanometer width. This anisotropy reduction can be done through post growth ion bombardment [365]. Here, the domains are fabricated periodically in triangular shaped closed nanochannels preserved by three narrow in-plane 60° head-to-head, head-to-tail or tail-to tail DWs for SW routing. We have excited such spin-texture and microspin domain structure using femtosecond laser pulses in presence of external magnetic field and

examined the tenability of the SW by varying the field direction in the plane of the sample. The experiment has been performed using time-resolved magneto optical Kerr effect (TR-MOKE) technique and the results have been supported by micromagnetic simulations. We demonstrate excitation, tunneling and localization of very short wavelength SWs dominated by dipole-exchange interaction. The external field is evidenced to have precise control over the domain orientation as well as the interplay between SWs and the domains. Further, reversible switching of symmetrical and asymmetrical SWs between neighbouring domains are obtained by varying the azimuthal angle of bias magnetic field. The experimental realization of reconfigurable SW dynamics in reprogrammable domains paves the way to design device architecture aiming towards SW computing.

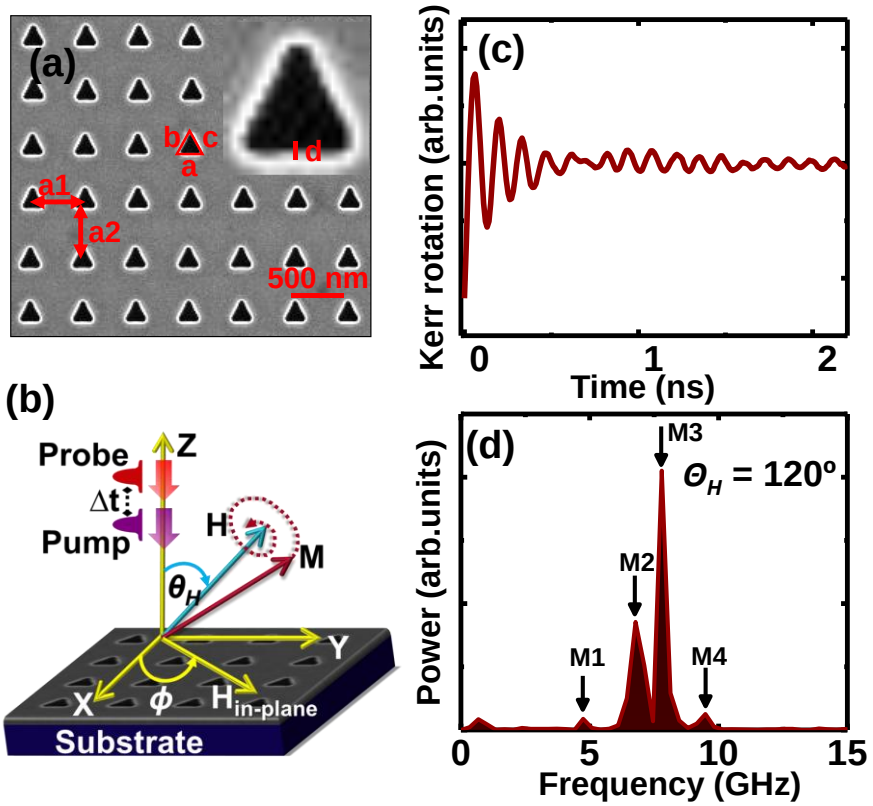


**Figure 8.1:** (a) The SEM image of the antidot lattice. (b) Schematic of the experimental geometry used in TR-MOKE microscopy technique. (c) Background subtracted time-resolved Kerr rotation data at $\phi$ = 120° of the bias magnetic field for $H$ = 2.3 kOe. (d) The corresponding FFT power spectrum showing the SW modes as indicated by the arrows.

## 8.2 Methods

**Sample Fabrication and Characterization:** To create the nanoscale domain structure at first the multilayer stack of [Co(0.75 nm)/Pd(0.9 nm)]$_8$ was deposited on Si/SiO$_2$ substrate by dc magnetron sputtering which exhibits strong PMA. The deposition was done in confocal sputter up geometry at a base pressure of 2 ×10$^{-8}$ millibar and Ar pressure of 4 $\mu$bar. Then periodic pattern in shape of equilateral triangle, i.e., the antidot lattice (ADL) was written (milled out) in a square lattice geometry on the

multilayer using focused ion beam (FIB) milling using liquid $Ga^+$ ions. The spatial resolution of the ion beam was ~10 nm at 30 kV voltage and 20 pA current. The $Ga^+$ ions are known to affect the PMA at the periphery of the holes within ~ 20 nm wide region. The PMA is reduced or destroyed in this nanometric area and the magnetic properties deviate largely from the unaffected PMA multilayer. In this region, named as shell, magnetization lies in the plane of the sample due to absence of PMA and domains are formed following the shape of triangle. The nominal value of the side of triangle (s) is 190 nm as extracted from the scanning electron microscopy (SEM) image shown in Figure 8.1(a). The lattice constants slightly differs along the X ($a_1$ = 490 nm) and Y ($a_2$ = 450 nm) axes as shown in the SEM image. The whole pattern is created over an area of 8 × 8 $\mu m^2$ in which the shells cover a very small fraction of that area.

**Time-Resolved Kerr Effect Experiment:** We have employed the custom built all-optical TR-MOKE microscope (details can be found in Chapter 3) to measure the magnetization dynamics in polar MOKE geometry. In this geometry, only the dynamics of $m_z$ (z component of dynamic magnetization) is measured as the change in Kerr rotation. Throughout the whole experiment, the probe fluence was kept fixed at ~ 2 mJ/cm$^2$ and the pump fluence was fixed at ~ 15 mJ/cm$^2$. A bias magnetic field ($H$) was applied at a tilt angle, $\theta_H$ ~ 15° with the surface normal of the sample during the measurement as depicted in Figure 8.1(b). For this particular $\theta_H$, the in-plane field angle i.e., the azimuthal angle ($\phi$) was varied keeping $H$ fixed. The dynamics of the magnetization precession obtained at those measurement conditions allows direct access to study the magnetic anisotropy through precessional frequency of different dynamic modes.

**Micromagnetic simulation:** To interpret the experimental observations, we have performed micromagnetic simulations using Mumax3. For simulations, the multilayer (ML) structure is considered as a single magnetic material with effective material parameters: saturation magnetization $M_S$ = 0.81 × $10^6$ A/m, gyromagnetic ratio, $\gamma$ = 187 GHz/T, PMA $K_u$ = 4.5 × $10^5$ J/m$^3$, exchange constant $A$ = 1.3 × $10^{-11}$ J/m and damping parameter, $\alpha$ = 0.01. The material parameters were derived from experimental data as in reference [366]. Since, the magnetic properties of the shell could not be determined experimentally, we assigned the shell parameters as $M_S$ = 0.3 × $10^6$ A/m and $A$ = 0.2 × $10^{-11}$ J/m which shows best agreement with the experimental results. The magnetic anisotropy within the shell was considered to be zero. The simulations have been performed for 3 × 3 unit cells close to the experimentally probed area. Also, two-dimensional periodic boundary conditions were applied along the X and Y axes. The discretization of the whole structure was done using finite difference cell size of 1 × 1 × 4.4 nm$^3$. At first, the ground state magnetization was obtained at each angle of $H$ by relaxing the initial magnetization of each cell. To do so, at zero magnetic field, the matrix was set to a random magnetization while the shell magnetization was stabilized into head-to-head, tail-to-tail or head-to-tail domain wall state. Subsequently, SWs were excited by application of a global out-of-plane magnetic field pulse in the form of a step function of magnitude 20 Oe and duration of 40 ps. The precessional dynamics was set to run for a time window of 5 ns after releasing the excitation field. The time dependent $m_z$ value is subtracted

from its ground state value $m_z(0)$ for next step of analysis. The SW frequency spectra is obtained by performing fast Fourier transform (FFT) on the $m_z(t)$ component.

## 8.3 Results and Discussions

The results of TRMOKE measurement and micromagnetic simulations are discussed in following.

The angular dependence of SWs are measured for $0° \leq \phi \leq 180°$ at an interval of 15° at $H$ = 2.3 kOe. The frequency of optically excited modes are extracted by analyzing the FFT power spectra of the experimental data. One representative time domain Kerr rotation data and corresponding FFT are shown in Figure 8.1(c) and (d). At each value of $\phi$, rich SW spectra consisting of four modes with different peak powers is observed, out of which the lowest frequency shows the lowest power. The modes are named as M1, M2, M3 and M4 as per increasing order in frequency. The frequency order of the modes is maintained throughout the entire angular range from $0° \leq \phi \leq 180°$. However, the relative power of the modes vary with angle. The angular variation of the precessional frequencies of M1, M2, M3 and M4 are shown as a function of $\phi$ in Figure 8.2(a). The lowest frequency mode, M1 displays a strong anisotropic character, while M2 exhibits a relatively weaker anisotropy. In M1, six-fold-like symmetry is present over the whole angular range from 0 to 180° with an opposite phase of the anisotropy profile of M2. The anisotropy gradually vanishes when approaching the high frequency modes M3 and M4. Thus, the results indicate the presence of anisotropic factor in the studied system where different modes are affected differently.

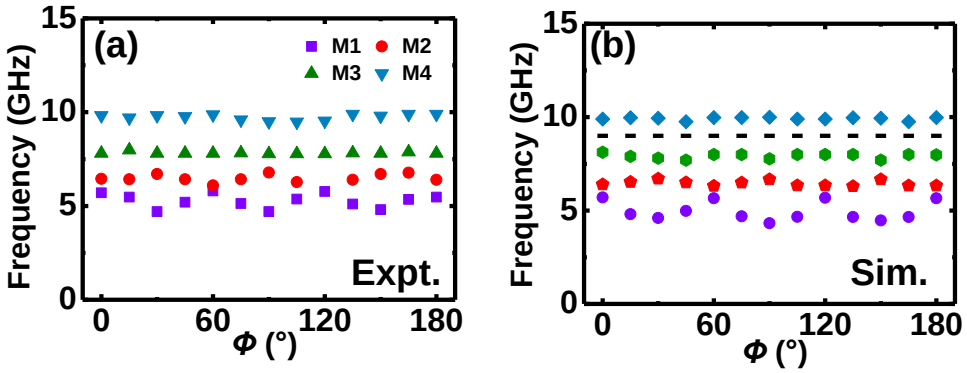


**Figure 8.2:** Angular dispersion of spin-wave modes obtained from (a) experiment and (b) simulation for $0° \leq \phi \leq 180°$ at $H$ = 2.3 kOe.

To understand the experimental results, micromagnetic simulations are performed replicating the experimental conditions. The simulated angular dispersion is presented in Figure 8.2(b). The simulated results reproduce the experimental results with excitation of four SW modes at each value of $\phi$. However, the anisotropy of the three lower frequency modes are significantly prominent having difference in the strength. Similar to the experiment, the highest frequency mode does not exhibit considerable anisotropy. The variation of the frequencies of M1, M2 and M3 with $\phi$ show a six-fold anisotropy, while the rotational anisotropy of the mode M2 is in anti-phase with the other two modes.

Angular-dependent SW frequency provides information mainly about the effective anisotropy strength which arises due to the competition between the in-plane configurational anisotropy and the strong out-of-plane anisotropy. Besides, the angular-dependent magnetization measurements show the positions of energy minimum at the given orientation of the sample with respect to the direction of the external magnetic field. The angular dispersions have clearly revealed significant evolution of the effective anisotropy. The easy axis of the six-fold magnetic symmetry is along three arms of the triangular shell. The six-fold symmetry is believed to originate from the intrinsic shape anisotropy of shell's triangular structure. It is suggested that the in-plane demagnetizing field modulation does not influence the rotational symmetry of the unit cell due to the lack of sufficient dipolar coupling by the uncompensated magnetic charges of individual shells. This result suggests that the anisotropy caused by lattice symmetry has been covered up by the shape anisotropy for PMA antidots with edge modulation. However, there is a slight deviation in the simulated results from the experiment in terms of the relative mode power, peak frequencies and the amplitude of anisotropic contribution. These deviations plausibly comes from the simulated structure. In simulation ideal triangular shape has been considered due to difficulty of exact incorporation of the rounded corner at the vertices of the real triangle. Further, the actual value of the shell width cannot be determined, as well as the magnetic properties of the shell region.

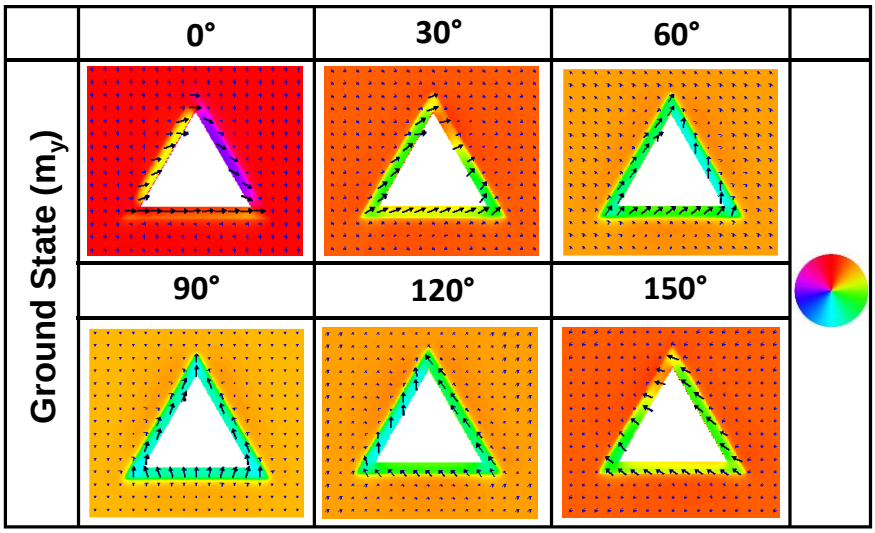


**Figure 8.3:** Simulated static magnetic configurations at different $\phi$ values. Here only y-component of magnetization has been displayed.

To take a microscopic insight of the dynamic features of the SW modes, the simulated static spin configurations are investigated because the static magnetization states play crucial role to build the SW character. Further, the spatial distribution of power and phase associated to these modes are calculated using Dotmag. The magnetic ground state is profoundly reconfigured within the azimuthal plane by varying $\phi$. It is observed that the magnetization within the matrix of the ADL is uniformly distributed and aligned along the field direction. Variation of $\phi$ cannot influence this magnetic homogeneity of the

matrix except the realignment of magnetization. Therefore, the observed variation of SW frequencies with $\phi$ comes from small in-plane component, while the out-of-plane component of the magnetization remains intact holding a high value due to strong PMA. The lack of the PMA in the shells enhances the in-plane shell demagnetizing field to distribute the magnetization into an in-plane domain structure around the triangular shaped holes. Due to dominance of the shape anisotropy in a triangle, the magnetization distribution becomes strongly inhomogeneous inside the narrow shell. Such nonuniform distribution of spins results multiple distinct SW spectra upon adequate excitation. Primarily, the magnetization in the three different arms of the triangle is oriented in three different directions forming three domains separated by three DWs located at the three vertices. The three DWs assume either of the head-to-head, head-to-tail or tail-to-tail configuration at an angle of 60°. Variation of $\phi$ leads to alter these configurations either symmetrically or asymmetrically with respect to the magnetic field direction by changing the direction of the macrospin of the three domains. However, DW positions and the relative angle of 60° remain invariant throughout the whole azimuthal rotation.

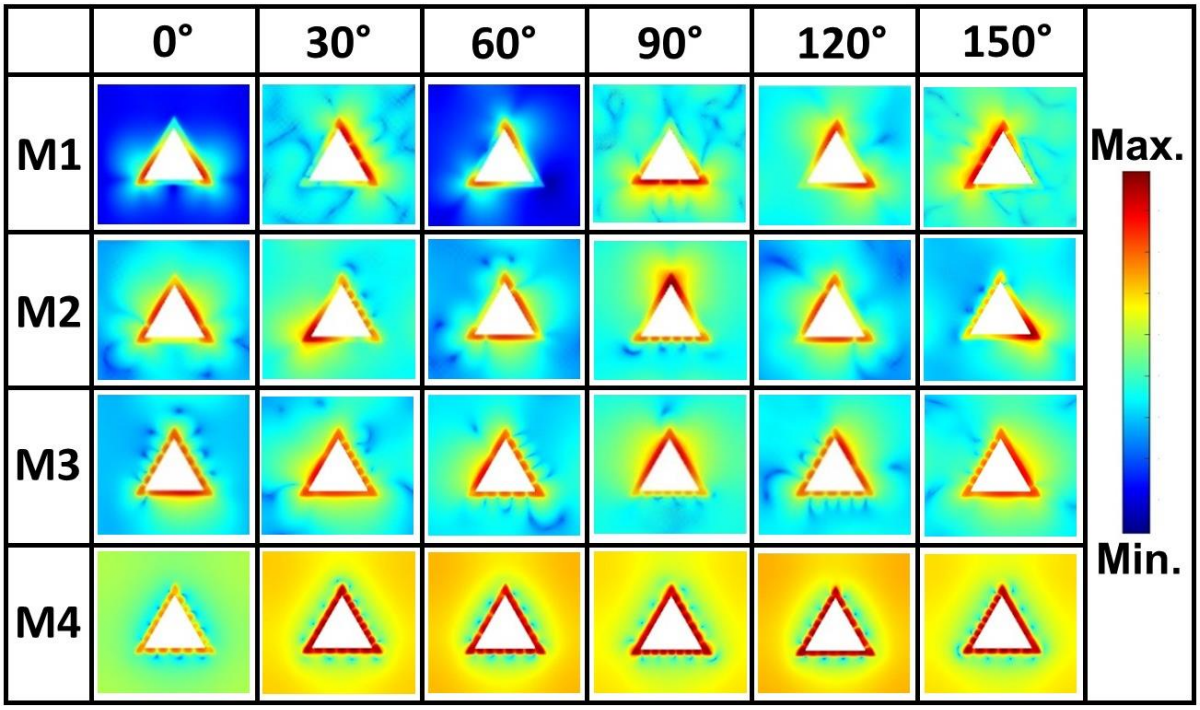


**Figure 8.4:** Simulated power profiles of the SW modes around a single antidot at different $\phi$ values.

To help further understanding, Figures 8.4 and 8.5 describe the spatial positions of all four experimentally observed SW modes within a unit cell. We observe that within the shell-domains of width 20 nm and length 190 nm, very short wavelength SWs are excited and mostly confined. The wavelength of such SW is simply defined as $\lambda = 2L$ where $L$ is the length of the arm of the triangular shell, which is 190 nm here. As displayed in the power-phase profile, each mode has different characteristics which drastically changes with $\phi$. The rotation of in-plane field angle breaks the symmetry of the magnetic structure which results asymmetrically excited SWs within the nanochannel. However, as displayed in

the spatial map, mode M1 is directly related to the symmetry of the structure. This mode is excited at the DWs for $\phi$ = 0°, 60°, 120°, i.e., when field is applied along the arms and the mirror symmetry axis is perpendicular to it. At these angles, M1 is symmetrically and partially distributed along the off-field arms. When field is applied along the mirror symmetry axis, i.e., $\phi$ = 30°, 90°, 150°, this mode is excited within the domain located perpendicular to the field direction, i.e., in Damon-Eshbach (DE) geometry.

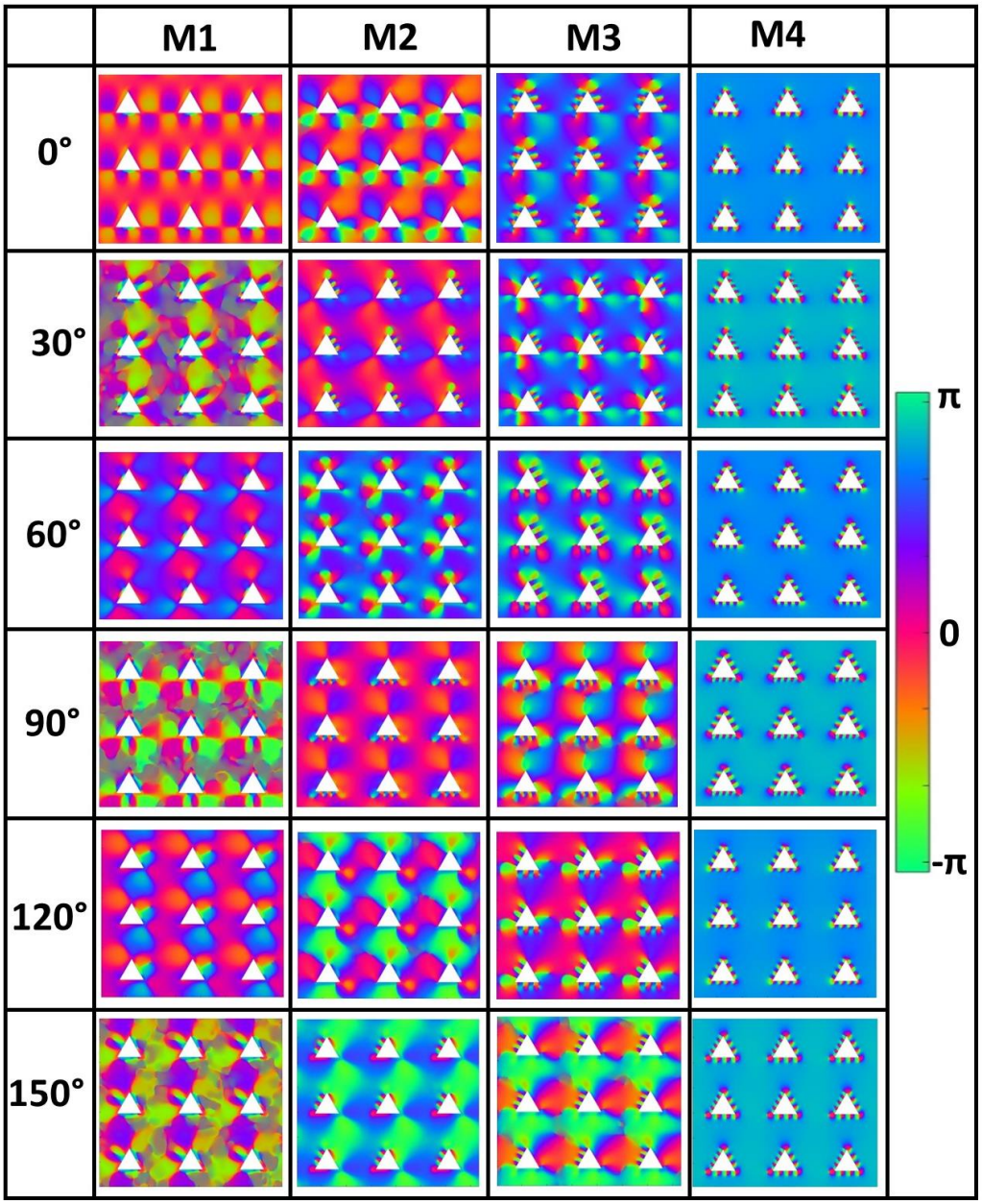


**Figure 8.5:** Simulated phase profiles of the SW modes within the antidot lattice at different $\phi$ values.

At these angles the mode forms standing wave inside the domain with quantization axis lies along the field direction. It seems that this mode is strongly reflected by the in-plane narrow DW but having a finite transmission into the matrix through the broad edge of the DW. Mode M2 and M3 are also excited

and confined within the shell-domain covering the entire shell area. Bound by the DW, these modes also form standing wave in the domains having different quantization numbers or more precisely different wavelengths at different domains. Interestingly, with variation of $\phi$, there is sequential switching of the wavelengths from one domain to another at a fixed interval of $\phi$. Thereby, the field angle plays the decisive role to determine the SWs' positions. In parallel, M2 and M3 are asymmetrically distributed within the shell. M2 shows a visible transmission through the DWs along the field direction at $\phi$ = 30°, 90°, 150° while M3 is uniformly distributed around those DWs within the associated domains. For $\phi$ = 0°, 60°, 120°, M2 is mostly excited within the off-field domains while M3 shows quantization along those domains in conjunction with almost uniform distribution in the domain along the filed direction. The highest frequency mode M4 is another spatially degenerate mode which exists both in the shell and in the matrix. This mode seems to be the bulk uniform mode of the triangular antidot. Still, there is a strong contrast in the frequency of this uniform mode excited within a purely PMA ADL. In case of the PMA lattice without a shell formation, the frequency of this mode is 9 GHz (shown by the dotted line in Figure 8.2(b)). To this regard, the modification of the anisotropy at the edges of the ADL (i.e. shell formation) results increase in the frequency to a higher value of ~10 GHz. Interestingly, the shell also becomes resonant with the same frequency. Within the shell, this mode is highly quantized mode, an azimuthal SW trapped by the broad edge of the domains and unable to tunnel through the boundary except from the vertices. Further interesting feature of M4 is its $\phi$ independency i.e. its quantization is not affected by $\phi$. The behavior of the modes are quite different from a PMA ADL. The PMA lattice in general lack the in-plane demagnetizing field which is accounted for controlling the SW dynamics of an ADL with in-plane anisotropy.

## 8.4 Conclusions

We have developed narrow domains at the edges of ADLs having triangular shape made of [Co(0.75 nm)/Pd(0.9 nm)]$_8$ multilayer and investigated the SW excitations using TR-MOKE microscope. The experimental observations are aided with rigorous micromagnetic simulations. In such a high PMA lattice, a slight incorporation of in-plane anisotropy or destruction of out-of-plane anisotropy near the edges leads to domain formation. Short wavelength SWs can be excited and confined in the domains with different quantization number. In addition, tunneling SW modes are observed with the amplitude concentrated in the domain walls at the corners of the antidot. Furthermore, the in-plane direction of the domain magnetization changes its orientation sharply with the bias field direction. As a result, a strong modification arises in the frequency and spatial position of localized SWs. The spatial profiles also confirm that multiple SWs of different wavelengths but same frequency can be excited just by breaking the symmetry by the magnetic field direction and also their location can be allotted by precisely choosing the field directions. Nevertheless, the generation of short wavelength localized SW in such a narrow width and their control by the field orientation can be useful for SW-based computing.

# Direct Evidence of Ultrafast Laser Induced Magnetoelastic Interaction in $Ni_{80}Fe_{20}$ Nanomagnets Chapter 9

## 9.1 Introduction

Spin-wave (SW) or magnon shows immense potential for next generation computing with capability of data storage, process and transport. Therefore, exploring new routes for energy-efficient manipulation and control of SW dynamics are paramount for fundamental understanding and future applications. Strain is one such pathway to control the spin degrees of freedom by the mechanical degrees of freedom of a material via Villari effect or inverse magnetostriction [367]. During the last decade, static and dynamic strain or surface acoustic wave (SAW) has been harnessed for magnetization switching [368,369], domain wall rotation [370,371], parametric amplification of SW [372] and generation of spin current through spin pumping [373] at a cost of ultralow energy consumption. As a matter of fact, the energy dissipation of the strain induced domain wall motion is several orders of magnitudes smaller as compared to the current induced domain wall motion. Furthermore, due to slower damping of acoustic wave than SW of equal frequency, it can reduce the propagation loss of SW over millimeter distances [374]. Besides, SAW can resonantly intensify SW [375] and modulate its damping [376] compensating the energy dissipation during the spin precession. In a magnetostrictive material, it leads to generation of hybrid magnetoelastic mode [377,378] which follows distinct dynamic nature solely different from the original magnetic or acoustic wave .

Henceforth, magnetoelastic dynamics [378–383] has been extensively explored in continuous magnetic media like ultrathin films, multilayers, heterostructures of highly magnetostrictive materials in addition to fewer works on single or an array of nanomagnets [384–387]. It is known that nanomagnets are promising candidates for logic gate [388,389], transistor [390], spin torque nano-oscillator [391] or memory component. Recently, nanomagnet array heralds significant interest as the mainstay of reservoir computing in neural network [392,393]. Additionally, nanomagnet array hosts topological spin states [394], spin-ice states [395], complex spin textures [396,397] adorned with flexible dipolar coupling, and can open both magnonic [212] and phononic [398,399] band gap which can be facilely tuned by various external parameters. Strain can essentially modify the magnetic landscape via lattice deformation inducing modulation in these properties of a nanomagnet. Thereby, manipulation of magnon by SAW in nanomagnet array of different geometrical parameters is of great importance because of the dependency of SAW frequency upon those parameters. Moreover, the impact of SAW on magnetization is assessed by the coefficient of magnetostriction of the magnetic material. Therefore, materials with high magnetostriction are pertinent for acoustic regulation of magnetization. Here, it is noteworthy that magnetostriction gives rise to an additional anisotropy field which might be perplexing during a specific function of a spin-based device. In this essence, permalloy ($Ni_{80}Fe_{20}$; Py hereafter) exhibits highly suppressed magnetostriction coefficient [400–403]. Therefore, Py stands as one of the most preferred materials in data storage and memory devices.

Here, we delineate the acoustic actuation by femtosecond laser pulses in two-dimensional (2D) array of square shaped Py nanodots on a $Si/SiO_2$ substrate. In the present study, in association with intrinsic magnon modes of the nanodot arrays, we have observed magnon modes strongly synchronized with SAW resulted from resonant magnetoelastic coupling. Further, variation of the lattice constant and lattice symmetry of the periodic structure ensures the dependency of the coupling on the geometrical parameters. Primarily, the experimental results show three important aspects. (i) In a low magnetostrictive material like Py, laser can enhance magnetostriction by instantaneous thermal annealing, so when exploring their application potential, the magnetostriction cannot be disregarded. The presence of magnetoelastic coupling suggests that the magnetostrictive anisotropy can be impelled which might be undesirable in some cases. (ii) In a nanomagnet array the SAW modes are highly sensitive to the geometrical parameters and hence the magnetoelastic coupling can be tuned by the same. (iii) SAW can drive magnetization dynamics even at sufficiently low magnetic field creating hybrid magnetoelastic mode which can play pivotal role for energy efficient device applications using nanomagnet array.

## 9.2 Methods

**Sample Fabrication and Characterization:** The square-shaped nanodot arrays of $Ni_{80}Fe_{20}$ (Py) were fabricated over $10 \times 10$ $\mu m^2$ area on self-oxidized silicon (Si)(100) substrate using a combined process of electron-beam lithography (EBL) and electron-beam evaporation (EBV). The nanodots of width ($d$) 200 nm were arranged in an array of hexagonal lattice symmetry with varying lattice constants: a = 300 nm (S1), 350 nm (S2), 400 nm (S3) and in square symmetry of a = 350 nm (S4). Images of the nanostructures obtained from SEM are displayed in Figure 9.1(a)-(d). At first, the substrate was prepared for electron-beam lithography by coating a bilayer MMA/PMMA (methyl methacrylate/polymethyl methacrylate) resist on top. During EBL process, the beam current was 100 pA for a dose time of 1.0 μs. Next, on the resist patterned substrate 20 nm thick Py was deposited using electron-beam evaporation at $1.3 \times 10^{-7}$ Torr base pressure. Subsequently, 5 nm thick $Al_2O_3$ was deposited on top of Py to avoid possible degradation caused by impulsive laser exposure during pump-probe experiment. This was followed by a lift-off process of the resist layer. Finally, good quality polished surface was obtained for optical measurement by etching out the residual resist using oxygen plasma

**TR-MOKE Measurement:** The collective magnetization and elastic dynamics of the nanodots were measured by a home built all-optical TR-MOKE microscopy set-up. The pump-probe measurement is carried out in polar MOKE geometry. In this experiment, a high-value bias magnetic field ($H_{ext}$= 2.1 kOe) was first applied at a tilt angle ($\theta_H$ = 10°) with the plane of the sample for in-plane saturation of the magnetization, while the tilt provides a sufficient demagnetization field in the out-of-plane direction to ensure laser induced precessional dynamics. The magnitude of $H_{ext}$ was gradually reduced in steps of almost equal interval keeping the direction fixed along the x-axis. At each value of $H_{ext}$, the reflected probe beam was collected and detected by the OBD. During the course of experiment, the probe fluence was fixed at 2 $mJ/cm^2$ far below the pump fluence. In our experiment, SAW is generated due to the

periodic thermal expansion and contraction due to the non-uniform absorption of thermal energy produced by the high-intense optical pulses. The signature of SAW is observed in the reflectivity data as damped sinusoidal oscillation on an exponential background. Similar nature is detected in the Kerr rotation implying the damped precessional dynamics of magnetization. The exponential background caused by the rapid increase of temperature is eliminated to extract information from the pure time domain SAW and SW dynamics.

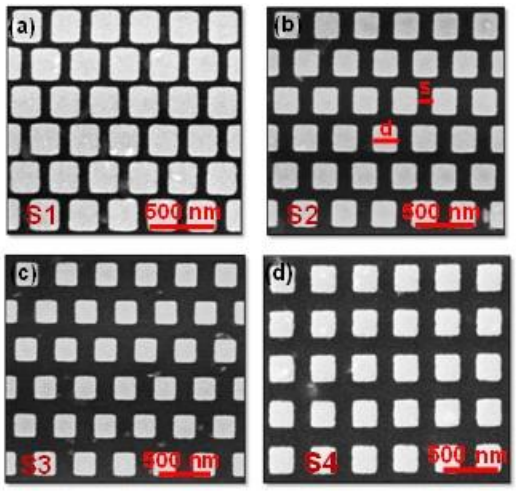


**Figure 9.1:** Scanning electron micrographs of $Ni_{80}Fe_{20}$ nanodots arranged in (a)-(c) hexagonal geometry with lattice constants 300 nm (S1), 350 nm (S2), 400 nm (S3), and (d) square geometry with lattice constant = 350 nm (S4).

**Numerical Model:** The dynamics of SAWs and SWs can be described by a continuous model based on the elastodynamic and Landau-Lifshitz equations, respectively. The conventional magnetostatic coupling between SAWs and SWs can be expressed phenomenologically as a nonzero free energy contribution:

$$F_{me} = \frac{1}{M_S^2} \sum_{i.j=\{x,y,z\}} \epsilon_{ij} M_i M_j \left[ b_1 \delta_{ij} + b_2 \left(1 - \delta_{ij}\right) \right] \quad \ldots 9.1$$

where $M_i$ are the components of magnetization vector, $\epsilon_{ij}$ are elements of strain tensor, and $b_1$, $b_2$ denote the magnetoelastic coupling constant. The coupling between the elastodynamic and Landau-Lifshitz equations is formally provided by additional contributions to dynamic effective field $\boldsymbol{h}_{me}$ and stress tensor $\boldsymbol{\sigma}_{me}$ being expressed by the functional derivatives of magnetoelastic free energy respect to magnetization and strain, respectively. The coupled Landau-Lifshitz and elastodynamic equations takes then the following forms.

$$\partial_t \boldsymbol{m} = -|\gamma|\mu_0 \left( \boldsymbol{M_0} \times (\boldsymbol{h} + \boldsymbol{h}_{me}) - \boldsymbol{H}_{eff} \times \boldsymbol{m} \right) \quad \ldots 9.2$$

$$\rho \partial_t^2 u_{x_i} = \partial_{x_k} \left( \sigma_{x_i,x_k} + \sigma_{me,x_i,x_k} \right) \quad \ldots 9.3$$

where $\boldsymbol{M}_0$ and $\boldsymbol{H}_{eff}$ are equilibrium component of magnetization and static component effective field ($M_0 \parallel H_{eff}$). The symbols $\boldsymbol{u}$ and $\boldsymbol{m}$ denote the displacement vector and dynamical component of magnetization, whereas $\boldsymbol{h}$ and $\boldsymbol{\sigma}$ stand for dynamic filed and stress tensor in the absence of magnetoelastic interactions. The parameter $\rho$, $\gamma$, $\mu_0$ are mass density, gyromagnetic ratio and

permeability of the vacuum, respectively. To solve linearized eqns. (9.2) and (9.3), we used Cartesian *x*-*y*-*x* for SAWs but the SWs are described in the coordinate system rotated around *z*-direction by the angle $\theta_H$, where the in-plane component of dynamic magnetization and field are perpendicular to the direction of applied field. Therefore, the magnetoelastic contribution to the effective field exhibits the mentioned anisotropy with respect to the magnetic field direction:

$$\mu_0 h_{me,\parallel} = 2b_2\left(\epsilon_{xz}\, cos\, \theta_H + \epsilon_{yz}\, sin\, \theta_H\right) \quad \ldots 9.4$$

$$\mu_0 h_{me,\perp} = b_1\left(\epsilon_{xx} - \epsilon_{yy}\right) sin\, 2\theta_H - 2b_2\epsilon_{xy}\, cos\, 2\theta_H \quad \ldots 9.5$$

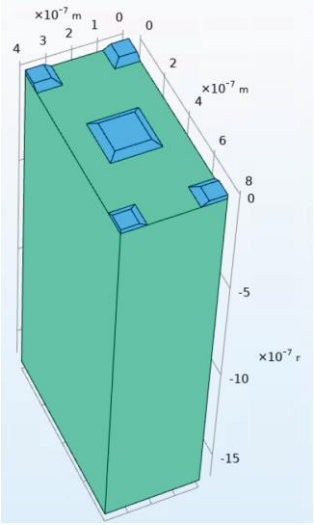


**Figure 9.2:** The geometry of the computational domain used in finite element method calculations of magneto elastic modes in hexagonal lattice of Py dots (blue regions) on Si/$SiO_2$ substrate.

We solve the linearized eqns. (9.2) and (9.3), assuming the harmonic dynamics of **m** and **u**, with a frequency ω, as an eigenvalue problem for Bloch modes of small $\boldsymbol{k}$ vector corresponding to the wavelength $\lambda$ = 1000 nm, equal to the diameter of the pump beam. The model was implemented in COMSOL Multiphysics which used the finite element method (FEM) for numerical computations. Figure 9.2 presents the computational domains for the hexagonal lattice of Py dots (blue regions) deposited on Si/$SiO_2$ substrate (green area). On the lateral boundaries of the domain, we applied the Bloch boundary conditions. For the remaining faces, we used the open boundary conditions. The height of the domain (i.e., size in to depth of substrate) was chosen large enough to account for the exponential decay of SAW in the substrate. In the considered system, there is a demagnetization field caused by the presence of the lateral surfaces of the dots, which depends on their inclination. We adjusted the inclination of these walls so that the numerical model reflected the real sample and the computed spin-wave spectrum was closest to the experimental one. For numerical calculations, we took the following values of the material parameters: $M_S$ = 0.75 × $10^6$ A/m, gyromagnetic ratio, $\gamma$ = 192 GHz/T, exchange constant $A$ = 1.2 × $10^{-11}$ J/m and magnetoelastic coefficient $b$ = 1.0 × $10^5$ J/$m^3$, and the dimensions obtained from static characterizations. We determined the eigen-frequencies of the hybrid magnonic-phononic modes depending on magnitude of external field applied in *x*-direction. The spatial profiles of **m** and **u** were

used to estimate the intensity of TR-MOKE signal for magnons and phonons. In addition, to extract the SAW of elastic volume mods, we numerically determined the localization of modes in the direction normal to the sample surface.

## 9.3 Results and Discussions

In the following, the experimental and calculated results are presented and discussed. Figure 9.3(a) displays the representative background subtracted time-resolved reflectivity data for S1, S2 and S3 at $H_{ext}$ = 1.75 kOe. SAW frequencies are extracted from the fast Fourier transformed (FFT) power spectra of the time-domain data as shown in Figure 9.3(b). In each sample, four distinct modes are detected within a frequency range of 5-20 GHz with varying intensities. These modes are named as R1, R2, R3 and R4. Among those, R2 is strongly dominating mode with comparatively higher intensity except in S1. Moreover, R1 and R2 are well separated from R3 and R4. Interestingly, the SAW frequencies systematically decrease with increasing lattice constant of the nanomagnet array. This feature indicates that the SAW generation is restricted by the geometrical parameters of the nanodot array.

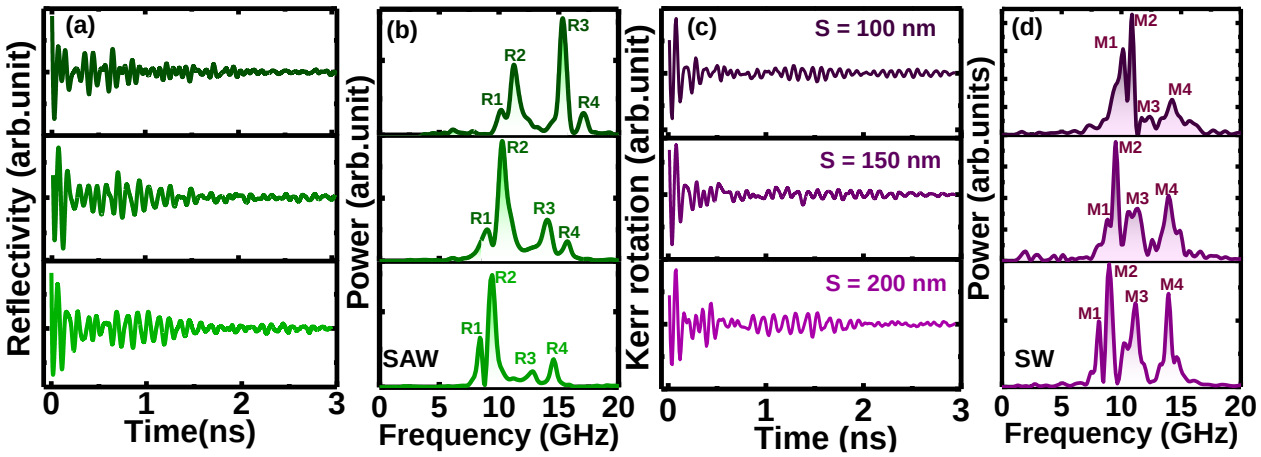


**Figure 9.3:** Background subtracted time-resolved (a) reflectivity and (c) Kerr rotation change indicating acoustic (SAW) and magnetization (SW) dynamics respectively detected for three different samples S1, S2, and S3 at a magnetic field of $H_{ext}$ = 1.75 kOe. (b) and (d) are fast Fourier transformed (FFT) power spectra of the time-resolved reflectivity and Kerr rotation, respectively. The peaks indicate the frequencies of the excited SW and SAW modes.

The time-domain Kerr rotation depicts the collective precessional dynamics of magnetization in Figure 9.3(c). Corresponding FFTs are presented in Figure 9.3(d) where multiple modes appear with different intensities which again vary with the lattice constant. The frequencies of SW modes M1 and M2 are almost equal to the frequency of SAW modes R1 and R2 with similar weightage of intensity distribution. The other higher frequency magnetic modes M3 and M4 do not overlap with the acoustic modes R3 and R4 at this value of $H_{ext}$. Thus, the appearance of SW modes at the same frequency of acoustic wave becomes an indication of coupling between precessing spins and propagating strain in the system.
The scenario is visually clearer in the surface plots of the bias field dependent frequency response of the magnetic and non-magnetic signal obtained for all three samples (Figure 9.4(a)-(f)).

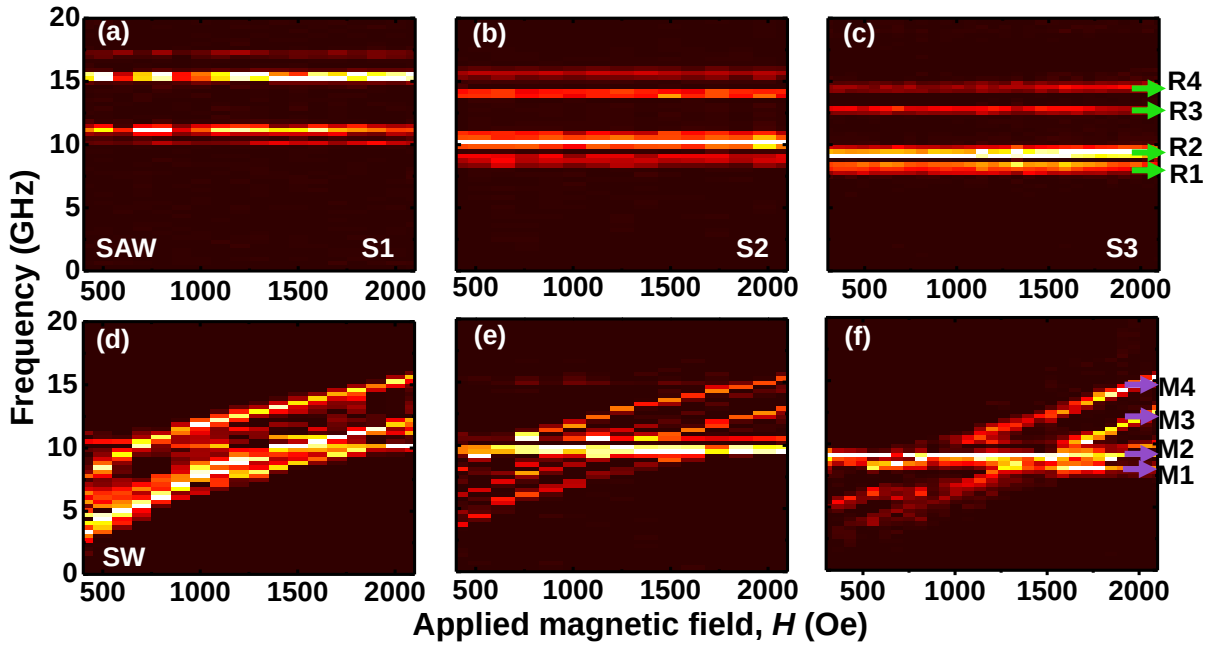


**Figure 9.4:** Experimentally obtained magnetic field dependence of (a)-(c) SAW and (d)-(f) SW frequencies for S1, S2, and S3.

The frequency of each SAW mode remains fixed throughout the whole field regime i.e., variation of $H_{ext}$ is ineffective for acoustic dynamics. This field independent nature confirms the absence of the reverse effect i.e., magnetization change with field does not modify the elastic properties of the nanomagnets. On the other hand, the magnetic channel shows an unusual complex response showing both field-dependent (M1 and M2) and field-independent (M3 and M4) SW modes. The field dependent modes are likely the intrinsic modes of the nanodot array resulting from uniform and non-uniform spin precession while the field independent modes are originated from the magnetization dynamics triggered by dynamic strain modulation. Therefore, these modes M1 and M2 can be recognized as the magnetoelastic modes with a direct correspondence to R1 and R2. Notably, the acoustic modes R3 and R4 do not couple to the magnetic modes. This might be due to insufficient energy transfer to drive the magnetization. The observation of magnetoelastic modes with sufficiently high intensity suggests a reasonably large magnetostrictive response of the nanomagnet array. At the same time, the magnetostrictive coefficient seems to have negligible values for R3 and R4. The nature of variation of M3 and M4 suggests their origin from the saturated and unsaturated spins of the nanomagnets. Moreover, these modes are resulted from the collective dynamics of the array where the nanomagnets are dipolar coupled. Thus, dipolar interaction which is a function of the lattice separation, plays a crucial role to determine the dynamic nature. This is evidenced from the downshift of the frequency with the increase of lattice constant. However, the modes follow the nonlinear field dispersion of dipolar dominated SW modes. A complex frequency behavior is prominent in all three samples' field dispersion when the frequencies of M3 and M4 approach the elastic modes with the reduction of $H_{ext}$. In each sample, the SW modes crosses the magnetoelastic branch. The crossing shifts to lower field value with an increase in the lattice constant.

At the crossing field resonance occurs due to overlap of two modes with a significant increase in the SW intensity. Additionally, the damping reduces due to injection of strain energy from the acoustic wave. Usually, the energy dissipation by the SW increases with a reduction of the external field (Zeeman field) contributions. This prompts the precessional motion to damp fast. Here, the damping seems to reduce with the decreasing field. Furthermore, in order to investigate the effect of geometrical arrangement, nanomagnet array of width 200 nm and lattice constant 350 nm arranged in square lattice symmetry is studied in the same substrate. Figure 9.5 shows the multimodal excitations of elastic modes in the square geometry similar to the hexagonal symmetry. In this case, slightly lower SAW frequencies confirm that the lattice arrangements control the SAW generation. Interestingly, the acoustic waves except R1 are unable to invade in the magnetization dynamics.

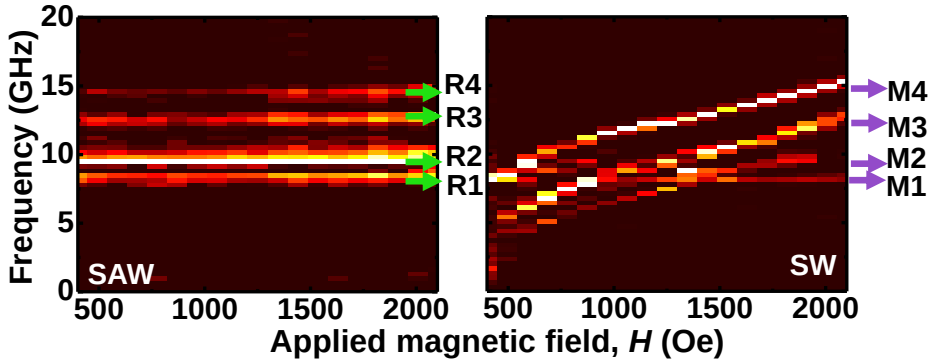


**Figure 9.5:** Experimental magnetic field dispersions of (a) SAW and (b) SW frequencies for S4.

In order to understand the interplay between the spin-wave and elastic wave due to their coexistence in the nanodot ensemble we have applied the hybrid model in one system (sample S3) as an exemplary. FEM calculations reproduce relatively well the main magnon (SAW) lines seen in the experiment, aligned diagonally (horizontally). Numerical calculations do not reveal a noticeable magnetoelastic interaction at the intersection of magnon and SAW branches, although a relatively large value of the magnetoelastic coefficient was chosen. Magnetoelastic interaction is, however, evident for selected elastic mods in a large range of the field, non-resonantly. Also for fields in which magnon modes do not exist spontaneously (i.e. without magnetoelastic pumping), non-zero amplitude of $m_z$ is observed for a long sections where SAW frequency appears. The non-vanishing $m_z$ profiles at H1, H2 and H3 basically indicate the magnetoelastically coupled mode behavior. It is worth to notice that for these modes the amplitude of elastic wave is concentrated in Py nanomagnets. In addition, there is a vertical distribution of the energy penetrating the substrate. This confirms that the SAW are being generated in the substrate and the magnets are being driven by that SAW.

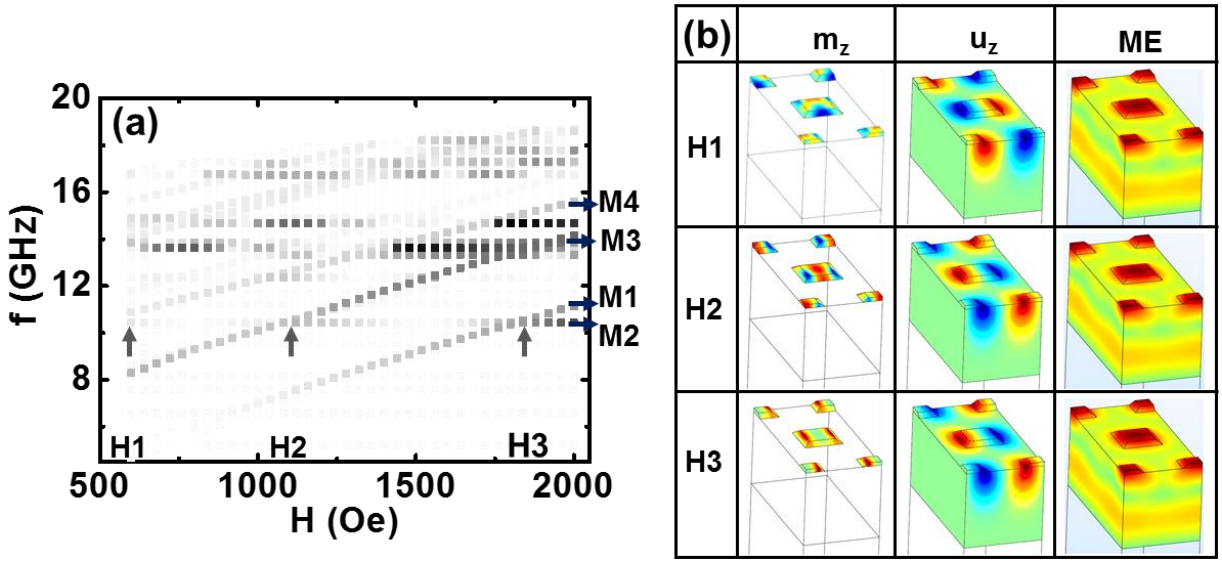


**Figure 9.6** (a) Calculated field dispersion for S3. The gray level of the lines denotes the amplitude of the out of plane component of (dynamic) magnetization. (b) Simulated spatial profiles isolated SW ($m_z$), SAW ($u_z$), and the magnetoelastic (ME) modes.

## 9.4 Conclusions

We have investigated the ultrafast kinetics of $Ni_{80}Fe_{20}$ nanomagnet arrays of different geometrical parameters. This study showcases simultaneous excitation of both elastic wave and spin-wave by ultrafast laser pulses. A profound coupling between the elastic degree and spin degree is evidenced in a broad range of applied magnetic field. Specially, hybrid magnetoelastic modes are observed near the degeneracy points indicating a transfer of energy between elastic mode and spin-wave. The features observed in experiment is almost reproduced by numerical calculations. Experimentally, the SAW frequencies shows tunability by the array geometry and the choice of underneath substrate. In addition, the coupling with SAW and SW has a strong dependence on the lattice symmetry of such patterned array. Nevertheless, this investigation opens interesting perspectives of tailoring spin-wave dynamics by surface acoustic wave in nanomagnets.

## 10.1 Summary

To summarize, this dissertation presents a comprehensive study of magnetization dynamics in diverse ferromagnetic systems. With the help of elegant experimental tools, various fundamental phenomena have been explored through the dynamics investigated in time domain, frequency domain and wave-vector domain. It has been shown that the static and dynamic features of periodic nanostructure are highly tunable under external magnetic field value, field direction or external stimulus like surface acoustic wave or ultrafast laser pulse. In this thesis, developed fabrication process like e-beam lithography has been widely used to scale down the feature size at nanoscale with verities of design. Similarly, electrochemical deposition and chemical vapor transport have been readily used to prepare magnetic film and flakes. SEM has been rigorously used to capture the surface images of the systems while AFM, MFM have been employed to measure thickness, to check surface topography and to examine magnetic remanent state. Quasistatic magnetization dynamics has been studied using static-MOKE magnetometer. The magnetostaic properties as well as the dynamics was further studied through various numerical methods and modelling.

At first, spin-wave band engineering has been evidenced in magnonic crystal using conventional Brillouin light scattering technique in agreement to plane wave method calculation. To start with, we investigated spin-wave anisotropy in an asymmetric sawtooth shaped waveguide array of $Ni_{80}Fe_{20}$ by varying the azimuthal angle of bias field direction ($\phi$). The nanostripes' shape and static spin configuration result in an asymmetric frequency anisotropy of different spin-wave modes. This leads to a tunable magnonic band gap, establishing reprogrammable characteristics of the waveguide. The anisotropic features originate from the continuous variation of magnetization direction with the bias field in each stripe. Further this is aided by pseudo-periodicity imprinted in the sawtooth shape and resulted inter-stripe dipolar coupling. Based on the investigation, prototype logic operation was proposed. Furthermore, this complexity of the anisotropic nature allows for applications such as GHz region broadband spin-wave filters and on-chip communication devices.

Our next study demonstrates fine-tuning the dynamic magnetic response of bicomponent magnonic crystals ($Ni_{80}Fe_{20}/Co_{50}Fe_{50}$) by adjusting filling fraction and bias magnetic field strength. The experiment was carried out employing broadband VNA-FMR spectrometer. Results of micromagnetic simulations reveal significant interface exchange interaction, coupling collective spin-wave dynamics of the two constituent materials. Also, dipolar field play crucial role to provide the channel for spin-wave propagation or confinement of spin-wave to for standing wave. Both the dipolar and exchange interaction were found to again vary with the geometrical parameter of the structure. Thus inter-material exchange interaction, combined with dipolar interaction, offers versatile manipulation of spin-waves in bicomponent magnonic crystals for high-speed reconfigurable magnonics applications.

The next research highlights the improved film quality achieved through electrochemical growth of a Heusler alloy film, $Co_2FeSn$ on a single crystalline Si substrate. Employing TR-MOKE magnetometer, we conducted a comprehensive study on magnetization dynamics, revealing insights into ultrafast demagnetization, relaxation times, precession frequency, and damping. The ultrafast demagnetization dynamics was subsequently modelled by the widely used three temperature model. Trends indicate increased demagnetization and relaxation times with fluence, accompanied by decreased damping. This intrinsic damping, inversely correlated with ultrafast demagnetization time, suggests its origin in a resistivity-like interband scattering mechanism. These results not only showcase the potential of electrochemically grown intermetallic alloy films on crystalline substrates but also open avenues for magneto-optical and spintronic applications.

In a separate investigation, we explored the ultrafast demagnetization and precessional magnetization of $Fe_xGeTe_2$ at room temperature using TR-MOKE microscopy. A type-I single-step demagnetization process was observed, accompanied by THz magnon generation during relaxation. Additionally, we successfully excited optical phonon modes, providing evidence of direct spin-phonon coupling. Ferromagnetic resonance mode and exchange-controlled perpendicular standing spin-waves were probed during nanosecond dynamics. The emergence of spin dynamics akin to well-studied ferromagnetic systems led us to conclude that the samples maintain a ferromagnetic state at room temperature, possibly due to ultrafast laser-tuned exchange interactions. This study underscores the need for further exploration of fundamental physical phenomena in 2D materials and highlights their promising potential for incorporation into spintronic devices.

In our exploration, we investigated short-wavelength spin-waves in narrow domains at the edges of triangular antidot lattices (ADLs) in Co/Pd multilayers. Using a TR-MOKE microscope and micromagnetic simulations, we confirmed their presence and explored their reconfigurability. These domains were formed around antidots due to disrupted out-of-plane anisotropy. The anisotropic nature of the spin-waves, influenced by the azimuthal angle of an external magnetic field, was rooted in the flexible ground state configuration. Short-wavelength spin-waves were excited and confined in the domain with different quantization numbers. The in-plane direction of the domain magnetization underwent a sharp change with the bias field direction, modifying the frequency and spatial position of those localized spin-waves. Spatial profiles confirmed the excitation of multiple spin-waves of different wavelengths but the same frequency by breaking symmetry through the magnetic field direction. The precise control of field orientation for generating tunable short-wavelength localized spin-waves within such narrow domains holds promising applications for spin-wave-based computing.

Finally, we elucidate the acoustic actuation induced by femtosecond laser pulses in a two-dimensional array of square-shaped $Ni_{80}Fe_{20}$ nanodots on a $Si/SiO_2$ substrate. The investigation reveals synchronized magnon modes strongly influenced by surface acoustic waves (SAWs) through magnetoelastic coupling, in conjunction with intrinsic magnon modes of the nanodot arrays. The

experimental results highlight three key aspects. Firstly, in low magnetostrictive materials like $Ni_{80}Fe_{20}$, the laser induces enhanced magnetostriction through instantaneous thermal annealing, underscoring the importance of considering magnetostriction in potential applications. Secondly, the sensitivity of SAW modes to geometrical parameters in a nanomagnet array allows tunability of magnetoelastic coupling. Lastly, the study demonstrates that SAW can drive magnetization dynamics even at low magnetic fields, creating a hybrid magnetoelastic mode with potential applications in energy-efficient devices utilizing nanomagnet arrays.

## 10.2 Outlook

The comprehensive investigations into various aspects of magnetoelastic coupling, spin dynamics, and acoustic actuation in the above-mentioned studies pave the way for exciting future prospects in the field of condensed matter physics. Here are some potential future directions. The spin-wave band engineering by magnetic field direction can lead to design of reconfigurable device suitable for microwave applications or logic operation. Further studies by choosing different material properties like low damping can enhance the performance level by maintain long range coherency of spin-wave required for signal transfer. The findings on fine-tuning dynamic magnetic responses in bicomponent magnonic crystals provide a foundation for reconfigurable magnonics applications. Future efforts could explore novel designs and materials to enhance the versatility and efficiency of magnonic devices, potentially revolutionizing information processing technologies. The study on the electrochemical growth of Co-based Heusler alloy films showcases improved film quality and dynamic responses. Future research might delve into exploring a broader range of intermetallic alloy films on crystalline substrates, aiming for advancements in magneto-optical and spintronic applications. The investigation into ultrafast demagnetization and precessional magnetization in $Fe_xGeTe_2$ at room temperature suggests the potential of 2D materials in spintronics. Future explorations could focus on uncovering more fundamental physical phenomena in 2D materials and harnessing their unique properties for practical spintronic device applications. The study on short-wavelength spin-waves in narrow domains offers a promising avenue for spin-wave-based computing. Future research might delve into optimizing the control parameters to enhance the precision and efficiency of short-wavelength localized spin-waves, potentially leading to spin-wave based computing. The insights gained from the acoustic actuation by femtosecond laser pulses in nanodot arrays provide a foundation for future developments. Researchers may explore applications in energy-efficient devices and investigate novel materials to further enhance the magnetoelastic coupling effects, offering new possibilities in magnonic and opto-magnonic technologies.

In conclusion, the future outlook for the physics explored in these studies is marked by the potential for advancements in magnonics and spintronics. These findings not only contribute to the fundamental understanding of condensed matter physics but also pave the way for innovative technologies with diverse applications in the field of information processing, energy harvesting, and beyond.

# Appendix I

## A.I.1 Extracted magnonic band gaps between various branches of magnonic bands

The magnonic band gaps (MBGs) obtained from BLS experiment and PWM calculation between the different spin-wave branches, i.e. M2 and M3, M3 and M4 is shown in Figure A.1 as the function of bias field direction ($\phi$). Here also, MBGs exhibit asymmetric behavior.

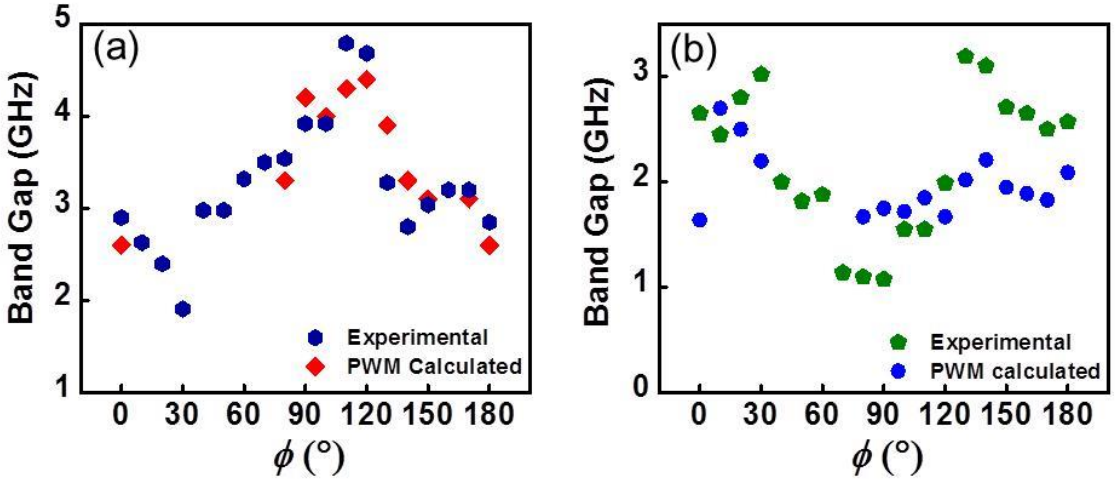


**Figure A.1:** Variation of MBG between (a) M3 and M4 and (b) M2 and M3 from PWM calculation and BLS experiment.

## A.I.2 Spin-wave amplitude and phase profiles calculated from plane wave method

We have used PWM to calculate the spatial distributions of amplitude and phase of SWs inside the ASMW. We have chosen the modulus of x-component of dynamic magnetization vector ($|m_x|$) to describe the SW amplitude and inverse of the tangent of the ratio of y-component to x-component of dynamic magnetization for phase ($\delta$) of the SWs which are given by the following expressions.

$$m_{x(y)}(\vec{r}) = \sum_{\vec{G}} m_{x(y)\vec{k}}(\vec{G}) e^{-i(\vec{k}+\vec{G})\cdot\vec{r}}$$

$$\delta = \tan^{-1}\left(\frac{m_x(\vec{r})}{m_y(\vec{r})}\right)$$

The coefficients $m_{x(y)\vec{k}}$ are the components of dynamic magnetization vector in reciprocal space which are obtained as the eigenvectors of the matrix formed from Landau-Lifshitz equation in PWM. Finally, the amplitude and phase associated to a particular frequency and wave vector are mapped at each spatial point of the real lattice taking the inverse Fourier transform as given by the above equations.

We show here the calculated amplitude and phase profiles of the dynamic magnetization vector associated with modes M1 and M2 of the ASMW at a small wave vector ($k \approx 0$) (Figure A.2). M1 appears as an extended mode but M2 shows both propagating and quantized nature. While M2 propagates along

the length of the ASMW, it shows quantized nature along its width. In Figure A3, we show the calculated amplitude profiles of the dynamic magnetization vector associated with all SW modes (M1, M2, M3 and M4) for a range of $\phi$ values barring those, which are shown in Figure 4.2(a) of chapter 4.

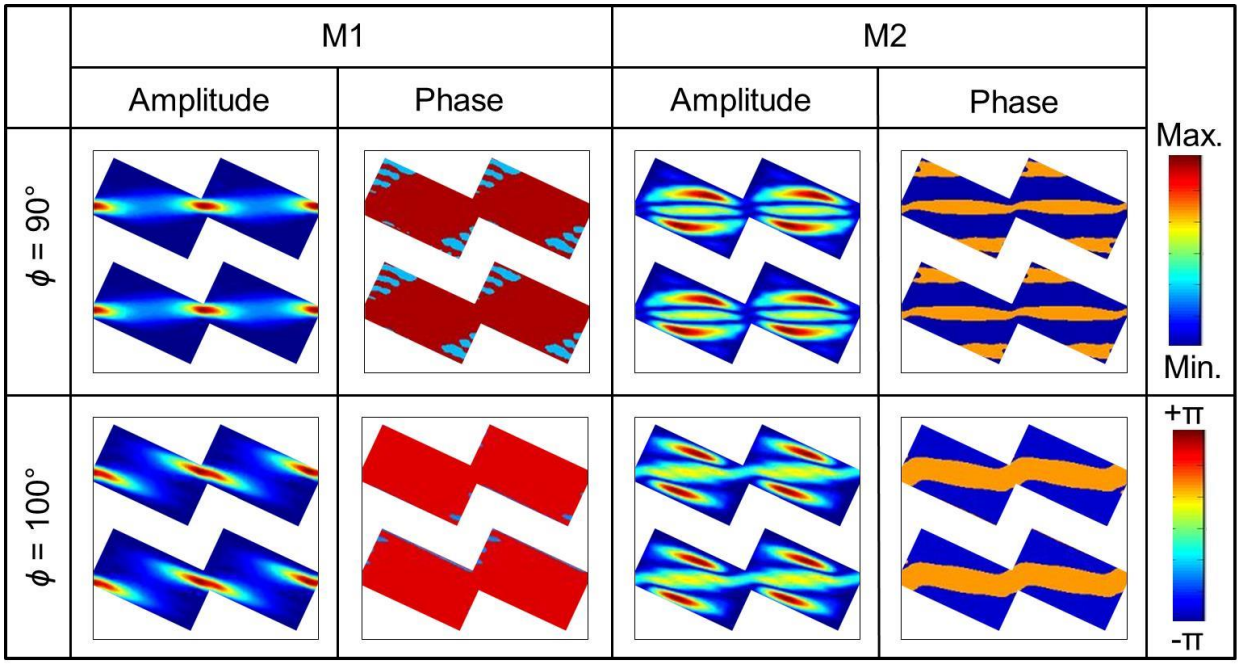


**Figure A.2:** Calculated amplitude and phase profiles by PWM of the dynamic magnetization vector associated with M1 and M2 at a small wave vector ($k \approx 0$). Corresponding color maps are shown at the right hand side.

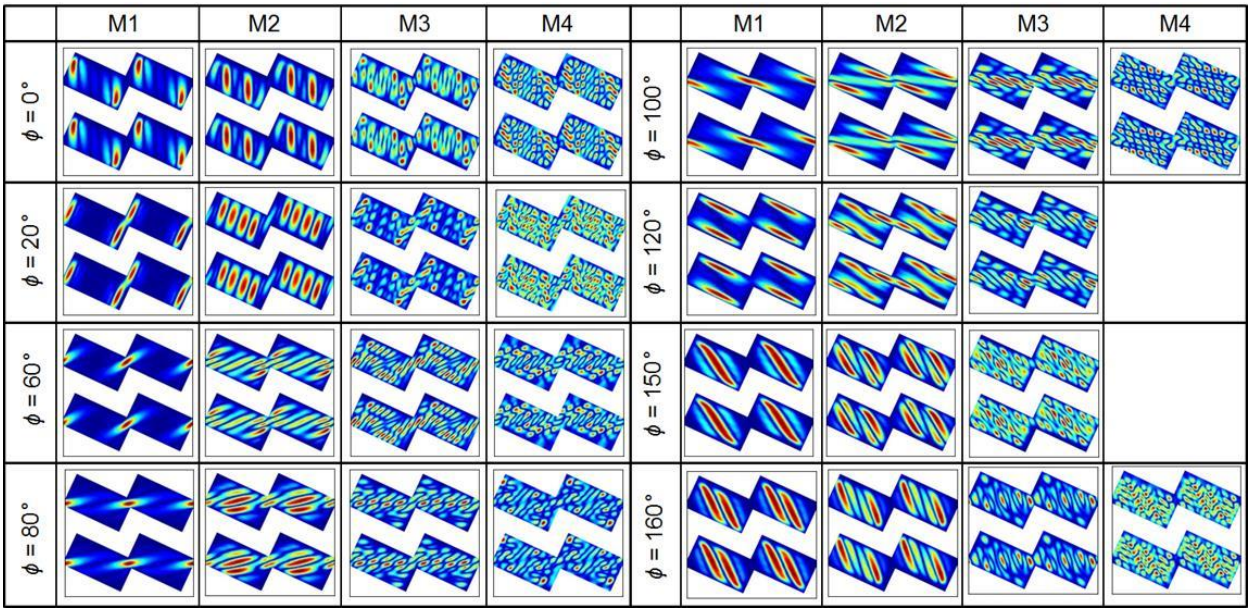


**Figure A.3:** Calculated amplitude profile by PWM of the dynamic magnetization vector associated with different SW modes.

## A.I.3 Complete angular variation of spin-wave frequency with $\phi$

We have used PWM to calculate the full angular dispersion and hence to show the anisotropy of spin-wave modes and to determine the anisotropy in MBG between the two low frequency modes.

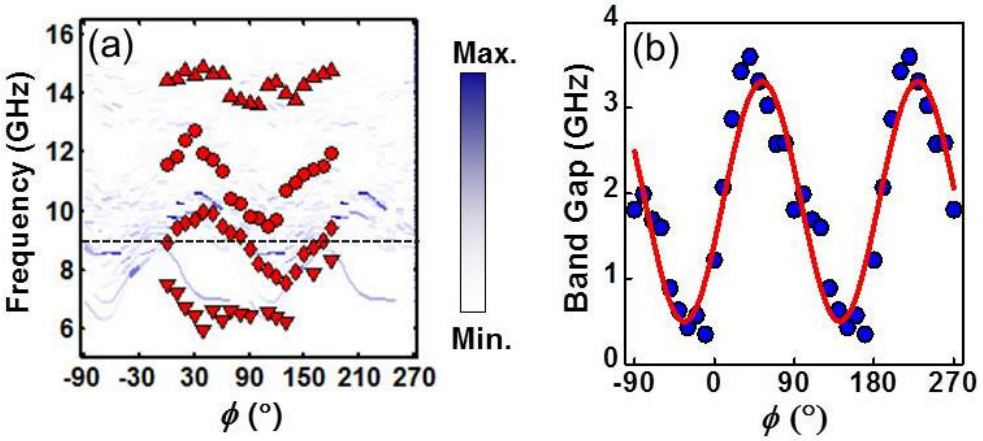


**Figure A.4:** (a) The angular variation of SW frequency w.r.t. at $H$ = 850 Oe and $k$ = 4.1 × $10^6$ rad/m. The symbols represent experimental data for 180° angular variation while the solid lines represent the PWM calculated data for full 360° angular variation. The variation in color contrast of the solid lines implies the intensity variation of the excited SW as predicted by PWM. The dashed line represents the reference frequency separating the higher frequency regime (HFR) from the lower frequency regime (LFR) of mode M2 (b) The first MBG of the studied system as calculated from the frequency difference between the two lower frequency modes is plotted as a function of $\phi$. The symbols and the dotted line represent the PWM calculated MBG and the fitted sine-curve, respectively.

# Appendix II

## A.II.1 Static magnetization profiles of bicomponent magnonic crystals

The simulated static magnetization configurations (ground states) for three different values of $H_{app}$ are shown in Figure A.5. Here, the $m_y$ component is displayed to show the demagnetizing regions. The demagnetizing regions appear near the interface and is extended in CoFe. Its volume reduces with increasing $H_{app}$ for a particular BMC. When $D$ is increased, the interface area also increases and the demagnetizing regions occur within an enlarged area around the interface. Thus, a gradual enhancement in the demagnetizing field is observed with increasing $D$.

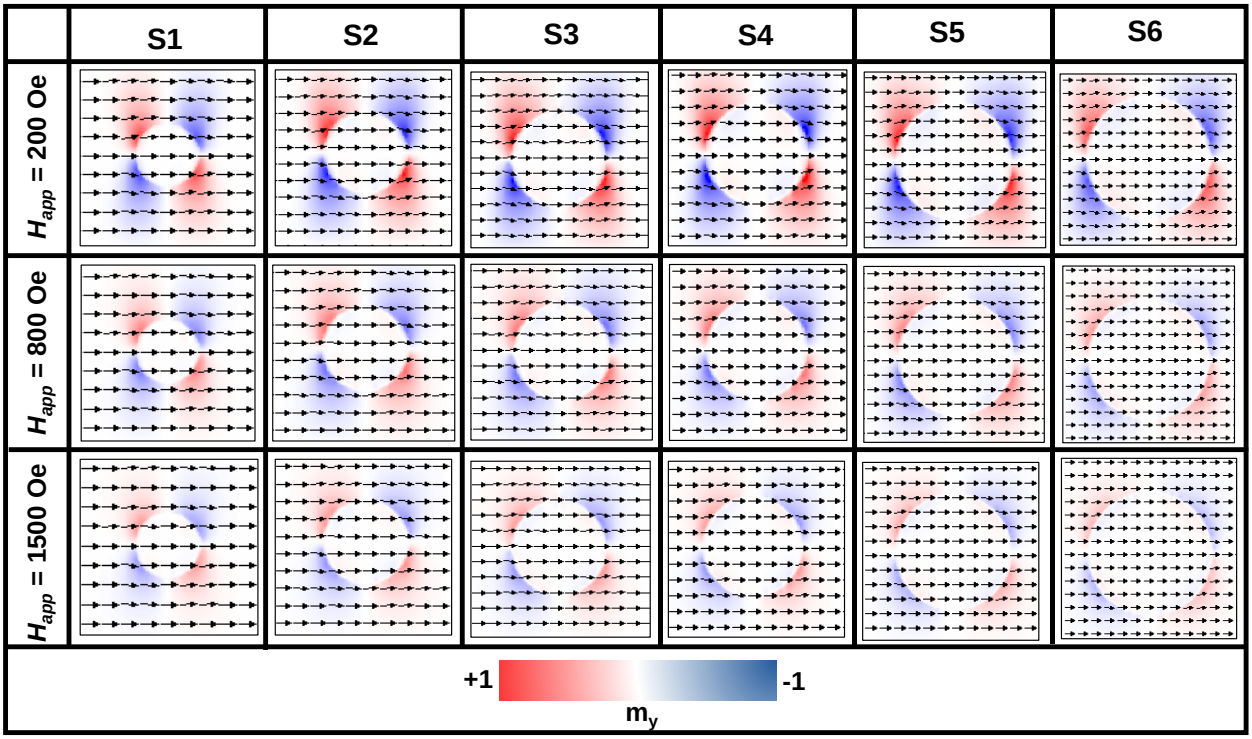


**Figure A.5:** Static magnetization profiles of all BMCs (S1-S6) at three different values of the externally applied magnetic field ($H_{app}$). The associated color bar is shown in the bottom.

## A.II.2 Spin-wave power and phase calculation

The spatial distribution of power helps to understand the spatial origin of different modes, i.e., involvement of spins of different regime. Meanwhile, the phase map gives the quantized or extended nature of the modes with their relative orientations about the applied magnetic field. In Figure A.6, we have shown the power and phase profiles of the high-frequency SW modes (M3 and M4) for two different samples ($D$ = 200 nm (S1) and 700 nm (S6)) at $H_{app}$ = 200 Oe ($H_{app}$ << $H_{cr}$) and $H$ = 1500 Oe ($H_{app}$ >> $H_{cr}$). In S1, M3 is nearly uniformly distributed in both the dots and the matrix and the quantization numbers are $n$ = 7 and $n'$ = 5. For S6, the mode profile of M3 is more complex. Here, mode power is uniformly distributed through both the dots and the matrix. However, additional mode quantization

occurs in the Damon Eshbach (DE)-like geometry (nodal lines parallel to magnetic field). Here, at $H_{app}$ = 200 Oe, $n$ = 15, $n'$ = 5 while at $H_{app}$ = 1500 Oe, $n$ = 17, $m$ = 3, $n'$ = 3, indicating higher frequency. The power and phase profiles of M4 however are too complex to visually identify their mode quantization numbers.

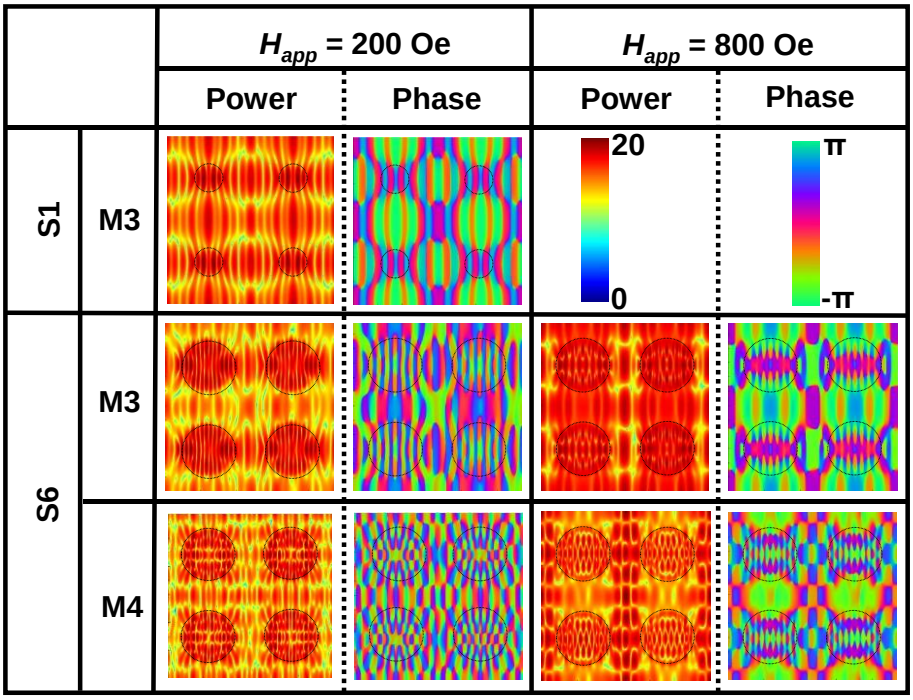


**Figure A.6:** Simulated power and phase profiles of the high-frequency SW modes (M3 and M4) for two different samples (S1 and S6) at two different values of bias magnetic field ($H_{app}$). The colour bars associated with power and phase are also shown at the top right corner.

## A.II.3 Simulated spin-wave spectra of $Ni_{80}Fe_{20}$ nanodisks and $Co_{50}Fe_{50}$ antidot and bicomponent magnonic crystal without interfacial exchange interaction

We have performed simulations to compare the field dependent SW spectra of one BMC ($D$ = 200 nm) with the constituent NiFe nanodisks and CoFe antidot lattices as depicted in Figure A.7. In the nanodisk, we observe a prominent high intense SW mode. The antidot lattice shows two different SW modes with higher frequency. Further simulations for one BMC ($D$ = 200 nm) without any interfacial exchange interaction show two prominent SW modes well separated in frequency scale at the low field regime. It seems that both the uniform nanodisk mode and the uniform antidot mode are dominant when the BMC is formed. With increasing bias field, the lower frequency mode disappears which is quite different from the BMC with a finite interfacial exchange coefficient. Therefore, the exchange interaction in the studied systems is not completely negligible as its effect is clear from the simulated results.

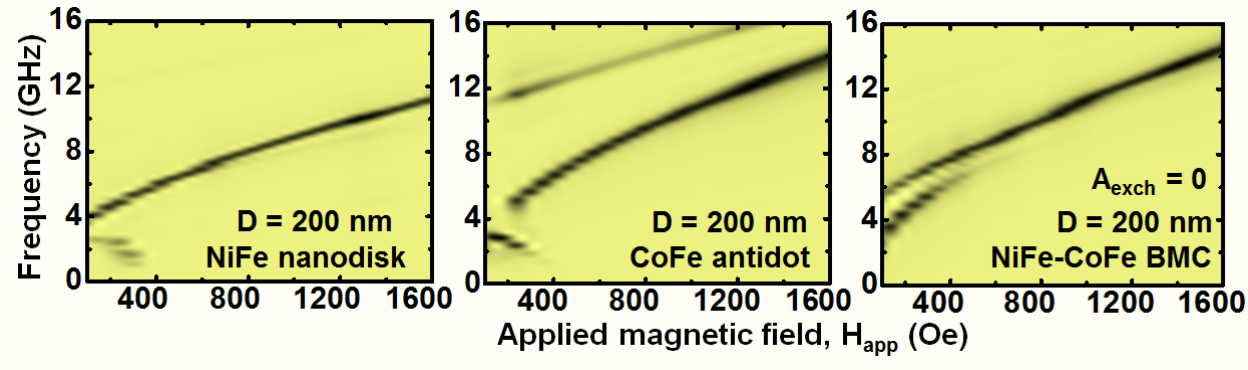


**Figure A.7:** Simulated spin-wave spectra of NiFe nanodisk, CoFe antidot and NiFe-CoFe bicomponent magnonic crystal with $A_{exch} = 0$ for $D = 200$ nm.

# Bibliography


[1] N. Taniguchi, *On the Basic Concept of'nano-Technology'*, in *Proc. Intl. Conf. Prod. Eng. Tokyo, Part II,* 1974 (Japan Society of Precision Engineering, 1974).

[2] R Skomski, J. Phys. Condens. Matter **15**, R841 (2003).

[3] M. N. Baibich, J. M. Broto, A. Fert, F. N. Van Dau, F. Petroff, P. Etienne, G. Creuzet, A. Friederich, and J. Chazelas, Phys. Rev. Lett. **61**, 2472 (1988).

[4] G. Binasch, P. Grünberg, F. Saurenbach, and W. Zinn, Phys. Rev. B **39**, 4828 (1989).

[5] A. Hirohata, K. Yamada, Y. Nakatani, I.-L. Prejbeanu, B. Diény, P. Pirro, and B. Hillebrands, J. Magn. Magn. Mater. **509**, 166711 (2020).

[6] B. Dieny et al., Nat. Electron. **3**, 446 (2020).

[7] A. Hoffmann and S. D. Bader, Phys. Rev. Appl. **4**, 47001 (2015).

[8] W. S. Zhao, Y. Zhang, T. Devolder, J. O. Klein, D. Ravelosona, C. Chappert, and P. Mazoyer, Microelectron. Reliab. **52**, 1848 (2012).

[9] K. Yakushiji, T. Saruya, H. Kubota, A. Fukushima, T. Nagahama, S. Yuasa, and K. Ando, Appl. Phys. Lett. **97**, 232508 (2010).

[10] U.-H. Hansen, V. E. Demidov, and S. O. Demokritov, Appl. Phys. Lett. **94**, 252502 (2009).

[11] A. A. Nikitin, V. V Vitko, A. A. Nikitin, A. B. Ustinov, V. V Karzin, A. E. Komlev, B. A. Kalinikos, and E. Lähderanta, IEEE Magn. Lett. **9**, 1 (2018).

[12] Y. Au, M. Dvornik, O. Dmytriiev, and V. V Kruglyak, Appl. Phys. Lett. **100**, 172408 (2012).

[13] S. Louis, I. Lisenkov, S. Nikitov, V. Tyberkevych, and A. Slavin, AIP Adv. **6**, 65103 (2016).

[14] K. Vogt, F. Y. Fradin, J. E. Pearson, T. Sebastian, S. D. Bader, B. Hillebrands, A. Hoffmann, and H. Schultheiss, Nat. Commun. **5**, 3727 (2014).

[15] A. V Chumak, A. A. Serga, and B. Hillebrands, Nat. Commun. **5**, 4700 (2014).

[16] S. J. Hämäläinen, M. Madami, H. Qin, G. Gubbiotti, and S. van Dijken, Nat. Commun. **9**, 4853 (2018).

[17] Á. Papp, W. Porod, Á. I. Csurgay, and G. Csaba, Sci. Rep. **7**, 9245 (2017).

[18] Q. Wang et al., Nat. Electron. **3**, 765 (2020).

[19] Q. Wang, P. Pirro, R. Verba, A. Slavin, B. Hillebrands, and A. V Chumak, Sci. Adv. **4**, e1701517 (2024).

[20] A. Khitun and K. L. Wang, Superlattices Microstruct. **38**, 184 (2005).

[21] Q. Wang, T. Brächer, M. Mohseni, B. Hillebrands, V. I. Vasyuchka, A. V Chumak, and P. Pirro, Appl. Phys. Lett. **115**, 92401 (2019).

[22] O. Zografos, S. Dutta, M. Manfrini, A. Vaysset, B. Sorée, A. Naeemi, P. Raghavan, R. Lauwereins, and I. P. Radu, AIP Adv. **7**, 56020 (2017).

[23] A. A. Nikitin, A. B. Ustinov, A. A. Semenov, A. V Chumak, A. A. Serga, V. I. Vasyuchka, E. Lähderanta, B. A. Kalinikos, and B. Hillebrands, Appl. Phys. Lett. **106**, 102405 (2015).

[24] T. Fischer, M. Kewenig, D. A. Bozhko, A. A. Serga, I. I. Syvorotka, F. Ciubotaru, C. Adelmann, B. Hillebrands, and A. V Chumak, Appl. Phys. Lett. **110**, 152401 (2017).

[25] A. Mahmoud, F. Vanderveken, C. Adelmann, F. Ciubotaru, S. Hamdioui, and S. Cotofana, AIP Adv. **10**, 35119 (2020).

[26] M. P. Kostylev, A. A. Serga, T. Schneider, B. Leven, and B. Hillebrands, Appl. Phys. Lett. **87**, 153501 (2005).

[27] J. Torrejon et al., Nature **547**, 428 (2017).

[28] M. Zahedinejad, A. A. Awad, S. Muralidhar, R. Khymyn, H. Fulara, H. Mazraati, M. Dvornik, and J. Åkerman, Nat. Nanotechnol. **15**, 47 (2020).

[29] M. Romera et al., Nature **563**, 230 (2018).

[30] Q. Wang, A. V Chumak, and P. Pirro, Nat. Commun. **12**, 2636 (2021).

[31] S. Watt and M. Kostylev, Phys. Rev. Appl. **13**, 34057 (2020).
[32] M. A. M. Gijs, S. K. J. Lenczowski, and J. B. Giesbers, Phys. Rev. Lett. **70**, 3343 (1993).
[33] M. Julliere, Phys. Lett. A **54**, 225 (1975).
[34] J. Mathon and A. Umerski, Phys. Rev. B **63**, 220403 (2001).
[35] S. S. P. Parkin, C. Kaiser, A. Panchula, P. M. Rice, B. Hughes, M. Samant, and S.-H. Yang, Nat. Mater. **3**, 862 (2004).
[36] S. Yuasa, T. Nagahama, A. Fukushima, Y. Suzuki, and K. Ando, Nat. Mater. **3**, 868 (2004).
[37] S. Ikeda, J. Hayakawa, Y. Ashizawa, Y. M. Lee, K. Miura, H. Hasegawa, M. Tsunoda, F. Matsukura, and H. Ohno, Appl. Phys. Lett. **93**, 82508 (2008).
[38] J. C. Slonczewski, J. Magn. Magn. Mater. **159**, L1 (1996).
[39] L. Berger, Phys. Rev. B **54**, 9353 (1996).
[40] I. M. Miron, K. Garello, G. Gaudin, P.-J. Zermatten, M. V Costache, S. Auffret, S. Bandiera, B. Rodmacq, A. Schuhl, and P. Gambardella, Nature **476**, 189 (2011).
[41] J. Sinova, S. O. Valenzuela, J. Wunderlich, C. H. Back, and T. Jungwirth, Rev. Mod. Phys. **87**, 1213 (2015).
[42] A. Manchon, H. C. Koo, J. Nitta, S. M. Frolov, and R. A. Duine, Nat. Mater. **14**, 871 (2015).
[43] G. E. W. Bauer, E. Saitoh, and B. J. van Wees, Nat. Mater. **11**, 391 (2012).
[44] Y. Tserkovnyak, A. Brataas, and G. E. W. Bauer, Phys. Rev. Lett. **88**, 117601 (2002).
[45] A. Brataas, Y. V Nazarov, and G. E. W. Bauer, Phys. Rev. Lett. **84**, 2481 (2000).
[46] M. Johnson, Phys. Rev. Lett. **70**, 2142 (1993).
[47] E. L. L. LANDAU, (n.d.).
[48] T. L. Gilbert, IEEE Trans. Magn. **40**, 3443 (2004).
[49] A. Melnikov, I. Radu, U. Bovensiepen, O. Krupin, K. Starke, E. Matthias, and M. Wolf, Phys. Rev. Lett. **91**, 227403 (2003).
[50] D. C. Worledge and T. H. Geballe, J. Appl. Phys. **88**, 5277 (2000).
[51] F. Goedsche, Phys. Status Solidi **39**, K29 (1970).
[52] S. Mansfeld, J. Topp, K. Martens, J. N. Toedt, W. Hansen, D. Heitmann, and S. Mendach, Phys. Rev. Lett. **108**, 47204 (2012).
[53] S. O. Demokritov, A. A. Serga, A. André, V. E. Demidov, M. P. Kostylev, B. Hillebrands, and A. N. Slavin, Phys. Rev. Lett. **93**, 47201 (2004).
[54] S. Choi, K.-S. Lee, and S.-K. Kim, Appl. Phys. Lett. **89**, 62501 (2006).
[55] H. Yu, J. Xiao, and H. Schultheiss, Phys. Rep. **905**, 1 (2021).
[56] Y. Li, W. Zhang, V. Tyberkevych, W.-K. Kwok, A. Hoffmann, and V. Novosad, J. Appl. Phys. **128**, 130902 (2020).
[57] E. Beaurepaire, J.-C. Merle, A. Daunois, and J.-Y. Bigot, Phys. Rev. Lett. **76**, 4250 (1996).
[58] A. V Chumak, A. A. Serga, and B. Hillebrands, J. Phys. D. Appl. Phys. **50**, 244001 (2017).
[59] B. Lenk, H. Ulrichs, F. Garbs, and M. Münzenberg, Phys. Rep. **507**, 107 (2011).
[60] M. Krawczyk and D. Grundler, J. Phys. Condens. Matter **26**, (2014).
[61] A. Barman, S. Mondal, S. Sahoo, and A. De, J. Appl. Phys. **128**, 170901 (2020).
[62] A. Barman et al., J. Phys. Condens. Matter **33**, (2021).
[63] T. Taniyama, E. Wada, M. Itoh, and M. Yamaguchi, NPG Asia Mater. **3**, 65 (2011).
[64] A. Hirohata, M. Kikuchi, N. Tezuka, K. Inomata, J. S. Claydon, Y. B. Xu, and G. van der Laan, Curr. Opin. Solid State Mater. Sci. **10**, 93 (2006).
[65] A. H. Claudia Felser, *Heusler Alloys Properties, Growth, Applications* (n.d.).
[66] E. Y. Vedmedenko, R. K. Kawakami, D. D. Sheka, P. Gambardella, A. Kirilyuk, A. Hirohata, C. Binek, O. Chubykalo-Fesenko, S. Sanvito, and B. J. Kirby, J. Phys. D. Appl. Phys. **53**, 453001 (2020).
[67] A. Hirohata and D. C. Lloyd, MRS Bull. **47**, 593 (2022).

[68] and S. S. P. P. T. Graf, C. Felser, *Heusler Compounds: Application in Spintronics. Handbook of Spintronics (2016)* (n.d.).
[69] T. Dietl, H. Ohno, F. Matsukura, J. Cibert, and D. Ferrand, Science **287**, 1019 (2000).
[70] S. Picozzi, A. Continenza, and A. J. Freeman, Phys. Rev. B **66**, 94421 (2002).
[71] H. C. Kandpal, G. H. Fecher, and C. Felser, J. Phys. D. Appl. Phys. **40**, 1507 (2007).
[72] Y. Kurtulus, R. Dronskowski, G. D. Samolyuk, and V. P. Antropov, Phys. Rev. B **71**, 14425 (2005).
[73] S. Wurmehl, G. H. Fecher, H. C. Kandpal, V. Ksenofontov, C. Felser, and H.-J. Lin, Appl. Phys. Lett. **88**, 32503 (2006).
[74] J. W. Jung, Y. Sakuraba, T. T. Sasaki, Y. Miura, and K. Hono, Appl. Phys. Lett. **108**, 102408 (2016).
[75] Z. Wen, H. Sukegawa, T. Furubayashi, J. Koo, K. Inomata, S. Mitani, J. P. Hadorn, T. Ohkubo, and K. Hono, Adv. Mater. **26**, 6483 (2014).
[76] K. Dutta, S. N. Panda, T. Seki, S. Pan, K. Takanashi, and A. Barman, Adv. Quantum Technol. **5**, 2200033 (2022).
[77] M. Oogane, T. Kubota, H. Naganuma, and Y. Ando, J. Phys. D. Appl. Phys. **48**, 164012 (2015).
[78] C. Sterwerf, S. Paul, B. Khodadadi, M. Meinert, J.-M. Schmalhorst, M. Buchmeier, C. K. A. Mewes, T. Mewes, and G. Reiss, J. Appl. Phys. **120**, 83904 (2016).
[79] C. Guillemard et al., Phys. Rev. Appl. **11**, 64009 (2019).
[80] Q. Zhang, A. V Nurmikko, G. X. Miao, G. Xiao, and A. Gupta, Phys. Rev. B **74**, 64414 (2006).
[81] G. M. Müller et al., Nat. Mater. **8**, 56 (2009).
[82] J. Walowski and M. Münzenberg, J. Appl. Phys. **120**, 140901 (2016).
[83] A. Mann et al., Phys. Rev. X **2**, 41008 (2012).
[84] A. K. Geim and I. V Grigorieva, Nature **499**, 419 (2013).
[85] Q. H. Wang et al., ACS Nano **16**, 6960 (2022).
[86] B. Huang et al., Nature **546**, 270 (2017).
[87] C. Gong et al., Nature **546**, 265 (2017).
[88] K. F. Mak, J. Shan, and D. C. Ralph, Nat. Rev. Phys. **1**, 646 (2019).
[89] S. N. Kajale, J. Hanna, K. Jang, and D. Sarkar, Nano Res. (2024).
[90] N. D. Mermin and H. Wagner, Phys. Rev. Lett. **17**, 1133 (1966).
[91] S. Yang, T. Zhang, and C. Jiang, Adv. Sci. **8**, 2002488 (2021).
[92] W. He, L. Kong, W. Zhao, and P. Yu, *Atomically Thin 2D van Der Waals Magnetic Materials: Fabrications, Structure, Magnetic Properties and Applications*, Coatings.
[93] Z. Fei et al., Nat. Mater. **17**, 778 (2018).
[94] J. Seo et al., Sci. Adv. **6**, 1 (2020).
[95] A. F. May, D. Ovchinnikov, Q. Zheng, R. Hermann, S. Calder, B. Huang, Z. Fei, Y. Liu, X. Xu, and M. A. McGuire, ACS Nano **13**, 4436 (2019).
[96] X. X. Zhang, L. Li, D. Weber, J. Goldberger, K. F. Mak, and J. Shan, Nat. Mater. **19**, 838 (2020).
[97] B. Liu et al., Phys. Rev. Lett. **125**, 267205 (2020).
[98] M. Dąbrowski, S. Guo, M. Strungaru, P. S. Keatley, F. Withers, E. J. G. Santos, and R. J. Hicken, Nat. Commun. **13**, 1 (2022).
[99] D. Afanasiev et al., Sci. Adv. **7**, 1 (2021).
[100] L. Zhang et al., Adv. Mater. **32**, 1 (2020).
[101] X. Hu, X. Hu, Y. Zhao, X. Shen, X. Shen, A. V. Krasheninnikov, A. V. Krasheninnikov, Z. Chen, and L. Sun, ACS Appl. Mater. Interfaces **12**, 26367 (2020).
[102] Q. Li et al., Nano Lett. **18**, 5974 (2018).
[103] E. Georgopoulou-Kotsaki et al., Nanoscale **15**, 2223 (2023).
[104] C. Gong and X. Zhang, Science (80-. ). **363**, eaav4450 (2019).
[105] C. Tan, J. Lee, S.-G. Jung, T. Park, S. Albarakati, J. Partridge, M. R. Field, D. G. McCulloch, L. Wang,

and C. Lee, Nat. Commun. **9**, 1554 (2018).
[106] T. Song et al., Science (80-. ). **360**, 1214 (2018).
[107] A. Aharoni, *Introduction to the Theory of Ferromagnetism* (Oxford University Press, 2000).
[108] S. Chikazumi, *Physics of Ferromagnetism* (OUP Oxford, 2009).
[109] R. M. Bozorth, *Ferromagnetism* (IEEE Press, 1993).
[110] D. J. Griffiths, *Introduction to Electrodynamics*, 5th ed. (Cambridge University Press, Cambridge, 2023).
[111] W. Heisenberg, Zeitschrift Für Phys. **38**, 411 (1926).
[112] C. D. G. B. D. Cullity, *Introduction to Magnetic Materials*, 2nd ed. (Wiley, 2009).
[113] J. M. D. Coey, *Magnetism and Magnetic Materials* (Cambridge University Press, Cambridge, 2010).
[114] A. H. Morrish, *The Physical Principles of Magnetism* (IEEE Press, 1980).
[115] J. Kaczér and L. Murtinová, Phys. Status Solidi **23**, 79 (1974).
[116] D.-X. Chen, J. A. Brug, and R. B. Goldfarb, IEEE Trans. Magn. **27**, 3601 (1991).
[117] H. J. G. Draaisma and W. J. M. de Jonge, J. Appl. Phys. **64**, 3610 (1988).
[118] E. Callen and H. B. Callen, Phys. Rev. **139**, A455 (1965).
[119] S. Iwasaki and K. Ouchi, IEEE Trans. Magn. **14**, 849 (1978).
[120] P. F. Carcia, A. D. Meinhaldt, and A. Suna, Appl. Phys. Lett. **47**, 178 (1985).
[121] B. Schulz and K. Baberschke, Phys. Rev. B **50**, 13467 (1994).
[122] R. P. Cowburn, A. O. Adeyeye, and M. E. Welland, Phys. Rev. Lett. **81**, 5414 (1998).
[123] V. V Kruglyak, P. S. Keatley, R. J. Hicken, J. R. Childress, and J. A. Katine, Phys. Rev. B **75**, 24407 (2007).
[124] L. Landau and E. Lifshits, **169**, 14 (2008).
[125] B. Heinrich, *Spin Relaxation in Magnetic Metallic Layers and Multilayers BT - Ultrathin Magnetic Structures III: Fundamentals of Nanomagnetism*, in edited by J. A. C. Bland and B. Heinrich (Springer Berlin Heidelberg, Berlin, Heidelberg, 2005), pp. 143–210.
[126] A. Barman and J. Sinha, *Spin Dynamics and Damping in Ferromagnetic Thin Films and Nanostructures* (Springer International Publishing, 2018).
[127] J. H. E. GRIFFITHS, Nature **158**, 670 (1946).
[128] C. Kittel, Phys. Rev. **73**, 155 (1948).
[129] B. Hillebrands and K. Ounadjela, *Spin Dynamics in Confined Magnetic Structures I* (Springer Berlin Heidelberg, 2010).
[130] F. Bloch, Phys. Rev. **70**, 460 (1946).
[131] C. Kittel and S. Johnson, *Introduction to Solid State Physics* (n.d.).
[132] A. G. Gurevich and G. A. Melkov, *Magnetization Oscillations and Waves* (Taylor \& Francis, 1996).
[133] D. D. Stancil, *Theory of Magnetostatic Waves* (Springer Science & Business Media, 2012).
[134] A. P. Daniel D Stancil, *Spin Waves: Theory and Applications* (Springer Science & Business Media, 2009).
[135] B A Kalinikos and A N Slavin, J. Phys. C Solid State Phys. **19**, 7013 (1986).
[136] R. W. Damon and J. R. Eshbach, J. Phys. Chem. Solids **19**, 308 (1961).
[137] B.A. Kalinikos, IEE Proc. H (Microwaves, Opt. Antennas) **127**, 4 (1980).
[138] M. G. Cottam and D. J. Lockwood, *Light Scattering in Magnetic Solids* (Wiley, 1986).
[139] B. Koopmans, G. Malinowski, F. Dalla Longa, D. Steiauf, M. Fähnle, T. Roth, M. Cinchetti, and M. Aeschlimann, Nat. Mater. **9**, 259 (2010).
[140] S. Pan, O. Hellwig, and A. Barman, Phys. Rev. B **98**, 214436 (2018).
[141] S. ~I. Anisimov, B. ~L. Kapeliovich, and T. ~L. Perel'Man, Sov. J. Exp. Theor. Phys. **39**, 375 (1974).
[142] F. Dalla Longa, J. T. Kohlhepp, W. J. M. De Jonge, and B. Koopmans, Phys. Rev. B - Condens. Matter Mater. Phys. **75**, 1 (2007).
[143] R. J. Elliott, Phys. Rev. **96**, 266 (1954).

[144] W.-G. Yang and H. Schmidt, Appl. Phys. Rev. **8**, 21304 (2021).
[145] B. Bhushan, *Springer Handbook of Nanotechnology* (Springer Berlin Heidelberg, 2010).
[146] J. Kerr, London, Edinburgh, Dublin Philos. Mag. J. Sci. **3**, 321 (1877).
[147] A. Kundt, London, Edinburgh, Dublin Philos. Mag. J. Sci. **18**, 308 (1884).
[148] J. Hamrle, J. Pištora, B. Hillebrands, B. Lenk, and M. Münzenberg, J. Phys. D. Appl. Phys. **43**, 325004 (2010).
[149] Z. Q. Qiu and S. D. Bader, Rev. Sci. Instrum. **71**, 1243 (2000).
[150] *User's Manual, Millenia EV: Diode-Pumped, CW Visible Laser System* (Spectra-Physics, California, USA, 2017).
[151] *User's Manual, Tsunami: Mode-Locked Ti:Sapphire Laser* (Spectra-Physics, California, USA, 2002).
[152] W. T. Silfvast, *Laser Fundamentals*, 2nd ed. (Cambridge University Press, 2004).
[153] *User's Manual, Model 3980: Frequency Doubler and Pulse Selector* (Spectra-Physics, California, USA, 2002).
[154] *Operator's Manual: Libra Ultrafast Amplifier Laser System* (Coherent, Santa Clara, USA, n.d.).
[155] *Operator's Manual: Vitesse Diode Pumped Mode-Locked Ti: Sapphire Laser* (Coherent, Santa Clara, USA, n.d.).
[156] *Operator's Manual: Evolution-15/30 High Energy High Average Power Q Switched Laser System* (Coherent, Santa Clara, USA, n.d.).
[157] J. R. Sandercock, *Operator Manual for the Tandem Fabry-Pérot Interferometer* (1999).
[158] J. R. Sandercock, *Operator Manual of Tandem Fabry-Pérot Interferometer TFP-1* (2010).
[159] V. P. Denysenkov and A. M. Grishin, Rev. Sci. Instrum. **74**, 3400 (2003).
[160] Z. Zhang, L. Zhou, P. E. Wigen, and K. Ounadjela, Phys. Rev. Lett. **73**, 336 (1994).
[161] M. Krawczyk, S. Mamica, M. Mruczkiewicz, J. W. Klos, S. Tacchi, M. Madami, G. Gubbiotti, G. Duerr, and D. Grundler, J. Phys. D. Appl. Phys. **46**, 495003 (2013).
[162] M. Krawczyk and H. Puszkarski, Phys. Rev. B - Condens. Matter Mater. Phys. **77**, 1 (2008).
[163] M. Donahue, *OOMMF User's Guide, Version 1.0*.
[164] A. Vansteenkiste, J. Leliaert, M. Dvornik, M. Helsen, F. Garcia-Sanchez, and B. Van Waeyenberge, AIP Adv. **4**, 107133 (2014).
[165] D. Kumar, O. Dmytriiev, S. Ponraj, and A. Barman, J. Phys. D. Appl. Phys. **45**, 15001 (2011).
[166] G. Venkat, D. Kumar, M. Franchin, O. Dmytriiev, M. Mruczkiewicz, H. Fangohr, A. Barman, M. Krawczyk, and A. Prabhakar, IEEE Trans. Magn. **49**, 524 (2013).
[167] *LLG Micromagnetics Simulator*, http://llgmicro.home.mindspring.com.
[168] A. Khitun, M. Bao, and K. L. Wang, J. Phys. D. Appl. Phys. **43**, 264005 (2010).
[169] B. Lenk, H. Ulrichs, F. Garbs, and M. Münzenberg, Phys. Rep. **507**, 107 (2011).
[170] M. Krawczyk and D. Grundler, J. Phys. Condens. Matter **26**, 123202 (2014).
[171] D. Grundler, Nat. Phys. **11**, 438 (2015).
[172] S. A. Nikitov, P. Tailhades, and C. S. Tsai, J. Magn. Magn. Mater. **236**, 320 (2001).
[173] Z. K. Wang, V. L. Zhang, H. S. Lim, S. C. Ng, M. H. Kuok, S. Jain, and A. O. Adeyeye, Appl. Phys. Lett. **94**, 83112 (2009).
[174] S. Tacchi, P. Gruszecki, M. Madami, G. Carlotti, J. W. Kłos, M. Krawczyk, A. Adeyeye, and G. Gubbiotti, Sci. Rep. **5**, 10367 (2015).
[175] S. Mamica, M. Krawczyk, and D. Grundler, Phys. Rev. Appl. **11**, 54011 (2019).
[176] L. Bai, M. Kohda, and J. Nitta, Appl. Phys. Lett. **98**, 172508 (2011).
[177] B. Rana and Y. Otani, Phys. Rev. Appl. **9**, 14033 (2018).
[178] H. Al-Wahsh, A. Akjouj, B. Djafari-Rouhani, J. O. Vasseur, L. Dobrzynski, and P. A. Deymier, Phys. Rev. B **59**, 8709 (1999).
[179] Z. K. Wang, V. L. Zhang, H. S. Lim, S. C. Ng, M. H. Kuok, S. Jain, and A. O. Adeyeye, ACS Nano **4**, 643

(2010).
[180] J. O. Vasseur, L. Dobrzynski, B. Djafari-Rouhani, and H. Puszkarski, Phys. Rev. B **54**, 1043 (1996).
[181] J. Topp, D. Heitmann, M. P. Kostylev, and D. Grundler, Phys. Rev. Lett. **104**, 207205 (2010).
[182] R. Silvani, M. Kostylev, A. O. Adeyeye, and G. Gubbiotti, J. Magn. Magn. Mater. **450**, 51 (2018).
[183] A. V Sadovnikov, V. A. Gubanov, S. E. Sheshukova, Y. P. Sharaevskii, and S. A. Nikitov, Phys. Rev. Appl. **9**, 51002 (2018).
[184] Y. Zhu, K. H. Chi, and C. S. Tsai, Appl. Phys. Lett. **105**, 22411 (2014).
[185] K. Vogt, F. Y. Fradin, J. E. Pearson, T. Sebastian, S. D. Bader, B. Hillebrands, A. Hoffmann, and H. Schultheiss, Nat. Commun. **5**, 1 (2014).
[186] A. V. Chumak, A. A. Serga, and B. Hillebrands, Nat. Commun. **5**, 1 (2014).
[187] M. Inoue, A. Baryshev, H. Takagi, P. B. Lim, K. Hatafuku, J. Noda, and K. Togo, Appl. Phys. Lett. **98**, 132511 (2011).
[188] V. E. Demidov, S. O. Demokritov, K. Rott, P. Krzysteczko, and G. Reiss, Appl. Phys. Lett. **92**, 232503 (2008).
[189] V. E. Demidov, J. Jersch, S. O. Demokritov, K. Rott, P. Krzysteczko, and G. Reiss, Phys. Rev. B **79**, 54417 (2009).
[190] M. Arikan, Y. Au, G. Vasile, S. Ingvarsson, and V. V Kruglyak, J. Phys. D. Appl. Phys. **46**, 135003 (2013).
[191] J. W. K\los, D. Kumar, J. Romero-Vivas, H. Fangohr, M. Franchin, M. Krawczyk, and A. Barman, Phys. Rev. B **86**, 184433 (2012).
[192] J. W. Kłos, D. Kumar, M. Krawczyk, and A. Barman, Sci. Rep. **3**, 2444 (2013).
[193] P. Frey et al., Commun. Phys. **3**, 17 (2020).
[194] K.-S. Lee, D.-S. Han, and S.-K. Kim, Phys. Rev. Lett. **102**, 127202 (2009).
[195] S.-K. Kim, K.-S. Lee, and D.-S. Han, Appl. Phys. Lett. **95**, 82507 (2009).
[196] H. Piao, J. Shim, M. Yang, L. Pan, and D. Kim, *Selective Behaviour of Spin Wave Propagation in Asymmetrically Modulated Ferromagnetic Nanowires*, in *2015 IEEE International Magnetics Conference (INTERMAG)* (2015), p. 1.
[197] A. V Chumak et al., Appl. Phys. Lett. **95**, 262508 (2009).
[198] F. Ciubotaru, A. V Chumak, N. Y. Grigoryeva, A. A. Serga, and B. Hillebrands, J. Phys. D. Appl. Phys. **45**, 255002 (2012).
[199] C. Banerjee, S. Choudhury, J. Sinha, and A. Barman, Phys. Rev. Appl. **8**, 14036 (2017).
[200] M. Krawczyk and H. Puszkarski, Phys. Rev. B **77**, 54437 (2008).
[201] A. V. Chumak, V. I. Vasyuchka, A. A. Serga, and B. Hillebrands, Nat. Phys. **11**, 453 (2015).
[202] D. Grundler, Nat. Phys. **11**, 438 (2015).
[203] A. K. Mondal, C. Banerjee, A. Adhikari, A. K. Chaurasiya, S. Choudhury, J. Sinha, S. Barman, and A. Barman, Phys. Rev. B **101**, 1 (2020).
[204] A. Kumar Mondal, S. Majumder, B. Kumar Mahato, S. Barman, Y. Otani, and A. Barman, Nanotechnology **34**, 135701 (2023).
[205] S. K. Kim, K. S. Lee, and D. S. Han, Appl. Phys. Lett. **95**, (2009).
[206] R. Silvani, M. Kostylev, A. O. Adeyeye, and G. Gubbiotti, J. Magn. Magn. Mater. **450**, 51 (2018).
[207] A. V. Sadovnikov, V. A. Gubanov, S. E. Sheshukova, Y. P. Sharaevskii, and S. A. Nikitov, Phys. Rev. Appl. **9**, 51002 (2018).
[208] D. Kumar, S. Barman, and A. Barman, Sci. Rep. **4**, (2014).
[209] Y. Zhu, K. H. Chi, and C. S. Tsai, Appl. Phys. Lett. **105**, 1 (2014).
[210] J. Ding, M. Kostylev, and A. O. Adeyeye, Appl. Phys. Lett. **100**, (2012).
[211] A. A. Nikitin, A. B. Ustinov, A. A. Semenov, A. V. Chumak, A. A. Serga, V. I. Vasyuchka, E. Lähderanta, B. A. Kalinikos, and B. Hillebrands, Appl. Phys. Lett. **106**, (2015).
[212] A. Adhikari, C. Banerjee, A. Kumar Mondal, A. Kumar Chaurasiya, S. Choudhury, J. Sinha, S. Barman,

and A. Barman, Mater. Sci. Eng. B Solid-State Mater. Adv. Technol. **272**, 115385 (2021).
[213] H. Yu, G. Duerr, R. Huber, M. Bahr, T. Schwarze, F. Brandl, and D. Grundler, Nat. Commun. **4**, (2013).
[214] A. Kozhevnikov, F. Gertz, G. Dudko, Y. Filimonov, and A. Khitun, Appl. Phys. Lett. **106**, (2015).
[215] M. Grassi, M. Geilen, D. Louis, M. Mohseni, T. Brächer, M. Hehn, D. Stoeffler, M. Bailleul, P. Pirro, and Y. Henry, Phys. Rev. Appl. **14**, 1 (2020).
[216] K. Szulc, P. Graczyk, M. Mruczkiewicz, G. Gubbiotti, and M. Krawczyk, Phys. Rev. Appl. **14**, 1 (2020).
[217] J. Lan, W. Yu, R. Wu, and J. Xiao, Phys. Rev. X **5**, 1 (2015).
[218] M. Jamali, J. H. Kwon, S. M. Seo, K. J. Lee, and H. Yang, Sci. Rep. **3**, 1 (2013).
[219] A. V. Chumak et al., IEEE Trans. Magn. **58**, (2022).
[220] A. Mahmoud, F. Ciubotaru, F. Vanderveken, A. V. Chumak, S. Hamdioui, C. Adelmann, and S. Cotofana, J. Appl. Phys. **128**, (2020).
[221] G. Csaba, Á. Papp, and W. Porod, Phys. Lett. Sect. A Gen. At. Solid State Phys. **381**, 1471 (2017).
[222] M. Romera et al., Nature **563**, 230 (2018).
[223] Á. Papp, W. Porod, and G. Csaba, Nat. Commun. **12**, 1 (2021).
[224] T. Brächer and P. Pirro, J. Appl. Phys. **124**, (2018).
[225] J. Vasseur, L. Dobrzynski, B. Djafari-Rouhani, and H. Puszkarski, Phys. Rev. B - Condens. Matter Mater. Phys. **54**, 1043 (1996).
[226] G. Duerr, M. Madami, S. Neusser, S. Tacchi, G. Gubbiotti, G. Carlotti, and D. Grundler, Appl. Phys. Lett. **99**, 1 (2011).
[227] Z. K. Wang, V. L. Zhang, H. S. Lim, S. C. Ng, M. H. Kuok, S. Jain, and A. O. Adeyeye, ACS Nano **4**, 643 (2010).
[228] X. M. Liu, J. Ding, and A. O. Adeyeye, Appl. Phys. Lett. **100**, (2012).
[229] F. S. Ma, H. S. Lim, Z. K. Wang, S. N. Piramanayagam, S. C. Ng, and M. H. Kuok, Appl. Phys. Lett. **98**, 2009 (2011).
[230] G. Gubbiotti, S. Tacchi, M. Madami, G. Carlotti, S. Jain, A. O. Adeyeye, and M. P. Kostylev, Appl. Phys. Lett. **100**, (2012).
[231] S. Tacchi, G. Duerr, J. W. Klos, M. Madami, S. Neusser, G. Gubbiotti, G. Carlotti, M. Krawczyk, and D. Grundler, Phys. Rev. Lett. **109**, 1 (2012).
[232] M. Krawczyk, S. Mamica, M. Mruczkiewicz, J. W. Klos, S. Tacchi, M. Madami, G. Gubbiotti, G. Duerr, and D. Grundler, J. Phys. D. Appl. Phys. **46**, (2013).
[233] G. Gubbiotti, S. Tacchi, M. Madami, G. Carlotti, Z. Yang, J. Ding, A. O. Adeyeye, and M. Kostylev, Phys. Rev. B **93**, 1 (2016).
[234] S. Mamica and M. Krawczyk, Phys. Rev. B **100**, 1 (2019).
[235] S. Mamica, M. Krawczyk, and D. Grundler, Phys. Rev. Appl. **11**, 1 (2019).
[236] S. Mamica, J. Magn. Magn. Mater. **546**, 168690 (2022).
[237] R. Shindou, R. Matsumoto, S. Murakami, and J. I. Ohe, Phys. Rev. B - Condens. Matter Mater. Phys. **87**, 2 (2013).
[238] A. Manzin and R. Ferrero, Appl. Phys. Lett. **115**, (2019).
[239] J. Chen, C. Liu, T. Liu, Y. Xiao, and K. Xia, 1 (n.d.).
[240] H. Wang et al., ACS Nano **15**, 9076 (2021).
[241] S. Choudhury, S. Saha, R. Mandal, S. Barman, Y. Otani, and A. Barman, ACS Appl. Mater. Interfaces **8**, 18339 (2016).
[242] S. Choudhury, S. Pan, S. Barman, Y. C. Otani, and A. Barman, J. Magn. Magn. Mater. **490**, 165484 (2019).
[243] Y. Zhou et al., Nano Lett. **22**, 4646 (2022).
[244] G. Porter, (n.d.).
[245] D. Kumar, O. Dmytriiev, S. Ponraj, and A. Barman, J. Phys. D. Appl. Phys. **45**, (2012).

[246] A. Hirohata, W. Frost, M. Samiepour, and J. Kim, Materials (Basel). **11**, (2018).
[247] W. Frost, M. Samiepour, and A. Hirohata, J. Magn. Magn. Mater. **484**, 100 (2019).
[248] Z. Wen, H. Sukegawa, S. Kasai, K. Inomata, and S. Mitani, Phys. Rev. Appl. **2**, 24009 (2014).
[249] C. Sterwerf, M. Meinert, J.-M. Schmalhorst, and G. Reiss, IEEE Trans. Magn. **49**, 4386 (2013).
[250] Y. Miura, K. Nagao, and M. Shirai, Phys. Rev. B **69**, 144413 (2004).
[251] S. Pan, T. Seki, K. Takanashi, and A. Barman, Phys. Rev. B **101**, 224412 (2020).
[252] T. Graf, C. Felser, and S. S. P. Parkin, Prog. Solid State Chem. **39**, 1 (2011).
[253] M. R. Karim, D. Panda, A. Adhikari, P. Sharangi, P. Mandal, S. Ghosh, S. Bedanta, A. Barman, and I. Sarkar, Mater. Today Commun. **25**, 101678 (2020).
[254] J. Duan and X. Kou, J. Electrochem. Soc. **160**, D471 (2013).
[255] N. Watanabe, K. Sano, N. Tasugi, T. Yamaguchi, A. Yamamoto, M. Ueno, R. Sumiyoshi, T. Arakawa, and I. Koiwa, APL Mater. **3**, 41804 (2015).
[256] Y. Liu, L. R. Shelford, V. V Kruglyak, R. J. Hicken, Y. Sakuraba, M. Oogane, Y. Ando, and T. Miyazaki, J. Appl. Phys. **101**, 09C106 (2007).
[257] Y. Liu, L. R. Shelford, V. V Kruglyak, R. J. Hicken, Y. Sakuraba, M. Oogane, and Y. Ando, Phys. Rev. B **81**, 94402 (2010).
[258] C. Cheng, K. Meng, S. Li, J. Zhao, and T. Lai, Appl. Phys. Lett. **103**, 232406 (2013).
[259] C. Fowley et al., J. Phys. D. Appl. Phys. **48**, 164006 (2015).
[260] S. Pan, S. Mondal, T. Seki, K. Takanashi, and A. Barman, Phys. Rev. B **94**, 184417 (2016).
[261] S. Pan, T. Seki, K. Takanashi, and A. Barman, Phys. Rev. Appl. **7**, 64012 (2017).
[262] J.-P. Wüstenberg, D. Steil, S. Alebrand, T. Roth, M. Aeschlimann, and M. Cinchetti, Phys. Status Solidi **248**, 2330 (2011).
[263] M. R. Karim, A. Adhikari, S. N. Panda, P. Sharangi, S. Kayal, G. Manna, P. S. A. Kumar, S. Bedanta, A. Barman, and I. Sarkar, J. Phys. Chem. C **125**, 10483 (2021).
[264] 2018 Barman, A.; Sinha, J. ; Springer, *Spin Dynamics and Damping in Ferromagnetic Thin Films and Nanostructures* (n.d.).
[265] E. Carpene, F. Boschini, H. Hedayat, C. Piovera, C. Dallera, E. Puppin, M. Mansurova, M. Münzenberg, X. Zhang, and A. Gupta, Phys. Rev. B **87**, 174437 (2013).
[266] B. Koopmans, M. van Kampen, J. T. Kohlhepp, and W. J. M. de Jonge, Phys. Rev. Lett. **85**, 844 (2000).
[267] M. Hofherr et al., Sci. Adv. **6**, eaay8717 (2020).
[268] D. Steil et al., Phys. Rev. Res. **2**, 23199 (2020).
[269] P. Tengdin et al., Sci. Adv. **6**, eaaz1100 (2020).
[270] F. Dalla Longa, J. T. Kohlhepp, W. J. M. de Jonge, and B. Koopmans, Phys. Rev. B **75**, 224431 (2007).
[271] J. Walowski, G. Müller, M. Djordjevic, M. Münzenberg, M. Kläui, C. A. F. Vaz, and J. A. C. Bland, Phys. Rev. Lett. **101**, 237401 (2008).
[272] D. Steil et al., New J. Phys. **16**, 63068 (2014).
[273] T. Cheng, J. Wu, T. Liu, X. Zou, J. Cai, R. W. Chantrell, and Y. Xu, Phys. Rev. B **93**, 64401 (2016).
[274] J. Walowski, M. D. Kaufmann, B. Lenk, C. Hamann, J. McCord, and M. Münzenberg, J. Phys. D. Appl. Phys. **41**, (2008).
[275] H. C. Yuan, S. H. Nie, T. P. Ma, Z. Zhang, Z. Zheng, Z. H. Chen, Y. Z. Wu, J. H. Zhao, H. B. Zhao, and L. Y. Chen, Appl. Phys. Lett. **105**, 72413 (2014).
[276] Z. Chen, Y. Yan, S. Li, X. Xu, Y. Jiang, and T. Lai, Sci. Rep. **7**, 42513 (2017).
[277] S. Mizukami et al., Phys. Rev. Lett. **106**, 117201 (2011).
[278] B. Koopmans, J. J. M. Ruigrok, F. D. Longa, and W. J. M. de Jonge, Phys. Rev. Lett. **95**, 267207 (2005).
[279] M. Fähnle, J. Seib, and C. Illg, Phys. Rev. B **82**, 144405 (2010).
[280] W. Zhang, W. He, X.-Q. Zhang, Z.-H. Cheng, J. Teng, and M. Fähnle, Phys. Rev. B **96**, 220415 (2017).
[281] R. S. Malik et al., Phys. Rev. B **104**, L100408 (2021).

[282] T. Roth, A. J. Schellekens, S. Alebrand, O. Schmitt, D. Steil, B. Koopmans, M. Cinchetti, and M. Aeschlimann, Phys. Rev. X **2**, 21006 (2012).
[283] B. Huang et al., Nature **546**, 270 (2017).
[284] C. Gong et al., Nature **546**, 265 (2017).
[285] Q. H. Wang et al., ACS Nano **16**, 6960 (2021).
[286] A. F. May, D. Ovchinnikov, Q. Zheng, R. Hermann, S. Calder, B. Huang, Z. Fei, Y. Liu, X. Xu, and M. A. McGuire, ACS Nano **13**, 4436 (2019).
[287] J. Seo et al., Sci. Adv. **6**, eaay8912 (2020).
[288] C. Bin, Y. JinHu, W. HangDong, I. Masaki, O. Hiroto, M. Chishiro, Y. Kazuyoshi, and F. MingHu, J. Phys. Soc. Japan **82**, 124711 (2013).
[289] Y. Deng et al., Nature **563**, 94 (2018).
[290] L. Zhang et al., Adv. Mater. **32**, 2002032 (2020).
[291] H. L. Zhuang, P. R. C. Kent, and R. G. Hennig, Phys. Rev. B **93**, 134407 (2016).
[292] N. León-Brito, E. D. Bauer, F. Ronning, J. D. Thompson, and R. Movshovich, J. Appl. Phys. **120**, 83903 (2016).
[293] Y. Zhang et al., Sci. Adv. **4**, eaao6791 (2018).
[294] S. Bera, S. Chatterjee, S. Pradhan, S. K. Pradhan, S. Kalimuddin, A. Bera, A. K. Nandy, and M. Mondal, Phys. Rev. B **108**, 115122 (2023).
[295] Z. Wang, D. Sapkota, T. Taniguchi, K. Watanabe, D. Mandrus, and A. F. Morpurgo, Nano Lett. **18**, 4303 (2018).
[296] K. H. Min et al., Nat. Mater. **21**, 1144 (2022).
[297] S. Jiang, L. Li, Z. Wang, J. Shan, and K. F. Mak, Nat. Electron. **2**, 159 (2019).
[298] L. Powalla et al., Adv. Mater. **35**, 2208930 (2023).
[299] Y. Wu et al., Adv. Mater. **34**, 2110583 (2022).
[300] T. Lichtenberg, C. F. Schippers, S. C. P. van Kooten, S. G. F. Evers, B. Barcones, M. H. D. Guimarães, and B. Koopmans, 2D Mater. **10**, 15008 (2022).
[301] F. Mertens et al., Adv. Mater. **35**, 2208355 (2023).
[302] J. Guo, W. Liang, and S. N. Luo, J. Phys. Chem. Lett. **11**, 9351 (2020).
[303] P. Padmanabhan et al., Nat. Commun. **13**, 4473 (2022).
[304] M. Khela, M. Dąbrowski, S. Khan, P. S. Keatley, I. Verzhbitskiy, G. Eda, R. J. Hicken, H. Kurebayashi, and E. J. G. Santos, Nat. Commun. **14**, 1378 (2023).
[305] T. Zhang, Y. Chen, Y. Li, Z. Guo, Z. Wang, Z. Han, W. He, and J. Zhang, Appl. Phys. Lett. **116**, 223103 (2020).
[306] D. Afanasiev et al., Sci. Adv. **7**, eabf3096 (2021).
[307] J. P. Van Der Ziel, P. S. Pershan, and L. D. Malmstrom, Phys. Rev. Lett. **15**, 190 (1965).
[308] H. Liu et al., Phys. Rev. B **106**, 35103 (2022).
[309] A. S. Disa et al., Nature **617**, 73 (2023).
[310] A. Ron, S. Chaudhary, G. Zhang, H. Ning, E. Zoghlin, S. D. Wilson, R. D. Averitt, G. Refael, and D. Hsieh, Phys. Rev. Lett. **125**, 197203 (2020).
[311] J. He, S. Li, L. Zhou, and T. Frauenheim, J. Phys. Chem. Lett. **13**, 2765 (2022).
[312] O. Neufeld, N. Tancogne-Dejean, U. De Giovannini, H. Hübener, and A. Rubio, Npj Comput. Mater. **9**, 39 (2023).
[313] T. Zhang, Y. Chen, Y. Li, Z. Guo, Z. Wang, Z. Han, W. He, and J. Zhang, Appl. Phys. Lett. **116**, 4 (2020).
[314] M. Salah, E. Hadri, M. Hehn, G. Malinowski, U. Bierbrauer, and S. T. Weber, 2D Mater. **8**, 045040 (2021).
[315] X. Yang, X. Zhou, W. Feng, and Y. Yao, Phys. Rev. B **104**, 104427 (2021).
[316] Y. Wang, C. Xian, J. Wang, B. Liu, L. Ling, L. Zhang, L. Cao, Z. Qu, and Y. Xiong, Phys. Rev. B **96**,

134428 (2017).
[317] Y. Liu, V. N. Ivanovski, and C. Petrovic, Phys. Rev. B **96**, 144429 (2017).
[318] S. Bera et al., J. Magn. Magn. Mater. **583**, 171052 (2022).
[319] S. Mondal, N. Khan, S. M. Mishra, B. Satpati, and P. Mandal, Phys. Rev. B **104**, 94405 (2021).
[320] S. Bera, S. K. Pradhan, M. S. Khan, R. Pal, B. Pal, S. Kalimuddin, A. Bera, B. Das, A. N. Pal, and M. Mondal, J. Magn. Magn. Mater. **565**, 170257 (2023).
[321] H. Zhang et al., Phys. Rev. B **102**, 64417 (2020).
[322] A. F. May, C. A. Bridges, and M. A. McGuire, Phys. Rev. Mater. **3**, 104401 (2019).
[323] M. Ribeiro et al., Npj 2D Mater. Appl. **6**, 1 (2022).
[324] D. Rana, M. Bhakar, B. G., S. Bera, N. Saini, S. K. Pradhan, M. Mondal, M. Kabir, and G. Sheet, Phys. Rev. B **107**, 224422 (2023).
[325] L. Du et al., Adv. Funct. Mater. **29**, 1904734 (2019).
[326] B. Koopmans, G. Malinowski, F. Dalla Longa, D. Steiauf, M. Fähnle, T. Roth, M. Cinchetti, and M. Aeschlimann, Nat. Mater. **9**, 259 (2010).
[327] X. Kong, T. Berlijn, and L. Liang, Adv. Electron. Mater. **7**, 2001159 (2021).
[328] T. K. Cheng, J. Vidal, H. J. Zeiger, G. Dresselhaus, M. S. Dresselhaus, and E. P. Ippen, Appl. Phys. Lett. **59**, 1923 (1991).
[329] H. J. Zeiger, J. Vidal, T. K. Cheng, E. P. Ippen, G. Dresselhaus, and M. S. Dresselhaus, Phys. Rev. B **45**, 768 (1992).
[330] S. Mizukami, Y. Ando, and T. Miyazaki, Japanese J. Appl. Physics, Part 1 Regul. Pap. Short Notes Rev. Pap. **40**, 580 (2001).
[331] J. Walowski, M. D. Kaufmann, B. Lenk, C. Hamann, J. McCord, and M. Münzenberg, J. Phys. D. Appl. Phys. **41**, 164016 (2008).
[332] J. A. Phys, A. Mahmoud, F. Ciubotaru, F. Vanderveken, and C. Adelmann, **161101**, (2020).
[333] J. Chen, J. Hu, and H. Yu, ACS Nano **15**, 4372 (2021).
[334] S. Finizio, A. Hrabec, M. Weigand, J. Fo, S. Mayr, S. Wintz, J. Raabe, H. Stoll, L. J. Heyderman, and M. Urba, (2021).
[335] G. Dieterle et al., Phys. Rev. Lett. **122**, 117202 (2019).
[336] L.-J. Chang et al., Nano Lett. **20**, 3140 (2020).
[337] S. Wintz, V. Tiberkevich, M. Weigand, J. Raabe, J. Lindner, A. Erbe, A. Slavin, and J. Fassbender, Nat. Nanotechnol. **11**, 948 (2016).
[338] V. Sluka et al., Nat. Nanotechnol. **14**, 328 (2019).
[339] Y. Henry, D. Stoeffler, J. V. Kim, and M. Bailleul, Phys. Rev. B **100**, (2019).
[340] E. Albisetti et al., Commun. Phys. **1**, (2018).
[341] S. J. Hämäläinen, M. Madami, H. Qin, G. Gubbiotti, and S. van Dijken, Nat. Commun. **9**, 1 (2018).
[342] O. Wojewoda et al., Appl. Phys. Lett. **117**, 3 (2020).
[343] S. J. Hämäläinen, F. Brandl, K. J. A. Franke, D. Grundler, and S. Van Dijken, Phys. Rev. Appl. **8**, 1 (2017).
[344] F. Garcia-sanchez, P. Borys, R. Soucaille, J. Adam, R. L. Stamps, and J. Kim, **247206**, 1 (2015).
[345] K. Wagner, A. Kákay, K. Schultheiss, A. Henschke, T. Sebastian, and H. Schultheiss, Nat. Nanotechnol. **11**, 432 (2016).
[346] B. Van De Wiele, S. J. Hämälaïnen, P. Baláz, F. Montoncello, and S. Van Dijken, Sci. Rep. **6**, 1 (2016).
[347] W. Wang, M. Albert, M. Beg, M. A. Bisotti, D. Chernyshenko, D. Cortés-Ortuño, I. Hawke, and H. Fangohr, Phys. Rev. Lett. **114**, 1 (2015).
[348] S. Woo, T. Delaney, and G. S. D. Beach, Nat. Phys. **13**, 448 (2017).
[349] Y. Fan, M. J. Gross, T. Fakhrul, J. Finley, J. T. Hou, S. Ngo, L. Liu, and C. A. Ross, Nat. Nanotechnol. **18**, 1000 (2023).

[350] L. D. A. Ho, M. T. Tran, X. H. Cao, V. A. Dao, D. T. Ngo, and D. Q. Hoang, RSC Adv. **8**, 14539 (2018).
[351] H. Qin, R. Dreyer, G. Woltersdorf, T. Taniyama, and S. van Dijken, Adv. Mater. **33**, 1 (2021).
[352] C. Liu et al., Nat. Nanotechnol. **14**, 691 (2019).
[353] R. Kohno, J. Sampaio, S. Rohart, and A. Thiaville, Phys. Rev. B **102**, 20410 (2020).
[354] C. T. Boone, J. A. Katine, M. Carey, J. R. Childress, X. Cheng, and I. N. Krivorotov, Phys. Rev. Lett. **104**, 1 (2010).
[355] J. P. Tetienne et al., Science (80-. ). **344**, 1366 (2014).
[356] T. Janda et al., Nat. Commun. **8**, 4 (2017).
[357] F. S. Ma, V. L. Zhang, Z. K. Wang, H. S. Lim, S. C. Ng, M. H. Kuok, Y. Ren, and A. O. Adeyeye, J. Appl. Phys. **108**, (2010).
[358] X. S. Wang and X. R. Wang, Phys. Rev. B - Condens. Matter Mater. Phys. **90**, 1 (2014).
[359] F. J. Buijnsters, Y. Ferreiros, A. Fasolino, and M. I. Katsnelson, Phys. Rev. Lett. **116**, 1 (2016).
[360] B. Mozooni and J. Mccord, **042402**, (2015).
[361] C. C. Faulkner, M. D. Cooke, D. A. Allwood, D. Petit, D. Atkinson, and R. P. Cowburn, J. Appl. Phys. **95**, 6717 (2004).
[362] X. Liang, Z. Wang, P. Yan, and Y. Zhou, Phys. Rev. B **106**, (2022).
[363] E. Jué et al., Phys. Rev. B **93**, 1 (2016).
[364] A. Hrabec, V. KřiŽáková, S. Pizzini, J. Sampaio, A. Thiaville, S. Rohart, and J. Vogel, Phys. Rev. Lett. **120**, 1 (2018).
[365] S. A. Bunyaev et al., Appl. Phys. Lett. **118**, (2021).
[366] S. Pal, B. Rana, O. Hellwig, T. Thomson, and A. Barman, Appl. Phys. Lett. **98**, 82501 (2011).
[367] C. Kittel, Phys. Rev. **110**, 836 (1958).
[368] L. Thevenard, J.-Y. Duquesne, E. Peronne, H. J. von Bardeleben, H. Jaffres, S. Ruttala, J.-M. George, A. Lemaître, and C. Gourdon, Phys. Rev. B **87**, 144402 (2013).
[369] O. Kovalenko, T. Pezeril, and V. V Temnov, Phys. Rev. Lett. **110**, 266602 (2013).
[370] Z. Xiao, R. Lo Conte, C. Chen, C.-Y. Liang, A. Sepulveda, J. Bokor, G. P. Carman, and R. N. Candler, Sci. Rep. **8**, 5207 (2018).
[371] J. Dean, M. T. Bryan, J. D. Cooper, A. Virbule, J. E. Cunningham, and T. J. Hayward, Appl. Phys. Lett. **107**, 142405 (2015).
[372] C. L. Chang, A. M. Lomonosov, J. Janusonis, V. S. Vlasov, V. V Temnov, and R. I. Tobey, Phys. Rev. B **95**, 60409 (2017).
[373] M. Weiler, H. Huebl, F. S. Goerg, F. D. Czeschka, R. Gross, and S. T. B. Goennenwein, Phys. Rev. Lett. **108**, 176601 (2012).
[374] B. Casals, N. Statuto, M. Foerster, A. Hernández-Mínguez, R. Cichelero, P. Manshausen, A. Mandziak, L. Aballe, J. M. Hernàndez, and F. Macià, Phys. Rev. Lett. **124**, 137202 (2020).
[375] A. De, J. L. Drobitch, S. Majumder, S. Barman, S. Bandyopadhyay, and A. Barman, Nanoscale **13**, 10016 (2021).
[376] W. G. Yang, M. Jaris, D. L. Hibbard-Lubow, C. Berk, and H. Schmidt, Phys. Rev. B **97**, 224410 (2018).
[377] P. Sivarajah, A. Steinbacher, B. Dastrup, J. Lu, M. Xiang, W. Ren, S. Kamba, S. Cao, and K. A. Nelson, J. Appl. Phys. **125**, 213103 (2019).
[378] D.-L. Zhang, J. Zhu, T. Qu, D. M. Lattery, R. H. Victora, X. Wang, and J.-P. Wang, Sci. Adv. **6**, eabb4607 (2020).
[379] M. Weiler, L. Dreher, C. Heeg, H. Huebl, R. Gross, M. S. Brandt, and S. T. B. Goennenwein, Phys. Rev. Lett. **106**, 117601 (2011).
[380] L. Dreher, M. Weiler, M. Pernpeintner, H. Huebl, R. Gross, M. S. Brandt, and S. T. B. Goennenwein, Phys. Rev. B **86**, 134415 (2012).
[381] M. Bombeck et al., Phys. Rev. B **85**, 195324 (2012).

[382] P. Graczyk, J. Kłos, and M. Krawczyk, Phys. Rev. B **95**, 104425 (2017).
[383] N. K. P. Babu, A. Trzaskowska, P. Graczyk, G. Centała, S. Mieszczak, H. Głowiński, M. Zdunek, S. Mielcarek, and J. W. Kłos, Nano Lett. **21**, 946 (2021).
[384] A. Comin et al., Phys. Rev. Lett. **97**, 217201 (2006).
[385] C. Giannetti et al., Phys. Rev. B **76**, 125413 (2007).
[386] S. Mondal, M. A. Abeed, K. Dutta, A. De, S. Sahoo, A. Barman, and S. Bandyopadhyay, ACS Appl. Mater. Interfaces **10**, 43970 (2018).
[387] C. Berk, M. Jaris, W. Yang, S. Dhuey, S. Cabrini, and H. Schmidt, Nat. Commun. **10**, 2652 (2019).
[388] D. B. Carlton, N. C. Emley, E. Tuchfeld, and J. Bokor, Nano Lett. **8**, 4173 (2008).
[389] A. Imre, G. Csaba, L. Ji, A. Orlov, G. H. Bernstein, and W. Porod, Science (80-. ). **311**, 205 (2006).
[390] D. Kumar, S. Barman, and A. Barman, Sci. Rep. **4**, 4108 (2014).
[391] P. Talatchian, M. Romera, F. A. Araujo, P. Bortolotti, V. Cros, D. Vodenicarevic, N. Locatelli, D. Querlioz, and J. Grollier, Phys. Rev. Appl. **13**, 24073 (2020).
[392] J. C. Gartside, K. D. Stenning, A. Vanstone, H. H. Holder, D. M. Arroo, T. Dion, F. Caravelli, H. Kurebayashi, and W. R. Branford, Nat. Nanotechnol. **17**, 460 (2022).
[393] W. Hu et al., Nat. Commun. **14**, 2562 (2023).
[394] H. Yu et al., Adv. Funct. Mater. **32**, 2203466 (2022).
[395] A. K. Chaurasiya, A. K. Mondal, J. C. Gartside, K. D. Stenning, A. Vanstone, S. Barman, W. R. Branford, and A. Barman, ACS Nano **15**, 11734 (2021).
[396] A. Barman and S. Barman, Phys. Rev. B **79**, 144415 (2009).
[397] A. K. Mondal, C. Banerjee, A. Adhikari, A. K. Chaurasiya, S. Choudhury, J. Sinha, S. Barman, and A. Barman, Phys. Rev. B **101**, 224426 (2020).
[398] H. Pan, V. L. Zhang, K. Di, M. H. Kuok, H. S. Lim, S. C. Ng, N. Singh, and A. O. Adeyeye, Nanoscale Res. Lett. **8**, 115 (2013).
[399] V. L. Zhang, F. S. Ma, H. H. Pan, C. S. Lin, H. S. Lim, S. C. Ng, M. H. Kuok, S. Jain, and A. O. Adeyeye, Appl. Phys. Lett. **100**, 163118 (2012).
[400] M. Pomerantz, Phys. Rev. Lett. **7**, 312 (1961).
[401] B. L. W. Mckeehan and P. P. Ciqffi, **273**, (1925).
[402] Y. K. Kim and T. J. Silva, Appl. Phys. Lett. **2885**, 2885 (1995).
[403] R. M. Bozorth and H. J. Williams, Rev. Mod. Phys. **17**, 72 (1945).

# List of Corrections

1. List of publications of this thesis on page no. ii has been updated.

2. In section 2.1 of Chapter 2, on page no. 8, in line no. 24, following sentence has been added, "These energies typically range from less than 1 kJ $m^{-3}$ to more than 10 MJ $m^{-3}$ [113]."

3. The Figure 4.2 of Chapter 4, on page no. 47 has been updated showing both Stokes and Anti-Stokes sides of BLS spectra.

4. The caption of Figure 4.2 of Chapter 4, on page no. 47 has been updated according to the abovementioned changes.

5. List of figures of this thesis on page no. vii has been updated accordingly to incorporate the change in caption of Figure 4.2.

6. In section 4.3 of Chapter 4, on page no. 48, in line no. 5, following sentences are added, "Here, the linewidth of the BLS peaks is proportional to SW damping. The non-uniform magnetic structure may enhance the damping due to dephasing or interaction of the SWs with the nonuniform spin textures. However, the observed frequency splitting between the modes, anisotropy in frequency and MBG are well above the linewidth of the BLS spectra. Hence, the dephasing effects due to nonuniform magnetic structure is not significant here.''

7. In section 5.2 of Chapter 5, on page no. 54, in line no. 37, following sentences are added, "In the following section, precise agreement between simulated dynamics and experimental dynamics has been discussed. Additionally, using the same parameters magnetic hysteresis loops are simulated since the 150 nm thick Au layer on the top of sample surface does not allow to perform experimental hysteresis loops. However, since the dynamic behavior is well reproduced in simulation as discussed later, the simulated hysteresis loops can mimic the experimental behavior as well.''

8. In section 6.3 of Chapter 6, on page no. 63, in line no. 12, following sentence has been added, "Related figures and descriptions are shown in the reference [263]".

9. In subsection 2.2.1 of Chapter 2, on page no.12, in line no. 9, one typo in the spelling of Lifshitz has been fixed.

10. In section 7.3 of Chapter 7, on page no.78, in line no.13, one typo in the spelling of Dynamics has been fixed.